NEUTRINO OSCILLATIONS

Present Status and Future Plans

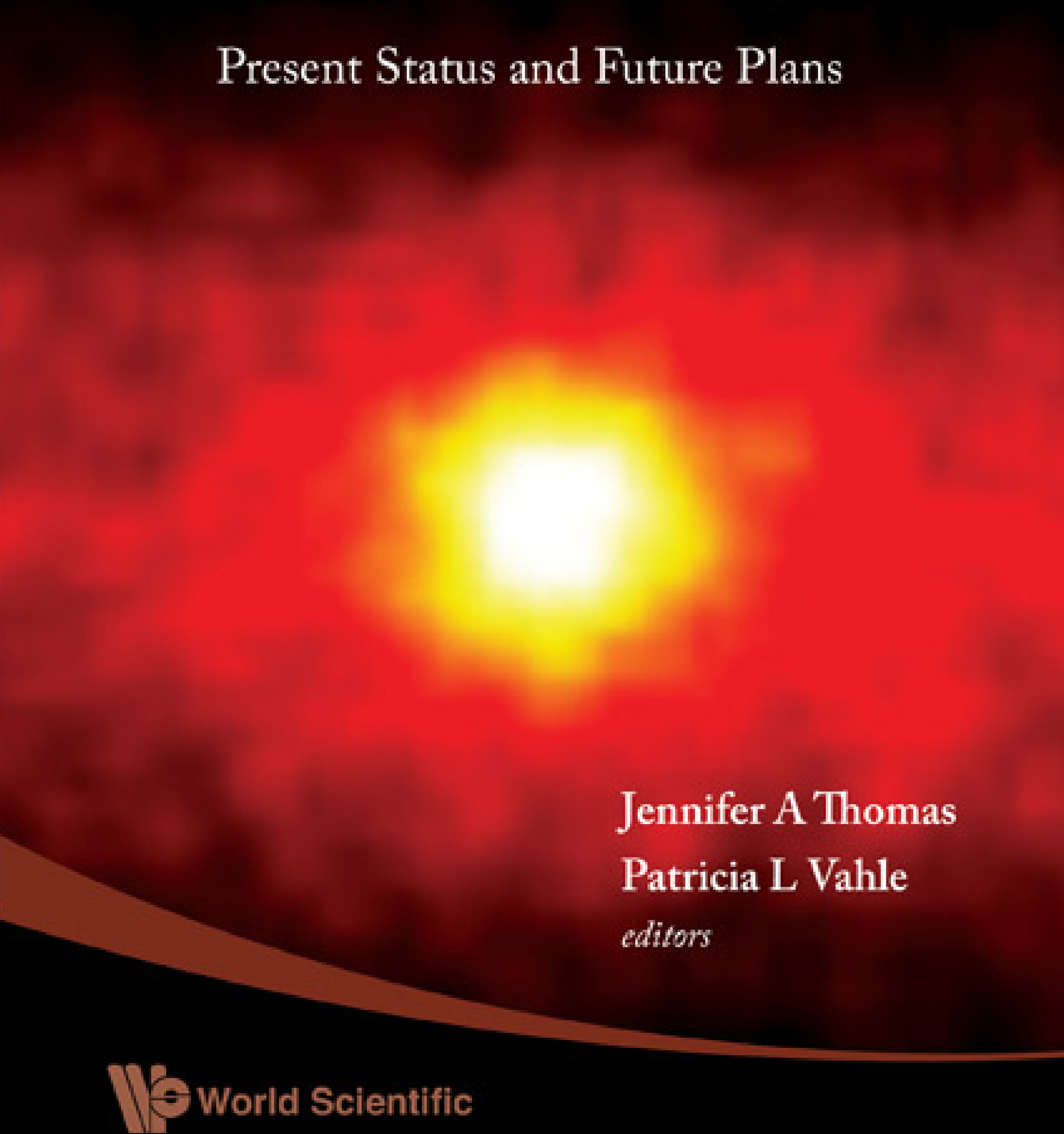

Jennifer A Thomas
Patricia L Vahle
editors

World Scientific

NEUTRINO OSCILLATIONS

Present Status and Future Plans

NEUTRINO OSCILLATIONS

Present Status and Future Plans

editors

Jennifer A Thomas

Patricia L Vahle

UCL, UK

World Scientific

NEW JERSEY • LONDON • SINGAPORE • BEIJING • SHANGHAI • HONG KONG • TAIPEI • CHENNAI

Published by

World Scientific Publishing Co. Pte. Ltd.
5 Toh Tuck Link, Singapore 596224
USA office: 27 Warren Street, Suite 401-402, Hackensack, NJ 07601
UK office: 57 Shelton Street, Covent Garden, London WC2H 9HE

British Library Cataloguing-in-Publication Data
A catalogue record for this book is available from the British Library.

NEUTRINO OSCILLATIONS
Present Status and Future Plans

ISBN-13 978-981-277-196-4
ISBN-10 981-277-196-4

Printed in Singapore.

Preface

This compilation of articles represents a snapshot of our understanding of neutrino oscillations after nearly a decade of discovery. Observation of neutrino oscillations represents physics beyond the three massless neutrinos of the Standard Model; it implies that neutrinos must have mass.

The neutrino mass discovery has been exclusively driven by experiment since the Standard Model with massless neutrinos was written down in 1967. With the advantage of hindsight, it is clear that the first hints of neutrino mass were apparent almost 40 years ago. Its origins reach back to the Homestake Mine in South Dakota when Ray Davis and John Bahcall first began to realize that there was a discrepancy between the predicted and measured number of neutrinos coming from the Sun. Even from the first run of that historic experiment, Ray Davis noted the discrepancy and quipped to his colleague, "We are ready now, turn on the sun.[1]" Much work went into understanding that anomaly, both experimental and theoretical, but it wasn't until the Germanium experiments GALLEX and SAGE also registered fewer neutrinos than expected that the "solar neutrino anomaly" really hit the headlines. In the mean time a number of experiments also discovered neutrino anomalies in detectors designed to look for something totally different: Proton decay. Proton decay was not observed, but careful studies of the neutrino background to those experiments registered fewer muon neutrinos than expected, pointing to a similar effect as that shown by the solar anomaly.

Over the last decade, neutrino oscillations have emerged as the favored explanation of the observed neutrino anomalies. Bruno Pontecorvo first posited the idea of neutrino oscillation in 1957, whereby neutrinos could transform into anti-neutrinos by means of mass eigenstate mixing. Using the formalism of Ziro Maki, Masami Nakagawa and Shoichi Sakata, this idea developed into a theory of flavor oscillations which could explain the

---

[1] R. Davis, Les Prix Nobel. The Nobel Prizes 2002, Editor Tore Frängsmyr, Nobel Foundation, Stockholm, 2003

experimentally observed discrepancies. While the originally proposed oscillation between neutrinos and anti-neutrinos has not been observed, most of the present findings can indeed be explained by mixing among the three neutrino flavor eigenstates, as described in the first chapter of this volume.

Departures from the Standard Model of three massless neutrinos have now been observed in man-made sources of neutrinos. Developments of accelerators such as the high power proton synchrotrons and the magnetic horn devised by Simon Van Der Meer have enabled high power, well understood muon neutrino beams, which have been able to cut across the neutrino production uncertainties which were associated with the experiments using naturally occurring neutrinos. Having provided the source for the first detection of the neutrino, nuclear reactors, with the improved knowledge of all aspects of their operation, are now being used regularly as copious sources of neutrinos. To be able to launch the final suite of experiments which are described in this book, monumental dedication and effort have been spent on developing and building the tools and techniques to enable huge detectors with extremely low backgrounds in deep underground laboratories. These developments have transformed the field from one that observes anomalies, to one that makes precision measurements of the physics behind the anomalies.

We have had to limit this book to articles describing results which have provided major steps forward in understanding the neutrino puzzle. History is also full of reports from experiments whose results were negative, or inconclusive, or presented results that have been superseded. For these many omissions we apologize. The experiments described here summarize the current body of evidence for neutrino oscillations and indicate the gaps in our knowledge. Each chapter describes a piece of the neutrino puzzle, including past, present and future endeavors. The picture has become much clearer in the past decade, but there are still pieces missing from the puzzle. There is perhaps, still room for something rather unexpected. Current experiments could be pointing to a difference between neutrinos and anti-neutrinos at low energy. Precise measurements of the values of the mixing parameters will hopefully provide insight into an underlying symmetry of nature. Mixing between the 1 and 3 mass eigenstates could lead to the observation of CP violation in the lepton sector, which could have far reaching consequences for the field of cosmology. The search for answers to these questions is leading to a proliferation of experiments, and as the development of the neutrino mass story has taught us, there is always scope for something unforeseen.

Contents

Preface v

1. Neutrino Oscillation Phenomenology 1
S. J. Parke

2. The Super-Kamiokande Experiment 19
C. W. Walter

3. Sudbury Neutrino Observatory 45
S. J. M. Peeters and J. R. Wilson

4. Neutrino Oscillation Physics with KamLAND: Reactor Antineutrinos and Beyond 71
K. M. Heeger

5. K2K: KEK to Kamioka Long-Baseline Neutrino Oscillation Experiment 91
R. J. Wilkes

6. MINOS 115
P. Vahle

7. The LSND and KARMEN Neutrino Oscillation Experiments 135

W. C. Louis

8. MiniBooNE 155

S. J. Brice

9. The OPERA Experiment in the CNGS Beam 173

D. Autiero, M. Komatsu, P. Migliozzi and F. Terranova

10. The T2K Experiment 197

D. L. Wark

11. The NOνA Experiment 217

G. J. Feldman

12. Double Chooz 233

G. A. Horton-Smith and T. Lasserre

13. Daya Bay: A Sensitive Determination of θ_{13} with Reactor Antineutrinos 249

K. B. Luk and Y. Wang

Author Index 261

Subject Index 263

Chapter 1

Neutrino Oscillation Phenomenology

Stephen J. Parke
Theoretical Physics Department, Fermi National Accelerator Laboratory,
P. O. Box 500, Batavia, IL 60510, USA
parke@fnal.gov

A summary of neutrino oscillation phenomenology is given within the context of the neutrino mixing model (3 active flavors only) for both the disappearance and appearance modes. Extensions of the model to include one of more sterile neutrinos are discussed.

Contents

1.1 Introduction 1
1.2 The ν_e Disappearance Channel 5
  1.2.1 Reactor Experiments at the Solar L/E 5
  1.2.2 Reactor Experiments at the Atmospheric L/E 6
  1.2.3 Solar Neutrinos 7
1.3 The ν_μ Disappearance Channel 10
1.4 The $\nu_\mu \to \nu_e$ Appearance Channel 11
1.5 Beyond the Neutrino Mixing Model 13
1.6 Summary and Conclusion 16
References 17

1.1. Introduction

In the Standard Model the neutrinos, $(\nu_e,\ \nu_\mu,\ \nu_\tau)$, are massless and interact diagonally in flavor, as follows:

$$\begin{array}{lll} W^+ \to e^+ + \nu_e & W^- \to e^- + \bar{\nu}_e & Z \to \nu_e + \bar{\nu}_e \\ W^+ \to \mu^+ + \nu_\mu & W^- \to \mu^- + \bar{\nu}_\mu & Z \to \nu_\mu + \bar{\nu}_\mu \\ W^+ \to \tau^+ + \nu_\tau & W^- \to \tau^- + \bar{\nu}_\tau & Z \to \nu_\tau + \bar{\nu}_\tau . \end{array} \tag{1.1}$$

Since they travel at the speed of light, their character cannot change from production to detection because the mass eigenstates are the same as the flavor eigenstates. Therefore, in flavor terms, massless neutrinos are relatively uninteresting compared to quarks.

As evidenced by the subsequent chapters of this volume, several experiments have observed neutrino behavior not explained by the massless neutrino described by the Standard Model. The observations of these experiments can most simply be described by introducing the phenomenon of neutrino flavor transitions. Such flavor transitions imply that neutrinos must have mass. Thus, as in the quark sector, there is a mixing matrix relating the flavor states with the mass eigenstates:

$$|\nu_\alpha\rangle = U^*_{\alpha j}|\nu_j\rangle, \tag{1.2}$$

where $\nu_\alpha = (\nu_e,\ \nu_\mu,\ \nu_\tau, \ldots)$, represent the flavor states and $\nu_j = (\nu_1,\ \nu_2,\ \nu_3, \ldots)$ represent the mass eigenstates with mass m_j. The mixing matrix $U_{\alpha j}$ is usually called the MNS[a] mixing matrix.[1]

Neutrino oscillation experiments typically measure the probability of a neutrino produced as flavor ν_α to be detected as flavor ν_β after traveling some distance. If $\alpha = \beta$, this probability is called the survival probability, and for massive neutrinos this probability is given by

$$\begin{aligned} P(\nu_\alpha \to \nu_\alpha) &= P(\bar{\nu}_\alpha \to \bar{\nu}_\alpha) \\ &= \left| \sum_j U^*_{\alpha j} e^{-im_j^2 L/2E} U_{\alpha j} \right|^2 . \end{aligned} \tag{1.3}$$

In words, this is the square of the sum of the amplitudes for the α flavor neutrino to produce a m_j mass state, times a propagator factor, times the amplitude for the m_j mass states to produce the α flavor neutrino. Invariance under CPT forces the survival probability for neutrinos and anti-neutrinos to be identical, in vacuum.

Except for the LSND anomaly, the subject of Chapter 7, all neutrino data can be explained by the following neutrino model:

- 3 light (m_i <1 eV) Neutrinos: only 2 independent Δm^2 ($\Delta m^2_{ij} = m_i^2 - m_j^2$)
- Three active neutrino flavors (no steriles): $\nu_e,\ \nu_\mu,\ \nu_\tau$
- Unitary Mixing Matrix: 3 angles ($\theta_{12},\ \theta_{23},\ \theta_{13}$), 1 Dirac phase ($\delta$), 2 Majorana phases ($\alpha, \beta$)

---

[a] Also referred to as the PMNS matrix.

where the MNS mixing matrix relating flavor to mass eigenstates, can be written as

$$U = \begin{pmatrix} c_{13}c_{12} & c_{13}s_{12} & s_{13}e^{-i\delta} \\ -c_{23}s_{12} - s_{13}c_{12}s_{23}e^{+i\delta} & c_{23}c_{12} - s_{13}s_{12}s_{23}e^{+i\delta} & c_{13}s_{23} \\ s_{23}s_{12} - s_{13}c_{12}c_{23}e^{+i\delta} & -s_{23}c_{12} - s_{13}s_{12}c_{23}e^{+i\delta} & c_{13}c_{23} \end{pmatrix}$$

$$\times \begin{pmatrix} 1 & & \\ & e^{i\alpha} & \\ & & e^{i\beta} \end{pmatrix} \tag{1.4}$$

where $s_{ij} = \sin\theta_{ij}$ and $c_{ij} = \cos\theta_{ij}$. This representation of the mixing matrix can also be written in the factorized form:

$$U = \begin{pmatrix} 1 & & \\ & c_{23} & s_{23} \\ & -s_{23} & c_{23} \end{pmatrix} \begin{pmatrix} c_{13} & & s_{13}e^{-i\delta} \\ & 1 & \\ -s_{13}e^{i\delta} & & c_{13} \end{pmatrix} \begin{pmatrix} c_{12} & s_{12} & \\ -s_{12} & c_{12} & \\ & & 1 \end{pmatrix}$$

$$\times \begin{pmatrix} 1 & & \\ & e^{i\alpha} & \\ & & e^{i\beta} \end{pmatrix} \tag{1.5}$$

In this form, the mixing matrix is decomposed into terms that can be associated with different regimes of mixing that have been explored by different classes of experiments. The (23) sector is identified with the atmospheric Δm^2_{atm} and the (12) sector is identified with the solar $\Delta m^2_{\odot}$. The (13) sector is responsible for ν_e flavor transitions at the atmospheric scale, which are so far unobserved. The Dirac phase, δ, allows for the possibility of CP violation in the appearance modes.

As will be described in this volume, the current best fit values or limits on these parameters are[b]

$$\begin{aligned} \sin^2\theta_{12} &= 0.31 \pm 0.03 \\ \sin^2\theta_{23} &= 0.50 \pm 0.15 \\ \sin^2\theta_{13} &< 0.04 \\ 0 \leq \delta &< 2\pi \end{aligned}$$

and the mass splittings are approximately:

$$|\Delta m^2_{32}| = 2.7 \pm 0.4 \times 10^{-3}\mathrm{eV}^2 \quad \text{and} \quad \Delta m^2_{21} = +8.0 \pm 0.4 \times 10^{-5}\mathrm{eV}^2.$$

---

[b] Some experiments report their results in terms of $\sin^2(2\theta)$, others in terms of $\tan^2\theta$. However, $\sin^2\theta$ is used here, since each of the three $\sin^2\theta$'s approximately corresponds to the fraction of a certain flavor in one of the mass eigenstates as follows: $\sin^2\theta_{13} = |U_{e3}|^2 \ll 1$, $\sin^2\theta_{23} \approx |U_{\mu 3}|^2$ and $\sin^2\theta_{12} \approx |U_{e2}|^2$.

Oscillation experiments are only sensitive to the differences in masses of the neutrinos. The mass of the lightest neutrino is unknown, but the heaviest one should be lighter than about 1 eV. These mixing angles and mass splittings are summarized in Fig. 1.1, which also shows the dependence of the flavor fractions on the CP violating Dirac phase, δ. Since the masses of the neutrinos are as yet unknown, there are two possible arrangements of the mass differences that are consistent with the oscillation experiments. These are called the "Normal Hierarchy" and the "Inverted Hierarchy". The Majorana phases, α and β are unobservable in oscillations since oscillations depend on $U^*_{\alpha i}U_{\beta i}$, but they have observable, CP conserving effects, in neutrinoless double beta decay. If the neutrinos are not Majorana particles, but instead are Dirac particles, then neutrinoless double beta decay will not be observed, and the Majorana phases in the MNS matrix are unobservable and can be set to zero.

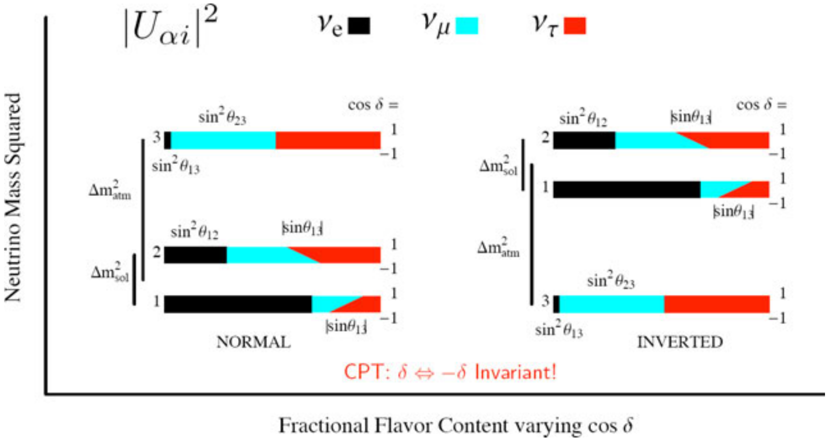

Fig. 1.1. Flavor content of the three neutrino mass eigenstates showing the dependence on the cosine of the CP violating phase, δ. If CPT is conserved, the flavor content must be the same for neutrinos and anti-neutrinos. This figure was adapted from Reference 3.

The unresolved questions within this model that can be addressed in oscillation experiments are

- What is the size of $|U_{e3}|^2$? i.e $\sin^2\theta_{13} = ?$
- Hierarchy: Is $m_3^2 >$ OR $< m_1^2$? i.e. what is the sign of Δm^2_{31}?
- Is there CP violation? i.e. $\sin\delta \neq 0$?
- Is $|U_{\mu 3}|^2 = |U_{\tau 3}|^2$? i.e. $\sin^2\theta_{23} = \frac{1}{2}$?
  If not, is $|U_{\mu 3}|^2 >$ or $< |U_{\tau 3}|^2$? i.e. $\sin^2\theta_{23} >$ or $< \frac{1}{2}$?

Other important questions include

- What is the mass of the lightest neutrino?
- Are Neutrinos Majorana or Dirac?
- Are there more than three neutrinos? Are there sterile neutrinos?
- Do exotic neutrinos interactions exist?

Neutrino oscillation experiments can not answer the first two questions, though they may yet shed light on the final two.

The phenomenology of neutrino oscillations can simplify considerably depending on the values of the parameters involved or on the value of the ratio L/E, the distance traveled divided by the neutrino energy, associated with a given experiment. The following sections discuss specific channels studied by different experiments, the parameters to which they are sensitive, and the approximations that hold in each case.

1.2. The ν_e Disappearance Channel

In the three flavor neutrino model the ν_e survival probability can be written as

$$\begin{aligned} P(\nu_e \to \nu_e) = 1 &- 4|U_{e3}|^2|U_{e1}|^2 \sin^2 \Delta_{31} \\ &- 4|U_{e3}|^2|U_{e2}|^2 \sin^2 \Delta_{32} \\ &- 4|U_{e2}|^2|U_{e1}|^2 \sin^2 \Delta_{21} \end{aligned} \tag{1.6}$$

where the kinematic phase is given by:

$$\Delta_{jk} \equiv \frac{\Delta m^2_{jk} L}{4\hbar c E} = 1.2669 \cdots \left(\frac{\Delta m^2_{jk}}{eV^2}\right)\left(\frac{L}{km}\right)\left(\frac{GeV}{E}\right) \tag{1.7}$$

and the unitarity properties of the MNS matrix have been used. The survival probability given in Equation 1.6 is plotted as a function of L/E in Figure 1.2.

1.2.1. *Reactor Experiments at the Solar L/E*

For experiments at the solar L/E (around 15 km/MeV) without the resolution to resolve the atmospheric oscillations on top of the dominant solar oscillation, such as KamLAND[5] (See Chapter 4), Eq. 1.6 can be written as

$$P(\bar{\nu}_e \to \bar{\nu}_e) = c_{13}^4(1 - \sin^2 2\theta_{12} \sin^2 \Delta_{21}) + s_{13}^4. \tag{1.8}$$

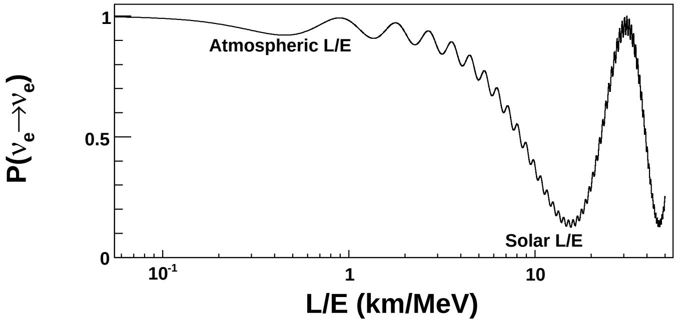

Fig. 1.2. The ν_e survival probability as a function of L/E for the oscillation parameters given in Section 1.1 and $\sin^2\theta_{13} = 0.02$.

Since s_{13}^4 is known to be very small, $< 10^{-3}$, the only effect of non-zero θ_{13} is a multiplicative reduction of the survival probability. To measure this overall reduction requires precise knowledge of the neutrino flux from the reactor(s). However, the solar parameters and in particular Δm_{21}^2 can be measured with high precision in such an experiment.

1.2.2. *Reactor Experiments at the Atmospheric L/E*

For experiments at the atmospheric L/E (around 0.5 km/MeV), such as CHOOZ,[6] Palo Verde,[7] Double-Chooz[8] and Daya Bay (See Chapters 12 and 13), the survival probability, Eq. 1.6, can be written as

$$P(\bar{\nu}_e \to \bar{\nu}_e) = 1 - \sin^2 2\theta_{13} \sin^2 \Delta_{ee} + \mathcal{O}(\Delta_{21}^2) \tag{1.9}$$

where $\Delta_{ee} = \Delta m_{ee}^2 L/4E$, and Δm_{ee}^2 is the effective atmospheric Δm^2 for the ν_e oscillation channel,[9] given by

$$\Delta m_{ee}^2 \equiv c_{12}^2 |\Delta m_{31}^2| + s_{12}^2 |\Delta m_{32}^2|. \tag{1.10}$$

That is, the electron flavor weighted average of Δm_{31}^2 and Δm_{32}^2. The experiments Double Chooz and Daya Bay are designed to measure or put a limit on the size of $\sin^2\theta_{13}$ significantly below the current limit of

$$\sin^2\theta_{13} < 0.04 \tag{1.11}$$

at the best fit value for the atmospheric Δm^2.

1.2.3. *Solar Neutrinos*

Solar neutrinos are somewhat more complicated because of the matter effects that the neutrinos experience from the production region until they exit the sun. As the neutrino propagates in matter, the electron neutrino plays a special role due to the forward scattering of the electron neutrino on the electrons in the matter coming from W-boson exchange, i.e. the charged current interaction[c]. This additional contribution to the Hamiltonian from $\nu_e + e$ scattering is $-\sqrt{2}G_F N_e$, which appears only for the electron neutrino. For $\bar{\nu}_e + e$ scattering the sign is flipped. G_F is the Fermi constant and N_e is the number density of electrons in matter. This implies that the matter mass eigenstates are different than the vacuum mass eigenstates and that the Δm^2 and mixing angle, θ, in matter are related to their vacuum values as follows:

$$\begin{aligned}\Delta m_N^2 \cos 2\theta_N &= \Delta m_0^2 \cos 2\theta_0 - 2\sqrt{2}G_F N_e E_\nu \\ \Delta m_N^2 \sin 2\theta_N &= \Delta m_0^2 \sin 2\theta_0 .\end{aligned} \tag{1.12}$$

The subscript on Δm^2 and θ denotes the value of the number density of electrons. For large values of the number density of electrons, the mixing angle in matter, θ_N, approaches $\pi/2$. Thus, the higher neutrino mass state becomes nearly completely ν_e. The minimum value of Δm_N^2 occurs when $\Delta m_0^2 \cos 2\theta_0 = 2\sqrt{2}G_F N_e E_\nu$ and $\theta_N = \pi/4$. This point is known as the Mikheyev-Smirnov resonance.

The matter effect is proportional to the energy of the neutrino. Since the pp (^{7}Be) have a mean energy of 0.2 MeV (0.9 MeV), these neutrinos are little affected by the matter and undergo quasi-vacuum oscillations. The ^{8}B neutrinos, on the other hand, have a mean energy of 10 MeV and because of matter effects are produced and exit the sun mainly as a ν_2 mass eigenstate and therefore do not undergo vacuum oscillations.

The kinematic phase for solar neutrinos is

$$\Delta_\odot = \frac{\Delta m_\odot^2 L}{4E} = 10^{7\pm1}. \tag{1.13}$$

where $\Delta m_\odot^2 = \Delta m_{21}^2$. Therefore, the solar neutrinos are "effectively incoherent" when they reach the earth. Hence the ν_e survival probability is given by

$$\langle P(\nu_e \to \nu_e)\rangle = f_1 \cos^2\theta_\odot + f_2 \sin^2\theta_\odot \tag{1.14}$$

$$\text{where} \quad f_1 + f_2 = 1 \quad \text{and} \quad \cos^2\theta_\odot + \sin^2\theta_\odot = 1,$$

---

[c] Interactions via Z-bosons are the same for all flavors and therefore effect all neutrinos equally.

where f_1 and f_2 are the fraction of neutrinos that are ν_1 and ν_2 respectively. The pp and ^{7}Be solar neutrinos behave essentially as in vacuum[d] and therefore $f_1 \approx \cos^2\theta_\odot = 0.69$ and $f_2 \approx \sin^2\theta_\odot = 0.31$, whereas the mass eigenstate fraction for the ^{8}B are substantially different, $f_2 \approx 0.9$ due to Mikheyev-Smirnov-Wolfenstein[10] matter effects (see Fig. 1.3).

In a two neutrino analysis, the *day-time* charged current to neutral current ratio (CC/NC) of SNO (See Chapter 3), which is equivalent to the day-time average ν_e survival probability, $\langle P_{ee}\rangle = P(\nu_e \to \nu_e)$, is given by

$$\left.\frac{\mathrm{CC}}{\mathrm{NC}}\right|_{\mathrm{day}} = \langle P_{ee}\rangle = \sin^2\theta_\odot + f_1 \cos 2\theta_\odot, \tag{1.15}$$

where f_1 and $f_2 = 1 - f_1$ are understood to be the ν_1 and ν_2 fractions, respectively, averaged over the ^{8}B neutrino energy spectrum weighted with the charged current cross section. Therefore, the ν_1 fraction (or how much f_2 differs from 100%) is given by

$$f_1 = \frac{\left(\left.\frac{\mathrm{CC}}{\mathrm{NC}}\right|_{\mathrm{day}} - \sin^2\theta_\odot\right)}{\cos 2\theta_\odot} = \frac{(0.347 - 0.311)}{0.378} \approx 10\ \%, \tag{1.16}$$

where the central values of the recent SNO analysis[11] have been used.

For solar neutrinos the matter effects on Δm^2 and θ are shown in Fig. 1.3. As the electron number density[e] times energy of the neutrinos gets larger, the mixing angle approaches $\pi/2$ and the Δm^2 approaches $2\sqrt{2}G_F N_e E_\nu$. Therefore, a solar ν_e born in an environment with high $2\sqrt{2}G_F N_e E_\nu$ is approximately born as a ν_2 matter mass eigenstate.

Using the analytical analysis of the MSW effect given in Reference 12, the mass eigenstate fractions are given by

$$f_2 = 1 - f_1 = \langle \sin^2\theta_\odot^N + P_x \cos 2\theta_\odot^N \rangle_{^8\mathrm{B}}, \tag{1.17}$$

where $\theta_\odot^N$ is the mixing angle defined at the ν_e production point and P_x is the probability of the neutrino to jump from one mass eigenstate to the other during the Mikheyev-Smirnov (MS) resonance crossing. In the large mixing angle region P_x is zero to high precision. The average $\langle \cdots \rangle_{^8\mathrm{B}}$ is over the electron density of the ^{8}B ν_e production region in the center of the Sun predicted by the Standard Solar Model and the energy spectrum

---

[d] In vacuum, a ν_e has a ν_1 fraction equal to $\cos^2\theta_\odot$ and a ν_2 fraction equal to $\sin^2\theta_\odot$. Whereas the probability of finding a ν_e in a ν_1 is $\cos^2\theta_\odot$, for a ν_2, the ν_e fraction is $\sin^2\theta_\odot$.

[e] $N_e = \rho Y_e / M_n$ where Y_e is the electron fraction, ρ is the density and M_n is the nucleon mass.

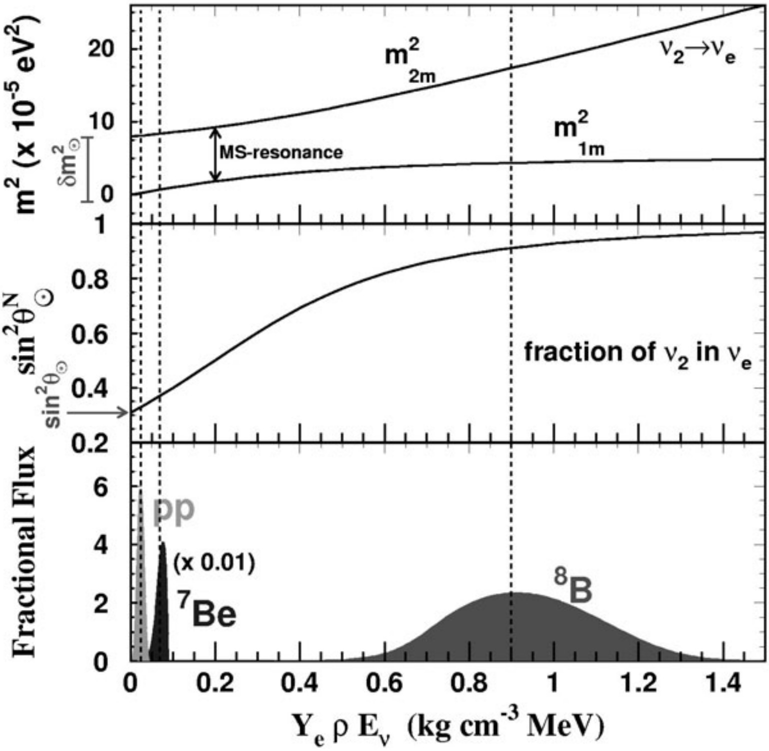

Fig. 1.3. The mass spectrum (top panel), the fraction of ν_2's produced, $\sin^2\theta_\odot^N$, (middle panel) and the fractional flux (bottom panel) versus the product of the electron fraction, Y_e, the matter density, ρ, and the neutrino energy, E_ν, for the best fit values $\Delta m_\odot^2 = 8.0 \times 10^{-5}\text{eV}^2$ and $\sin^2\theta_\odot = 0.310$. The vertical dashed lines give the value of $Y_e\rho E_\nu$ which reproduces the average ν_2 fractions, 91, 37 and 33% for ^{8}B, ^{7}Be and pp respectively. This value of $Y_e\rho E_\nu = 0.89\,\text{kg cm}^{-3}$ MeV, for the ^{8}B neutrinos, gives a production mixing angle equal to 73° and a production $\Delta m_N^2 = 13 \times 10^{-5}\,\text{eV}^2$. The matter potential, A, is related to density factor, $Y_e\rho E_\nu$, by $A \equiv 2\sqrt{2}G_F(Y_e\rho/M_n)E_\nu = 15.3 \times 10^{-5}\text{eV}^2\,\big(Y_e\rho\ E_\nu/\text{kg cm}^{-3}\text{ MeV}\big)$. Reproduced from Reference 13.

of ^{8}B neutrinos weighted with SNO's charged current cross section. Thus, the ^{8}B energy weighted average fraction of ν_2's observed by SNO is[13]

$$\begin{aligned} f_2 = \langle \sin^2\theta_\odot^N \rangle_{^8\text{B}} &= \frac{1}{2} + \frac{1}{2}\left\langle \frac{(A - \Delta m_\odot^2 \cos 2\theta_\odot)}{\sqrt{(\Delta m_\odot^2 \cos 2\theta_\odot - A)^2 + (\Delta m_\odot^2 \sin 2\theta_\odot)^2}} \right\rangle_{^8\text{B}} \\ &= 91 \pm 2\% \quad \text{at the 95\% CL,} \end{aligned} \tag{1.18}$$

where $A = 2\sqrt{2}G_F(Y_e\rho/M_n)E_\nu$. Hence, the ^{8}B solar neutrinos are the purest mass eigenstate neutrino beam known so far, and Super-K's[14], famous picture of the sun taken with neutrinos is more than 80% ν_2!

1.3. The ν_μ Disappearance Channel

In vacuum, the ν_μ survival probability is given by

$$\begin{aligned} P(\nu_\mu \to \nu_\mu) = 1 &- 4|U_{\mu 3}|^2|U_{\mu 1}|^2 \sin^2 \Delta_{31} \\ &-4|U_{\mu 3}|^2|U_{\mu 2}|^2 \sin^2 \Delta_{32} \\ &-4|U_{\mu 2}|^2|U_{\mu 1}|^2 \sin^2 \Delta_{21}. \end{aligned} \quad (1.19)$$

The ν_μ survival probability is plotted as a function of E at a fixed L in Figure 1.4.

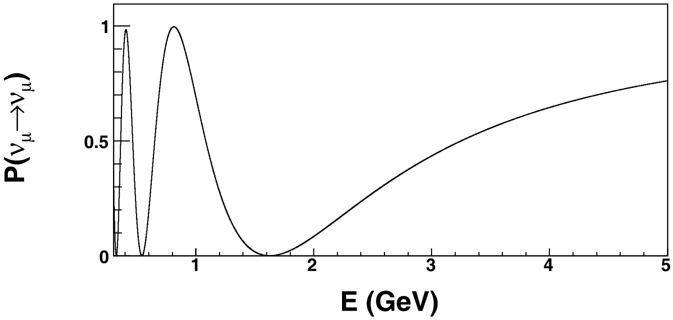

Fig. 1.4. The ν_μ survival probability as a function of E for the oscillation parameters given in Section 1.1 and $L = 735$ km.

For experiments at the atmospheric L/E (around 500 km/GeV), such as K2K,[15] MINOS,[16] T2K[17] and NOνA[18] (See Chapters 5, 6, 10, and 11) in $\nu_\mu \to \nu_\mu$ mode , Eq. 1.19, can be written as

$$P(\nu_\mu \to \nu_\mu) = 1 - 4|U_{\mu 3}|^2(1 - |U_{\mu 3}|^2) \sin^2 \Delta_{\mu\mu} + \mathcal{O}(\Delta_{21}^2) \quad (1.20)$$

where $|U_{\mu 3}|^2 = c_{13}^2 s_{23}^2$ and $\Delta_{\mu\mu} = \Delta m_{\mu\mu}^2 L/4E$. $\Delta m_{\mu\mu}^2$ is the effective atmospheric Δm^2 for the ν_μ disappearance channel[f] given by

$$\Delta m^2_{\mu\mu} \equiv \frac{|U_{\mu 1}|^2 |\Delta m^2_{31}| + |U_{\mu 2}|^2 |\Delta m^2_{32}|}{(|U_{\mu 1}|^2 + |U_{\mu 2}|^2)}, \tag{1.21}$$

i.e. the muon flavor weighted average of Δm^2_{31} and Δm^2_{32}. In the limit that $\theta_{13} \to 0$

$$4|U_{\mu 3}|^2(1 - |U_{\mu 3}|^2) = \sin^2 2\theta_{23} \tag{1.22}$$

$$\text{and} \quad \Delta m^2_{\mu\mu} = s^2_{12}|\Delta m^2_{31}| + c^2_{12}|\Delta m^2_{32}|. \tag{1.23}$$

The difference between $\Delta m^2_{\mu\mu}$ and $|\Delta m^2_{32}|$ is given by $\pm s^2_{12}\Delta m^2_{21}$ which is approximately a 1% shift whose sign depends on the hierarchy. This form of the oscillation probability is used by Super-K (See Chapter 2) in their two flavor analysis of atmospheric neutrinos.

1.4. The $\nu_\mu \to \nu_e$ Appearance Channel

The most likely genuine three flavor effects to be first observed are long baseline $\nu_\mu \to \nu_e$ or one of its CP and T conjugate processes. That is, in one of following transitions:

$$\begin{tikzcd}
\nu_\mu \to \nu_e \arrow[r, Leftrightarrow, "\mathrm{CP}"] \arrow[d, Leftrightarrow, "\mathrm{T}"'] & \bar{\nu}_\mu \to \bar{\nu}_e \arrow[d, Leftrightarrow, "\mathrm{T}"] \\
\nu_e \to \nu_\mu \arrow[r, Leftrightarrow, "\mathrm{CP}"'] & \bar{\nu}_e \to \bar{\nu}_\mu
\end{tikzcd}$$

Processes across the diagonal are related by CPT. The first row will be explored in very powerful conventional beams, called Superbeams. Such beams are accessible with extensions of currently available technologies. The second row could be explored using more exotic techniques involving a Neutrino Factory or a Beta Beam, a pure beam of ν_e produced via the beta decay of accelerated radioactive ions.

---

[f] The difference between the two effective atmospheric Δm^2 is small and depends on the hierarchy. $\Delta m^2_{ee} - \Delta m^2_{\mu\mu} = \pm \Delta m^2_{21}(\cos 2\theta_{12} - \cos\delta \sin\theta_{13} \sin 2\theta_{12} \tan\theta_{23})$ where the + (-) is for the normal (inverted) hierarchies.[9]

In vacuum, the probability for $\nu_\mu \to \nu_e$ is derived like so:[19]

$$\begin{aligned} P(\nu_\mu \to \nu_e) &= |\, U^*_{\mu 1} e^{-im_1^2 L/2E} U_{e1} + U^*_{\mu 2} e^{-im_2^2 L/2E} U_{e2} + U^*_{\mu 3} e^{-im_3^2 L/2E} U_{e3} \,|^2 \\ &= |2U^*_{\mu 3} U_{e3} \sin\Delta_{31} e^{-i\Delta_{32}} + 2U^*_{\mu 2} U_{e2} \sin\Delta_{21}|^2 \\ &\approx |\sqrt{P_{atm}} e^{-i(\Delta_{32}+\delta)} + \sqrt{P_{sol}}|^2 \end{aligned} \tag{1.24}$$

where the unitarity of the MNS matrix has been used, $U^*_{\mu 1} U_{e1} + U^*_{\mu 2} U_{e2} + U^*_{\mu 3} U_{e3} = 0$, and $\sqrt{P_{atm}} = \sin\theta_{23} \sin 2\theta_{13} \sin\Delta_{31}$ and $\sqrt{P_{sol}} \approx \cos\theta_{23} \sin 2\theta_{12} \sin\Delta_{21}$. For anti-neutrinos δ must be replaced with $-\delta$ and the interference term changes:

$$2\sqrt{P_{atm}}\sqrt{P_{sol}} \cos(\Delta_{32}+\delta) \Rightarrow 2\sqrt{P_{atm}}\sqrt{P_{sol}} \cos(\Delta_{32}-\delta).$$

Expanding $\cos(\Delta_{32} \pm \delta)$, one has a CP conserving part,

$$2\sqrt{P_{\rm atm}}\sqrt{P_{\rm sol}} \cos\Delta_{32} \cos\delta \tag{1.25}$$

and the CP violating part,

$$\mp 2\sqrt{P_{\rm atm}}\sqrt{P_{\rm sol}} \sin\Delta_{32} \sin\delta, \tag{1.26}$$

where - (+) sign is for neutrino (anti-neutrino). This allows for the possibility that CP violation could be observed in the neutrino sector since it allows for $P(\nu_\mu \to \nu_e) \neq P(\bar{\nu}_\mu \to \bar{\nu}_e)$.

In matter, $\sqrt{P_{atm}}$ and $\sqrt{P_{sol}}$ are modified as follows:

$$\begin{aligned} \sqrt{P_{atm}} &\Rightarrow \sin\theta_{23} \sin 2\theta_{13} \frac{\sin(\Delta_{31} - aL)}{(\Delta_{31} - aL)} \Delta_{31} \\ \sqrt{P_{sol}} &\Rightarrow \cos\theta_{23} \sin 2\theta_{12} \frac{\sin(aL)}{(aL)} \Delta_{21}, \end{aligned} \tag{1.27}$$

where $a = \pm G_F N_e/\sqrt{2} \approx (4000\ km)^{-1}$, and the sign is positive for neutrinos and negative for anti-neutrinos. This change follows since in both the (31) and (21) sectors, the product $\{\Delta m^2 \sin 2\theta\}$ is approximately independent of matter effects. Figure 1.5 shows the ν_e appearance probability as a function of the distance for neutrinos and anti-neutrinos for both mass orderings at an energy appropriate for T2K, E=0.6 GeV. Fig. 1.6 shows the ν_e appearance probability as a function of the neutrino energy at a distance appropriate for NOνA, L=810 km. In Figs. 1.7 and 1.8 the correlation between the ν_e appearance oscillation probabilities for neutrinos and antineutrinos are shown for both T2K, and NOνA. It is possible that these two experiments will determine the mass ordering (normal or inverted hierarchy, see Fig. 1.1), and observe CP violation in the neutrino sector.

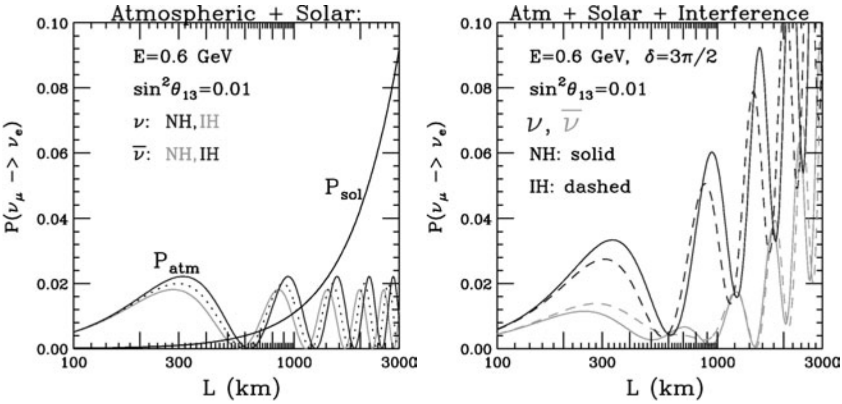

Fig. 1.5. The left panel shows the atmospheric and solar components of the ν_e appearance probability for a neutrino energy of 0.6 GeV for both neutrinos and anti-neutrinos and both mass orderings as a function of the baseline. The dotted P_{atm} curve is the vacuum atmospheric appearance probability. P_{sol} is independent of the hierarchy and the same for neutrinos and anti-neutrinos. The T2K experiment will be performed at approximately this energy at a distance of 295 km and, if constructed, T2KK will be around 1000 km. The right panel shows the full appearance probability including the interference term for $\delta = 3\pi/2$. The appearance probabilities for $\delta = \pi/2$ can be obtained from these, by interchanging normal and inverted as well as neutrinos and anti-neutrinos.

1.5. Beyond the Neutrino Mixing Model

Except for the LSND anomaly[20] (See Chapter 7), all neutrino flavor transitions observed so far can be explained using three massive neutrinos that are orthogonal mixtures of the three neutrinos of given flavor. The LSND anomaly is the observation of $\bar{\nu}_\mu \rightarrow \bar{\nu}_e$ at an L/E of order 500 m/GeV with a transition probability of 0.2%. This suggested the possibility of one or more additional neutrinos which have a squared mass splitting from the active neutrinos of order 1 eV^2. These additional light neutrinos cannot have $SU(2) \times U(1)$ quantum numbers, otherwise their effects would have been observed in other processes, e.g. the decay of Z-boson. Hence, they are called sterile neutrinos. One additional sterile neutrino is marginally compatible with all existing data in the 3+1 scenario[g]. The strongest constraints on this model come from ν_e and ν_μ disappearance experiments. The disappearance of ν_e at the LSND L/E depends on the fraction, $|U_{e4}|^2$, of ν_e in the additional 4th-neutrino and similarly for ν_μ. The non-observation

---

[g] In the 3+1 model the additional neutrino is split from the other neutrinos by order of 1 eV^2.

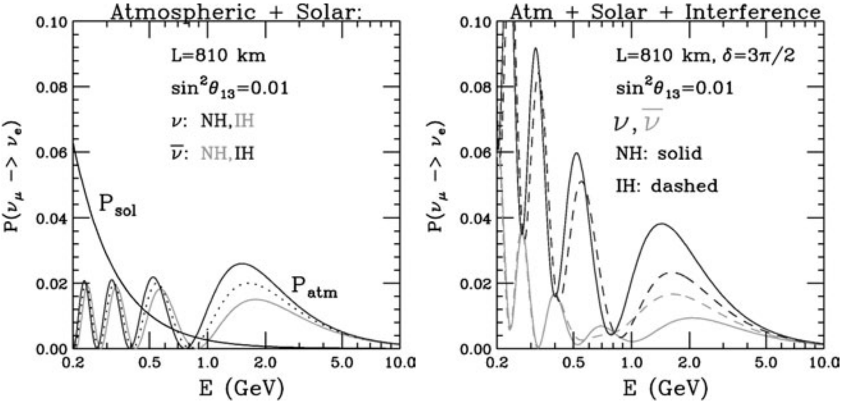

Fig. 1.6. The left panel shows the atmospheric and solar components of the ν_e appearance probability at a distance of 810 km for both neutrinos and anti-neutrinos and both mass orderings as a function of the neutrino energy. The dotted P_{atm} curve is the vacuum atmospheric appearance probability. P_{sol} is independent of the hierarchy and the same for neutrinos and anti-neutrinos. The NOνA experiment will be performed at this distance with an energy centered at 2 GeV. If an experiment is mounted at the second oscillation maximum at this distance the energy would be approximately 0.6 GeV. The right panel shows the full appearance probability including the interference term for $\delta = 3\pi/2$. The appearance probabilities for $\delta = \pi/2$ can be obtained from these, by interchanging normal and inverted as well as neutrinos for anti-neutrinos.

of disappearance of both ν_e and ν_μ implies that both $|U_{e4}|^2$ and $|U_{\mu4}|^2$ are small. In this 3+1 model, the LSND appearance of $\bar{\nu}_e$ from $\bar{\nu}_\mu$ depends on the product of these two small quantities, $|U_{e4}|^2|U_{\mu4}|^2$. Thus, moderate limits on the disappearance modes can severely constrain the appearance mode. In a full analysis of both the disappearance and appearance channels, only a few small atolls are not excluded at high confidence level in the $\{\Delta m^2, \sin^2 2\theta\}_{LSND}$ plane. The 2+2 scenario[h] is strongly disfavored, since both the solar and atmospheric oscillations are primarily due to active neutrino oscillations. In this model one or both of these phenomena would have to have a substantial sterile neutrino component.

What about the possibility of more than one sterile neutrino? With two or more additional neutrinos the parameters can be chosen so as to be compatible with all existing data, even with the recent non-observation by MiniBooNE[21] (See Chapter 8) of $\nu_\mu \to \nu_e$ at the same L/E and sensitivity as LSND.[22] This can occur because of the possibility of CP violation at

---

[h] In the 2+2 model the solar neutrino pair is split from the atmospheric neutrino pair by order of 1 eV^2.

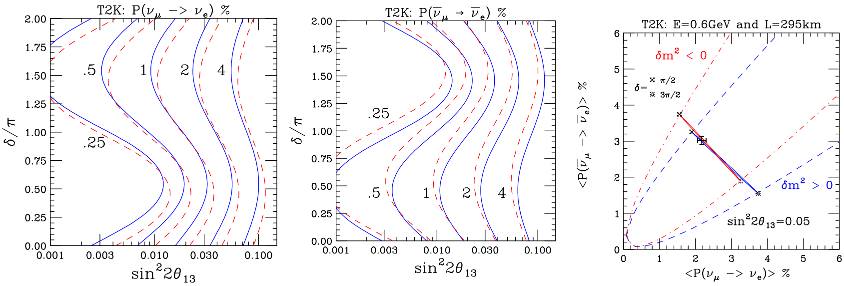

Fig. 1.7. The left and middle panels are the iso-probability contours for T2K as a % for the neutrino (left) and anti-neutrino (middle) channels. The solid (blue) line is for the normal hierarchy whereas the dashed (red) line is for the inverted hierarchy. The right panel is the bi-probability plot showing the correlation between the two probabilities and is reproduced from Reference 4. The matter effect is small but non-negligible for T2K.

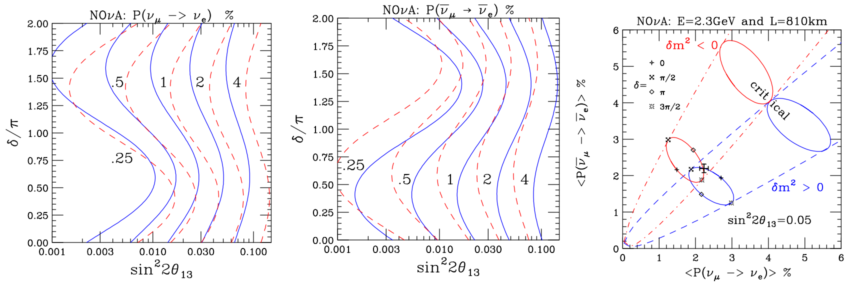

Fig. 1.8. The left and middle panels are the iso-probability contours for NOνA as a % for the neutrino (left) and anti-neutrino (middle) channels. The solid (blue) line is for the normal hierarchy whereas the dashed (red) line is for the inverted hierarchy. The right panel is the bi-probability plot showing the correlation between the two probabilities and is reproduced from Reference 4. The matter effects, and hence the separation between the hierarchies, is 3 times larger for NOνA than T2K primarily due to the fact NOνA has three times the baseline as T2K. The difference in the matter effect between T2K and NOνA can be used to untangle CP violation and the mass hierarchy.

the LSND L/E in models with two or more additional neutrinos. Let us consider the 3+2 model in some detail. If we label the masses of the two additional neutrinos m_4 and m_5 then following Eq. 1.24 gives

$$\begin{aligned} P(\nu_\mu \to \nu_e) &= |2U^*_{\mu 5}U_{e5}\sin\Delta_{51}e^{-i\Delta_{54}} + 2U^*_{\mu 4}U_{e4}\sin\Delta_{41}|^2 \\ &= 4|U_{\mu 5}|^2|U_{e5}|^2\sin^2\Delta_{51} + 4|U_{\mu 4}|^2|U_{e4}|^2\sin^2\Delta_{41} \\ &\quad + 8|U_{\mu 5}||U_{e5}||U_{\mu 4}||U_{e4}| \\ &\quad \times \sin\Delta_{51}\sin\Delta_{41}\cos(\Delta_{54}+\delta_{54}) \end{aligned} \tag{1.28}$$

where $\delta_{54} = \pm \arg(U^*_{\mu 5} U_{e5} U_{\mu 4} U^*_{e4})$. The positive sign is for $\nu_\mu \to \nu_e$ whereas the negative sign is for $\bar{\nu}_\mu \to \bar{\nu}_e$. At the LSND L/E the difference between the masses, m_1, m_2 and m_3 is too small to be relevant, so m_1 has been used as the common mass of these neutrinos, i.e. $\Delta_{51} \approx \Delta_{52} \approx \Delta_{53}$ and $\Delta_{41} \approx \Delta_{42} \approx \Delta_{43}$. The last term of Eq. 1.28 is the interference term between the two amplitudes which can be constructive for $\bar{\nu}_\mu \to \bar{\nu}_e$ and destructive for $\nu_\mu \to \nu_e$, allowing for the possibility that

$$P(\bar{\nu}_\mu \to \bar{\nu}_e) > P(\nu_\mu \to \nu_e). \tag{1.29}$$

This is a possible explanation of why LSND saw a signal in anti-neutrinos, whereas MiniBooNE does not see a signal in neutrinos at approximately the same sensitivity. The ν_e and ν_μ survival probabilities are given by

$$\begin{aligned} P(\nu_\alpha \to \nu_\alpha) &= P(\bar{\nu}_\alpha \to \bar{\nu}_\alpha) \\ &\approx 1 - 4|U_{\alpha 5}|^2 \sin^2 \Delta_{51} - 4|U_{\alpha 4}|^2 \sin^2 \Delta_{41} \\ &\quad + \mathcal{O}((|U_{\alpha 4}|^2 + |U_{\alpha 5}|^2)^2) \end{aligned} \tag{1.30}$$

where $\nu_\alpha = \nu_e$ or ν_μ. The spreading of the limit on the survival probabilities between two distinct Δm^2, Δm^2_{41} and Δm^2_{51}, reduces the severity of the constraints on the appearance modes compared to the 3+1 models. An improvement on the limit of both disappearance modes by a factor of $\sqrt{2}$ would improve the constraint on the appearance mode by a factor of 2 for all values of the CP violating phase δ_{54}.

1.6. Summary and Conclusion

A summary of neutrino oscillation phenomenology has been presented. The oscillation probabilities in the disappearance channels for ν_e and ν_μ flavors have been presented with the relevant approximations for the experiments that will be discussed later in this volume. The appearance probability for $\nu_\mu \to \nu_e$ and $\bar{\nu}_\mu \to \bar{\nu}_e$ has been discussed in some detail with particular attention to the unresolved questions associated with the neutrino mass hierarchy and CP violation. This channel is the most likely one to provide the first observation of genuine three flavor effects.

Beyond the 3 flavor mixing model, the addition of one or more sterile neutrinos has been discussed. In these models, there are additional L/E's for which oscillation phenomena can potentially be observed. If there is more than one additional neutrino, CP violating effects can be important.

Acknowledgments

I would like to thank the editors of this review for their critical reading of this article and their suggestions for improvements. Fermilab is operated by URA under DOE contract DE-AC02-76CH03000.

References

1. Z. Maki, M. Nakagawa and S. Sakata, Prog. Theor. Phys. **28**, 870 (1962).
2. W. M. Yao *et al.* [Particle Data Group], J. Phys. G **33**, 1 (2006).
3. O. Mena and S. J. Parke, Phys. Rev. D **69**, 117301 (2004) [arXiv:hep-ph/0312131].
4. O. Mena and S. J. Parke, Phys. Rev. D **70**, 093011 (2004) [arXiv:hep-ph/0408070].
5. K. Eguchi *et al.* [KamLAND Collaboration], Phys. Rev. Lett. **90**, 021802 (2003). T. Araki *et al.* [KamLAND Collaboration], Phys. Rev. Lett. **94**, 081801 (2005).
6. M. Apollonio *et al.* [CHOOZ Collaboration], Phys. Lett. B **466**, 415 (1999).
7. F. Boehm *et al.*, Phys. Rev. D **64**, 112001 (2001) [arXiv:hep-ex/0107009].
8. F. Ardellier *et al.* [Double Chooz Collaboration], arXiv:hep-ex/0606025.
9. H. Nunokawa, S. J. Parke and R. Zukanovich Funchal, Phys. Rev. D **72**, 013009 (2005) [arXiv:hep-ph/0503283]. H. Minakata, H. Nunokawa, S. J. Parke and R. Zukanovich Funchal, Phys. Rev. D **74**, 053008 (2006) [arXiv:hep-ph/0607284].
10. L. Wolfenstein, Phys. Rev. D **17**, 2369 (1978) and Neutrino 1978, pg C3-C6 edited by E. C. Fowler. S. P. Mikheyev and A. Yu. Smirnov, Yad. Fiz. **42**, 1441 (1985) [Sov. J. Nucl. Phys. **42**, 913 (1985)]; Nuovo Cim. C **9**, 17 (1986).
11. B. Aharmim *et al.* [SNO Collaboration], arXiv:nucl-ex/0502021. Also in this volume.
12. S. J. Parke, Phys. Rev. Lett. **57**, 1275 (1986); S. J. Parke and T. P. Walker, Phys. Rev. Lett. **57**, 2322 (1986).
13. H. Nunokawa, S. J. Parke and R. Zukanovich Funchal, Phys. Rev. D **74**, 013006 (2006) [arXiv:hep-ph/0601198].
14. K. S. Hirata *et al.* [KAMIOKANDE-II Collaboration], Phys. Rev. Lett. **65**, 1297 (1990); M. B. Smy *et al.* [Super-Kamiokande Collaboration], Phys. Rev. D **69**, 011104 (2004); J. Hosaka *et al.* [Super-Kamkiokande Collaboration], arXiv:hep-ex/0508053.
15. E. Aliu *et al.* [K2K Collaboration], Phys. Rev. Lett. **94**, 081802 (2005) [arXiv:hep-ex/0411038].
16. D. G. Michael *et al.* [MINOS Collaboration], Phys. Rev. Lett. **97**, 191801 (2006) [arXiv:hep-ex/0607088].
17. Y. Itow *et al.*, arXiv:hep-ex/0106019.
18. D. S. Ayres *et al.* [NOvA Collaboration], arXiv:hep-ex/0503053.
19. A. Cervera, A. Donini, M. B. Gavela, J. J. Gomez Cadenas, P. Hernandez, O. Mena and S. Rigolin, Nucl. Phys. B **579**, 17 (2000) [Erratum-ibid. B **593**,

731 (2001)] [arXiv:hep-ph/0002108].

20. A. Aguilar *et al.* [LSND Collaboration], Phys. Rev. D **64**, 112007 (2001) [arXiv:hep-ex/0104049].
21. A. A. Aguilar-Arevalo *et al.* [The MiniBooNE Collaboration], arXiv: 0704.1500 [hep-ex].
22. G. Karagiorgi, A. Aguilar-Arevalo, J. M. Conrad, M. H. Shaevitz, K. Whisnant, M. Sorel and V. Barger, Phys. Rev. D **75**, 013011 (2007) [arXiv:hep-ph/0609177].

Chapter 2

The Super-Kamiokande Experiment

Christopher W. Walter*
Department of Physics, Duke University, Durham, NC 27708 USA
chris.walter@duke.edu

Super-Kamiokande is a 50 kiloton water Cherenkov detector located at the Kamioka Observatory of the Institute for Cosmic Ray Research, University of Tokyo. It was designed to study neutrino oscillations and carry out searches for the decay of the nucleon. The Super-Kamiokande experiment began in 1996 and in the ensuing 10 years of running has produced extremely important results in the fields of atmospheric and solar neutrino oscillations. Furthermore, it has set stringent limits on the decay of the nucleon and the existence of dark matter and astrophysical sources of neutrinos. Perhaps most crucially, Super-Kamiokande was the first to definitively show that neutrinos have mass and undergo flavor oscillations. This chapter will summarize the published scientific output of the experiment with a particular emphasis on the atmospheric neutrino results.

Contents

2.1 Introduction and Physics Goals 19
2.2 The Super-Kamiokande Detector 20
2.3 Published Results from Super-Kamiokande 22
  2.3.1 Atmospheric Neutrino Oscillations 22
  2.3.2 Solar Neutrino Oscillations 32
  2.3.3 The Search for Proton Decay 36
  2.3.4 The Search for Astrophysical Phenomenon 37
2.4 Conclusions 39
References 41

2.1. Introduction and Physics Goals

The Super-K collaboration is the combination of two previous successful collaborations. The first was the Kamiokande[1,2] experiment which was

---

*for the Super-Kamiokande collaboration

located in the same mine as Super-K and had a fiducial mass approximately 20 times smaller than Super-K. The second was the IMB experiment[3,4] which was located in the Morton Salt mine in Ohio. Grand Unified models such as SU(5)[5] predicted that the proton would decay at a rate visible by modest size detectors and both of these experiments were originally built to search for nucleon decay into the mode favored by SU(5) which is $p \rightarrow e^+\pi^0$.

Although neither of these experiments observed the decay of the proton, they did measure a statistically significant anomaly in the expected background to the proton decay search from neutrino interactions on the water in the tanks. One explanation for this effect was that some of the neutrinos were oscillating into an unobservable flavor and thus giving less background than expected. At the same time two detectors made of iron, the NUSEX[6] and Frejus[7] experiments, saw a result which was consistent with the expectation but with much lower statistics. Super-Kamiokande was designed to definitively determine whether or not oscillations were indeed taking place.

Additionally, by scaling up the size from previous detectors, Super-Kamiokande offered new hope to finally observe the decay of the nucleon and also to try to answer the crucial question of whether neutrinos produced in the nuclear burning in the sun oscillated into non-detectable flavors on their way to the earth. Previous generations of experiments had not seen as many neutrinos from the sun as predicted by solar models. With a large mass, good energy resolution, and the ability to point neutrinos back to the sun in real-time, Super-Kamiokande was designed first of all to confirm the effect with high statistics and then to determine what the parameters of oscillation were.

2.2. The Super-Kamiokande Detector

Super-Kamiokande is a 50 kiloton water Cherenkov detector located at the Kamioka Observatory of the Institute for Cosmic Ray Research, University of Tokyo. Figure 2.1 shows a diagram of the Super-Kamiokande detector. The detector is in the Mozumi mine of the Kamioka Mining Company in Gifu prefecture, in the Japanese alps. Super-K consists of two concentric, optically separated water Cherenkov detectors contained in a stainless steel tank 42 meters high and 39.3 meters in diameter. The inner detector is comprised of 11,146 Hamamatsu R3600 50 cm diameter photomultiplier tubes, viewing a cylindrical volume of pure water 16.9 m in radius and 36.2 m high.

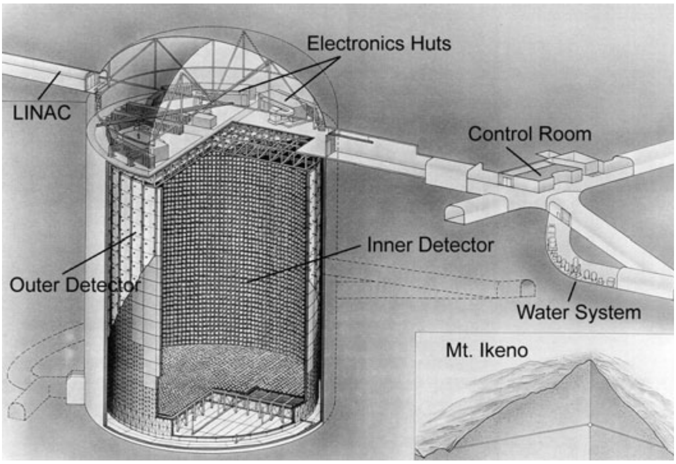

Fig. 2.1. An overview of the Super-Kamiokande detector site, under Mt. Ikeno from Ref. 8. The cutaway shows the inside lined with photomultiplier tubes comprising a photo-cathode coverage of about 40%.

As described more fully in Ref. 8, the detector is calibrated in energy at the 2% level over energies ranging from the MeV to the tens of GeV range. This careful calibration is key to the successful extraction of physics. It relies both on natural calibration sources such as the expected energy deposit of muons created by the cosmic rays and the decay of neutral pions produced by neutrino interactions inside the Super-Kamiokande tank, and on artificial sources including lasers, a Xenon light source, a linear accelerator[9] and a ^{16}N source.[10] Low energy radioactive backgrounds were also carefully studied, a description of the measurement of radon concentrations at Super-Kamiokande is given in Ref. 11.

Data from the detector is first collected by an on-line data acquisition system and then, after a calibration step, passed into several streams of reduction for the various analyses. Selection steps are performed to remove the background from non-neutrino induced interactions. For example, the outer detector region is used as a veto to reject cosmic-ray muons. Using the time and charge information at each photo-tube, reconstruction algorithms are applied to the data to determine a vertex for the Cherenkov light and any rings associated with the particles of the interaction. Additional likelihood-based algorithms are used to determine the properties of the particles that generated the light including their type, momenta and directions. These reconstructed physics quantities are then used for analysis. More detail about the acquisition and analysis reconstruction techniques can be found in Refs. 8, 12 and 13.

The Super-Kamiokande running periods are divided into three parts. The first, SK-I ran from 1996 to 2001. In November of 2001 an accident destroyed many of the photo-tubes of Super-K and, after a year of rebuilding the detector with half of the previous photo-tube density, SK-II ran for approximately 800 days. In June of 2006 after restoring Super-Kamiokande to its full photo-tube density, a period of running known as SK-III began. During the SK-I and SK-II running periods Super-Kamiokande acted as the target for the long-baseline K2K experiment (See Chapter 5). Starting in 2009, Super-Kamiokande will once again be the target of an accelerator produced neutrino beam when the T2K (See Chapter 10) experiment begins.

2.3. Published Results from Super-Kamiokande

The published scientific output of the Super-Kamiokande experiment can be roughly divided into four main categories:

(1) Studies of atmospheric neutrino oscillations
(2) Studies of solar neutrino oscillations
(3) Searches for the decay of the nucleon
(4) Searches for astrophysical sources of neutrinos

In the sections that follow, papers from all of these subjects will be reviewed. Particular attention will be paid to the history of the published papers in the atmospheric neutrino analysis.

2.3.1. *Atmospheric Neutrino Oscillations*

The sub-GeV R ratio[14]

In the previous results from the IMB and Kamiokande experiment it was observed that the flavor ratio of neutrinos below 1 GeV did not agree with expectation. If one took the results at face value, either there were more electron neutrinos than expected or too few muon neutrinos. In order to study the question experimentally a measurement was made of:

$$R \equiv (\mu/e)_{DATA}/(\mu/e)_{MC}, \tag{2.1}$$

which served to cancel uncertainties in neutrino flux and cross-sections. In Eqn. 2.1, (μ/e) means the ratio of the number of measured neutrino interactions which are inferred to have come from electron and muon neutrinos respectively. The ratio is calculated separately for the reconstructed data and Monte Carlo. If there is perfect agreement between data and expectation, the expected value of R is unity. In Super-Kamiokande, the measured value of R was:

$$R = 0.61 \pm 0.03(stat.) \pm 0.05(sys.). \tag{2.2}$$

This was a statistically significant result and the collaboration concluded in Ref. 14:

"The first measurements of atmospheric neutrinos in the Super-Kamiokande experiment have confirmed the existence of a smaller atmospheric ν_μ/ν_e ratio than predicted. We obtained $R = 0.61 \pm 0.03(stat.) \pm 0.05(sys.)$ for events in the sub-GeV range. The Super-Kamiokande detector has much greater fiducial mass and sensitivity than prior experiments. Given the relative certainty in this result, statistical fluctuations can no longer explain the deviation of R from unity."

The multi-GeV R ratio[15]

The previous result relied on events which had visible energy less than 1.33 GeV deposited in the Super-K tank (so called sub-GeV events). Although less numerous, multi-GeV events were also expected to oscillate and had the extra advantage that at high-energy the outgoing lepton direction closely followed the incoming neutrino direction. Since the neutrino oscillation probability is a function of both the distance traveled and the energy, knowing the direction of the incoming neutrino allowed the separation of neutrinos into bins of angular zenith. Based on the results of the previous experiments, it was expected that neutrinos of a few GeV would need to travel thousands of kilometers before they oscillated. Also, if muon neutrinos were oscillating into tau neutrinos, the vast majority of them would not have the energy necessary to interact and produce a tau lepton. In this case, the expectation was that there would be a deficit of muon interactions coming from below.

From the data analyzed, the R ratio for the multi-GeV events was reported in Ref. 15 to be:

$$R = 0.66 \pm 0.06(stat.) \pm 0.08(sys.). \tag{2.3}$$

confirming the result seen in the sub-GeV sample. Crucially, the expected zenith suppression was also seen.

Evidence for oscillations[16]

In 1998, the paper "*Evidence for oscillation of atmospheric neutrinos*" was published.[16] In this paper, 535 days of data were analyzed and subdivided into sub-GeV and multi-GeV e-like and mu-like events. In this data set, a strong suppression of upward going events from muon-neutrino interactions was observed. This was quantified in terms of an asymmetry defined as $A = (U - D)/(U + D)$ where U is the number of upward-going events ($-1 < \cos\Theta < -0.2$) and D is the number of downward-going events ($0.2 < \cos\Theta < 1$). Due to the isotropic nature of the cosmic rays this asymmetry is expected to be close to zero. For the electron-neutrino sample this was found to be the case. For the muon-like events the asymmetry was found to be:

$$A = \frac{(U-D)}{(U+D)} = -0.296 \pm 0.048(stat.) \pm 0.01(sys.) \tag{2.4}$$

which deviates from zero by more than 6 standard deviations. Figure 2.2, taken from Ref. 16, shows this asymmetry as a function of momentum for both the e-like and mu-like samples. The deficit of high energy upward-going mu-like events is clearly seen.

A fit was performed over the oscillation parameter space to the $\nu_\mu \leftrightarrow \nu_\tau$ oscillation hypothesis. There were eight systematic uncertainty terms that were allowed to vary within their known ranges. Fits were also performed to the $\nu_\mu \leftrightarrow \nu_e$ hypothesis but the data did not fit this hypothesis well. The data-samples and the results of the fit are shown in Fig. 2.3, which is also from Ref. 16.

This analysis resulted in the first allowed region for atmospheric neutrino oscillations from Super-Kamiokande resulting in a somewhat lower allowed region then was previously obtained from the Kamiokande collaboration. In this paper the conclusion was:

"*Both the zenith angle distribution of μ-like events and the value of R observed in this experiment significantly differ from the best predictions in the absence of neutrino oscillations. While uncertainties in the flux prediction, cross sections, and experimental biases are ruled out as explanations of the observations, the present data are in good agreement with two-flavor $\nu_\mu \leftrightarrow \nu_\tau$ oscillations with* $\sin^2 2\theta > 0.82$ *and* $5 \times 10^{-4} < \Delta m^2 < 6 \times 10^{-3}$ eV^2 *at 90% confidence level. We conclude that the present data give evidence for neutrino oscillations.*"

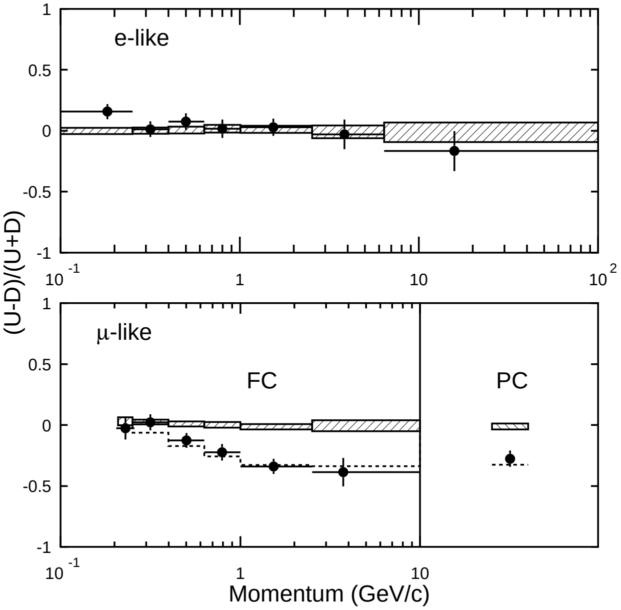

Fig. 2.2. The $(U-D)/(U+D)$ asymmetry as a function of momentum for FC e-like and μ-like events and PC events. While it is not possible to assign a momentum to a PC event, the PC sample is estimated to have a mean neutrino energy of 15 GeV. The Monte Carlo expectation without neutrino oscillations is shown in the hatched region with statistical and systematic errors added in quadrature. The dashed line for μ-like is the expectation for $\nu_\mu \leftrightarrow \nu_\tau$ oscillations with ($\sin^2 2\theta$=1.0, Δm^2= 2.2 $\times 10^{-3}$ eV^2). Figure and caption from Ref. 16.

Upward-going[17] and Stopping[18] muon samples

Also analyzed separately in Refs. 17 and 18 were upward through-going and stopping muon samples. Muons are created by neutrino interactions in the rock under the Super-K tank and then travel upward, either passing through or stopping inside the detector. The through-going events were of a higher energy than the events analyzed in Ref. 16 which were completely contained inside the Super-K tank, and the stopping events were of comparable energy to the events previously considered in which the produced muon escaped the tank. The reduction process for these events was somewhat more involved since it was more difficult to remove backgrounds from entering downward-going muons.

In these two papers, the two sub-samples were fit to the oscillation hypothesis as was their ratio as a function of zenith angle. It was found that

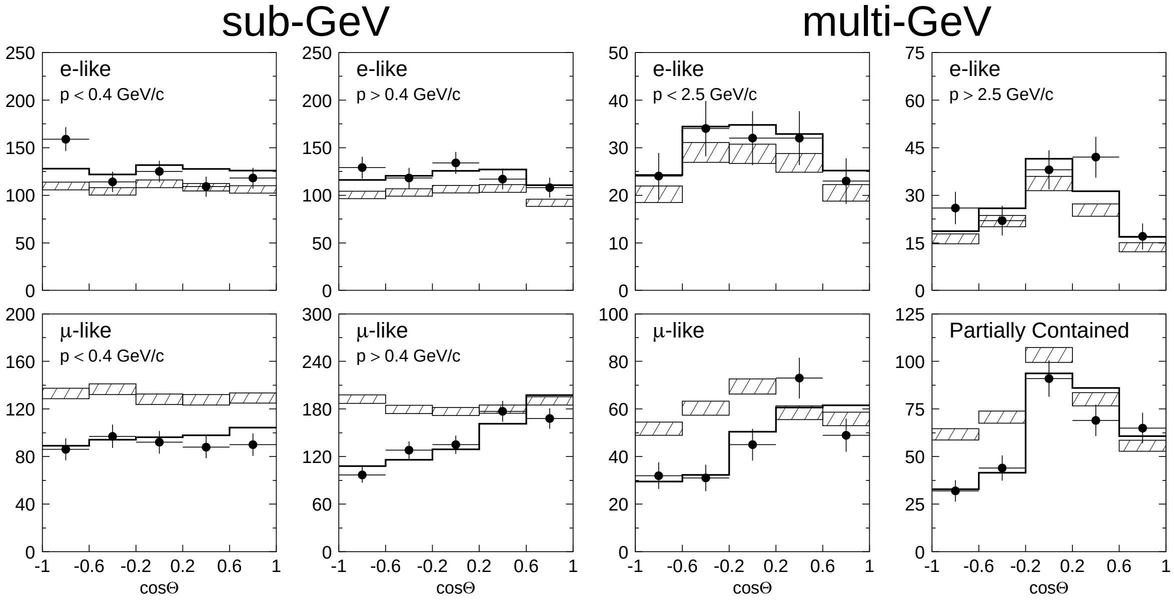

Fig. 2.3. Zenith angle distributions of μ-like and e-like events for sub-GeV and multi-GeV data sets. Upward-going particles have $\cos\Theta < 0$ and downward-going particles have $\cos\Theta > 0$. Sub-GeV data are shown separately for $p <$ 400 MeV/c and $p >$ 400 MeV/c. Multi-GeV e-like distributions are shown for $p <$ 2.5 GeV/c and $p >$ 2.5 GeV/c and the multi-GeV μ-like are shown separately for FC and PC events. The hatched region shows the Monte Carlo expectation for no oscillations normalized to the data live-time with statistical errors. The bold line is the best-fit expectation for $\nu_\mu \leftrightarrow \nu_\tau$oscillations with the overall flux normalization fitted as a free parameter. Figure and caption from Ref. 16.

they also gave results consistent with neutrino oscillations as presented in Ref 16.

The East-West[19] effect

In Ref 19 the east-west effect was seen in neutrinos for the first time. This effect, first seen in cosmic ray showers, is a direct confirmation of the mostly positively charged nature of the cosmic rays. Low-energy cosmic rays are deflected by the Earth's magnetic field distorting the measured azimuthal spectra. By selecting a subset of events sensitive to the Earth's magnetic field, this effect was observed as shown in Fig. 2.4 taken from 19.

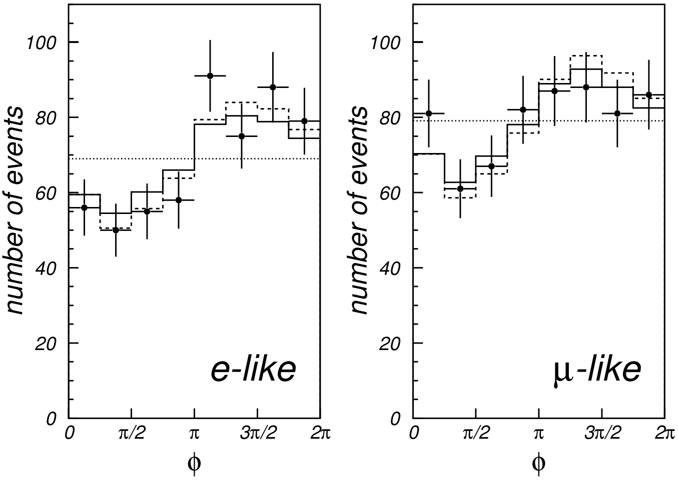

Fig. 2.4. Azimuthal angle distributions of e-like and μ-like events. The crosses represent the data points, the histogram drawn by solid line (dashed-line) shows the prediction of the Monte Carlo (based on the flux of two different flux models). Data are shown with statistical errors. The Monte Carlo has 10 times more statistics than the data. The Monte Carlo histogram is normalized to the total number of the real data. ϕ represents the azimuthal angle. $\phi = 0$, $\pi/2$, π and $3\pi/2$ shows particles going to north, west, south, and east, respectively. Figure and caption from Ref. 19.

While the previous analyses explored only zenith angle distortions caused by oscillations, by confirming the expected azimuthal distortion it was demonstrated that the geomagnetic effects on the production of GeV energy neutrinos was well understood.

Tests for non-standard oscillation models[20]

As more data was collected and the techniques were improved, much effort was put into trying to test if any other explanation was as good as the $\nu_\mu \leftrightarrow \nu_\tau$ at explaining the observed data.

In Ref. 20 with over 1000 days of data, the fully and partially contained events were fit together along with the upward-going muons and a multi-ring sample which had been enriched with neutral-current interactions. In $\nu_\mu \leftrightarrow \nu_\tau$ oscillations, a simple disappearance of only the charged current events would be expected since tau neutrinos would still have neutral current interactions. On the other-hand, if the oscillations were to sterile neutrinos, which have no interactions at all, two additional effects would arise. First, there would also be a reduction in the neutral current sample. Second, because of a difference in the forward scattering cross-sections in the two cases, the normal charged current oscillations would be suppressed at high energies. This suppression is known as the "matter effect." A fit was done to the data samples looking for these effects and they were not seen. Instead, the data fit the standard $\nu_\mu \leftrightarrow \nu_\tau$ hypothesis extremely well and excluded oscillations into sterile neutrinos at greater than the 99% confidence level.

Observation of the oscillation pattern[21]

In 2004 in Ref. 21 the standard oscillation hypothesis was given strong confirmation by the observation of a sinusoidal form in the oscillation pattern.

Since the oscillation equation contains a sine function, in principle one should be able to see a sinusoidal dip if the data is plotted as a function of L/E. However, in the standard analyses, low resolution in reconstructed L (distance from production) and E (neutrino energy) washes out the effect when the data is plotted in these combinations of variables. In Ref. 21 a subset of events were selected which had high resolution in these variables. After plotting the observed suppression relative to the expectation as a function of L/E, the tell-tale dip from oscillations was observed. Additionally, by comparing the χ^2 of the data to the standard oscillation scenario to that of neutrino decay and decoherence, those other exotic hypothesis could be rejected with high significance. Figure 2.5, demonstrating the effect, is taken from Ref. 21.

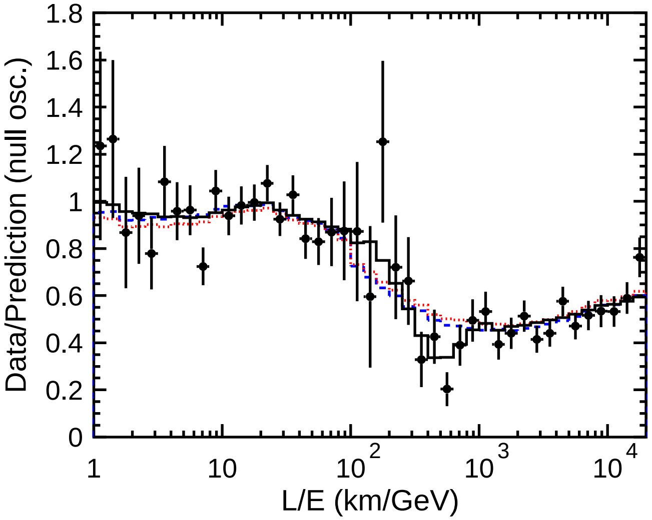

Fig. 2.5. Ratio of the data to the MC events without neutrino oscillation (points) as a function of the reconstructed L/E together with the best-fit expectation for 2-flavor $\nu_\mu \leftrightarrow \nu_\tau$ oscillations (solid line). The error bars are statistical only. Also shown are the best-fit expectation for neutrino decay (dashed line) and neutrino decoherence (dotted line). Figure and caption from Ref. 21

Measurement of atmospheric neutrino parameters[12]

In 2005 all of the data from SK-I was refitted. This time the fit was done jointly with all of the data including upward-going and multiple ring-samples together. Ref. 12 describes this analysis in detail along with details of the atmospheric neutrino Monte Carlo and reconstruction algorithms and reduction.

Thirty-nine systematic uncertainties were accounted for in the fit, and the best fit for $\nu_\mu \leftrightarrow \nu_\tau$ oscillations with $\sin^2 2\theta = 1.00$ and $\Delta m^2 = 2.1 \times 10^{-3}$ eV^2 was found. Figure 2.6, taken from Ref. 12, shows all of the data samples and the results of the fit. Over 15,000 atmospheric neutrino events were used in the analysis. In Fig. 2.7 the final allowed region is shown along with the allowed region that is found by the L/E analysis from Ref. 21. Both of these analyses give consistent results. The better constraint in $\sin^2 2\theta$ in the zenith angle analysis is due to higher statistics in the sample, while the better constraint in Δm^2 in the L/E analysis is due to finer binning in the fit. Later, as yet unpublished analyses combine the best features of both techniques to extract the maximum information.

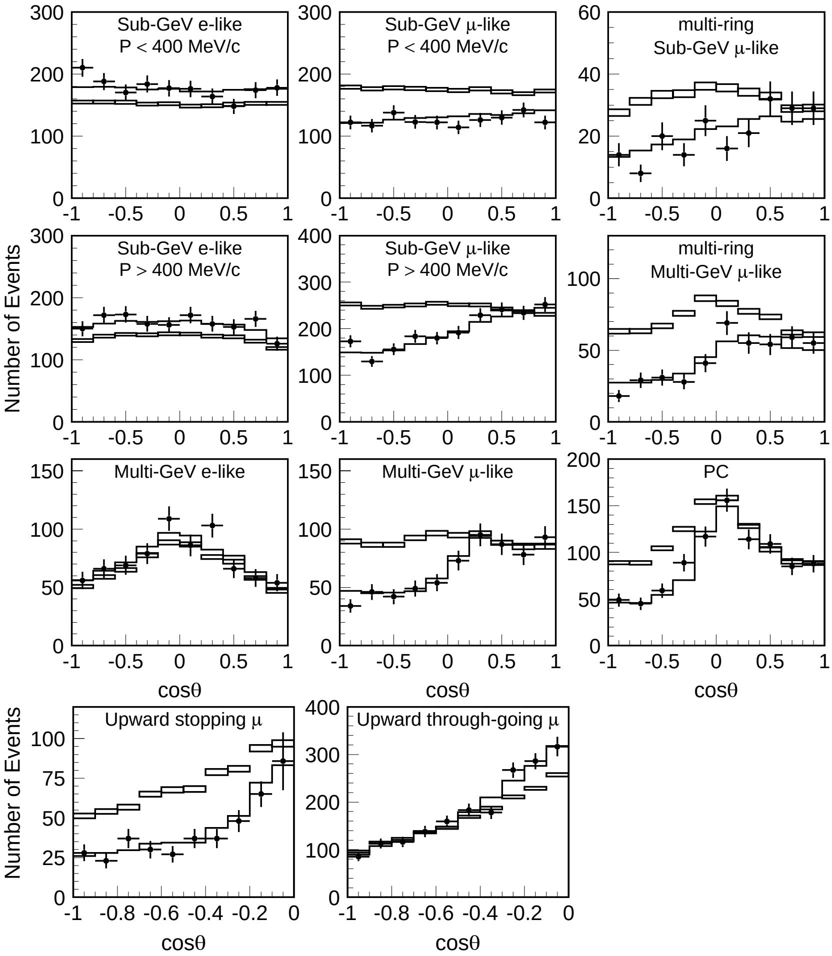

Fig. 2.6. The zenith angle distribution for fully-contained 1-ring events, multi-ring events, partially-contained events and upward muons. The points show the data, box histograms show the non-oscillated Monte Carlo events and the lines show the best-fit expectations for $\nu_\mu \leftrightarrow \nu_\tau$ oscillations with $\sin^2 2\theta = 1.00$ and $\Delta m^2 = 2.1 \times 10^{-3}$ eV^2. The best-fit expectation is corrected by the 39 systematic error terms, while the correction is not made for the non-oscillated Monte Carlo events. The height of the boxes shows the statistical error of the Monte Carlo. Figure and caption from Ref. 12.

Three Flavor Oscillations[23]

In Ref. 12 the data was fit assuming that there were only oscillations between two flavors of neutrinos. However, we know there are three flavors of neutrinos and one can write down a three-flavor mixing matrix with three

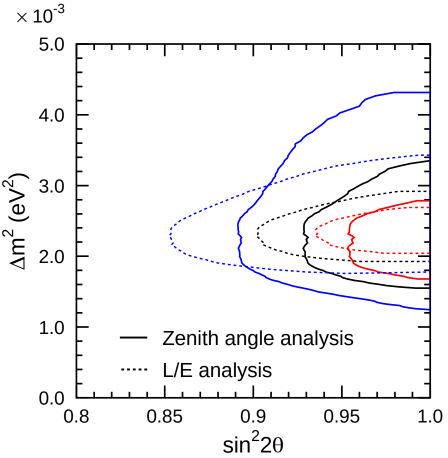

Fig. 2.7. The 68, 90 and 99 % confidence level allowed oscillation parameter regions obtained by an L/E analysis[21] and by the 2005 complete data-set analysis are compared. Note the use of the linear y-scale in the figure. Figure from Ref 12.

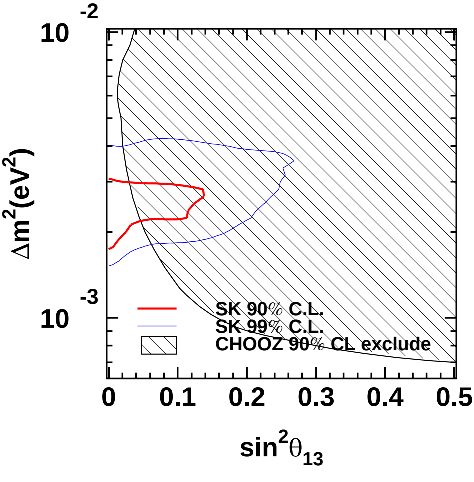

Fig. 2.8. Allowed regions of θ_{13} as found in the SK-I data set in the three flavor oscillation analysis. 90 % (thick line) and 99 % (thin line) confidence level allowed regions are shown in Δm^2 vs $\sin^2\theta_{13}$. Normal mass hierarchy ($\Delta m^2 > 0$) is assumed. The shaded area shows the region excluded by the CHOOZ reactor neutrino experiment.[22] Figure from Ref 23.

mixing angles. Two that have been measured (θ_{12} and θ_{23}) control solar and atmospheric mixing respectively. However, the third as unmeasured mixing angle θ_{13} would allow all three of these neutrinos to oscillate into each other and produce a small amount of high energy electron neutrino appearance in the upward going data of Super-K. The question of the value of θ_{13} is particularly pressing since if it is extremely small or zero it will not be possible to measure CP violation in the neutrino sector using the oscillation technique.

In order to measure or constrain the value of θ_{13} using the Super-K data set, a fit was performed using full three flavor oscillation probabilities, taking into account the resonance effects that can occur in the earth for such oscillations. The data was binned so as to be maximally sensitive to upward going electrons in the relevant energy regions. As detailed in Ref. 23 no evidence for non-zero θ_{13} was found. A plot showing the Super-K θ_{13} allowed region overlaid with the exclusion region for the CHOOZ reactor experiment[22] is shown in Fig. 2.8.

Search for tau lepton appearance[24]

None of the previous analyses explicitly searched for the appearance of the tau lepton from oscillations. The number of tau leptons in the data sample is expected to be small. Only on the order of 80 events with tau leptons were expected to be produced in the fiducial volume of Super-Kamiokande during the SK-I running period. In Ref. 24 an explicit search for tau lepton appearance was undertaken.

This search relied on the fact that events containing heavy tau leptons which decay hadronically, decay symmetrically with more pions in the final state than the charged current deep-inelastic events which form the background to the search. A statistical separation of signal to background was made using both a likelihood and a neural-network. The background was normalized with downward going events, taking advantage of the fact that the entire tau signal comes from below. Figure 2.9 from Ref. 24 shows the results of the fit. This analysis measured a tau appearance signal which was consistent with that expected from $\nu_\mu \leftrightarrow \nu_\tau$ oscillations.

2.3.2. *Solar Neutrino Oscillations*

The neutrinos produced in the nuclear burning of the Sun are of lower energy than atmospheric neutrinos. Super-Kamiokande is sensitive mostly to neutrinos from the ^8B branch of the pp nuclear fusion chain in solar

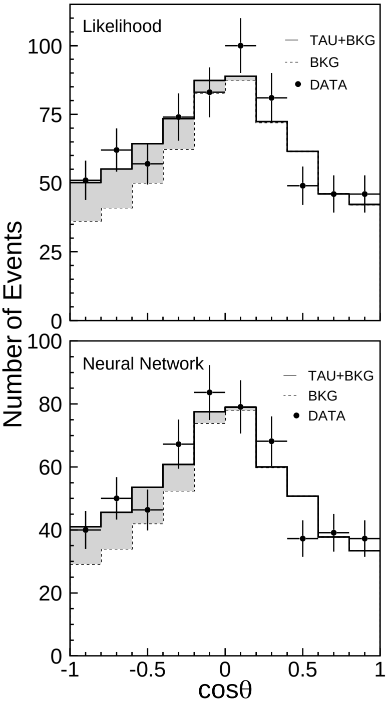

Fig. 2.9. The zenith angle distributions for the likelihood (top) and neural network (bottom) analyses. Zenith angle cosθ $= -1$ (cosθ $= +1$) indicates upward-going (downward-going). The data sample is fitted after tau neutrino event selection criteria are applied. The solid histogram shows the best fit including ν_τ, and the dashed histogram shows the backgrounds from atmospheric neutrinos (ν_e and ν_μ). An excess of tau-like events is observed in the upward-going direction (shaded area). From Ref. 24

burning. At very low energies the experiment is dominated by radioactive backgrounds. However, above approximately 4 MeV the detector can pick-out the scattering of solar neutrinos off atomic electrons which make Cherenkov light in the tank. The ^8B and rarer HEP neutrinos have a spectrum which ends near 20 MeV.

Unlike previous radio-chemical experiments which relied on extraction of isotopes, Super-Kamiokande collects its data in real time and the electrons which are scattered by neutrinos point in a direction that is correlated with the Sun. Therefore, by plotting the direction between low energy events in the tank and the Sun, one can pick out a peak containing solar neutrinos. This is clearly demonstrated in Fig. 2.10, in which the cosine of the angle between the events and the Sun is plotted.

The first solar neutrino results from Super-Kamiokande were presented in 1998 in Ref. 25 and reported the measured flux from the first 300 days of data. In this paper, only the measured rate was reported, and Super-Kamiokande confirmed the deficit of neutrinos expected from the Sun. It

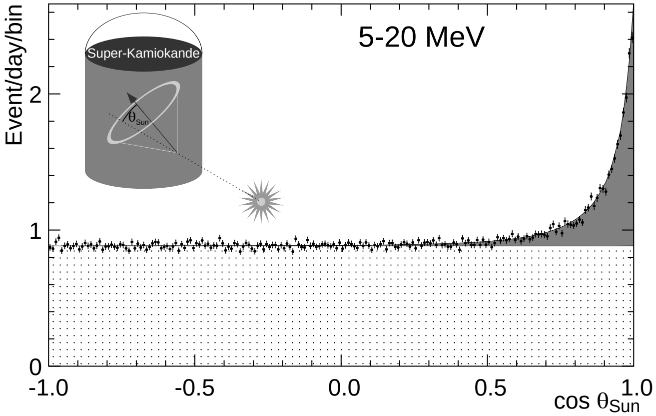

Fig. 2.10. Angular distribution of solar neutrino event candidates. The shaded area indicates the elastic scattering peak. The dotted area is the contribution from background events. From Ref. 13.

was consistent with the previous Kamiokande measurement and reported a flux which was 36% of the standard solar model of 1995. For this first analysis, the energy threshold was set at 6.5 MeV which was later lowered.

The next two papers used 504 days of data and reported searches for distinctive signs of neutrino oscillation. In Ref 26, a measurement was made of the solar flux in the day and the night separately. During the day, neutrinos from the sun travel down from above, traveling through very little earth. In the night they travel from the other side of the Earth, and, during some parts of the year actually travel through the outer core of the Earth. This is relevant because, for some regions of oscillation space, a regeneration of the original flux can happen inside high density materials. In this paper, no statistically significant sign of this was seen, thereby excluding parts of the oscillation space previously allowed by other experiments. At the same time, an analysis of the measured energy spectrum shape was published in Ref. 27 using the 504 day data set. It was found that a χ^2 analysis gave a probability of 4.6% for being in agreement with the standard solar model.

In 2001, with more than twice as much data, the analysis threshold was lowered to 5 MeV and the systematics of the measurement were reduced due to extensive calibrations and improvements in the analysis techniques. In Ref. 28 a precise measurement of the solar flux was made. Additionally, the spectrum was found to have no significant energy spectrum distortions, and no statistically significant day-night effect was seen. The small but expected seasonal variation of the flux due to the eccentricity of the Earth's orbit was observed and new stringent limits on the flux of HEP neutrinos were presented. The lack of spectral and zenith angle distortions placed strong constraints on the oscillation solutions to the solar neutrino problem and in Ref. 29 an oscillation analysis was performed using both the spectral and flux information from Super-Kamiokande. The result of this analysis was a preference for the Large Mixing Angle solution.

In 2002 an analysis including all 1496 days of SK-I was published.[30] The lack of spectral distortion and daily variation in the flux strongly constrained the regions allowed for neutrino oscillation from other experiments, leaving only the high-mass LMA and quasi-vacuum region allowed. If the Super-K interaction rate and either the standard solar model prediction of the ^8B flux or the rates as measured by SNO were combined, the LMA angle was uniquely allowed at high confidence level. This single allowed region could uniquely explain the solar neutrino problem.

The full SK-I data set was also used to search for other exotic signals from the Sun. First was the search for anti-electron neutrinos in Ref. 31. The motivation for this search was to exclude the possibility that the electron-neutrinos from the sun are disappearing due to a spin-flavor-precession where neutrinos with a large magnetic moment are transformed into their anti-particles in the strong magnetic field of the sun. Unlike the standard solar neutrino analysis the reaction here is inverse beta-decay off protons in the nucleus. No signal was found and a limit was set at 0.8% of the standard solar neutrino flux between 8-20 MeV.

Next, in Ref. 32, searches for periodicity in the solar neutrino data using the Lomb test[33] were performed. No significant statistical fluctuation was found. Finally, in 2004 a search for the magnetic moment of the neutrino was presented in Ref. 34. The SK data set was used to look for an energy distortion of the electron recoil spectrum. Using Super-Kamiokande's allowed oscillation parameters a limit of $< 3.6 \times 10^{-10}\mu_B$ was set. If the constraints on oscillation parameters from other experiments were also included then the limit was reduced to $< 1.1 \times 10^{-10}\mu_B$.

In 2004, in Ref. 35, the full SK-I data set was once again analyzed but this time with a maximum likelihood analysis applied to the zenith angle dependence of the data. A dependence of the ν_e rate on solar zenith angle is predicted, the size of which depends on the mixing parameters. This results in a difference between the ν_e rate during the day compared to the night owing to matter effects as the neutrinos traverse the earth. This new analysis lowered the statistical uncertainty on the day/night (D/N) ratio by

25% compared to the previous measurement. This was equivalent to adding three years of live-time running using the previous method. Figure 2.11, from Ref. 35, shows the data and best fit spectrum in the LMA region along with the D/N asymmetry as a function of energy.

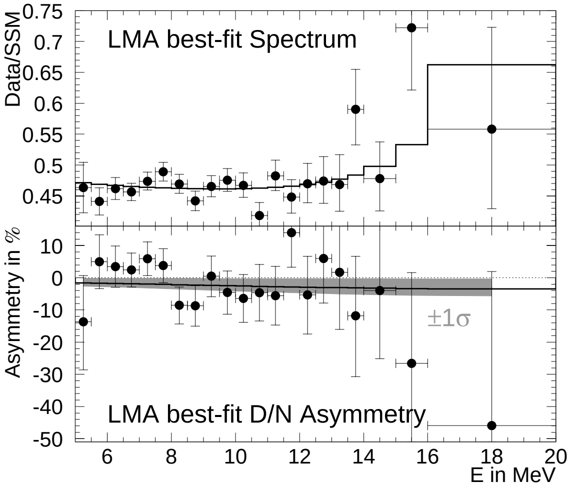

Fig. 2.11. LMA Spectrum (top) and D/N Asymmetry (bottom). The predictions (solid lines) are for $\tan^2\theta = 0.55$ and $\Delta m^2 = 6.3 \times 10^{-5}\mathrm{eV}^2$ with $\phi_{8_B} = 0.96\times$Standard Solar Model [BP2000] and $\phi_{hep} = 3.6\times$Standard Solar Model. Each energy bin is fit independently to the rate (top) and the day/night asymmetry (bottom). The gray bands are the $\pm1\sigma$ ranges corresponding to the fitted value over the entire range 5-20 MeV: $A = -1.8 \pm 1.6\%$. Figure and caption from Ref. 35.

In 2005 a full detailed description of the SK-I solar neutrino analysis was published in Ref. 13. This paper included descriptions of the simulation, reconstruction and analysis techniques. In the large mixing angle region the day-night asymmetry was found to be:

$$A = \frac{(\Phi_D - \Phi_N)}{\frac{1}{2}(\Phi_D + \Phi_N)} = -1.7\% \pm 1.6\%(stat.)^{+1.3\%}_{-1.2\%}(sys.) \pm .04\%(\Delta m^2) \quad (2.5)$$

which is statistically compatible with zero and is to be compared with the expected asymmetry which ranges from -1.7% to 1.0%.

2.3.3. *The Search for Proton Decay*

Super-K has also set important limits on the decay of the nucleon. The limits from Super-K have ruled out SU(5) and the minimal super-symmetric model. The published limits on $p \to e^+\pi^0$ as predicted in SU(5) are found in Ref. 36.

Many models of super-symmetry predict that the nucleon should decay with strange quarks in the final state. The first 535 days of SK data were analyzed to search for $p \to \bar{\nu}K^+$ and the limits were presented in Ref. 37. In 2005 the full SK-I data set was employed to search for SUSY mediated decays of the proton. In the analysis presented in Ref. 38 stringent limits were set on $p \to \bar{\nu}K^+$, $n \to \bar{\nu}K^0$, $p \to \mu^+K^0$ and $p \to e^+K^0$ modes.

A related search for SUSY generated physics is the search for neutral Q-Balls as presented in Ref. 39. Q-balls are topological solitons predicted in some SUSY models and interact as they pass through the Super-K tank leaving a trail of pions in their wake. A search was carried out using 542 days of the SK-II data set. No evidence for Q-balls was found, and Super-K finds the lowest limits in the world for Q-ball cross-sections below 200 mb.

2.3.4. *The Search for Astrophysical Phenomenon*

Super-Kamiokande has been used to search for several sources of neutrinos from outside our solar system. Gamma Ray Bursters are among the most luminous sources that have ever been observed in the universe. Super-K performed a search for neutrinos that were in coincidence with the BATSE detector located on NASA's Compton Gamma Ray Observatory. The entire Super-K data sample from 7 MeV to ∼100 TeV was compared with the BATSE on-line catalog in the period of April 1996 to May of 2000. The results were presented in Ref. 40, and no statistically significant signal was found.

A supernova which occurred in the center of our galaxy would produce on the order of 10,000 interactions inside the Super-Kamiokande tank, yielding a rich sample of events for analysis. In the period of Super-K running there has been no observed galactic supernova (though the Kamiokande experiment did observe neutrinos from SN1987a[41]). A paper currently under preparation for publication will set a limit on the rate of core collapse supernovae out to 100 kiloparsecs using the SK-I and SK-II data sets of $\sim<$ 0.3/year. Although no core collapse was detected by Super-Kamiokande, it is believed that the universe should be bathed in the relic neutrinos of all of the supernovas that have exploded in the past. In Ref. 42 the SK-I data sample was examined for such events. There is a region of energy between the endpoint of the solar neutrino spectrum and before the decay electrons of cosmic ray muons where one can hope to see the small number of expected events. No excess over background was observed, setting a limit just above the expected signal from many models.

The upward-going muons used for the atmospheric oscillation analysis can also be used to search for high energy sources of neutrinos. The only muons that come from below the tank are generated by neutrinos and the neutrinos that produce them range from approximately 100 GeV to 100 TeV.

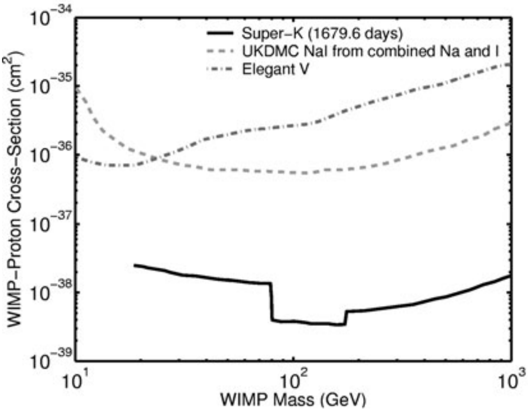

Fig. 2.12. Super-K 90% CL exclusion region in WIMP parameter space for a WIMP with spin-dependent coupling along with corresponding 90 % CL exclusion limits from UKDMC (dashed) and ELEGANT (dot-dashed). Figure and caption from Ref. 43.

In addition to looking for neutrinos from astrophysical objects there is an expected neutrino signal from WIMP dark matter. Since WIMPs undergo gravitational attraction, they are expected to gravitate around heavy bodies such as the Earth and the Sun. If a WIMP and anti-WIMP annihilate near the center of one of these objects where they have accumulated, they will decay into standard model particles, some of which decay into neutrinos.

Therefore, if there is an excess signal of upward going neutrinos coming from either the center of the Earth or the Sun it can be interpreted as a signal for dark matter. It is shown in Ref. 43 that the limit on spin-dependent couplings inferred from the lack of an excess in the direction of the Sun is on the order of 100 times more sensitive than comparable terrestrial direct dark matter experiments. Figure 2.12, taken from Ref. 43, shows a comparison of the Super-K limit with limits from other experiments.

Additionally, several pure astronomical analyses have been performed with Super-K using samples of both downward-going and upward-going muons. In Ref. 44 the anisotropy of the primary cosmic ray flux with a mean energy of 10 TeV was measured by studying the relative sidereal variation of downward-going muons in the Super-K tank.

By using upward-going muons, searches were performed for sources of high energy astrophysical neutrinos. In Ref. 45 the sample of upward-going muons were used to search the sky for point sources and signatures of a diffuse flux of neutrinos from the galactic plane. Additional time correlated searches with some known sources were also performed. Above 1 TeV of muon energy, the flux of upward going muons from atmospheric neutrinos becomes small enough to look for a diffuse flux of extremely high energy neutrinos from astrophysical sources such as active galactic nuclei. In Ref. 46 the outer detector of Super-K was used to measure the direction of extremely high energy events. One event was found which was consistent with the background expectation and limits were set on this flux.

2.4. Conclusions

This review of the published work of the Super-Kamiokande collaboration has shown the depth and importance of the work that the experiment has achieved. From astronomy and astrophysics, to tests of grand unified models, and to the observation of neutrino mass using neutrinos from the atmosphere and the Sun, Super-K has had a major impact on particle physics.

It would be a mistake to take this snapshot of the published work of Super-Kamiokande as its final word. There is a large data set from SK-II which is currently being analyzed, and will soon be published. These analyses will increase the precision of the parameters Super-Kamiokande has already measured. In addition, the larger data set will allow analyses for more subtle effects which have not yet been studied.

As one example of this, Fig. 2.13 shows the latest result of the atmospheric oscillation analysis using the combined SK-I and SK-II data sets. In addition to the increase in statistics, this analysis has improvements in the binning and systematic errors. It should be noted that in this figure the y-axis is plotted on a linear scale.

This analysis employed 380 bins and 70 systematic errors. The best fit to the atmospheric oscillation parameters gives:

$$\Delta m^2 = 2.5 \times 10^{-3}\ eV^2 \quad \sin^2 2\theta = 1.00, \tag{2.6}$$

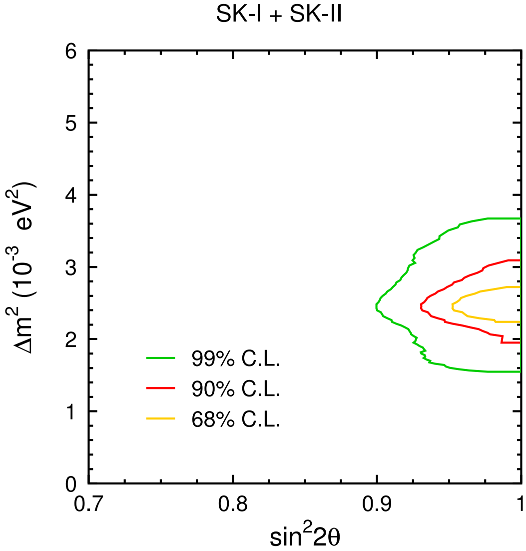

Fig. 2.13. Preliminary allowed region of atmospheric oscillation parameters using the combined data sets of SKI and SK-II. The fit to the data employed 380 bins, 70 systematic errors and had a Chi-squared probability of 18%. Note the use of the linear y-scale in the figure.

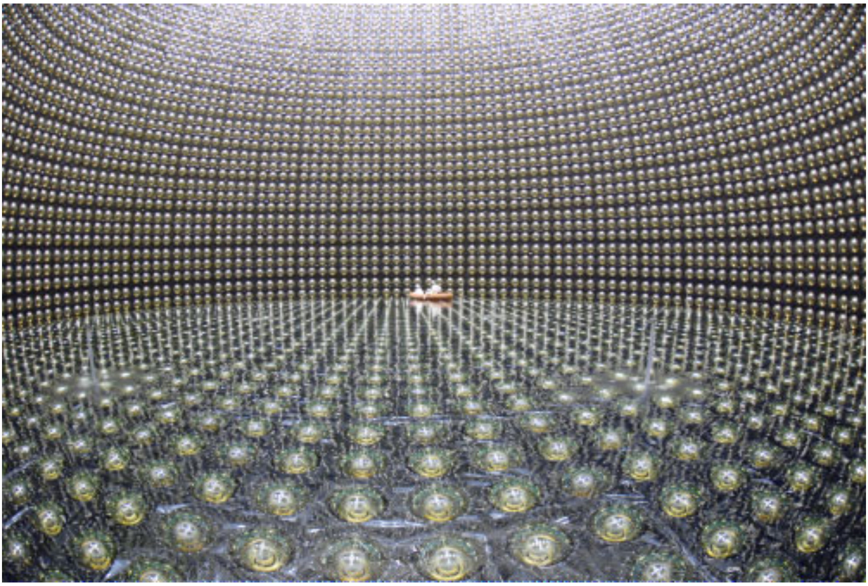

Fig. 2.14. Picture of SK-III during filling and before the beginning of operations. *Photo-credit: Kamioka Observatory, ICRR(Institute for Cosmic Ray Research), The University of Tokyo.*

with the allowed region at 90% CL being equal to:

$$1.9 \times 10^{-3}\ eV^2 < \Delta m^2 < 3.1 \times 10^{-3}\ eV^2 \quad \sin^2 2\theta > 0.93. \tag{2.7}$$

Since June of 2006 SK-III has been operational. Figure 2.14 is a picture of SK-III during filling before operations commenced. Super-Kamiokande will continue to collect data, wait for supernovae, and in 2009 will once again become a target for an accelerator based neutrino beam.

Acknowledgments

The author and the Super-Kamiokande collaboration gratefully acknowledge the cooperation of the Kamioka Mining and Smelting Company. The Super-Kamiokande experiment has been built and operated from funding by the Japanese Ministry of Education, Culture, Sports, Science and Technology, the United States Department of Energy, and the U.S. National Science Foundation.

References

1. K. S. Hirata et al., Experimental study of the atmospheric neutrino flux, *Phys. Lett.* **B205**, 416, (1988).
2. K. S. Hirata et al., Observation of a small atmospheric ν_μ/ν_e ratio in kamiokande, *Phys. Lett.* **B280**, 146–152, (1992).
3. D. Casper et al., Measurement of atmospheric neutrino composition with IMB-3, *Phys. Rev. Lett.* **66**, 2561–2564, (1991).
4. R. Becker-Szendy et al., The electron-neutrino and muon-neutrino content of the atmospheric flux, *Phys. Rev.* **D46**, 3720–3724, (1992).
5. H. Georgi and S. L. Glashow, Unity of all elementary particle forces, *Phys. Rev. Lett.* **32**, 438–441, (1974).
6. M. Aglietta et al., Experimental study of atmospheric neutrino flux in the NUSEX experiment, *Europhys. Lett.* **8**, 611–614, (1989).
7. K. Daum et al., Determination of the atmospheric neutrino spectra with the Frejus detector, *Z. Phys.* **C66**, 417–428, (1995).
8. Y. Fukuda et al., The Super-Kamiokande detector, *Nucl. Instrum. Meth.* **A501**, 418–462, (2003).
9. M. Nakahata et al., Calibration of Super-Kamiokande using an electron linac, *Nucl. Instrum. Meth.* **A421**, 113–129, (1999).
10. E. Blaufuss et al., N-16 as a calibration source for Super-Kamiokande, *Nucl. Instrum. Meth.* **A458**, 638–649, (2001).
11. Y. Takeuchi et al., Measurement of radon concentrations at Super-Kamiokande, *Phys. Lett.* **B452**, 418–424, (1999).
12. Y. Ashie et al., A measurement of atmospheric neutrino oscillation parameters by Super-Kamiokande I, *Phys. Rev.* **D71**, 112005, (2005).

13. J. Hosaka et al., Solar neutrino measurements in Super-Kamiokande-I, *Phys. Rev.* **D73**, 112001, (2006).
14. Y. Fukuda et al., Measurement of a small atmospheric ν_μ/ν_e ratio, *Phys. Lett.* **B433**, 9–18, (1998).
15. Y. Fukuda et al., Study of the atmospheric neutrino flux in the multi-GeV energy range, *Phys. Lett.* **B436**, 33–41, (1998).
16. Y. Fukuda et al., Evidence for oscillation of atmospheric neutrinos, *Phys. Rev. Lett.* **81**, 1562–1567, (1998).
17. Y. Fukuda et al., Measurement of the flux and zenith-angle distribution of upward through-going muons by Super-Kamiokande, *Phys. Rev. Lett.* **82**, 2644–2648, (1999).
18. Y. Fukuda et al., Neutrino-induced upward stopping muons in Super-Kamiokande, *Phys. Lett.* **B467**, 185–193, (1999).
19. T. Futagami et al., Observation of the east-west anisotropy of the atmospheric neutrino flux, *Phys. Rev. Lett.* **82**, 5194–5197, (1999).
20. S. Fukuda et al., Tau neutrinos favored over sterile neutrinos in atmospheric muon neutrino oscillations, *Phys. Rev. Lett.* **85**, 3999–4003, (2000).
21. Y. Ashie et al., Evidence for an oscillatory signature in atmospheric neutrino oscillation, *Phys. Rev. Lett.* **93**, 101801, (2004).
22. M. Apollonio et al., Search for neutrino oscillations on a long base-line at the chooz nuclear power station, *Eur. Phys. J.* **C27**, 331–374, (2003).
23. J. Hosaka et al., Three flavor neutrino oscillation analysis of atmospheric neutrinos in Super-Kamiokande, *Phys. Rev.* **D74**, 032002, (2006).
24. K. Abe et al., A measurement of atmospheric neutrino flux consistent with tau neutrino appearance, *Phys. Rev. Lett.* **97**, 171801, (2006).
25. Y. Fukuda et al., Measurements of the solar neutrino flux from Super-Kamiokande's first 300 days, *Phys. Rev. Lett.* **81**, 1158–1162, (1998).
26. Y. Fukuda et al., Constraints on neutrino oscillation parameters from the measurement of day-night solar neutrino fluxes at Super- Kamiokande, *Phys. Rev. Lett.* **82**, 1810–1814, (1999).
27. Y. Fukuda et al., Measurement of the solar neutrino energy spectrum using neutrino electron scattering, *Phys. Rev. Lett.* **82**, 2430–2434, (1999).
28. S. Fukuda et al., Constraints on neutrino oscillations using 1258 days of Super-Kamiokande solar neutrino data, *Phys. Rev. Lett.* **86**, 5656–5660, (2001).
29. S. Fukuda et al., Solar B-8 and hep neutrino measurements from 1258 days of Super-Kamiokande data, *Phys. Rev. Lett.* **86**, 5651–5655, (2001).
30. S. Fukuda et al., Determination of solar neutrino oscillation parameters using 1496 days of Super-Kamiokande-I data, *Phys. Lett.* **B539**, 179–187, (2002).
31. Y. Gando et al., Search for $\overline{\nu}_e$ from the sun at Super-Kamiokande-I, *Phys. Rev. Lett.* **90**, 171302, (2003).
32. J. Yoo et al., A search for periodic modulations of the solar neutrino flux in Super-Kamiokande-I, *Phys. Rev.* **D68**, 092002, (2003).
33. W. H. Press et al., *Numerical Recipes in C.* (Cambridge University Press, Cambridge, England, 1999), second edition.

34. D. W. Liu et al., Limit on the neutrino magnetic moment using 1496 days of Super-Kamiokande-I solar neutrino data, *Phys. Rev. Lett.* **93**, 021802, (2004).
35. M. B. Smy et al., Precise measurement of the solar neutrino day/night and seasonal variation in Super-Kamiokande-I, *Phys. Rev.* **D69**, 011104, (2004).
36. M. Shiozawa et al., Search for proton decay via $p \to e^+\pi^0$ in a large water Cherenkov detector, *Phys. Rev. Lett.* **81**, 3319–3323, (1998).
37. Y. Hayato et al., Search for proton decay through p −> anti-nu K+ in a large water Cherenkov detector, *Phys. Rev. Lett.* **83**, 1529–1533, (1999).
38. K. Kobayashi et al., Search for nucleon decay via modes favored by supersymmetric grand unification models in Super- Kamiokande-I, *Phys. Rev.* **D72**, 052007, (2005).
39. Y. Takenaga et al., Search for neutral q-balls in Super-Kamiokande II, *Phys. Lett.* **B647**, 18–22, (2007).
40. S. Fukuda et al., Search for neutrinos from gamma-ray bursts using Super-Kamiokande, *Astrophys. J.* **578**, 317–324, (2002).
41. K. Hirata et al., Observation of a neutrino burst from the supernova sn 1987a, *Phys. Rev. Lett.* **58**, 1490–1493, (1987).
42. M. Malek et al., Search for supernova relic neutrinos at Super-Kamiokande, *Phys. Rev. Lett.* **90**, 061101, (2003).
43. S. Desai et al., Search for dark matter WIMPs using upward through-going muons in Super-Kamiokande, *Phys. Rev.* **D70**, 083523, (2004).
44. G. Guillian et al., Observation of the anisotropy of 10-TeV primary cosmic ray nuclei flux with the Super-Kamiokande-I detector, *Phys. Rev.* **D75**, 062003, (2007).
45. K. Abe et al., High energy neutrino astronomy using upward-going muons in Super-Kamiokande-I, *Astrophys. J.* **652**, 198, (2006).
46. M. E. C. Swanson et al., Search for diffuse astrophysical neutrino flux using ultra- high energy upward-going muons in Super-Kamiokande I, *Astrophys. J.* **652**, 206–215, (2006).

Chapter 3

Sudbury Neutrino Observatory

S. J. M. Peeters
Department of Physics, Lancaster University, Lancaster, LA1 4YB, UK
s.peeters@lancaster.ac.uk

J. R. Wilson*
Department of Physics and Astronomy, University of Sussex,
Brighton, BN1 9QH, UK
j.wilson@sussex.ac.uk

We present a review of the solar neutrino results of the Sudbury Neutrino Observatory, which unambiguously showed that neutrinos change flavor between their production in the Sun, and observation on Earth. We start with a description of the main properties of the detector and how it was used to observe the different components of the solar neutrino flux. After this introduction we describe in more detail the three phases of the experiment: the pure D_2O phase, the salt phase, during which the sensitivity to the total neutrino flux was enhanced, and the NCD phase which used an added, independent detector system to independently measure the total neutrino flux. We conclude by summarizing the main results of this landmark experiment which ceased data-taking in November 2006.

Contents

3.1 Introduction 46
3.2 The SNO Detector 47
  3.2.1 Signals 47
  3.2.2 Calibration 49
  3.2.3 Backgrounds 50
3.3 Analysis Strategy 51
  3.3.1 Signal Extraction 52
3.4 Phase 1 – D_2O 55
3.5 Phase 2 – Salt 58

---

*For the SNO Collaboration as represented in the author lists quoted in Ref. 1.

3.6 Phase 3 – Neutral Current Detection Array 62
  3.6.1 The Counter System 62
  3.6.2 The Backgrounds 63
  3.6.3 The Installation of the NCD System 64
  3.6.4 Data-Taking Period 64
3.7 Conclusions 65
References 67

3.1. Introduction

The Sudbury Neutrino Observatory (SNO) was first proposed by Herb Chen in 1985 to provide direct evidence for solar neutrino flavor change.[2] The experiment was designed to observe non-electron neutrino flavors, allowing a flavor-independent measurement of the total neutrino flux from the Sun. The detector was an imaging Cherenkov detector using heavy water (D_2O) as both the interaction and detection medium.[3] As all water Cherenkov detectors, it was only sensitive to the ^{8}B (and hep[4]) solar neutrinos. It was located in INCO Ltd.'s Creighton Mine, near Sudbury, Canada, 2092 meters below sea level (6020 meters water equivalent).

Solar neutrino flavor change is observed through comparison of the neutrino flux obtained from three different processes:

$$\nu_x + e^- \to \nu_x + e^- \qquad \text{(ES)}$$

$$\nu_e + d \to p + p + e^- \qquad \text{(CC)}$$

$$\nu_x + d \to p + n + \nu_x \qquad \text{(NC)}$$

The first reaction, elastic scattering (ES) of electrons, has been used to detect solar neutrinos in other water Cherenkov experiments (e.g. Super-Kamiokande, see Chapter 2). It has the great advantage that the recoil electron direction is strongly correlated with the direction of the incident neutrino, and hence the direction to the Sun. It is sensitive to all neutrino flavors. However, for electron neutrinos, the elastic scattering reaction has both charged and neutral current components, making the cross sections approximately 6.5 times larger for these reactions compared to muon or tau neutrinos.

The $\nu_e - d$ charged current reaction (CC) only occurs for electron neutrinos, which interact with the loosely bound neutrons in deuterium. This reaction provides exclusive sensitivity to electron neutrinos and has the advantage that the recoil electron spectrum is strongly correlated with the incident neutrino energy. It can thus provide a measurement of the ^{8}B energy spectrum. The electron momentum only has a weak angular correlation with the direction to the Sun.

The third reaction, also unique to heavy water, is the $\nu_x - d$ neutral current (NC) reaction, and is equally sensitive to all neutrino flavors. It thus provides a direct measurement of the total active flux of ^{8}B neutrinos from the Sun. Like the CC reaction, the NC reaction has a cross section nearly an order of magnitude larger than the ES reaction.

3.2. The SNO Detector

An artist's impression of the SNO detector is shown in Fig. 3.1. One thousand tons of heavy water were contained in a 12 m diameter, transparent acrylic vessel (AV). The Cherenkov light produced by neutrino interactions and radioactive backgrounds was detected by an array of 9456 Hamamatsu 8-inch photomultiplier tubes (PMTs). Each PMT was surrounded by a light concentrator, which increased the photocathode coverage to nearly 55%. The PMTs plus concentrators were supported by a stainless steel support geodesic sphere (PSUP).

Over seven kilotons of light water surrounded the AV, shielding the heavy water from external radioactive backgrounds: 1.7 kilotons between the AV and the PSUP and 5.7 kilotons between the PSUP and the surrounding rock. The light water outside the PSUP was viewed by 91 outward-facing 8-inch PMTs that were used for identification of cosmic-ray muons.

3.2.1. *Signals*

The SNO detector was designed to observe the Cherenkov light produced by ultra-relativistic electrons. The threshold for the emission of Cherenkov light is 0.767 MeV, although in practice the analysis thresholds were set much higher than this. The observed electrons produced light in a cone around the direction of the particle at a characteristic angle of approximately 42 degrees.

Electrons with sufficient energy were produced in three ways. Firstly, the ES and CC neutrino reactions produce energetic electrons directly. Secondly, gammas with enough energy are likely to Compton scatter, thus producing an electron which produces Cherenkov light. Most importantly, however, neutron capture produces high energy gamma-rays, which also have a high probability to Compton scatter, and thus produce Cherenkov light. The SNO experiment went through three different phases, each using a different mechanism to detect the neutrons produced in the NC reaction, as will be described in the corresponding sections.

Fig. 3.1. The SNO detector. Reproduced from Reference 1.

A complex trigger algorithm, which could be satisfied by a number of different criteria, was used to determine whether the SNO detector should record an event.[a] An approximate definition is that if more than about 16 PMTs were hit[b] within approximately 93 ns the event was read out (although the exact number also underwent small changes throughout the course of the experiment). The PMT trigger rate varied through the three phases of SNO, but the average was around 20 Hz.

---

[a] The peaked structure of the raw data at low NHIT in Fig. 3.2 is a consequence of the multiple trigger algorithms.

[b] The front-end electronics were set to fire on a quarter of a photoelectron of charge.

The SNO detector recorded the following parameters of an event: the position of the PMTs that were hit, the charges recorded in those PMTs, and the arrival times of the PMT signals. From these parameters, the following physics parameters were derived: event vertex position, direction, energy and isotropy. The latter parameter quantifies the spread in PMT positions, which was used to distinguish single electrons (or gammas) from multi-electron events.

3.2.2. *Calibration*

The interpretation of SNO's signals required the measurement and calibration of the detector components and response. The detector was equipped with a versatile calibration system, able to deploy sources in both the light and heavy water and maneuver them to various positions with a precision of a few centimeters. Table 3.1 shows the list of sources used in the SNO experiment. Besides these source calibrations, a number of electronics calibrations were performed on a regular basis. The extensive list of different sources, which were deployed through most of the volume of the detector, ensured a thorough understanding of the response of the detector for the different physics events, for the entire volume used in the analysis, over a large energy range, and for the entire data-taking period.

Table 3.1. Primary calibration sources.

Calibration source	Details	Calibration	Ref.
Pulsed nitrogen laser	337, 369, 385, 420, 505, 619 nm	Optical & timing calibration	5
^{16}N	6.13 MeV γ-rays	Energy & reconstruction	6
^{8}Li	β spectrum	Energy & reconstruction	7
^{252}Cf	neutrons	Neutron response	3
AmBe	neutrons	Neutron response	
^{3}H(p,γ)^{4}He("pT")	19.8 MeV γ-rays	Energy linearity	8
U,Th	$\beta - \gamma$	Backgrounds	3
^{88}Y	$\beta - \gamma$	Backgrounds	
In-situ ^{24}Na activation	$\beta - \gamma$	Backgrounds	
Dissolved ^{24}Na	$\beta - \gamma$	Backgrounds	
Dissolved ^{222}Rn	$\beta - \gamma$	Backgrounds	

The calibration data formed an important input to a detailed model of the detector, which was used to perform Monte-Carlo simulations of events and backgrounds.[1] In order to fully understand the data, a complete and accurate representation of the detector's true response was required so the detector model described everything from the physics of neutrino interactions and the propagation of particles and optical photons through the detector media, to the behavior of the data acquisition system. The model made full use of the information of the state of PMTs from the electronics calibrations. The extensive calibration data were used to test the detector model and also allowed us to understand how accurately each observable parameter could be determined and assess the relevant systematic uncertainties.

3.2.3. *Backgrounds*

The recorded events were not only from recoil electrons and gamma-rays produced in association with neutrino interactions, but also included instrumental, radioactive, and cosmogenic backgrounds.

SNO's great depth reduced the number of cosmic rays passing through the detector to an extremely low rate — roughly three through-going muons per hour within the PSUP enclosure. Nevertheless, cosmic-ray interactions may have produced both radioactive nuclides and neutrons, so two data selection criteria were developed to exclude these events. The first eliminated all events that occurred within 20 s of a tagged muon event. The second, intended to remove neutrons from untagged muon events, removed all events in a 250 ms window following any event with a large number of hit PMTs.

The most dangerous background to the NC measurement were neutrons produced through photodisintegration of deuterons by low-energy radioactivity. In particular, naturally occurring ^{232}Th and ^{238}U have gamma-rays at the end of their decay chains that are above the 2.22 MeV deuteron binding energy. To reduce this background contribution the SNO detector was built with very stringent radio-purity targets for all components and uranium and thorium levels present in both the H_2O and D_2O were continually monitored using both *ex-situ*[9,10] and *in-situ* techniques. This was especially challenging for the D_2O target, for which the radiopurity requirement was of order of 10^{-15} gram ^{232}Th or ^{238}U per gram D_2O. Events due to neutrons and low-energy radioactivity from the environment penetrating the H_2O shielding were taken into account in the analysis (see Sec. 3.3).

By far the highest rate of background events, however, was due to electronic pick-up, small discharges from within the PMTs and other instrumental effects. These did not involve Cherenkov light and therefore could be rejected based on uncharacteristic timing, spatial or charge distributions of PMT hits. A series of cuts was designed to remove nearly all the background events without sacrificing a substantial number of signal events (see Fig. 3.2). The remaining contamination was determined by a bifurcated analysis.

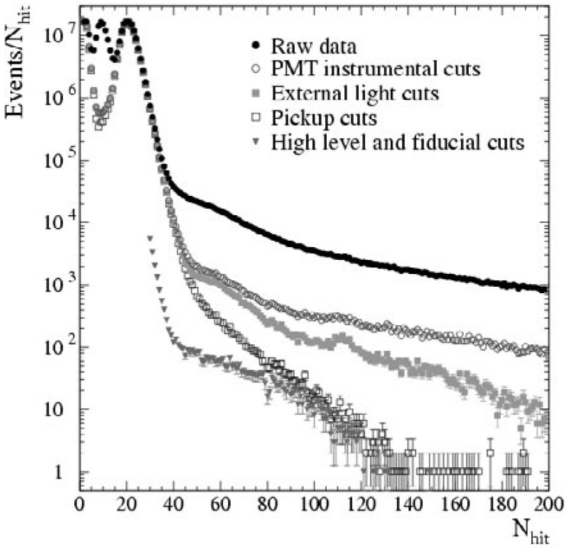

Fig. 3.2. The reduction in the total number of events for the D_2O phase, as a function of the number of hit PMTs, for successive applications of the instrumental background rejection criteria, or cuts. In the figure, 1 MeV corresponds roughly to 8.5 hit PMTs. Reproduced from, and for more details, see Reference 1.

3.3. Analysis Strategy

The main goal of the SNO analysis was to determine the relative sizes of the three signals (CC, ES, and NC) and to compare their rates. We could not separate the signals on an event-by-event basis; instead we 'extracted' the signals statistically using distributions of observable parameters that showed different characteristics for each signal. These included the effective kinetic energy, T_{eff},[c] the angle between the event direction and the direction to the Sun, $\cos\theta_{\odot}$, and the volume weighted radial position, R^3.[d]

---

[c] The calculated equivalent kinetic energy of an electron.

[d] $R^3 = R_{\mathrm{fit}}/R_{\mathrm{AV}}$ where R_{fit} is the event radius determined from the timing distribution of PMT hits and R_{AV} is the radius of the acrylic vessel.

The detector model was used to perform Monte Carlo simulations of all three neutrino interactions assuming Standard Solar Model (SSM)[11] predictions for the flux and energies of ^{8}B neutrinos. The major background components were also simulated using this model. From these simulations, binned Probability Density Functions (PDFs) were constructed in each of the selected observable parameters.

3.3.1. *Signal Extraction*

Signal extraction involved an extended maximum likelihood fit to the data with the binned PDFs (included in Fig. 3.3 and Fig. 3.4). By maximizing a product of probabilities known as the likelihood function, the most likely combination of signal components making up the data was obtained. The likelihood function was parameterized to make efficient use of the information available, and consequently, slightly different functions were used for the different phases of the experiment. Using the D_2O phase as an example, the total number of neutrino events, ν, was expressed in the following manner:

$$\nu(T_{\text{eff}}, R^3, \cos\theta_\odot) = \sum_i N_i f_i(T_{\text{eff}}, R^3, \cos\theta_\odot) \tag{3.1}$$

where N_i is the number of events of each type i and f_i is the probability distribution for events of that type, normalized to unity. The sum is taken over all signal types and over classes of background events for which PDFs may be constructed.

The extended log likelihood then takes the form:

$$\log L = -\sum_i N_i + \sum_j n_j \ln\left(\nu(T_{\text{eff}}, R^3, \cos\theta_\odot)\right) \tag{3.2}$$

where j is the sum over all bins in the three signal extraction parameters T_{eff},R^3, and $\cos\theta_\odot$, and n_j is the number of detected events in each bin. The likelihood function was maximized over the free parameters, N_i, so that the best fit point yielded the most likely number of events of each signal type.

Ideally multi-dimensional PDFs would have been used to return the probability that an event belonged to a given signal i given the values of each observable. However, when a number of observable parameters are used, this results in large multi-dimensional distributions which are impractical to use and to produce with sufficient statistical sampling. For this reason, the probability distributions, f_i, were factorized into products of one, two- and three-dimensional PDFs (see Sec. 3.4 and Sec. 3.5 for more details).

Statistical uncertainties for each fitted signal were obtained from the fit directly, with 1σ uncertainties relating to the variation in a fit parameter that caused the log-likelihood to decrease by 0.5. Other uncertainties, caused by possible systematic differences between the data and simulated events, such as energy scale and resolution, and angular and positional resolution, were also taken into account in the analysis. The magnitude of all these systematic effects was determined by comparison of calibration data and simulated calibration events. The effect of each systematic on the fitted fluxes was then assessed by distorting the PDF observables by $\pm 1\sigma$ and repeating the fit. The change in each fit parameter with respect to the fit with undistorted PDFs was taken as the 1σ uncertainty for each systematic. All the contributions to systematic uncertainty were then added in quadrature.

3.3.1.1. *Flux Calculations*

The raw number of extracted events of each signal type, N_i, was converted to a flux using the predicted number of events from the Monte Carlo simulations:

$$\Phi_i = \frac{N_i}{N_{\mathrm{MC}}} C. \tag{3.3}$$

Here, Φ_i is the flux for signal i in units of 10^6 neutrinos cm^{-2} s^{-1}, and N_{MC} is the number of Monte Carlo events of signal type i satisfying data-selection criteria for a total simulated ^{8}B flux of 10^6 cm^{-2} s^{-1}. The factor C accounts for small (of order 1%) differences between data and Monte Carlo, such as livetime losses due to time-correlated cuts applied to the data and corrections to the exact number of target electrons and deuterons.[12]

3.3.1.2. *Spectrum Measurement*

Since there is a correlation between the effective kinetic energy of an event and the incoming neutrino energy for CC interactions, the energy PDFs are model-dependent. Therefore, using energy PDFs derived from SSM predictions in the signal extraction implicitly assumes that the spectrum of electron neutrinos arriving at the detector is the same as that emitted by the Sun. However, neutrino oscillations may manifest themselves as a change in the shape of the electron neutrino energy spectrum, as well as a reduction in the electron neutrino flux. For this reason, an additional analysis was performed on SNO data to extract an effective energy spectrum for the CC events, the integral of which gave a model independent measure of the CC flux.[13]

The spectrum analysis treated the number of CC events in each energy bin as a separate parameter in the fit. Since the energy distribution of NC events bears no information on the neutrino energy, E_ν, the number of NC events was still treated as a single fit parameter. Equation (3.1) then becomes

$$\nu(T_{\text{eff}}, R^3, \cos\theta_\odot) = \sum_i N_i f_i(T_{\text{eff}}, R^3, \cos\theta_\odot) + \sum_j \left(\sum_{k=1}^{N_{\text{bins}}} \left(N_{jk} f_{jk}(R^3, \cos\theta_\odot) \right) \right) \quad (3.4)$$

where i is summed over signals with E_ν-independent energy distributions (i.e. NC, backgrounds), and j is summed over signals with E_ν-dependent energy distributions (i.e. CC). N_{jk} is the number of events in energy bin k for signal j and a separate PDF, f_{jk}, was constructed for each energy bin of signal j.

Systematic differences between data and simulated events can vary with energy. For example, the chance of reconstructing an event vertex at the wrong radius depends on the number of PMT hits in that event, and thus on the event energy. Therefore, for the spectral analysis, energy dependent systematic uncertainties were evaluated using calibration data at a range of energies.

3.3.1.3. *Day-Night Neutrino Flux Asymmetry*

SNO was also in a position to test for possible MSW effects in the Earth. This effect manifests itself as an asymmetry between day-time and night-time fluxes of the CC and ES reactions measured in SNO. An asymmetry could only occur in the NC flux if oscillations to sterile neutrinos were induced. Therefore, the NC rate can be constrained to be the same through day and night. This was achieved by fitting both day and night data sets together, with one parameter describing the rate of NC events, but separate parameters to describe the number of CC and ES events during the day and the night. The asymmetry ratio is defined as

$$A = \frac{N - D}{(N + D)/2} \quad (3.5)$$

where N is the night time event rate and D is the day event rate. This ratio has the advantage that many common systematic effects will cancel.

This measurement sounds simple but it can be complicated by variations in the rate of background events, or changes in the PDF shapes between day and night. There were a number of reasons for such systematic changes, for example, the majority of work done in the underground laboratory occurred during the day-time causing minor temperature variations and changes to the lab power voltages, which had a slight effect on the energy response of the detector. These, and many other effects, were considered and careful checks were devised to assess the magnitude of any variations. A solitary point of high background radioactivity on the acrylic vessel proved particularly fortuitous for these studies. The origin of this so-called "hot-spot" was uncertain, but the event rate was stable and provided an excellent test for diurnal variations.

Due to the direction of incoming neutrinos, day-time and night-time events were also likely to populate different detector regions. Therefore rigorous checks for any anisotropies in the detector response were performed using calibration data taken in a range of positions within the detector.[14]

3.4. Phase 1 – D_2O

The first phase of data taking commenced in November 1999 and continued until June 2001. During this phase, which shall be referred to as the **D_2O Phase**, neutrons were detected through their capture on the deuterons present in the heavy water. This capture occurred with about 30% efficiency and produced a 6.25 MeV gamma that subsequently Compton scattered electrons to energies sufficient to produce Cherenkov radiation. Due to the analysis threshold of an effective kinetic energy of 5 MeV, only approximetely half of these events are observed.

Figure 3.3 shows the three distributions used to separate the signals in the D_2O phase data, each scaled by the fitted number of events. Although small correlations existed between these three parameters, the effects were negligible and therefore, the probabilities were simply determined from the product of the three sets of 1-dimensional PDFs. Plot (a) shows how the observable $\cos\theta_{\odot}$ is strongly peaked away from the Sun for ES events, and has a weak correlation for CC events. There is no correlation with the solar direction for the NC reaction since the gamma from neutron capture bears no information about the incoming neutrino.

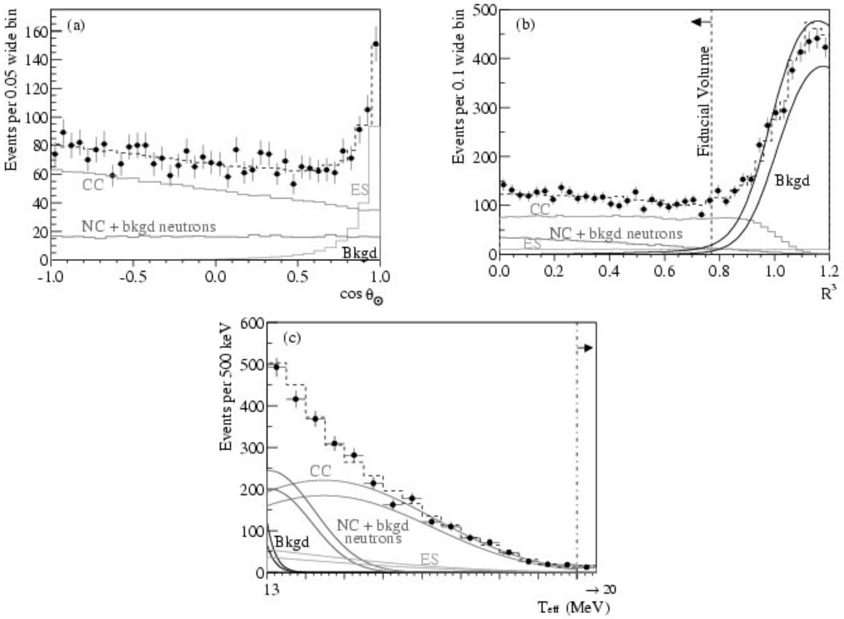

Fig. 3.3. Distribution of the D_2O data in three observable parameters: (a) $\cos\theta_{\odot}$, (b) Radial variable $R^3 = (R_{\rm fit}/R_{\rm AV})^3$ (as in the caption of Figure 3.4) and (c) Kinetic energy, $T_{\rm eff}$. Also shown are the Monte Carlo predictions for CC, ES and NC + background neutron events scaled to the fit results, and the calculated spectrum of beta-gamma background (Bkgd) events. The dashed lines represent the summed components, and the bands in the lower plot show $\pm 1\sigma$ statistical uncertainties from the signal extraction fit. Reproduced from Reference 1.

The distributions of volume weighted event position, R^3, shown in Figure 3.3 (b), are normalized to the radius of the acrylic vessel. Since the CC reaction only occurs on deuterons, it drops off at the acrylic vessel, while the ES reaction occurs on any electron and is uniformly distributed across the H_2O region as well. The NC signal does not exhibit a uniform distribution across the heavy water but decreases at higher radii. This is because the thermal diffusion length for neutrons in D_2O is long ($\sim$120 cm) and therefore neutrons produced nearer to the edge of the D_2O volume were likely to be captured on the hydrogen making up the acrylic vessel and the water outside it.

Figure 3.3(c) shows the effective electron kinetic energy distribution, $T_{\rm eff}$. For CC events, the strong correlation between the effective energy and the incident neutrino energy produces a spectrum which resembles the initial ^{8}B spectrum, while the recoil spectrum for the ES reaction is much softer. The NC energy PDF indicates the resolution for observation of the 6.25 MeV gamma produced in every neutron capture and includes neutrons from background events as well as NC signals. These background contributions were evaluated independently and subtracted from the fit result (see Ref. 1 for more details).

The beta-gamma background events clearly increase at radii approaching the acrylic vessel, justifying the selection criteria of $R_{\text{fit}} < 550\,\text{cm}$ for neutrino events. This background also increased sharply at low energies so the criteria $T_{\text{eff}} > 5\,\text{MeV}$ was also applied. The small number of beta-gamma background events remaining in the data set was determined from detailed calibrations and calculations and subtracted in the fit.

The first published SNO analysis was actually performed above a threshold of $T_{\text{eff}} = 6.75\,\text{MeV}$ on the first 241 days of D_2O data.[15] Above this energy, the major components of the data were CC and ES events, since only the tail of the neutron distribution could be seen. Assuming an undistorted ^{8}B neutrino spectrum,[16] fluxes of

$$\begin{aligned}\phi_{CC}^{SNO} &= 1.75 \pm 0.07(\text{stat.})^{+0.12}_{-0.11}(\text{syst.}) \pm 0.05(\text{theor.}) \times 10^6\ \text{cm}^{-2}\text{s}^{-1}\\ \phi_{ES}^{SNO} &= 2.39 \pm 0.34(\text{stat.})^{+0.16}_{-0.14}(\text{syst.}) \times 10^6\ \text{cm}^{-2}\text{s}^{-1}\end{aligned}$$

were obtained. However, since the statistics of the ES signal were fairly low, the more precise measurement of the ES signal from Super-Kamiokande[17]

$$\phi_{ES}^{SK} = 2.32 \pm 0.03(\text{stat.})^{+0.08}_{-0.07}(\text{syst.}) \times 10^6\ \text{cm}^{-2}\text{s}^{-1},$$

was used for comparison with the SNO CC measurement. The difference between these two fluxes was $0.57 \pm 0.17 \times 10^6\ \text{cm}^{-2}\text{s}^{-1}$, violating the hypothesis of no neutrino flavor change at the 3.3σ level – the first unambiguous demonstration of neutrino flavor change.

The final D_2O data set, comprising 0.65 kiloton-years and a total of 2928 neutrino candidates, was analyzed above the 5 MeV energy threshold for the first neutral current flux measurement[18] (For more details of the full analysis see Ref. 1). The fits shown in Fig. 3.3 resulted in the following neutrino fluxes, when the undistorted CC energy spectrum[16] was assumed:

$$\begin{aligned}\phi_{CC} &= 1.76^{+0.06}_{-0.05}(\text{stat.})^{+0.09}_{-0.09}(\text{syst.}) \times 10^6\ \text{cm}^{-2}\text{s}^{-1}\\ \phi_{ES} &= 2.39^{+0.24}_{-0.23}(\text{stat.})^{+0.12}_{-0.12}(\text{syst.}) \times 10^6\ \text{cm}^{-2}\text{s}^{-1}\\ \phi_{NC} &= 5.09^{+0.44}_{-0.43}(\text{stat.})^{+0.46}_{-0.43}(\text{syst.}) \times 10^6\ \text{cm}^{-2}\text{s}^{-1}\end{aligned}$$

The flux of neutrinos measured by ϕ_{NC} was in agreement with the predictions of standard solar models and significantly larger than that measured by ϕ_{CC}. The non-electron neutrino component, derived from a fit assuming both electron and non-electron active neutrino fluxes was

$$\phi_{\nu,\tau} = 3.41^{+0.45}_{-0.45}(\text{stat.})^{+0.48}_{-0.48}(\text{syst.}) \times 10^6 \text{ cm}^{-2}\text{s}^{-1}.$$

This result violates a hypothesis of no other detected neutrino flavors at the 5.3σ level, providing clear evidence for neutrino flavor change. Day-night asymmetries were also determined from the D_2O data, as shown in Table 3.2. These data were analyzed in the context of two-flavor neutrino oscillations to produce MSW exclusion plots and limits on neutrino flavor mixing parameters. The results of a χ^2 fit to SNO and other solar neutrino experimental data was found to strongly favor the LMA-mixing scenario (see Ref. 19 for more details).

Table 3.2. Day-night flux asymmetries determined from the D_2O, salt and combined SNO data sets (with statistical and systematic errors).

Signal	Asymmetry (%)		
	SSM spectral shape		Shape unconstrained
	No constraint	$A_{NC} = 0$	$A_{NC} = 0$
$\phi^{D_2O}_{CC}$	$+14.0 \pm 6.3^{+1.5}_{-1.4}$	$\phi_e = +7.0 \pm 4.9^{+1.3}_{-1.2}$	–
$\phi^{D_2O}_{ES}$	$-17.4 \pm 19.5^{+2.4}_{-2.2}$	–	–
$\phi^{D_2O}_{NC}$	$-20.4 \pm 16.9^{+2.4}_{-2.5}$	–	–
ϕ^{salt}_{CC}	$-2.1 \pm 6.3 \pm 3.5$	$-1.5 \pm 5.8 \pm 2.7$	$-3.7 \pm 6.3 \pm 3.2$
ϕ^{salt}_{ES}	$+6.6 \pm 19.8 \pm 5.7$	$+7.0 \pm 19.7 \pm 5.4$	$+15.3 \pm 19.8 \pm 3.0$
ϕ^{salt}_{NC}	$+1.8 \pm 7.9 \pm 5.2$	–	–

3.5. Phase 2 – Salt

In June 2001, two tonnes of NaCl were added to the D_2O for the **Salt Phase** of the experiment in which neutrons were detected through their capture on chlorine nuclei. Neutron capture on chlorine not only occurs with a higher efficiency than capture on deuterium (nearly a factor of three), it also releases more energy so that the distribution of NC events can be more easily distinguished from the low energy backgrounds. The 8.6 MeV released in each neutron capture is typically distributed among a number of gammas, unlike capture on deuterium which releases a single gamma, and thus results in a more isotropic distribution of Cherenkov light.

For this reason an additional parameter, β_{14}, was introduced for signal extraction purposes (see Ref. 12 for a full definition). This parameter is a measure of the isotropy, or uniformity of the distribution of triggered PMTs in each event. A number of parameterizations of isotropy were considered, but β_{14}, a combination of Legendre polynomials of the angle between each pair of PMT hits from the event vertex, was selected for its separation power and simple parameterization. In the D_2O phase, the CC and ES events produced a single primary electron, and the NC events produced a single gamma-ray, hence all three signals showed very similar distributions in β_{14}. However, in the salt-phase, isotropy was an effective separation tool for neutron events as shown in Fig. 3.4(a). Again it was impossible to distinguish between NC events and neutron backgrounds originating inside the D_2O so these contributions were evaluated separately and subtracted from the fitted neutrons.

The higher capture efficiency on ^{35}Cl also caused a larger background from neutrons originating outside the detector. However, the shorter thermal neutron diffusion length meant this background exhibited a characteristic distribution in R^3, which increased at higher radii and was used to separate the external neutron background statistically in the fit. Other background contributions, such as gamma-rays from the acrylic vessel, PMTs and H_2O are also shown in Fig. 3.4(c). These distributions were included in the fit as well, although additional information from analyses in an energy window below the neutrino-analysis threshold was used to constrain the magnitude of these components.

Figure 3.4 also shows the predicted distributions in the other parameters used to separate the signals in the salt data. Comparison with Fig. 3.3 shows that for the salt phase the mean energy for NC events was increased and that the NC radial distribution became significantly flatter for salt-data, due to the higher capture efficiency for neutrons. The $\cos\theta_\odot$ distribution still provided good separation for ES events.

Simulation and calibration studies showed that the parameter β_{14} is correlated with T_{eff}, and to a lesser extent with R^3. Therefore, to avoid biases in the signal extraction it was necessary to account for these correlations with multi-dimensional PDFs:

$$f_i(T_{\text{eff}}, \beta_{14}, R^3, \cos\theta_\odot) = P_i(T_{\text{eff}}, \beta_{14}, R^3) \cdot P_i(\cos\theta_\odot | T_{\text{eff}}, R^3). \qquad (3.6)$$

Here the first factor is a 3-dimensional PDF, whilst the second is the conditional PDF for $\cos\theta_\odot$ given T_{eff} and R^3 to account for the slight correlations of $\cos\theta_\odot$.

Another background contribution, specific to the salt phase arose from the activation of Na to produce ^{24}Na, which has a half-life of 15 hours.

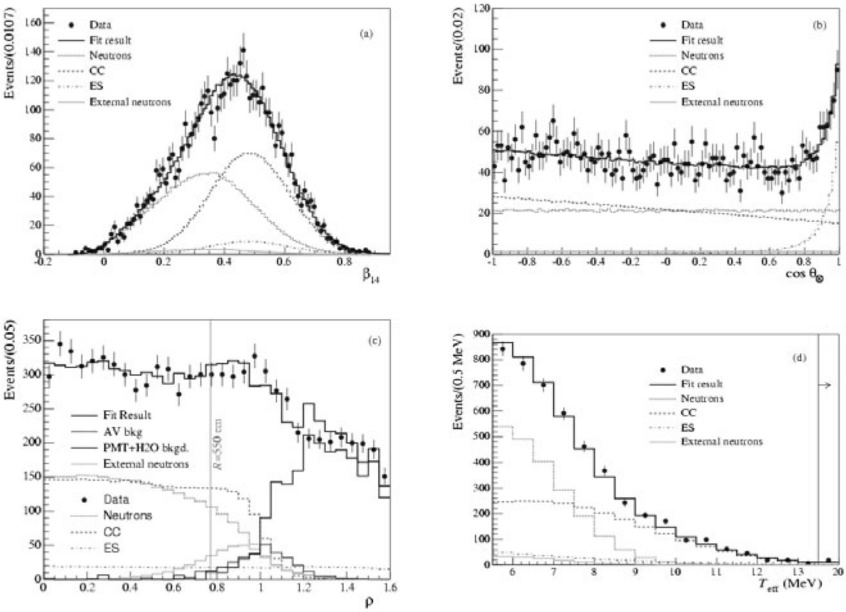

Fig. 3.4. Distribution of the salt data in four observable parameters: (a) β_{14}, a measure of event isotropy, (b) $\cos\theta_{\odot}$, (c) Radial variable $\rho = (R_{\rm fit}/R_{AV})^3$ and (d) Kinetic Energy. Also shown are the Monte Carlo predictions for CC, ES, neutron events (including the NC signal) and External neutrons, scaled to the fit results. Additional background contributions are also shown on the radial plot. Reproduced from Reference 12.

To avoid the backgrounds from ^{24}Na, resulting from neutron activation during calibration, a period of data following each calibration was removed from the data set. However, events from ^{24}Na were a useful additional means of calibrating the detector, so at one point a strong neutron source was introduced into the detector to activate the salt specifically for this purpose.

As for the D_2O phase, selection criteria were applied to the observable parameters to minimize the systematic uncertainties associated with backgrounds, especially low energy backgrounds external to the D_2O. For the salt-data, analysis cuts of $R < 550\,\mathrm{cm}$ and $T_{\rm eff} > 5.5\,\mathrm{MeV}$ were applied.

The salt was removed from the SNO detector in October 2003 after 391 live days of salt data had been collected. Due to the additional separation power of the isotropy parameter, signal extraction could be performed without constraints on either the CC or ES energy distributions to test the shape of the CC spectrum. The resulting spectrum is shown in Fig. 3.5 compared to the spectrum predicted for both the undistorted SSM and that expected with LMA oscillations. The spectrum obtained was consistent with both models. Since the difference between the two predicted spectra is most apparent at low energies, future studies will focus on a low-energy-threshold analysis of SNO data and the reduction of systematic uncertainties.

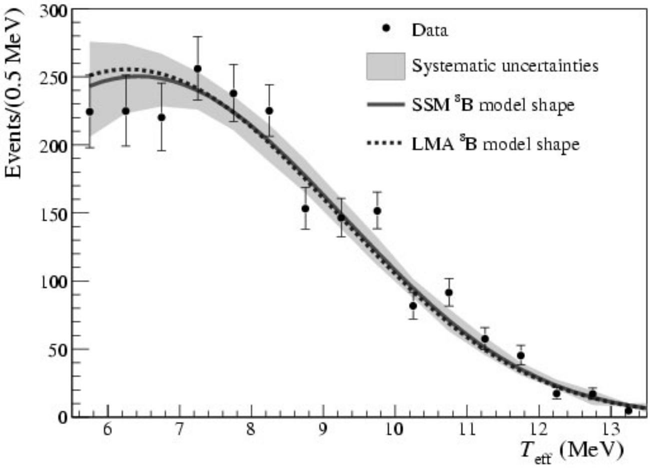

Fig. 3.5. CC spectrum extracted from the salt data set with statistical uncertainties (points) compared to two predicted spectra: the undistorted SSM prediction and that expected with LMA oscillations. The band on the undistorted prediction represents the 1σ uncertainty determined from detector systematic uncertainties. Reproduced from Reference 12.

The energy-unconstrained fit resulted in the following fluxes for each signal, with a noticeable improvement over the D_2O phase for the precision of the NC measurement.[12,20]

$$\phi_{CC} = 1.68^{+0.06}_{-0.06}(\text{stat.})^{+0.08}_{-0.09}(\text{syst.}) \times 10^6 \text{ cm}^{-2}\text{s}^{-1}$$

$$\phi_{ES} = 2.35^{+0.22}_{-0.22}(\text{stat.})^{+0.15}_{-0.15}(\text{syst.}) \times 10^6 \text{ cm}^{-2}\text{s}^{-1}$$

$$\phi_{NC} = 4.94^{+0.21}_{-0.21}(\text{stat.})^{+0.38}_{-0.34}(\text{syst.}) \times 10^6 \text{ cm}^{-2}\text{s}^{-1}$$

More precise day-night asymmetries were also obtained as shown in Table 3.2 for scenarios with the CC spectral shape both constrained and unconstrained.

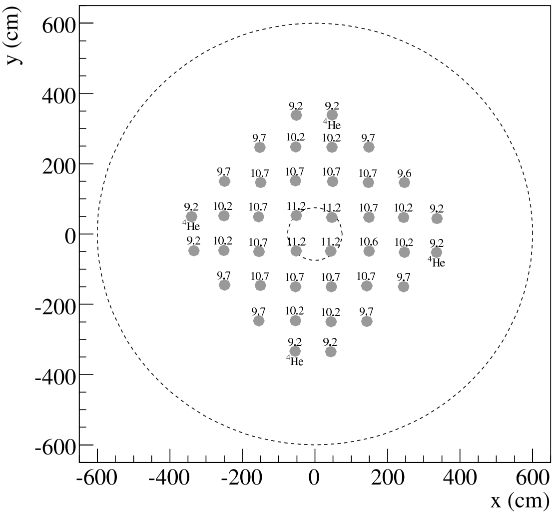

Fig. 3.6. The layout of the NCD array in the heavy water. The numbers give the NCD length in meters and the position of ^{4}He counters are also indicated. The dotted lines indicate the maximum AV radius and the radius of the neck. Reproduced from Reference 21.

3.6. Phase 3 – Neutral Current Detection Array

The third and final phase of SNO, the **NCD phase**, used a detector system to measure the neutrons produced in the NC reaction independently of the PMT array: the Neutral Current Detection array (NCD).

The NCD system consisted of an array of proportional counters made from ultra-pure nickel and filled with ^{3}He gas. Neutrons were observed through ionization produced in the proportional counter due to the following reaction:

$$^3\mathrm{He} + n \rightarrow \; ^3\mathrm{H} + p + 764\,\mathrm{keV}. \tag{3.7}$$

3.6.1. *The Counter System*

The layout of the array is shown in Fig. 3.6.[21] Also shown in this figure are the positions of four ^{4}He counters used to check the understanding of backgrounds in the NCDs. The proportional counters, 5 cm in diameter and several meters long (consisting of 3 or 4 separate volumes), were distributed throughout the inner region of the SNO heavy water volume. This geometry was an optimization between the loss of Cherenkov light observed by the PMT array and the neutron capture efficiency of the array. In this configuration, the NCD array captured about 26% of the neutrons, with nearly 100% detection efficiency. The D_2O captured approximately 17% of the neutrons, but the detection efficiency for neutron capture on D_2O was only about 50% of this because of the energy threshold restriction on the Cherenkov light from the 6.25 MeV gammas. Light from the Cherenkov events in the centre of the detector was only attenuated by about 8% by the array of NCDs.

This configuration ensured that the NC signal was effectively separated from the CC and ES measurement. This meant the systematic error of this measurement is uncorrelated with the previous two phases, making it an "independent" measurement to confirm the previous results from SNO.

The NCD array was read out by two separate systems. A fast shaper-ADC system read out only the total charge deposited and a slower digitizing-oscilloscope system measured the full signal shape after it crossed a preset threshold.

3.6.2. *The Backgrounds*

Instrumental backgrounds in the NCDs, due to micro-discharges, noise, and oscillatory noise, occurred at a rate of approximately 0.3 Hz. These pulse shapes were easily distinguished from physics events.

The internal background for the NCD phase was the same as in the D_2O phase: the neutrons produced in the D_2O by the U- and Th-chain. However, the NCD array could also have contained these elements, adding to this background. In order to limit the photodisintegration neutron production rate from the full NCD array to less than 2% of the NC production rate, the NCD bodies had to contain less than $0.5\,\mu$g of ^{232}Th and less than about $4\,\mu$g of ^{238}U in the entire array. To reach the required cleanliness, the NCDs were designed and built by the SNO collaboration using low-radioactivity materials, especially the bodies of the counters, which were made of nickel, purified through a chemical-vapor deposition process. After construction, the NCDs were transported to Sudbury and brought underground as quickly as possible to maximize the amount of cool down of cosmogenic activity, which could cause signals at similar energies to those from neutron capture on ^{3}He. This reduced the expected cosmogenic activity to less than 10^{-6} events per day.

Radioactivity in the counters themselves also caused a direct background: α-activity in the nickel walls of the counters could cause signals similar to those from neutron-capture on ^{3}He. ^{210}Po, deposited by ^{222}Rn in the air,[e] which produces a 5.3 MeV alpha, was particularly important in this case. Only a small fraction of α-decays caused a signal in the energy region where the neutron peak occurred. In the final analysis, the distinctive shape of the neutron-capture energy spectrum from the alpha background will be used to extract the NC interaction rate. The additional information available in the digitized pulses will also give an extra handle to separate the signals from neutrons and those from alphas. External neutrons, produced by photo-disintegration of deuterons by gammas originating from sources external to the SNO D_2O volume were only captured in a few percent of the cases.

3.6.3. *The Installation of the NCD System*

Due to the physical limitations posed by the SNO cavern, only counter-segments shorter than 5.5 m could be lowered into the neck of the acrylic vessel. The NCD strings had to be welded in the extremely clean environment of the SNO underground laboratory. Next, a remotely-operated submersible vehicle (ROV) was used to maneuver each string to a pre-installed anchor point. After this, the NCD string was tested using an AmBe neutron calibration source. The final step of installation was to secure the high-voltage/signal cable. NCD deployment began in December, 2003 and the last string was deployed in February, 2004. Commissioning of the NCD array proceeded until November, 2004.

3.6.4. *Data-Taking Period*

The successful data-taking period of the third phase of SNO continued until November 2006. During this period, the calibration of the PMT array continued in the same manner as in the previous phases. The calibration of the NCD array was performed using a ^{252}Cf source, and several AmBe sources. Due to the complex geometry, and therefore very complex neutron capture profile of the detector, a new calibration was devised. Based on the successful use of ^{24}Na events for calibration in the salt-phase, a small quantity of activated brine was put in the center of the SNO detector and compared to the ^{252}Cf source. This technique gave a source of neutrons

---

[e] The levels of ^{222}Rn are considerably higher in the mine air than in air above ground.

geometrically very similar to the NC-flux with an accurately known strength. The analysis of the data taken during this phase is still ongoing at the time of writing.

3.7. Conclusions

The SNO experiment has been extremely successful so far, having unambiguously proved solar neutrino flavor change and solved the long-standing solar neutrino problem. Further results from the NCD phase, a combined analysis of all three phases, and a spectral measurement for a low-energy threshold can be expected in the future. The most precise flux measurements so far, from the salt phase, are shown in Fig. 3.7 in terms of ν_e and non-ν_e ($\phi_{\mu\tau}$) fluxes.[12] The bands showing the fluxes, with 1σ uncertainties for each of the three signal types have different gradients due to the different sensitivities to non-electron neutrinos. The diagonal NC band is in good agreement with standard solar model[22] predictions (dashed band) and the intercept, for which 68%, 95% and 99% error contours are shown, can be used for the best estimate of the $\phi_{\mu\tau}$ flux which is clearly non-zero, confirming the flavor change of solar neutrinos.

These results can be analyzed in terms of neutrino oscillations with the CC/NC flux ratios placing strong constraints on the allowed values of θ_{12}. Other parameters, such as day-night asymmetry, have more sensitivity to the value of Δm^2_{12}.[23] Day-night analyses, performed on both the D_2O and salt data[12,14,19] result in a combined day-night asymmetry in the electron neutrino flux of

$$A_e = 0.037 \pm 0.040 \tag{3.8}$$

under the assumption of undistorted CC energy spectra and no NC asymmetry. This result is consistent with no day-night effect and also with the small effect predicted for LMA oscillations.

The flux, spectrum and day-night results obtained from both the D_2O and salt phases were used in a χ^2 analysis of MSW parameter space, in which Δm^2 and $\tan^2\theta$ for two-flavor oscillations were free parameters (see Ref. 12 for more details). The total ^{8}B flux, ϕ_B, was also allowed to float in this fit, which resulted in the best-fit parameters:

$$\Delta m^2_{12} = 5.0 \times 10^{-5}\,\text{eV}^2, \;\; \tan^2\theta_{12} = 0.45, \;\; \text{and} \;\; \phi_B = 5.11 \times 10^6\,\text{cm}^{-2}\text{s}^{-1}.$$

These results favored the LMA mixing solution but did not exclude other regions of MSW parameter space as shown in Fig. 3.8 (left). When data

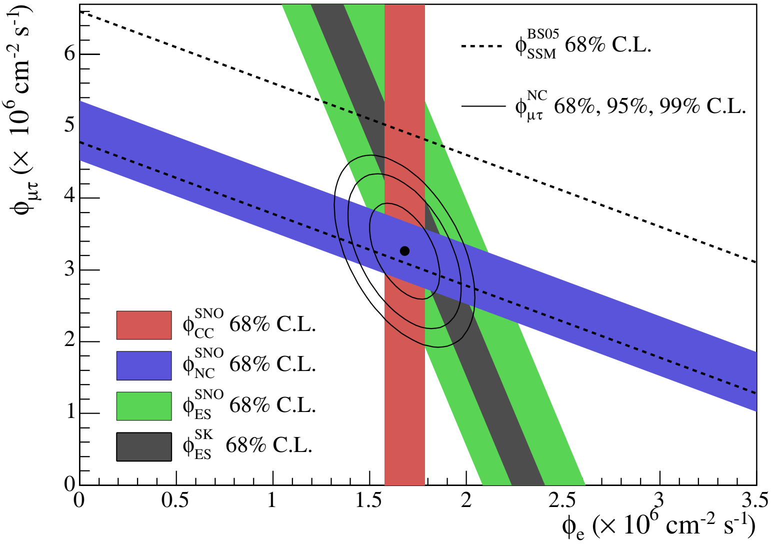

Fig. 3.7. Flux of μ and τ neutrinos versus flux of e neutrinos derived from SNO CC, ES and NC measurements. The diagonal NC band can be compared to the total ^{8}B flux predicted by the standard solar model[22] shown with dashed lines. The narrow band parallel to the SNO ES result is the Super-Kamiokande result.[25] Reproduced from Reference 12.

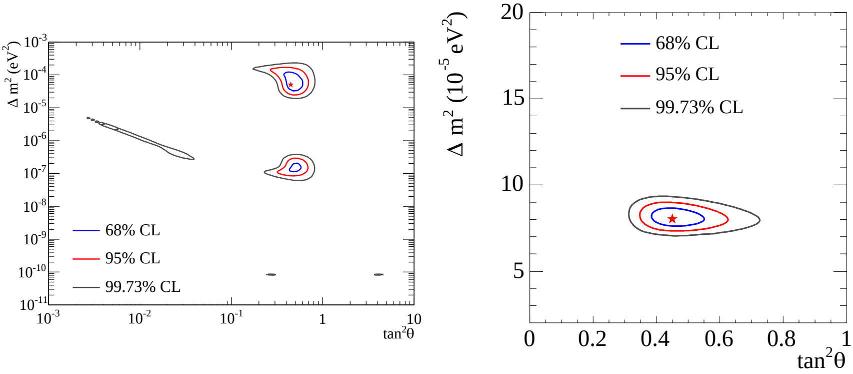

Fig. 3.8. Allowed parameter space from MSW neutrino oscillation analysis of (left) SNO-only data and (right) SNO data combined with results from other solar neutrino experiments and the KamLAND 766 ton-year data. Both Figures reproduced from Reference 12.

from other neutrino experiments, including Super Kamiokande's solar neutrino zenith spectra and KamLAND's (see Chapter 4) 766 ton-year data,[24] were included in the χ^2 analysis, all parameter space except the LMA-mixing region was excluded as shown in Fig. 3.8 (right), and the allowed mixing parameters were tightly constrained. Inclusion of the SNO data also eliminated all solutions where $\tan^2\theta > 1$, thus setting the mass hierarchy to be $m_2 > m_1$.

To obtain the results reviewed here, SNO had to overcome significant technical difficulties. The creation of the large underground cavern, the construction of the SNO acrylic vessel, and the creation of a very clean environment and detector at 2 km depth in a operational nickel mine were all unique technical challenges that had never been attempted on this scale before. Furthermore, without the development of new, highly sensitive, low-level radiation background measurements and novel calibration techniques, the groundbreaking physics measurements presented here would have been impossible.

Acknowledgments

This research was supported by: Canada: Natural Sciences and Engineering Research Council, Northern Ontario Heritage Fund, Atomic Energy of Canada, Ltd., Ontario Power Generation, High Performance Computing Virtual Laboratory, Canada Foundation for Innovation; US: Dept. of Energy, National Energy Research Scientific Computing Center; UK: Particle Physics and Astronomy Research Council. We thank the SNO technical staff for their strong contributions. We thank Inco for hosting this project.

References

1. B. Aharmim et al., Measurement of the ν_e and total B-8 solar neutrino fluxes with the Sudbury Neutrino Observatory phase I data set, *Phys. Rev.* **C75**, 045502, (2007).
2. H. H. Chen, Direct approach to resolve the solar-neutrino problem, *Phys. Rev. Lett.* **55**, 1534–1536, (1985).
3. J. Boger et al., The Sudbury Neutrino Observatory, *Nucl Instr. and Meth.* **A**(449), 172, (2000).
4. B. Aharmim et al., A search for neutrinos from the solar hep reaction and the diffuse supernova neutrino background with the Sudbury Neutrino Observatory, *Astrophys. J.* **653**, 1545–1551, (2006).
5. B. A. Moffat et al., Optical calibration hardware for the Sudbury Neutrino Observatory, *Nucl. Instr. and Meth.* **A**(554), 255–265, (2005).

6. M. Dragowsky et al., The ^{16}N calibration source for the Sudbury Neutrino Observatory, *Nucl. Instr. and Meth.* **A**(481), 284, (2002).
7. N. J. Tagg et al., The ^{8}Li calibration source for the Sudbury Neutrino Observatory, *Nucl. Instr. and Meth.* **A**(489), 178, (2002).
8. A. W. Poon et al., A compact ^{3}H(p,gamma)^{4}He 19.8-MeV Gamma-ray source for energy calibration at the Sudbury Neutrino Observatory, *Nucl. Instr. and Meth.* **A**(452), 115, (2000).
9. T. C. Andersen et al., A radium assay technique using hydrous titanium oxide adsorbent for the Sudbury Neutrino Observatory, *Nucl. Instr. and Meth.* **A** (501), 386–398, (2003).
10. T. C. Andersen et al., Measurement of radium concentration in water with Mn-coated beads at the Sudbury Neutrino Observatory, *Nucl. Instr. and Meth.* **A**(501), 399–417, (2003).
11. J.N.Bahcall, M.H. Pinsonneault, S. Basu, Solar models: current epoch and time dependences, neutrinos, and helioseismological properties, *Astro-phys. J.* **555**, 990–1012, (2001).
12. B. Aharmim et al., Electron energy spectra, fluxes, and day-night asymmetries of ^{8}B solar neutrinos from measurements with NaCl dissolved in the heavy-water detector at the Sudbury Neutrino Observatory., *Phys. Rev. C.* **72**, 055502, (2005).
13. J. R. Wilson. *A Measurement of the ^{8}B Solar Neutrino Energy Spectrum at the Sudbury Neutrino Observatory.* PhD thesis, Oxford University, Oxford, UK, (2004).
14. K. K. S. Miknaitis. *A Search for Matter Enhanced Neutrino Oscillations through Measurements of Day and Night Solar Neutrino Fluxes at the Sudbury Neutrino Observatory.* PhD thesis, University of Washington, Seattle, USA, (2005).
15. Q. R. Ahmad et al., Measurement of charged current interactions produced by ^{8}B solar neutrinos at the Sudbury Neutrino Observatory, *Phys. Rev. Lett.* **87**, 071301, (2001).
16. C. E. Ortiz et al., Shape of the ^{8}B alpha and neutrino spectra, *Phys. Rev. Lett.* **85**, 2909–2912, (2000).
17. S. Fukuda et al., ^{8}B and hep neutrino measurements from 1258 days of Super-Kamiokande data, *Phys. Rev. Lett.* **86**, 5651, (2001).
18. Q. R. Ahmad et al., Direct evidence for neutrino flavor transformation from neutral-current interactions in the Sudbury Neutrino Observatory, *Phys. Rev. Lett.* **89**, 011301, (2001).
19. Q. R. Ahmad et al., Measurement of day and night neutrino energy spectra at SNO and constraints on neutrino mixing parameters., *Phys. Rev. Lett.* **89**, 011302, (2002).
20. Q. R. Ahmad et al., Measurement of the total active ^{8}B solar neutrino flux at the Sudbury Neutrino Observatory with enhanced neutral current sensitivity, *Phys. Rev. Lett.* **92**, 181301, (2002).

21. J. F. Amsbaugh et al., An array of low-background ^{3}He proportional counters for the Sudbury Neutrino Observatory, *Nucl. Instrum. Meth.* **A579**, 1054–1080, (2007).
22. J. N. Bahcall, A. M. Serenelli, and S. Basu, New solar opacities, abundances, helioseismology, and neutrino fluxes, *Astro-phys. J.* **621**, L85–88, (2005).
23. P. C. de Holanda and A. Y. Smirnov, LMA MSW solution of the solar neutrino problem and first KamLAND results., *JCAP*. **0302**, 001, (2003).
24. T. Araki et al., Measurement of neutrino oscillation with KamLAND: Evidence of spectral distortion, *Phys. Rev. Lett.* **94**, 081801, (2005).
25. S. Fukuda et al., Determination of solar neutrino oscillation parameters using 1496 days of Super-Kamiokande-I data, *Phys. Lett. B*. **539**, 179, (2002).

Chapter 4

Neutrino Oscillation Physics with KamLAND: Reactor Antineutrinos and Beyond

Karsten M. Heeger
University of Wisconsin, Physics Department,
Madison, WI 53706, USA
heeger@wisc.edu

The discovery of flavor transformation in atmospheric, solar, and accelerator neutrinos has provided unambiguous evidence that neutrinos have mass and mix flavors. Data obtained in the past decade have revolutionized our understanding of neutrinos and provided the first evidence of physics beyond the Standard Model. In the long history of reactor neutrino physics, KamLAND has added to these recent discoveries the first direct observation of reactor $\overline{\nu}_e$ disappearance, the evidence of spectral distortion as a signature of neutrino oscillation, and provided terrestrial confirmation for neutrino oscillation as the solution to the solar neutrino problem. With its long baseline of ~175 km KamLAND makes the most precise determination of the mass splitting Δm^2_{12} and, together with the solar neutrino experiments, has determined under the assumption of CPT invariance the oscillation parameters to unprecedented precision: $\Delta m^2 = 7.9^{+0.6}_{-0.5} \times 10^{-5}$ eV^2 and $\tan^2\theta = 0.40^{+0.10}_{-0.07}$. Besides the measurement of the reactor $\overline{\nu}_e$ flux, KamLAND has also observed geological antineutrinos from inside the Earth and set limits on the $\overline{\nu}_e$ flux from the Sun. By purifying its liquid scintillator target and reducing internal detector backgrounds, KamLAND is preparing for the direct observation of low-energy, ^{7}Be solar neutrinos that may allow the first direct test of the MSW mechanism of solar neutrino oscillation.

Contents

4.1 Neutrino Physics at Reactors: From the Discovery of $\overline{\nu}_e$ to Nuclear Non-Proliferation 72
4.2 The KamLAND Detector 73
  4.2.1 Observation of Reactor Antineutrino Disappearance 76
4.3 Spectral Distortion as a Signature of Neutrino Oscillation 77
4.4 Toward a Precision Measurement of Δm^2_{12} and θ_{12} 80
4.5 Other Neutrino Physics with KamLAND 82

4.6 Test of MSW and Non-Standard Interactions in the KamLAND Low-Background Phase 84
4.7 Summary and Conclusions 87
References 88

4.1. Neutrino Physics at Reactors: From the Discovery of $\overline{\nu}_e$ to Nuclear Non-Proliferation

From the first direct observation of the antineutrino by Reines and Cowan in 1956[1] to the searches for neutrino oscillation at the Institut Laue-Langevin (ILL), Goesgen, Bugey, Krasnoyarsk, Palo Verde, and CHOOZ,[2–6] reactor neutrino experiments have played a key role in the history of neutrino physics. Experiments at reactors have placed the best laboratory limit on the neutrino magnetic moment[7] and provide the best limit on the yet unknown neutrino mixing angle θ_{13}.[6] Reactor antineutrinos have also found an application in recent efforts to remotely monitor the fuel composition of nuclear reactors for non-proliferation purposes by measuring the time-dependent variation of the $\overline{\nu}_e$ flux and spectrum.[10]

The pure electron flavor content of the antineutrinos produced in the β-decay products of the fission isotopes make nuclear reactors a desirable source for neutrino studies. The Sun and nuclear reactors are two of the few sources that provide pure flavor beams of neutrinos free of other contamination. Reactor experiments use the electron antineutrinos resulting from the decay of fission products. Solar neutrino experiments use the pure ν_e flux from the Sun's fusion reactions and β-decays. The vastly different baselines and environments of reactor and solar experiments allow them to probe both the propagation of neutrinos through vacuum and the neutrino interaction with matter.

Nuclear power plants emit copious numbers of $\overline{\nu}_e$. They are produced in the decay of the fission products inside the reactor.[16] Fission products are generally neutron rich nuclei that can undergo successive β-decays, each yielding one $\overline{\nu}_e$. Each fission produces on average 6 $\overline{\nu}_e$'s with an accompanying energy release of ∼200 MeV. A typical nuclear power plant operating at 3 GW thermal output produces on average 7×10^{20} $\overline{\nu}_e$'s per second. The intensity of the antineutrino flux from reactors and its flavor content make it a unique laboratory for the study of neutrino properties. From the energy release and the nuclear fuel composition of a reactor, the total number of electron antineutrinos emitted from the nuclear reactor can be predicted. Due to the small cross-section, antineutrinos leave the reactor core isotropically. Knowing the total number of $\overline{\nu}_e$'s emitted from the core, we can predict the expected $\overline{\nu}_e$ flux and interaction rate at any distance from the reactor. Over time the nuclear fuel composition of reactors change as neutron absorption and beta decay lead to nuclear transmutation. This is taken into account in a detailed analysis of the $\overline{\nu}_e$ flux calculation from nuclear reactors. Four isotopes, ^{235}U, ^{238}U, ^{239}Pu, ^{241}Pu contribute more than 99.9% to the total power generation of a reactor. Contributions from other elements are usually ignored.[16]

Over the past five decades a series of reactor experiments with increasing baselines have searched for electron antineutrino disappearance as a signature of neutrino oscillation. Detectors filled with liquid scintillator were placed near nuclear plants at distances from tens of meters up to about one kilometer to measure the flux of $\overline{\nu}_e$ emitted from the nuclear reactor. For all experiments up to a distance of 1 km from the reactor, the observed reactor $\overline{\nu}_e$ flux was found to be consistent with the expectations from no oscillations. This ruled out $\nu_\mu \leftrightarrow \nu_e$ as an explanation for the atmospheric neutrino anomaly.[5,6]

As early as 1967 Bruno Pontecorvo suggested that lepton flavor may not be conserved and neutrinos might change flavor.[8] Existence of neutrino mass directly implies flavor transformation through oscillation. For reactor antineutrinos created in the electron flavor state, the survival probability is to a good approximation given by

$$P(\overline{\nu}_e \rightarrow \overline{\nu}_e) \simeq \cos^4\theta_{13}\left(1 - \sin^2(2\theta_{12})\sin^2\frac{\Delta m^2_{12}L}{4E_\nu}\right) \tag{4.1}$$

where L is the distance the neutrinos travel and E_ν is the (anti)neutrino energy. Reactor neutrinos typically have a mean energy of ∼4 MeV. Matter effects that arise in the interaction of neutrinos with the electrons inside matter[29] are usually negligible for reactor neutrinos.

4.2. The KamLAND Detector

Following the observation of the zenith angle dependence of atmospheric neutrinos in Super-Kamiokande[11] (See Chapter 2) and the discovery of the solar neutrino flavor transformation at SNO[12] (See Chapter 3), the KamLAND experiment started data taking in 2002 to make a measurement of the integrated flux of $\overline{\nu}_e$'s from all nuclear power plants in Japan. The KamLAND experiment is located at 36° 25' 26" N, 137° 18' 43" E, approximately 1,000 m below the summit of Mt. Ikenoyama in the Gifu prefecture, Japan, with an average rock over burden of 2,700 m.w.e. It occupies the site of the original Kamiokande experiment.

KamLAND is a high resolution liquid scintillator detector designed to observe reactor antineutrinos from nuclear power plants in Japan. It consists of 1 kton of ultra-pure liquid scintillator contained in a 13-m-diameter spherical balloon made of 135-μm thick transparent nylon/EVOH composite film. The balloon is supported and constrained by a network of Kevlar ropes. The liquid scintillator is a mixture of 80% dodecane, 20% pseudocumene, and 1.52 g/l of PPO as a fluor. The balloon is housed in a 18 m diameter stainless steel vessel inside a cavity filled with water. A buffer region of dodecane and isoparaffin oils in between the balloon and the stainless steel containment vessel shields the liquid scintillator target from external radiation. Methods for water extraction and nitrogen bubbling were used to purify the liquid scintillator and buffer oil during the filling of KamLAND.

Antineutrinos from the decays of fission products in a nuclear reactor interact with the protons in the scintillator through the inverse beta reaction $\overline{\nu}_e + p \rightarrow e^+ + n$ with a 1.8 MeV energy threshold. The cross-section for this inverse beta-decay process is well established[17]. The scintillation light from the prompt e^+ annihilation gives an estimate of the incident $\overline{\nu}_e$ energy. Neglecting the small neutron recoil, the positron energy and the $\overline{\nu}_e$ energy are related through $\mathrm{E}_{\overline{\nu}_e} \simeq \mathrm{E}_{e^+} + 0.8$ MeV, where E_{e^+} is the kinetic energy of the positron plus the $\mathrm{e}^+\mathrm{e}^-$ annihilation energy. Electron antineutrinos are detected through the coincidence signature of positron annihilation followed by neutron capture on protons. The mean neutron capture time is typically 200 μsec. Neutron capture on protons produces a deuteron and a 2.2 MeV γ-ray. On average neutrons are captured within 9 cm. Some 1325 17-inch and 554 20-inch photomultipliers (PMT's) mounted on the inside of the 18-m steel containment vessel are used to detect the scintillation light following the positron annihilation and neutron capture. The spatial and temporal correlation of the prompt and delayed events is used to discriminate events from radioactive backgrounds and other sources. A 3.2 kton water Cherenkov detector surrounds the spherical containment vessel. It shields the inner detector from γ-rays and neutrons from the surrounding rock and, with an efficiency of over 92%, is used to identify muons entering the detector. Figure 4.1 shows a cross-section of the KamLAND detector. With this detector configuration KamLAND has a photocathode coverage of 34%, including both the 17-inch and 20-inch PMT's, with a combined energy resolution of $6.2\%/\sqrt{E(\mathrm{MeV})}$. The detector triggers when 200 of

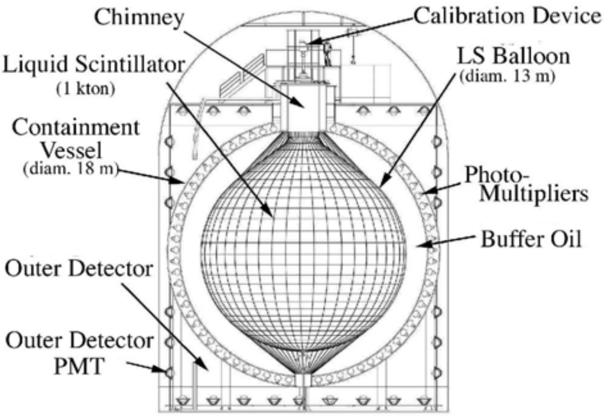

Fig. 4.1. Technical drawing of the KamLAND detector.[13] Reproduced from Reference 14.

the 17-inch PMT's register hits, which corresponds to about 0.7 MeV at the detector center. The trigger efficiency close to 100%.

The principal contribution to the reactor $\overline{\nu}_e$ flux measured by KamLAND comes from 53 Japanese power reactors. The flux of $\overline{\nu}_e$ from a reactor a at distance L from KamLAND is approximately proportional to the thermal power flux, $P_{th}/4\pi L^2$, where P_{th} is the reactor thermal power. Most reactors are located within a distance range of $L = 175 \pm 35$ km from KamLAND. Given this spread of distances and the relation between the mass, the survival probability and the distance the neutrino travels, shown in Eq. 4.1, KamLAND is most sensitive to neutrino oscillations corresponding to a splitting of the neutrino mass eigenstates of $\sim 3 \times 10^{-5}$ eV^2. This provides KamLAND with good conditions to confirm the solar ν_e oscillation observed in SNO[12] with terrestrial $\overline{\nu}_e$. The expected $\overline{\nu}_e$ flux from the Japanese reactors is calculated from the reactor operation data, including thermal power generation, fuel burn up, exchange and enrichment records. The expected flux is calculated using fission rates and $\overline{\nu}_e$ spectra. The $\overline{\nu}_e$ contribution from Japanese research reactors and all reactors outside Japan is 4.5%, and we assume that these reactors have the same average fuel composition as the Japanese power reactors. The averaged relative fissions yields for the first run period of the KamLAND experiment was $^{235}\mathrm{U} : {}^{238}\mathrm{U} : {}^{239}\mathrm{Pu} : {}^{241}\mathrm{Pu} = 0.568 : 0.078 : 0.297 : 0.057$.

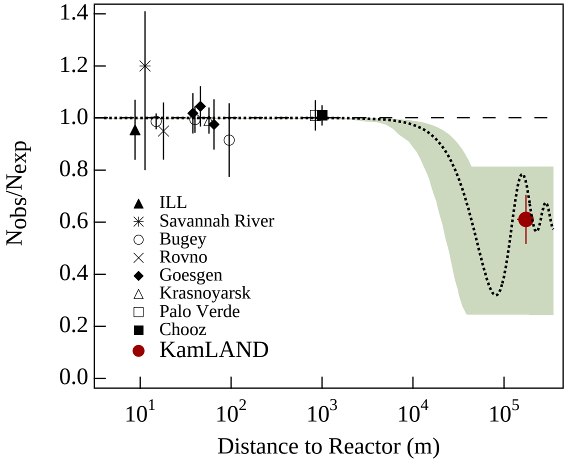

Fig. 4.2. Ratio of the measured to expected $\overline{\nu}_e$ flux from reactor experiments. The solid dot is the KamLAND measurement at a flux-weighted average distance. It falls into the region of flux predictions (shaded) corresponding to the 95% CL region found in a global analysis of the solar neutrino data. The dotted line is representative of a best-fit LMA prediction. Reproduced from Reference 14.

4.2.1. *Observation of Reactor Antineutrino Disappearance*

KamLAND began data taking in early 2002. With an exposure of 162 ton-yr corresponding to 145.1 days of data taking, KamLAND reported first results.[14] It measured 54 events compared to an expectation of 88.4 events. The ratio of the number of observed $\overline{\nu}_e$ candidate events minus backgrounds to the expected number of $\overline{\nu}_e$ events was found to be

$$\frac{N_{observed} - N_{bkgd}}{N_{expected}} = 0.611 \pm 0.085(stat.) \pm 0.041(syst.) \qquad (4.2)$$

This result demonstrated for the first time reactor $\overline{\nu}_e$ disappearance at the 99.95% confidence level and confirmed that the so-called large-mixing angle (LMA) solution preferred by data from the solar neutrino experiments is the solution to the solar neutrino problem. Figure 4.2 shows the measurement of the reactor neutrino flux by KamLAND with 162 ton-yr of exposure in 2002 along with past reactor $\overline{\nu}_e$ flux measurements. The shaded region of Fig. 4.2 indicates the range of flux predictions corresponding to the 95% C.L. region found in a global analysis of the solar neutrino data at that time. The dotted curve corresponds to and is representative of a best-fit LMA prediction. With this measurement KamLAND found the first evidence for reactor $\overline{\nu}_e$ disappearance at high confidence level and confirmed with terrestrial neutrinos the oscillation solution preferred by a global fit to all solar neutrino data.[14]

4.3. Spectral Distortion as a Signature of Neutrino Oscillation

Two years after the discovery of reactor antineutrino disappearance, KamLAND reported on a precision measurement of the reactor $\overline{\nu}_e$ flux with higher statistics.[15] With 766 ton-year of exposure corresponding to a threefold increase in exposure and a 33% increase in the usable fiducial volume over the first results, the experiment observed 258 $\overline{\nu}_e$ candidate events compared to the 365.2 events expected in the absence of oscillations. With this exposure it became possible to make a detailed analysis of the prompt energy spectrum. The data increased the statistical significance for reactor $\overline{\nu}_e$ disappearance to 99.998% from the difference in the expected and observed $\overline{\nu}_e$ rate. Furthermore, a detailed analysis of the energy spectrum showed that the observed shape of the prompt energy spectrum is inconsistent with the expected spectral shape at 99.6% CL. Figure 4.3 shows the measured prompt energy spectrum of $\overline{\nu}_e$ above 2.6 MeV compared to expectations and estimated backgrounds. We note that the measured spectrum is not only suppressed, but its shape differs from the expected spectrum. Above the analysis threshold the possible contributions from accidental and other backgrounds is small. The energy-dependent distortion of the prompt energy spectrum is direct evidence of an energy-dependent $\overline{\nu}_e$ disappearance mechanism. The model of neutrino oscillation fits the data well. Together, the observed $\overline{\nu}_e$ rate difference and spectral distortion reject the hypothesis of no oscillation at 99.999995% C.L.

Below the analysis threshold of 2.6 MeV, backgrounds dominate the prompt energy spectrum. Natural low-energy radioactive backgrounds in the detector and its construction materials contribute to the uncorrelated accidental background. One source of correlated backgrounds comes indirectly from the α-decays of the radon daughter ^{210}Po in the liquid scintillator. The 5.3 MeV α-particle is quenched below threshold but the secondary reaction $^{13}\text{C}(\alpha, \text{n})^{16}\text{O}$ produces events above 2.6 MeV. Figure 4.3 shows the contribution of this background to the observed prompt energy spectrum. Also, geo-neutrinos from the decay chains of ^{238}U and ^{232}Th contribute to the observed signal in the region between ~1–3 MeV. Since much of the

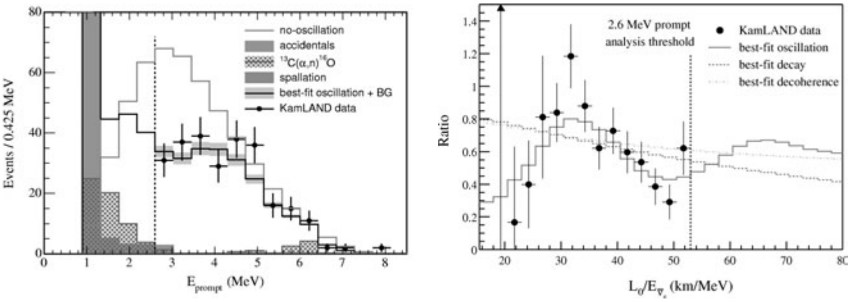

Fig. 4.3. Left panel: Prompt event energy spectrum of $\overline{\nu}_e$ above 2.6 MeV observed in KamLAND and associated background spectra. The shaded band indicates the systematic error in the best-fit reactor spectrum. The hatched-shaded region shows the $^{13}C(\alpha,n)^{16}O$ background. The spectrum from accidentals is shown in grey and peaks in the lowest energy bin. Spallation is only a very small contribution to the spectrum. Right panel: Ratio of the observed $\overline{\nu}_e$ spectrum to the expectation for no-oscillation versus L_0/E, where L_0 is the flux-weighted average distance to the reactors. The curves show the expectation for the best-fit oscillation, best-fit decay, and best-fit decoherence models. The oscillation model matches the observed L_0/E or spectral distortion best.[14,15]

spectral distortion in the prompt energy spectrum of reactor $\overline{\nu}_e$'s is expected between 2–4.5 MeV, efforts are underway to extend the KamLAND analysis to lower energies. A lower analysis threshold will allow KamLAND to perform a combined geo- and reactor neutrino analysis of the data set. Possible improvements in the sensitivity of the neutrino oscillation parameters and in the geo-neutrino studies may be limited by the $^{13}C(\alpha, n)^{16}O$ background. Removal of this background requires the purification of the liquid scintillator. Section 4.6 describes this goal of the KamLAND low-background phase in more detail.

With the data collected from 2002–2004,[15] the measurement of the $\overline{\nu}_e$ flux at KamLAND is systematics limited. The total uncertainty is 6.5%. Table 4.1 summarizes the contributions to the systematic uncertainty. It is dominated by the knowledge of the fiducial volume of the detector, the energy scale near the threshold, and the knowledge of the thermal power output from the reactors. The fiducial volume is established using a radial cut on the reconstructed event position of R = 5.5 m. The position and energy reconstruction of events in the detector is checked with optical and radioactive calibration sources deployed along the central, vertical axis of the detector. Energy- and position-dependent reconstruction biases impact the determination of the position vertex and the fiducial target volume.

Table 4.1. Systematic uncertainties in KamLAND's measurement of the $\overline{\nu}_e$ flux and spectrum.[15]

Fiducial volume	4.7%	Reactor power	2.1%
Energy threshold	2.3%	Fuel composition	1.0%
Efficiency of cuts	1.6%	$\overline{\nu}_e$ spectra[16]	2.5%
Livetime	0.06%	Cross-section[17]	0.2%
Total systematic uncertainty			6.5%

Without source calibration data near the fiducial volume boundary and throughout the detector volume, the current analysis of the KamLAND $\overline{\nu}_e$ data leaves room for improvement in the fiducial volume determination. To reduce the fiducial volume uncertainty and to enable the calibration of the detector response throughout the entire fiducial volume, the collaboration developed a 4π calibration system. This system was commissioned in 2005–2006 and allows the placement of radioactive sources throughout the detector. Energy and vertex reconstruction algorithms used in the KamLAND analysis can be tested directly with the 4π calibration. This system will be an invaluable tool in reducing the fiducial volume systematics and fully understanding the detector response. An extensive calibration of the detector was performed in 2006 and early 2007 and an improved analysis of the reactor $\overline{\nu}_e$ data with more statistics and reduced systematics is underway.

Assuming CPT invariance, a global analysis of data from KamLAND and the solar neutrino experiments is used to determine the oscillation parameters Δm^2_{12} and θ_{12}. Together KamLAND and the solar neutrino experiments reject all but the large-mixing angle MSW solution. The spectral distortions observed in KamLAND are a unique signature of the energy-dependent oscillation effect and yield a precise measurement of the mass splitting Δm^2_{12} between the eigenstates involved. The solar neutrino experiments measure precisely the total amount of neutrino flavor transformation and provide the best constraint on the mixing angle θ_{12}. Figure 4.4 shows the results of KamLAND's measurement (shaded) overlaid with the results of the solar neutrino experiments (black dashed lines) and the combined contours derived from a global analysis of all experiments.

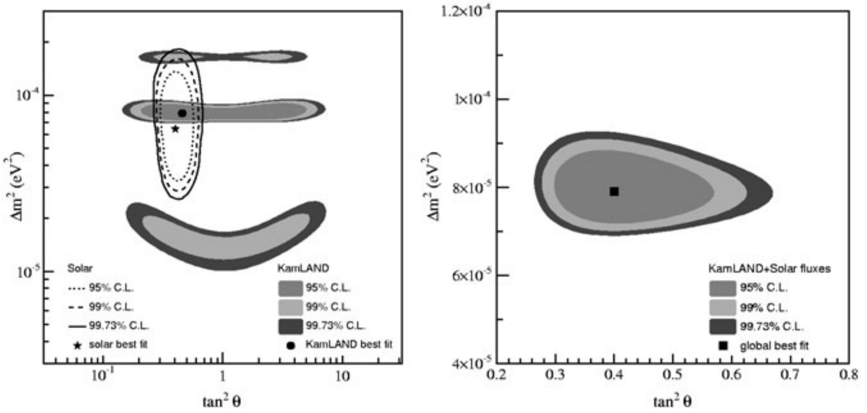

Fig. 4.4. Left panel: Neutrino oscillation parameter regions from KamLAND antineutrino data (shaded regions) and solar neutrino experiments (lines). Right panel: Combined two-neutrino oscillation analysis of KamLAND and the observed solar neutrino fluxes under the assumption of CPT invariance. The best-fit parameters are $\Delta m^2 = 7.9^{+0.6}_{-0.5} \times 10^{-5}$ eV^2 and $\tan^2\theta = 0.40^{+0.10}_{-0.07}$. Reproduced from Reference 15.

4.4. Toward a Precision Measurement of Δm^2_{12} and θ_{12}

With its long baseline KamLAND is uniquely positioned to provide the best possible measurement of Δm^2_{12} for the foreseeable future. To further reduce systematics and improve the precision of the reactor $\overline{\nu}_e$ measurement, KamLAND is taking steps to improve its detector calibration and reduce the internal detector backgrounds. The 4π calibration system is the last major upgrade to the KamLAND detector prior to the scintillator purification and the low-background phase. It allows the calibration of the entire detector volume away from the central z-axis with a variety of radioactive sources and provides a direct test of the vertex and energy reconstruction at radii out to R = 5.5 m near the fiducial volume boundary. An example of a typical 4π calibration run is shown in Figure 4.5. Radioactive sources (^{60}Co, ^{68}Ge, and AmBe) were moved around the entire detector volume to map out the detector response in θ, ϕ, and r. It is found that the position reconstruction in KamLAND is energy dependent which is likely an artifact of the treatment of the optical response, in particular the speed of light and attenuation length, in the different detector zones. With a thorough calibration of the detector response and careful analysis of the 4π calibration data, it is expected that the fiducial volume uncertainty can be reduced from 4.7% to 1–2%. With additional improvements in understanding the energy scale, a total systematic uncertainty of about 3–4% may be achievable. Key to the interpretation of the 4π calibration data is the precise knowledge of the source position. The determination of the fiducial volume at a radius of R = 5.5 m is directly related to the positioning accuracy of the calibration system, or the precision of the relative position of calibration sources throughout the fiducial volume.

Further improvements in the oscillation analysis will be gained from the reduction of internal detector backgrounds, in particular the correlated backgrounds from $^{13}C(\alpha, n)^{16}O$, and a lower analysis threshold. A new purification system for the liquid scintillator was constructed in the Kamioka mine and started operation in spring 2007. Projections show that the sensitivity of KamLAND to θ_{12} may reach similar precision to that obtained in solar neutrino experiments (see Figure 4.5). A high-precision measurement of both Δm^2_{12} and θ_{12} with KamLAND together with the latest solar neutrino result will make it possible to make a direct comparison of the oscillation parameters and test the CPT invariance of neutrinos by comparing the measurement of θ_{12} with solar ν_e and reactor $\overline{\nu}_e$.

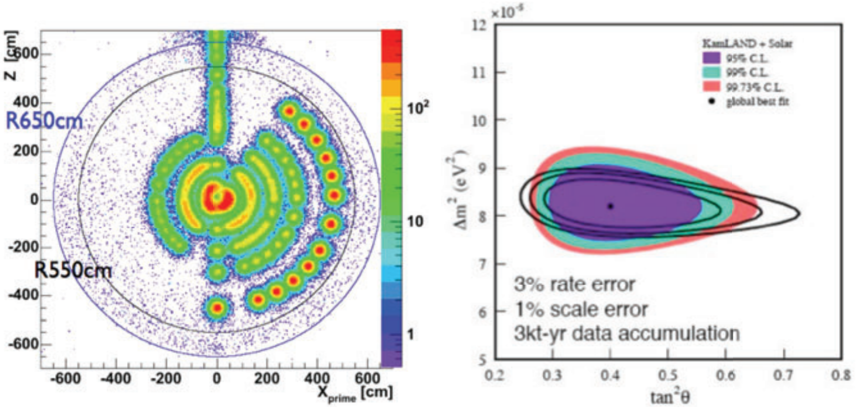

3% rate error
1% scale error
3kt-yr data accumulation

Fig. 4.5. Left panel: Reconstructed position of ^{60}Co calibration data taken with the 4π calibration system throughout the entire fiducial volume. Right panel: Currently allowed oscillation parameters from a global analysis of reactor+solar neutrino experiments (shaded) and projected contours from KamLAND only (solid black lines) after calibration with the 4π system. Improved calibration and better understanding of the energy response and vertex reconstruction as a function of θ, ϕ, and r in the detector will yield an improved measurement of Δm^2_{12} and θ_{12}.

4.5. Other Neutrino Physics with KamLAND

The discovery of neutrino oscillation in the solar, atmospheric, and accelerator experiments and the observation of reactor $\overline{\nu}_e$ disappearance with KamLAND has led to a revolution in neutrino particle and astrophysics. In particular, we have learned that the neutrino flavor and mass eigenstates are related through U_{PMNS}, the neutrino mixing matrix. The determination of the neutrino oscillation parameters, the mass splittings Δm^2_{ij} and the mixing angle θ_{ij}, have been of primary interest. However, neutrino oscillation also plays an important role in other aspects of neutrino physics to which KamLAND has contributed. This section illustrates the relationship among neutrino oscillation measurements, neutrino magnetic moments, and neutrino mass measurements. For a discussion of KamLAND's measurement of geo-antineutrinos we refer the reader to References 23.

Antineutrinos from the Sun and Other Sources

The data from KamLAND and the solar neutrino experiments strongly favor neutrino oscillation as the model to explain the solar neutrino problem. Assuming CPT invariance the observation of $\overline{\nu}_e$ disappearance by KamLAND combined with direct measurements of the solar neutrino flux indicate that the oscillation parameters lie in the MSW LMA region.[12,15] However, other flavor-changing mechanisms have not been excluded from playing a sub-dominant role. For example, non-zero transition magnetic moments[19] can lead to a transformation of ν_e into $\overline{\nu}_\mu$ or $\overline{\nu}_\tau$ in the presence of strong magnetic fields.[19] These neutrinos can in turn evolve into $\overline{\nu}_e$ via flavor oscillation. Such a scenario is conceivable for neutrinos emitted from the core of the Sun where strong magnetic fields are present and the fusion reactions and beta-decays produce neutrinos in a pure electron flavor state. As a result, if the neutrino magnetic moment is non-zero, ν_e from the Sun can turn into $\overline{\nu}_e$ when they pass through the intense magnetic fields in the solar core. KamLAND was designed to study the flux of reactor $\overline{\nu}_e$'s but can also be used to detect $\overline{\nu}_e$'s from other possible sources such as the Sun, Weakly Interacting Massive Particle (WIMP) annihilation in the Sun and the Earth, and relic supernova neutrinos.

The ^{8}B solar neutrino spectrum extends up to ∼15 MeV, well beyond the endpoint of the reactor spectrum at about 8.5 MeV. This allows KamLAND to search for $\overline{\nu}_e$'s in the solar neutrino flux in an energy window largely free of reactor $\overline{\nu}_e$ events. Using the KamLAND liquid scintillator detector a high-sensitivity search for $\overline{\nu}_e$'s from the Sun and other sources has been performed.[20] The detector's source independent sensitivity allows for the measurement of $\overline{\nu}_e$ fluxes independent of origin. For a detector exposure of 0.28 kton-year, no candidate $\overline{\nu}_e$ events were found in the energy range of $8.3 < \mathrm{E}_{\overline{\nu}_e} < 14.8$ MeV with an expected background of 1.1±0.4 events. Assuming no other sources of $\overline{\nu}_e$ than the Sun and the characteristic ^{8}B ν_e energy spectrum, the upper limit on the $\overline{\nu}_e$ flux is $\Phi_{\overline{\nu}_e} < 3.7 \times 10^2$ cm^{-2}s^{-1} at 90% C.L. This limit can be interpreted corresponding to 2.8×10^{-4} of the Standard Solar Model ^{8}B ν_e flux in the framework of spin-flavor precession and neutrino decay models[18] and represents a factor of 30 improvement over previous measurements. These results assume a non-oscillatory solar $\overline{\nu}_e$ flux. Assuming that the oscillation parameters for solar neutrinos fall into the LMA region and MSW is the dominant mechanism for the flavor transformation of neutrinos, one can derive a limit on the product of the neutrino transition magnetic moment μ and the transverse component of the magnetic field B_T in the Sun at a radius of 0.05 $\mathrm{R}_\odot$.

$$\frac{\mu}{10^{-12}\mu_B}\frac{B_T(0.05R_{odot})}{10\ \mathrm{k}G} < 1.3 \times 10^3 \tag{4.3}$$

For comparison, the current best limit on the neutrino magnetic moment from the MUNU experiment is $\mu_{\overline{\nu}_e} < 1.0 \times 10^{-10}\mu_B$ at 90% C.L.[7]

Oscillation Parameters and Neutrino Mass Measurements

Precision measurements of the neutrino oscillation parameters are important ingredients to the determination of the neutrino mass and mass spectrum as well as the analysis of data from future long-baseline accelerator neutrino experiments. The most precise measurement of Δm^2_{12} currently comes from KamLAND, and the global analysis of KamLAND and solar neutrino data. Several proposals have been made to build a next-generation reactor experiment for a more precise measurement of Δm^2_{12} and $\sin^2\theta_{12}$.[25] Such experiments would allow a determination of Δm^2_{12} and $\sin^2\theta_{12}$ with uncertainties of approximately 1% and 10% at 3σ respectively. The projected accuracies would be comparable to those that will be reached in the measurement of the atmospheric neutrino oscillation parameters Δm^2_{23} and $\sin^2\theta_{23}$ in long-baseline superbeam experiments.

4.6. Test of MSW and Non-Standard Interactions in the KamLAND Low-Background Phase

Four of the six parameters describing the oscillation of neutrinos have now been measured but our understanding of the physics of massive neutrinos is far from complete. The mixing angle θ_{13} and the CP-violating phase δ_{CP} are yet unknown. Additional experiments are necessary to complete our measurements of the neutrino mixing parameters and test predictions of this new framework. The results of the solar neutrino experiments suggest that mixing parameters are in a region where the matter-enhanced Mikheyev-Smirnov-Wolfenstein (MSW) effect plays an important role in describing solar neutrino oscillation.[29] However, a specific signature of the MSW effect has not yet been seen.[26]

Over the past thirty years a number of experiments have measured the solar neutrino flux: from the pioneering experiment by Ray Davis for which he was awarded the Nobel prize in 2002 to the recent discovery of solar neutrino flavor transformation at the Sudbury Neutrino Observatory.[12] Solar neutrino experiments to date have studied extensively the high-energy ^{8}B ν_e flux and made measurements of the total solar neutrino flux down to low energies.

In the framework of neutrino oscillation, matter can strongly affect the neutrino survival probability in regions of high density. MSW predicts that the survival probability of solar neutrinos is higher at lower energies compared to higher energies. Figure 4.6 shows the expected change in survival probability as a function of energy from 0.1–20 MeV. The matter effect can be tested by comparing the measured survival probability at higher energies to that at low energies. Super-Kamiokande and SNO have measured the survival probabilities of solar ^{8}B ν_e at higher energies in the matter-dominated region. The measurements of the Chlorine and GALLEX solar neutrino experiments combined with the predictions of the Standard Solar Model find that the low-energy region is in agreement with the vacuum dominated oscillations. The experimental uncertainties, however, are currently too large for a test of the MSW scenario. Furthermore, observation of the sub-MeV mono-energetic ^{7}Be solar neutrinos has only recently been reported.[30] A measurement of the ^{7}Be or pp low-energy solar neutrino fluxes with higher precision is needed to demonstrate the vacuum/matter transition with solar neutrinos.

In early 2007 KamLAND concluded its first phase of operation. A new underground distillation system started operation in spring 2007 to purify

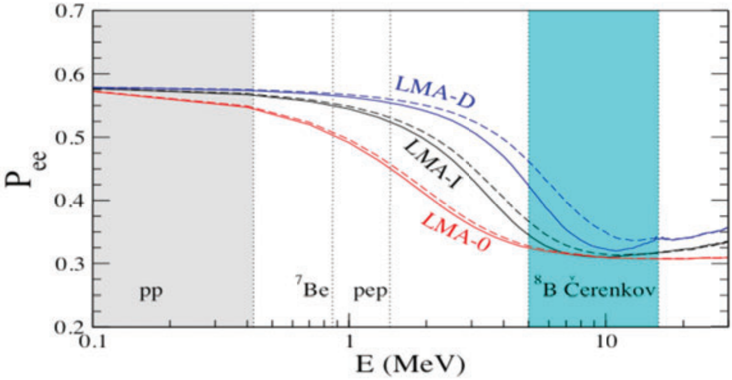

Fig. 4.6. Electron neutrino survival probability as a function of energy for different oscillation solutions and non-standard interactions.[28] Standard matter-enhanced MSW oscillations follow the LMA-1 line. The shaded regions indicate the sensitivity of various experiments to different regions of the energy spectrum. Low-energy solar neutrino experiments (pp and ^{7}Be) mostly measure the vacuum oscillation probability while the oscillation of neutrinos above 5 MeV is dominated by matter-enhanced MSW oscillation.[29]

the liquid scintillator in the KamLAND detector. This will enable KamLAND to lower its analysis threshold for the measurement of reactor and geo-$\overline{\nu}_e$'s and it may also allow it to detect solar ^{7}Be ν_e through elastic scattering. If the internal detector backgrounds of the KamLAND experiment can be reduced sufficiently, low-energy solar ^{7}Be neutrinos can be detected through neutrino-elastic scattering $\nu_e + e^- \to \nu_e + e^-$. The mono-energetic ^{7}Be neutrinos with $E_\nu = 862$ keV will result in a Compton-like continuous recoil spectrum with a maximum energy of $T_{max} = 665$ keV. Calibration of the fiducial volume and the energy scale at <1 MeV will be critical to this measurement of elastic scattering rates. The signal event rate will be of the order of 130 events/day for a volume of 408 tons. A prerequisite for this measurement is the purification of the KamLAND scintillator and reduction of internal detector backgrounds by factors of 10^5–10^6 in ^{85}Kr, ^{29}Ar, ^{210}Bi, and ^{210}Po over current values.

Neutrino masses and mixing are not the only mechanism to describe the deficit of charged current neutrino interactions. They can also be generated by a variety of forms of nonstandard neutrino interactions or properties.[28] The search for non-standard interactions can be an important tool to constrain other neutrino properties such as magnetic moments and sterile ν, and hence probe physics above the electroweak scale. Recent results from

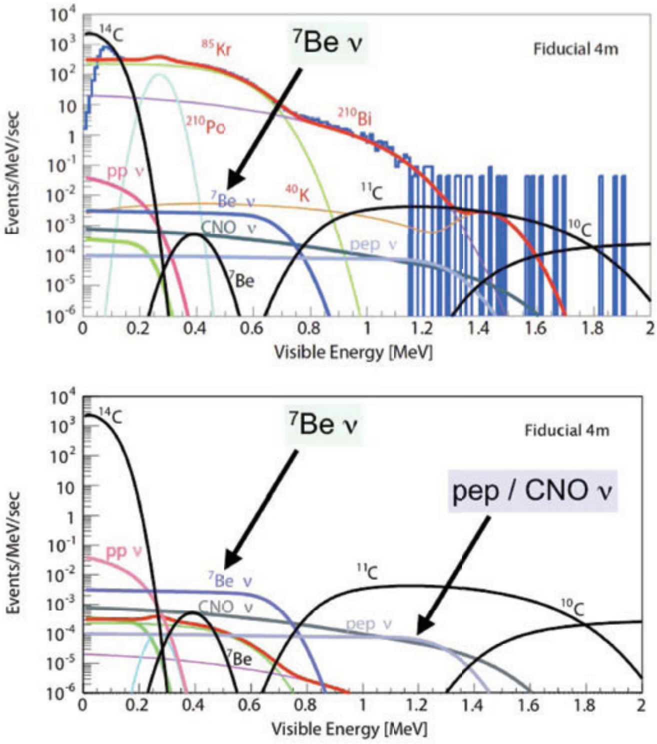

Fig. 4.7. Top panel: Current KamLAND singles spectrum. Bottom Panel: Expected energy spectrum in KamLAND assuming a reduction of ^{210}Pb, ^{85}Kr and ^{40}K by a factor of 10^{6} in the liquid scintillator. The signature of ^{7}Be neutrinos will be a Compton-like edge in the singles spectrum. The ^{7}Be signal will be extracted from a combined fit to the backgrounds and recoil spectrum. Reproduced from Reference 27.

KamLAND have ruled out a large number of these scenarios as a dominant source for solar neutrino oscillation,[15] but they may still contribute at the sub-dominant level. A 5% measurement of the solar ^{7}Be flux is the next step in testing matter-enhanced neutrino oscillation[26] and helping constrain scenarios of non-standard neutrino interactions.

Figure 4.7 shows the expected energy spectrum in KamLAND after purification of the liquid scintillator. The ^{7}Be signal is extracted from a combined fit to the backgrounds and recoil spectrum. The extraction of this signal and the measurement of the ^{7}Be signal will critically depend on understanding the shape of the background spectra and the α/β separation.

A low-energy calibration program with a variety of new calibration sources will be important for this future phase of the experiment.

4.7. Summary and Conclusions

KamLAND has played a key role in the discovery of antineutrino oscillation. Designed to observe antineutrinos from nuclear power plants in Japan, KamLAND has made the first observation of the disappearance of reactor antineutrinos at a flux-weighted average distance of about 175 km from reactors in Japan, found direct evidence for neutrino oscillation in spectral distortions, and provides for the foreseeable future the best measurement of Δm^2_{12}. A continued program of high-precision studies will allow KamLAND to improve on its existing results and provide the most precise measurements of Δm^2_{12} and θ_{12} with reactor antineutrinos. KamLAND's current measurements are limited by systematics and internal detector backgrounds. With improvements in detector calibration and through the reduction of internal backgrounds, KamLAND may be able to improve on its measurement of Δm^2_{12} by as much as a factor of two. It may also be able to make a competitive measurement of the mixing angle θ_{12} and study the spectral distortion of the reactor neutrino spectrum with greater precision and at lower energies. The mass splitting Δm^2_{12} is one of the key ingredients in understanding the physics and spectrum of massive neutrinos. Together, solar neutrino experiments and KamLAND provide unambiguous evidence that neutrinos have mass and their flavors mix, and they provide the most precise determination of the neutrino oscillation parameters Δm^2_{12} and θ_{12} to date. The comparison of the measurement of θ_{12} with reactor $\overline{\nu}_e$'s at KamLAND and with solar ν_e's provides a test of CPT in the neutrino sector.

Next-generation reactor antineutrino experiments such as Double Chooz and Daya Bay (See Chapters 12 and 13) are now under construction to make a precision measurement of the $\overline{\nu}_e$ flux at short distances of 0.2–2 km to search for and measure the yet unknown mixing angle θ_{13}. Fifty years after the discovery of the antineutrino, nuclear reactors still play an important role in understanding the mysteries of neutrinos and may hold the clue to understanding the phenomenology of lepton mixing and to opening the path toward the study of CP violation in neutrinos.

Acknowledgments

The KamLAND collaboration is an international collaboration of some 80 scientists from Japan, the United States, and France led by the Research Center for Neutrino Science, Tohoku University, Sendai, Japan.[13] The experiment is supported by the Japanese Ministry of Education, Culture, Sports, Science, and Technology and the United States Department of Energy. The Kamioka Mining and Smelting Company has provided services for activities in the mine. The author is grateful to the KamLAND Collaboration for their support and discussions and would like to acknowledge the support by the University of Wisconsin.

References

1. F. Reines, C. L. Cowan, Phys. Rev. **90**:492–493, (1953); F. Reines, C. L. Cowan, Phys. Rev. **92**:830–831, (1953); C. L. Cowan, F. Reines, F. B. Harrison, H. W. Kruse, and A. D. McGuire, Science **124**, 103–104 (1956); F. Reines, C. L. Cowan, Nature **178**:446–449,(1956); F. Reines, C. L. Cowan, F. B. Harrison, A. D. McGuire, and H. W. Kruse, Phys. Rev. **117**, 159–173 (1960); F. Reines, Rev. Mod. Phys. **68**:317–327, (1996); F. Reines, C. Cowan, Los Alamos Sci. **25**, 4–27, (1997).
2. H. Kwon *et al.*, Phys. Rev. D**24**, 1097 (1981).
3. G. Zacek *et al*, Phys. Rev. D**34**, 2621 (1986).
4. J. F. Cavaignac, A. Hoummada, D.H. Koang, B. Vignon , Y. Declais, H. de Kerret, H. Pessard, J.M. Thenard, Phys. Lett. B**148**:387–394, (1984); Y. Declais *et al.*, Phys. Lett. B**338**:383–389, (1994); B. Achkar *et al.*, Nucl. Phys. B**434**:503–534, (1995); H. Minakata, Phys. Rev. D**52**:6630–6633, (1995).
5. F. Boehm *et al.*, (Palo Verde Collaboration), Phys. Rev. Lett. **84**:3764–3767, (2000); Phys. Rev. **D62**, 072002 (2000); Phys. Rev. D**64**:112001, (2001).
6. M. Apollonio *et al.*, (CHOOZ Collaboration), Phys. Lett. B **466**, 415, (1999); Eur. Phys. J. C**27**:331–374 (2003).
7. Z. Daraktchieva *et al.* (MUNU Collaboration), Phys. Lett. B**564**, 190–198 (2003); Phys. Lett. B**615**: 153–159, (2005).
8. B. Pontecorvo, Sov. Phys. JETP **7**:172–173, (1958); Zh. Eksp. Teor. Fiz. **34**:247, (1957); B. Pontecorvo, Sov. Phys. JETP **26**:984–988, (1968); Zh. Eksp. Teor. Fiz. **53**:1717–1725, (1967); V. N. Gribov, B. Pontecorvo, Phys. Lett. B28:493, (1969); S. M. Bilenky, B. Pontecorvo, Phys. Lett. B61:248, (1976).
9. S. M. Bilenky, B. Pontecorvo, Sov. J. Nucl. Phys. **43**:786, (1986); Yad. Fiz. **43**:1225–1230, (1986); S. M. Bilenky, B. Pontecorvo, Lett. Nuovo Cim. **40**:161, (1984).
10. A. Bernstein, Y. Wang, G. Gratta, and T. West, J. Appl. Phys. **91**,4672–4676, (2002); M. M. Nieto, A. C. Hayes, W. B. Wilson, C. M. Teeter, http://arxiv.org/abs/nucl-th/0309018

(2003); M. Cribier, http://arxiv.org/pdf/0704.0548 (2007); M Cribier, http://arxiv.org/pdf/0704.0891 (2007).

11. Y. Fukuda *et al.*, (Super-K Collaboration), Phys. Rev. Lett. **81**, 1158 (1998).
12. Q. R. Ahmad *et al.*, (SNO Collaboration), Phys. Rev. Lett. **87**:071301, (2001); Phys. Rev. Lett. **89**:011301, (2002); Phys. Rev. Lett. **89**:011302, (2002); S.N. Ahmed *et al.*, (SNO Collaboration), Phys. Rev. Lett. **92**:181301, (2004); B. Aharmim *et al.*, (SNO Collaboration), Phys. Rev. C**72**:055502, (2005); Phys. Rev. C**75**:045502, (2007).
13. KamLAND project web sites: http://www.awa.tohoku.ac.jp/KamLAND/ and http://kamland.lbl.gov/.
14. K. Eguchi *et al.* (KamLAND Collaboration), Phys. Rev. Lett. **90**:021802 (2003).
15. T. Araki *et al.* (KamLAND Collaboration), Phys. Rev. Lett. **94**:081801 (2005).
16. K. Schreckenbach *et al.*, Phys. Lett. B**160**, 325 (1985); A. A. Hahn *et al.*,, Phys. Lett. B**218**, 365 (1989); P. Vogel *et al.*, Phys. Rev. C**14**, 1543, (1981); P. Vogel and J. Engel, Phys. Rev. D**39**, 3378, (1989); K. Nakajima *et al.*, Nucl. Instrum. Meth. **A569**:837–844, (2006).
17. P. Vogel and J.F. Beacom, Phys. Rev. D**60**, 053003 (1990); A. Kurylov *et al.*, Phys. Rev. C**67**, 035502 (2003).
18. J. F. Beacom and N. F. Bell, Phys. Rev. D**65**, 113009 (2002).
19. A. Cisneros, Astrophys. Space Sci. **10**:87–92, (1971); J. Pulido, Phys. Rept. **211**:167–199, (1992); E.K. Akhmedov, J. Pulido, Phys. Lett. B485:178–186, (2000); E. K. Akhmedov, J. Pulido, Phys. Lett. B**553**:7–17, (2003).
20. K. Eguchi *et al.* (KamLAND Collaboration), Phys. Rev. Lett. **92**:071301 (2004).
21. G. Eder *et al.*, Nucl. Phys. **78**, 657–662 (1966).
22. G. Marx, CZech. J. Phys. B**19**, 1471–1479 (1969).
23. T. Araki *et al.* (KamLAND Collaboration), Nature **436**:499–503 (2005); S. Enomoto, E. Ohtani, K. Inoue, A. Suzuki, hep-ph/0508049 (2005).
24. Working group report of the APS neutrino study, “Neutrinoless Double Beta Decay and Direct Searches for Neutrino Mass”, http://www.aps.org/neutrino/ (2005).
25. S. Petcov and T. Schwetz, hep-ph/0607155 (2006).
26. Working group report of the APS neutrino study, “Report of the Solar and Atmospheric Neutrino Experiments Working Group of the APS Multidivisional Neutrino Study”, http://www.aps.org/neutrino/ (2005).
27. I. Shimizu, “Present Status and Future Prospects of KamLAND”, DBD07, Osaka, Japan (2007).
28. O. G. Miranda, M. A. Tortola, J. W. F. Valle, JHEP0610:008, (2006).
29. L. Wolfenstein, Phys. Rev. D**17**: 2369 (1978); S. P. Mikheyev, A. Yu. Smirnov, Prog. Part. Nucl. Phys. **23**:41-136 (1989).
30. C. Arpesella, *et. al.*, arXiv:0708.2251v1;

Chapter 5

K2K: KEK to Kamioka Long-Baseline Neutrino Oscillation Experiment

R. Jeffrey Wilkes, for the K2K Collaboration*

Dept. of Physics,
University of Washington,
Seattle, WA 98195 USA
wilkes@u.washington.edu

Evidence for neutrino mass was confirmed by K2K, the KEK to Kamioka long-baseline neutrino oscillation experiment, with parameter estimates consistent with atmospheric neutrino results from Super-Kamiokande. A total of 112 beam-associated neutrino events were observed in Super-Kamiokande, with 158 events expected in the absence of neutrino oscillations. Furthermore, distortion of the neutrino energy spectrum consistent with the oscillation prediction was observed. The probability that the K2K data were due to random fluctuations assuming no neutrino oscillations is 0.0015% . A 2-flavor oscillation analysis shows the allowed region for mass difference and mixing angle to be consistent with the results from Super-Kamiokande. K2K provided a valuable opportunity to prepare for current and future high-precision long-baseline experiments such as T2K.

Contents

5.1 Introduction 92
5.2 Neutrino Beam 93
5.3 Beam Simulation 95
5.4 The Near Detectors 97
5.5 The Far Detector 102
5.6 Neutrino Interaction Simulations 103
5.7 Event Rates and Oscillation Analysis 104
5.8 Summary and Conclusions 110
References 112

---

*See Reference 4 for full K2K collaboration list.

5.1. Introduction

Using the arrival angle and energy distributions of atmospheric neutrinos, Super-Kamiokande (SK, See Chapter 2) reported the characteristic disappearance signature predicted for neutrino oscillations and measured the parameters of $\nu_\mu - \nu_\tau$ oscillations in 1998, the first generally-accepted evidence for neutrino mass, with results refined in later publications as additional data were accumulated.[1,2] The KEK to Kamioka long-baseline neutrino oscillation experiment (K2K)[3,4] was organized several years earlier, to provide a prompt test of early Kamiokande[5] results using a man-made, high-purity muon neutrino beam directed 250 km across Japan from the KEK particle accelerator lab toward SK. To reduce the time needed to stage the experiment and begin data taking, K2K (formally, KEK E-362) made as much use as possible of existing detector and beam line elements on hand at KEK. Bending magnets were borrowed from SLAC for the beam line, new horn magnets and monitors were constructed, and a new Scintillating Fiber detector was developed and built. Most other detector elements were recycled from previous experiments.

K2K was the first long-baseline neutrino experiment to take data, and its results confirmed SK estimates of neutrino oscillation parameters,[6,7] although limited statistics did not permit improvement of confidence limits.

In K2K, the near detector system, located 300 m downstream from the proton target, was used to measure the direction, flux, composition, and energy spectrum of the neutrino beam before it traveled through the earth to SK, a 50 kt water Cherenkov neutrino detector, located 1000 m underground.[8] The near detector (ND) complex consisted of a 1 kt water Cherenkov detector (1KT) and a fine grained detector system (FGD).

Previous sections have already discussed the basic physics of neutrino oscillations, whose effects create both a deficit in the total number of events observed at SK and a distortion of the measured energy spectrum compared to that measured near the production point. In the energy range around 1 GeV, the dominant process is $\nu_\mu - \nu_\tau$ oscillations, so a 2-flavor analysis was appropriate. To study distortion of the energy spectrum, a subsample of events for which the incoming neutrino energy can be accurately reconstructed was separately analyzed.

If the neutrino interaction observed is a charged-current (CC) quasi-elastic (QE) event, the incoming neutrino energy can be accurately estimated with two-body kinematics using the observed momentum of the muon, neglecting Fermi momentum in the target nucleus. In the K2K beam energy range, only the muon in this reaction is energetic enough to produce Cherenkov light and be detected at SK, but observations of the muon alone were adequate to reconstruct the energy for these events. One-ring events (1R) identified as having a muon track were selected as a subset with a high probability of being CC-QE. For these events, the energy of the parent neutrino was estimated by

$$E_\nu^{rec} = \frac{m_n E_\mu - m_\mu^2/2}{m_n - E_\mu + P_\mu \cos\theta_\mu}$$

where $m_n, E_\mu, m_\mu, P_\mu, \theta_\mu$ are the nucleon mass, muon energy, the muon mass, the muon momentum, and the scattering angle relative to the neutrino beam direction, respectively.

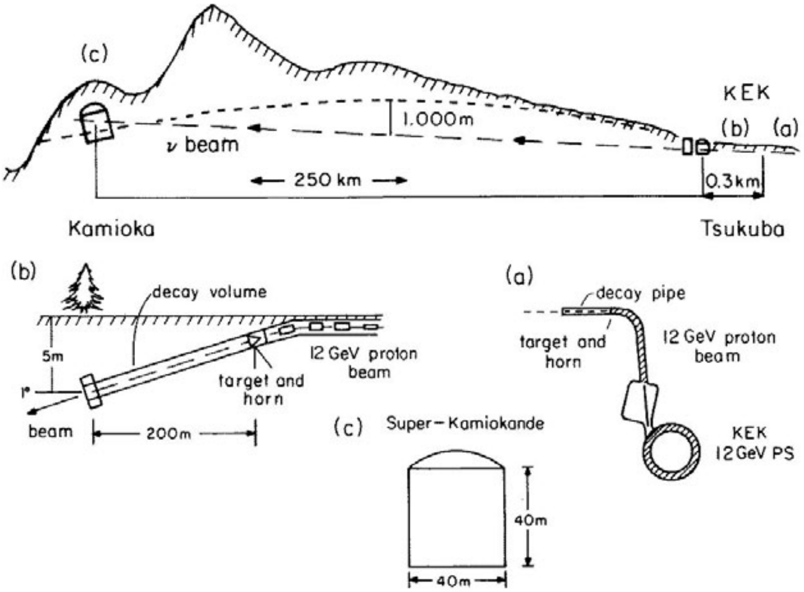

Fig. 5.1. Overview of K2K. The front detector (b) and Super-Kamiokande (c) were located at 300 m and 250 km from the proton target (a).

5.2. Neutrino Beam

A schematic view of the KEK-PS and neutrino beam line is shown in Fig. 5.1. The KEK 12 GeV proton synchrotron (KEK-PS) accelerator beam was directed into the earth, aimed toward the SK site. The beam line and all its components were aligned during construction with an accuracy of 0.1 mrad with respect to the required beam axis, which was defined using GPS surveying techniques accurate to 0.01 mrad between the KEK and Kamioka sites.[9] Protons were extracted in a single turn into the neutrino beam line, in "spills" of duration 1.1 μs, each containing 9 buckets or bunches of protons at 125 ns intervals.

Proton beam intensity was monitored by current transformers (CTs) installed along the beam line. Beam intensities were typically about 5×10^{12} protons per spill. In addition, segmented plate ionization chambers (SPICs) were used to monitor and steer the beam, and to estimate beam size and divergence, needed as an input to the K2K beam Monte Carlo (MC) simulation.

An aluminum hadron production target was embedded in the first of two horn magnets placed in the target station. The target diameter was increased from 2 cm to 3 cm in November 1999 after an initial target failure. The magnetic horns focused positively charged particles, mainly pions, into a 200m long decay volume. The momenta of focused pions were ranged from $2-3$ GeV/c, which corresponds to about 1.0–1.5 GeV energy for neutrinos produced in the forward direction.

A pion monitor (PIMON) was temporarily inserted twice, just downstream of the horn magnets, to directly measure the momentum and angular distributions of pions emerging from the horns. The PIMON system also helped confirm the validity of the beam MC simulation, providing the vector momentum for pions entering the decay volume after focusing by the horn magnetic fields, although the PIMON was not sensitive to pions below 2 GeV/c (corresponding to neutrinos below 1 GeV). Details of pion monitor design and operation are given elsewhere.[4]

The decay volume was filled with helium at 1 atm to reduce pion absorption and minimize secondary interactions in the decay volume itself. The beam dump, located at the end of the decay volume to absorb all particles except neutrinos, consisted of 3.5 m thick iron, 2 m thick concrete, and a layer of earth about 60 m thick. Just downstream of the iron and concrete shields, a muon monitor provided spill-by-spill measurements of the neutrino beam aiming and intensity. A change in the beam direction by 3 mrad would correspond to a change in the neutrino flux and spectrum at SK of about 1%. Muon monitor data show that the beam direction remained constant within about 1 mrad throughout K2K data taking.

In total, 1.049×10^{20} protons on target (POT) were delivered during the entire time of K2K operation, including beam commissioning and tuning periods, of which about 90%, the equivalent of 0.922×10^{20} POT, was used for physics data analysis.

K2K data taking occurred at intervals from June 1999 to November 2004, with several different beam line and detector arrangements, as listed in Table 5.1. K2K-I refers to runs taken when the far detector was in the SK-I configuration, and K2K-II refers to data taken with the SK-II configuration. Near detector elements are described in Section 5.4.

Table 5.1. Beam and detector configurations for K2K running periods. SK-I had the full complement of ID PMTs, SK-II had $\sim 53\%$ fewer PMTs.

Run	Dates	Horn Cur. (kA)	Target Diam. (cm)	SK config.	ND
Ia	6/99	200	2	SK-I	LG in place
Ib	11/99-7/01	250	3	SK-I	LG in place
IIa	12/02-6/03	250	3	SK-II	LG $\mapsto$ 4-layer Scibar
IIb	10/03-2/04	250	3	SK-II	Full SciBar in place
IIc	10/04-11/04	250	3	SK-II	SciFi $H_2O \mapsto Al$

5.3. Beam Simulation

A neutrino beam Monte Carlo (MC) simulation was required to estimate neutrino beam properties from limited measurements made in the near detectors. The beam line was simulated using GEANT[10], and the tracks of neutrinos were extrapolated to the near detector (ND) and Super-Kamiokande (SK), allowing the fluxes and energy spectrum at these sites to be estimated. Details of the K2K beam MC are given in Reference 4.

Figure 5.2 shows the energy spectra predicted by the K2K beam MC for each type of neutrino at the ND and SK. About 97.3% of beam neutrinos at the ND and 97.9% at SK were muon neutrinos. The beam was contaminated with a small proportion of other neutrino flavors: the ratios were $(\nu_e/\nu_\mu) = 0.013$, $(\overline{\nu}_\mu/\nu_\mu) = 0.015$, $(\overline{\nu}_e/\nu_\mu) = 1.8 \times 10^{-4}$ at the ND, and $0.009, 0.012, 2.2 \times 10^{-4}$ respectively, at SK. The validity of the beam MC simulation was confirmed by data from both the HARP experiment at CERN[12] and PIMON measurements.

Because of the finite size of the K2K decay volume, and the location of the near detectors, the far/near (F/N) flux ratio did not follow a simple $1/L^2$ law, with L the distance from the neutrino source, but had some dependence on neutrino energy. The F/N flux ratio was estimated using

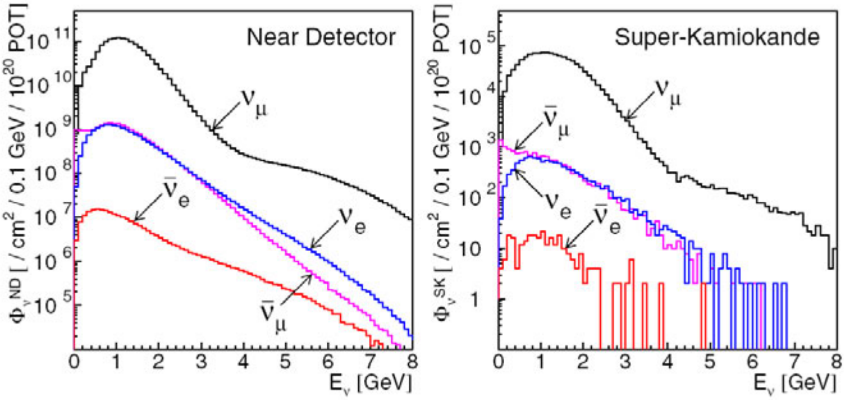

Fig. 5.2. The energy spectrum for each type of neutrino at ND (left) and SK (right) estimated by the beam MC simulation.

the K2K beam MC simulation. The dominant uncertainty in neutrino flux prediction comes from the uncertainties in pion production by protons in nuclear targets. The Cho-CERN compilation of production measurements in proton-beryllium interactions[13] was used as a reference model, supplemented by results provided by HARP, which measured π^+ production by 12.9 GeV/c protons in a thin aluminum target.

Allowances for uncertainties in the proton-aluminum hadronic interaction length, the overall charged and neutral kaon production normalization, secondary hadronic interactions, such as absorption in the target and horns, the horn magnetic fields were all included. The flux ratio uncertainty integrated over all neutrino energies was 2.0%. The predictions of F/N flux ratio from Cho-CERN were consistent with those based on HARP results, for all neutrino energies. The K2K-Ia period (see Table 5.1) differed from the later configuration, so the F/N ratio for June 1999 was separately estimated, with the same methods. The F/N predictions for the two beam configurations, integrated over all neutrino energies, differ by about 0.4%. These independent predictions of the F/N ratio were consistent with each other within their uncertainties, so the ratio predicted using HARP data was employed for the oscillation analysis, since it has the most accurate information on hadron production.

5.4. The Near Detectors

A schematic view of the ND system is shown in Fig. 5.3. The ND included two main detectors: a 1 kt water Cherenkov detector and a fine-grained detector (FGD) system. The FGD in turn consisted of a scintillating-fiber/water-target tracker (SciFi), and a muon range detector (MRD). Between these, there was initially a lead-glass calorimeter (LG), which was later replaced by a fully-active fine-segmented scintillator-bar tracker (SciBar).

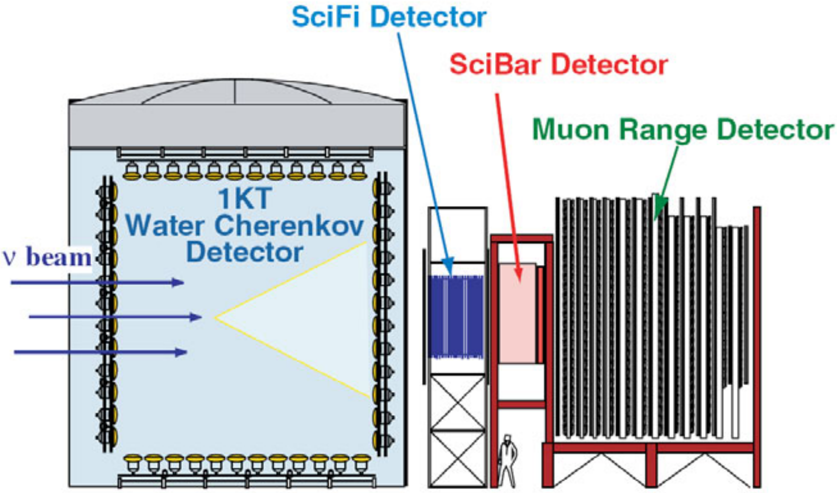

Fig. 5.3. Schematic view of K2K near detectors in K2K-II configuration. In K2K-I, the Pb-glass calorimeter was in the place occupied by the SciBar detector shown here.

The 1KT detector in the ND was a miniature version of SK, with the same neutrino interaction target and identical instrumentation. The primary role of the 1KT detector was to measure the neutrino interaction rate and the energy spectrum. The 1KT detector also provided a high statistics measurement of neutrino-water interactions. The cylindrical tank, 10.8 m in diameter and 10.8 m in height, was filled with approximately 1000 tons of ultra-pure water, and like SK, was optically separated into an inner detector (ID) and outer detector (OD) by opaque black sheets and reflective white sheets. The steel tank had previously been used in a calibration experiment at KEK performed jointly by the Kamiokande and IMB collaborations, to confirm particle identification efficiencies in water Cherenkov detectors.[14]

The ID was a cylindrical volume with 8.6[m] diameter and height, viewed by 680 50-cm diameter photomultiplier tubes (PMTs) facing inward to detect Cherenkov light from neutrino events. The PMTs and their arrangement were identical to those of SK-I, providing 40% photocathode coverage on the inner surface of the ID. The fiducial volume used for selecting neutrino events in the 1KT was defined as a cylinder of diameter 4 m and length 2 m, with its axis aligned with the beam direction, containing 25 tons of water. The OD covered the upstream third of the tank side wall and the whole of the bottom wall, and was viewed by 68 20-cm diameter PMTs, facing outward to veto incoming particles. The OD was also used to trigger cosmic ray muon events for detector calibrations. To compensate for the geomagnetic field, Helmholtz coils surrounded the water tank. The water purification and recirculation system kept the electrical resistance and temperature of the water constant, around $10M\Omega$-cm and 11^oC respectively.

The 1KT detector data acquisition system used the same front-end electronics modules used in the SK experiment,[1] which automatically digitized charge and timing information for each PMT with signal level over a threshold equivalent to about 0.25 photoelectrons. The event trigger threshold was about 40 PMT hits (roughly equivalent to the signal from a 6 MeV electron) within a 200 ns time window during the 1.2 μsec beam spill gate, which was distributed to all near detectors from the accelerator control system. In addition, the pulse shape of the analog sum of all 680 PMTs signals (PMTSUM) was recorded for every beam spill using a 500 MHz flash analog-to-digital converter (FADC), allowing identification of multiple interactions within a single spill gate. The number of interactions in each spill was determined by counting peaks in PMTSUM above a threshold equivalent to a 100 MeV electron signal.

The physics parameters of an event in the 1KT detector were determined using the same data reduction algorithms used in SK.[1] First, the vertex position of an event was estimated from PMT timing data. Given the vertex estimate, the number of Cherenkov rings and their directions were determined by a maximum-likelihood procedure, and each ring was classified as e-like or μ-like, using its ring pattern and Cherenkov opening angle. The particle ID algorithm used was the same as that used in SK, which had been confirmed by a beam test at KEK[14] before SK data taking began in 1996. The vertex position for single-ring events was further refined taking into account the particle ID, and the momentum of each ring was determined from the Cherenkov light intensities. Fully contained (FC) neutrino events, which deposit all of their Cherenkov light within the inner detector, were selected by requiring the maximum number of photoelectrons on a single PMT at the projected exit point of the most energetic particle to be less than 200. Events above this threshold were identified as partially contained (PC) events.

Resolutions and uncertainties for event parameters were estimated from MC data processed by the data reduction algorithms. Vertex resolution was about $12 - 15$ cm for PC and FC single-ring events, while resolution for multi-ring events was about $34 - 39$ cm. The angular resolution for single-ring CC-QE events was $1.05°$ for FC events and $0.84°$ for PC events. An estimated 0.3% of muon neutrino CC quasi-elastic events with a single ring were misidentified as e-like, while 3.3% of electron neutrino CC quasi-elastic events with a single ring were misidentified as μ-like. The momentum resolution for muons was estimated to be 2.0-2.5% over the full momentum range of the 1KT.

Regular calibration procedures, described in Reference 7, kept the absolute energy scale uncertainty within +3%/-4%, while the vertical/horizontal asymmetry of the energy scale due to the detector was 1.7%. The energy scale was stable within about 1% between 2000 and 2004. The accuracy of vertex reconstruction was experimentally studied by special cosmic ray muon data runs, taken by inserting a pipe with scintillating strips at each end vertically into the tank. Cosmic ray muons going through the pipe emulate the neutrino-induced muons whose vertex position was defined at the bottom end of the pipe. These studies confirmed the resolution estimates obtained from the Monte Carlo simulation.

The SciFi detector, which was used throughout K2K, had a total mass of 6 tons, with scintillating fiber tracking layers interleaved with water-target layers. Details of the design and performance of the detector are described in References 15 and 16. The SciFi detector, with capabilities complementary to the 1KT detector, was used to measure the neutrino spectrum, to reconstruct charged particle tracks produced in neutrino interactions with high resolution, to provide rates for quasi-elastic and inelastic interactions, and was sensitive to higher energy events than the 1KT.

The SciFi detector consisted of 20 layers of $2.6\,\mathrm{m}\times 2.6\,\mathrm{m}$ tracking modules, placed 9 cm apart, each containing a double layer of sheets of 0.692 mm diameter scintillating fibers arranged in XY directions. Between the fiber tracking modules, there were 19 layers of water target contained in extruded aluminum tanks. The water level was monitored and remained constant within 1% throughout the experiment, except for a few tanks which leaked following an earthquake. Measurements when the tanks were initially filled and later drained, along with monitoring, allowed definition of the fiducial mass of 5590 kg with 1% accuracy. During the last run, the water tanks were drained and filled with an equal mass of aluminum rods.

The scintillating fibers were coupled to an image intensifier tube (IIT) with CCD readout system. The relationship between the fibers and the CCD coordinate system was calibrated periodically by illuminating fiducial fibers with an electro-luminescent plate. In addition, cosmic rays were used to monitor the gain of the system. Raw SciFi data consisted of hit CCD pixel coordinates and their digitized signals. Clusters of hit pixels were combined and matched to the location of specific scintillating fibers. After cluster-finding, tracks were reconstructed using conventional fitting techniques. The efficiency to find a track was also estimated using cosmic ray muons, and was 70% for tracks with length of three layers, 87% for four layers, and approached 100% for longer tracks.

Plastic scintillator hodoscopes surrounded the SciFi detector. One was downstream of SciFi and gave track timing and position information and also served as a preshower detector for the lead-glass calorimeter. Another was upstream of SciFi and was used to veto muons and other particles from the beam, primarily from neutrino interactions in the upstream 1KT detector, but also from cosmic rays. A detailed description of the hodoscope system can be found in Reference 17.

The LG calorimeter was located between SciFi and MRD during the K2K-I run period. The purpose of the LG was to distinguish electrons from muons by observing energy deposited by electromagnetic cascades. The LG calorimeter had been constructed for the TOPAZ experiment[18] and was recycled for the K2K experiment. It contained 600 cells, each approximately 12 cm×12 cm×34 cm, viewed by a 3 inch diameter PMT. Nine selected LG cells were calibrated prior to installation using a beam from the electron synchrotron with energy range from 50 MeV to 1.1 GeV. The other LG cells were calibrated relative to the standard cells by cosmic ray muons.

The SciBar detector[19] replaced the LG after K2K-I to measure the neutrino energy spectrum and to study neutrino interactions with higher detection efficiency for low momentum particles. The main part of the SciBar detector consisted of an array of plastic scintillator bars produced at Fermilab,[20] each with dimensions 1.3 cm thick, 2.5 cm wide, and 300 cm long. In total, 14,848 scintillator strips were arranged in 64 layers, alternating vertical and horizontal planes. The total weight of the detector was about 15 tons. The fiducial volume of SciBar was defined as an area 2.6 m×2.6 m around the beam axis, from the second to 53rd layer of scintillator bars, containing a fiducial mass of 9.38 tons. Wavelength shifting fibers in the center of each scintillator bar were bundled and coupled to the photocathodes of Hamamatsu 64-anode PMTs. Both charge and arrival time of the PMT signals were recorded using custom-made electronics.[21] Gain stability was monitored with precision better than 1%. Cosmic ray data were collected between beam spills to calibrate the multianode PMT gain and scintillator light yield.

An electromagnetic calorimeter was located downstream of the tracker section of SciBar to measure electron neutrino contamination in the beam and neutral pion production in neutrino interactions. The calorimeter was built from bars consisting a sandwich of lead and scintillating fibers, originally made for the spaghetti calorimeter of the CHORUS experiment at CERN.[22] Thirty-two bars formed a plane of vertical elements, followed by a plane of 30 horizontal bars. The two planes, each 4 cm thick, cover an area of $270 \times 262\,\mathrm{cm}^2$ and $262 \times 250\,\mathrm{cm}^2$, respectively. The tracking section of SciBar was about 4 radiation lengths deep in the beam direction, and the calorimeter added 11 radiation lengths. The energy resolution was about $14\%/\sqrt{E(\mathrm{GeV})}$ as measured with a test beam.[22]

Charged particles were reconstructed by track-finding in each two-dimensional projection (x-z and y-z), using a cellular automaton algorithm.[23] Track candidates in the two views were then combined, based on matching of the track edges in the z direction plus timing information. Reconstructed tracks were required to have minimum length of 8 cm, corresponding to 450 MeV/c for protons. The reconstruction efficiency for an isolated track longer than 10 cm was 99%.

The MRD[24] was the final element of the near detector and had two purposes. One was to monitor the stability of the neutrino beam direction, profile, and energy spectrum by measuring the energy, angle, and production point of muons produced in charged-current neutrino interactions in its own iron layers. The other was to identify muons produced in the upstream detectors, and to measure their energy and angle in combination with the other FGD elements, allowing estimation of the energy of the incident neutrino.

The MRD consisted of 12 layers of iron absorber sandwiched between 13 sets of vertical and horizontal drift-tube layers. The 6632 drift tubes used were made of aluminum channels with cross sectional dimensions $5\,\mathrm{cm}\times 7\,\mathrm{cm}$, filled with P10 gas ($\mathrm{Ar{:}CH_4}$ = 490%:10%). The transverse dimensions of each layer were approximately 7.6 m × 7.6 m. The upstream four iron layers were 10 cm thick, while the remaining eight plates were 20 cm thick. The total iron thickness of 2.00 m stopped muons with energy up to 2.8 GeV. The total weight of iron was 864 tons and the total mass of MRD including the aluminum drift tubes was 915 tons. A conventional track finding algorithm was employed to reconstruct tracks from drift tube hits, with track finding efficiency 66%, 95%, and 97.5% for tracks traversing one, two, and three iron plates, respectively, rising to 99% for longer tracks. The energy resolution of MRD was 0.12 GeV for forward-going muons. The track angular resolution was about 5° and the resolution of the vertex point perpendicular to the beam direction was about 2 cm.

5.5. The Far Detector

The far detector for K2K was Super-Kamiokande, operated by the Institute for Cosmic Ray Research, University of Tokyo, a cylindrical water Cherenkov detector, 41 m tall and 39 m in diameter, holding a total mass of 50 kilotons of purified water. The water tank is optically separated into concentric inner and outer detectors by opaque sheets attached to the support structure for the PMTs. The ID was viewed by 11,146 50-cm PMTs facing inward, providing 40% photocathode coverage over the total ID surface area, from June, 1999 to July, 2001. A cascade of PMT implosions in late 2001 forced a temporary reduction in ID PMT coverage. From December, 2002 (SK-II and K2K-II), ID PMT coverage was reduced temporarily to 5182 PMTs, each enclosed in a fiber reinforced plastic shell with acrylic front cover, providing 19% photocathode area. The acrylic covers introduced absorption and reflection factors of 3% and 1%, respectively, in the relevant wavelength region. In the OD, 1885 outward-facing 20-cm PMTs equipped with wavelength shifting plates were attached to the outer side of the PMT support structure; the OD volume was also lined with reflective material to enhance light collection. The OD PMT complement was restored fully for SK-II/K2K-II, and no protective covers were installed.

The SK fiducial volume was defined to be a cylinder whose surface was 2 m inward from the ID PMT wall, providing a fiducial mass of 22.5 kilotons. Details of the detector performance and systematic uncertainties in SK-I have been given elsewhere.[1,8] For SK-II, these quantities were estimated using similar methods as used in SK-I. Momentum resolution for SK-II was slightly worse than SK-I: 2.4% and 3.6% for 1 GeV/c muons in SK-I and SK-II, respectively. However, vertex reconstruction, ring counting, and particle identification accuracies in SK-II were only slightly affected relative to SK-I. The uncertainty in the energy scale was estimated to be 2.0% for SK-I and 2.1% for SK-II.

Timing information was used to distinguish beam-induced neutrino events from cosmic ray induced background events in the SK detector. GPS data were used to synchronize clocks at SK and KEK. At both sites a free running 50 MHz (32-bit) Local Time Counter (LTC) connected to GPS receivers was used to time stamp an event trigger (at Super-K) or the beam spill trigger (at KEK). Initially a quartz oscillator was used as the LTC time base with good result; later, oscillator drift was further reduced by using a rubidium clock. The LTC counters were synchronized using the one pulse-per-second (1PPS) signal from the GPS system. In this way, timestamps between sites were synchronized within approximately 50 ns, after compensating for oscillator drift, transmission line delays and other factors. The K2K GPS timing system was accurate well beyond the 200 ns precision of a portable atomic clock, which was transported between sites as a final check. This was confirmed by comparing a second, independent GPS timing system at each site which gives the same result as the primary system within 35 ns 99% of the time. Accuracy was sufficient to observe the bunch substructure of the KEK beam in the SK neutrino data, and the probability that a cosmic ray neutrino event was identified as beam induced was negligible. The system was described more completely in Reference 25.

5.6. Neutrino Interaction Simulations

The neutrino interaction simulation program used in K2K (NEUT) plays an important role both in estimating the expected number of neutrino interactions and in deriving the energy spectrum of neutrinos from the data. The Monte Carlo program simulates neutrino interactions with protons, oxygen, carbon, and iron, the basic materials which make up the near and far neutrino detectors. As described in more detail elsewhere,[4] the program includes effects of quasi-elastic scattering, single-meson production, coherent production, and deep-inelastic scattering. For neutrino interactions in oxygen or other nuclei, secondary interactions of produced particles within the nucleus were also simulated.

The quasi-elastic and single-meson production models use a phenomenological parameter, the axial vector mass M_A, which was estimated at 1.1 GeV, based on K2K's own near detector data.[6] The intranuclear interactions of the mesons and nucleons produced in neutrino interactions in the carbon, oxygen, or iron nuclei were simulated with a cascade model, and each of the particles was traced until it escaped from the nucleus. Intranuclear inelastic scattering, charge exchange, and absorption of produced pions were simulated, and MC results were checked using existing data for pion scattering on carbon and oxygen, and pion photoproduction.

Intranuclear rescattering of the recoil protons and neutrons produced in neutrino interactions was also important, because proton tracks were used to select quasi-elastic events in the SciFi and SciBar near detectors, allowing kinematic estimation of the neutrino energy. Both elastic scattering and pion production were tracked using the same code as for produced mesons.

5.7. Event Rates and Oscillation Analysis

Neutrino oscillations cause an apparent reduction in the number of muon neutrino events and a distortion of the neutrino energy spectrum observed at SK, compared to the values expected in the absence of oscillation. ND measurements of the neutrino flux and spectrum before neutrinos had time to significantly oscillate were extrapolated by the F/N flux ratio, to predict the number of neutrino events and energy spectrum expected in SK for the no-oscillations hypothesis.

The neutrino event rate at the ND represents the neutrino interaction cross section folded into the neutrino beam flux. K2K used the event rate at the 1KT detector as the standard for oscillation studies; since the 1KT uses a water target and essentially the same hardware and software as SK, many systematic effects in the predicted number of interactions at the near and far site tend to cancel.

The fiducial volume (FV) of the 1KT was defined to provide an almost pure neutrino sample, rejecting cosmic rays or beam-induced muons. Cosmic ray events usually occurred near the upper wall of the inner tank, but some events contaminated the fiducial volume due to uncertainties in the vertex reconstruction. A beam-off run of the 1KT showed that cosmic rays in the fiducial volume were 1.0% of the neutrino event candidates. The other important background source was beam-induced muons which had not been tagged by the OD. The remaining event sample was scanned with a visual event display and the fraction of beam-induced muons found was 0.5% . The total background fraction, including other minor effects, was estimated to be 1.5% for runs starting in 2000, and 3.1% before 2000. From the comparison of neutrino interactions in data and the MC simulation, we estimate 3.0% systematic uncertainty on the fiducial volume.

The energy scale uncertainty of the 1KT was estimated from cosmic ray muons stopping inside of the detector, and the reconstructed mass of π^0 from neutral current interactions. The absolute energy uncertainty of the 1KT was estimated to be 3% .

Events with an electron in the final state in the LG and SciBar data were ν_e interaction candidates. "Electron-like" neutrino events essentially came only from the ν_e component of the beam, since the $\overline{\nu}_e$ fluxes were orders of magnitude smaller. The measurement of e-like events validated the prediction of the ν_e/ν_μ flux ratio at the near site from the beam MC simulation. The data-MC comparison also involved the cross sections of ν_e and ν_μ interactions, and the measurement was thus also an important check of the MC simulation's predictions of the number of ν_e interactions in SK. From LG data, the ν_e/ν_μ interaction ratio was estimated to be $1.6 \pm 0.4(\text{stat.})^{+0.8}_{-0.6}(\text{sys.})\%$. Similarly, data from the SciBar detector, which replaced the LG, produced an estimate for the interaction ratio $1.6 \pm 0.3(\text{stat.}) \pm 0.2(\text{sys.})\%$. The two independent results are in agreement with each other and the beam MC prediction of 1.3%. Consistency of LG and SciBar results between themselves and with the MC predictions confirms the quality of the data and of the MC simulation. Since the ND measurements were limited to a restricted energy region, K2K used the ν_e values predicted by the MC simulation in the oscillation analysis.

The muon neutrino energy spectrum was measured at the ND with the 1KT, SciFi, and SciBar CC event samples. Neutrino energy was calculated from the produced muon's kinematic parameters, assuming a QE interaction. Two-dimensional distributions of p_μ vs θ_μ were used to determine the neutrino energy spectrum. The observed spectrum was fit to the MC expectation. Free parameters in the fit were the neutrino flux for eight energy bins, and R_{nQE}, the ratio of CC-non-QE events to CC-QE events. Systematic uncertainties, such as nuclear effects, energy scale, track finding efficiency, and other detector related systematics, were also incorporated as adjustable parameters. The χ^2 functions separately defined for each sub-detector were summed to form a combined ND χ^2 function. Finally, a set of the fitted parameters was found by minimizing the χ^2. The best-fit values, their error sizes, and the correlations between them were used as inputs to the oscillation analysis. Details of the fitting procedures are given in Reference 4. All the fitted parameters for individual detectors were in good agreement with one another within their errors, except for R_{nQE}, which had best-fit values 0.76, 0.99 and 1.06 for the 1kT, SciFi and SciBar detectors, respectively. This discrepancy was treated as a systematic error, and an uncertainty of 0.20 was assigned to R_{nQE}.

Beam-induced neutrino event candidates in SK were selected by first considering only events within a narrow time window around the beam spill time, taking into account light-speed transit time from KEK. Figure 5.4 shows the relative arrival time ($\Delta T = 0$ represents spill time plus calculated delays) of events within the 1200 ns acceptance window; the accuracy of time synchronization makes the beam bucket structure clearly visible. (Outside this window, the nearest rejected event is over 100,000 ns away.)

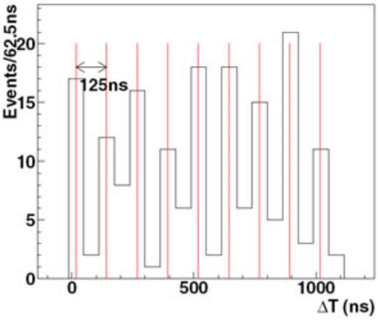

Fig. 5.4. Relative time distribution for fully contained SK events. The nine bunches in the beam can be clearly seen.

Following the timing cuts, FC event candidates with their vertex in the SK fiducial volume (FC-FV events) were selected using data-quality cuts and reconstruction methods similar to those used in the SK atmospheric neutrino reduction.[1] The efficiency for these cuts was 77.2% for K2K-I and 77.9% for K2K-II. The main inefficiency was due to NC interactions which were cut by these criteria. In total, 112 beam-induced FC events were observed in the SK fiducial volume, with 58 events reconstructed as one-ring muon-like.

Figure 5.5 shows the integrated event rate as a function of integrated POT at KEK. A Kolmogorov-Smirnov test confirmed the hypothesis that the event rate was proportional to POT, with a probability of 79% for consistency. The energy distribution of the events was compared to expectation in several ways. Figure 5.6 shows the visible energy distribution, which was

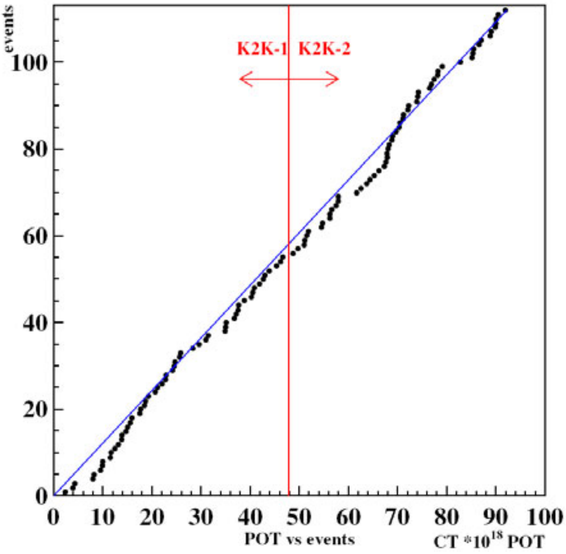

Fig. 5.5. Integral plot of event rate for interactions identified as beam-induced at SK versus POT at KEK.

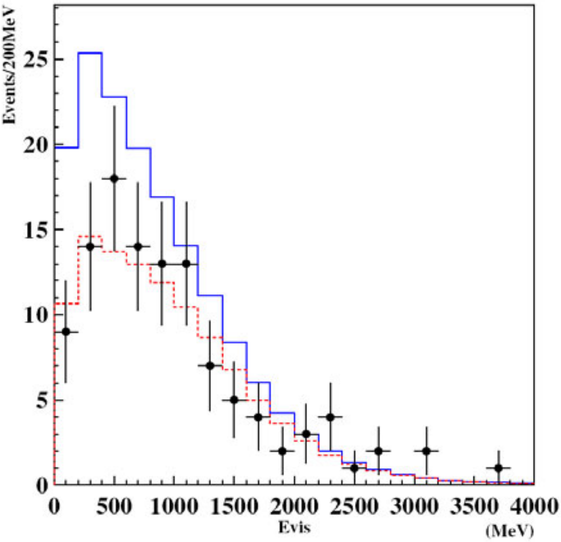

Fig. 5.6. Distribution of visible energy (total energy deposited in the ID) for all fully-contained events in SK with their vertex in the fiducial volume. Closed circles are the observed data, solid histogram is MC expectation for no neutrino oscillations, and dashed histogram is MC expectation with best-fit parameters for neutrino oscillation.

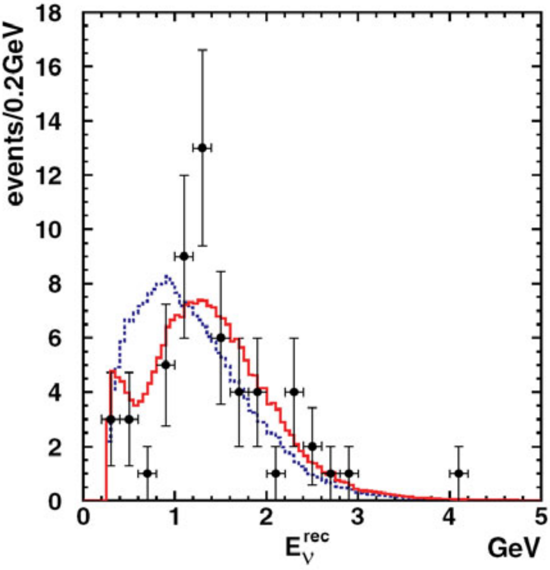

Fig. 5.7. Distribution of reconstructed energy (calculated from muon momentum assuming CC-QE kinematics) for 1-ring fully-contained muon-like events in SK with vertex in the fiducial volume. Points with error bars are the observed data; the dashed histogram is MC expectation for no neutrino oscillations, and the solid histogram is the expectation for the best-fit oscillation parameters, both normalized to the total number of observed events.

estimated from the energy deposited in the inner detector for all of the FC-FV events. In this figure, the observed data are compared to MC expectation with and without oscillations. Figure 5.7 shows the distribution for reconstructed energy E_{rec}, which is calculated from measured muon momentum assuming CC-QE kinematics, for the smaller sample of 1-ring FC-FV muon-like events in SK, in comparison with expectation for no oscillations.

The systematic uncertainties for estimating the expected number of neutrino events in SK (N_{SK}), and the reconstructed neutrino energy in SK (E_{rec}) were evaluated using atmospheric neutrinos as a control sample. The dominant uncertainty in N_{SK} comes from vertex reconstruction, since a systematic shift in or out of this volume will either over- or underestimate the number of events expected.

The two-flavor neutrino oscillation analysis used the maximum-likelihood method. The signature effects of neutrino oscillations are a reduction in the total number of observed muon neutrino events, and also a distortion in the neutrino energy spectrum. Thus, the likelihood function was defined as the product of the likelihoods for the observed number of events in the SK fiducial volume (L_{norm}, taken to be Poisson-distributed) and the shape of the E_{rec} spectrum (L_{shape}). In addition, systematic uncertainties were also treated as adjustable parameters in the likelihood function. They were included in a constraint likelihood term (L_{syst}, assuming Gaussian deviations), thus affecting the expected numbers of events. Details of the likelihood functions and fitting procedures are given in Reference 4.

The likelihood was maximized in terms of the two oscillation parameters, Δm^2, $\sin^2 2\theta$, representing mass difference squared and mixing respectively. One-hundred and twelve FC events were used in L_{norm}, and 58 FC 1-ring events were used for L_{shape}. The systematic parameters in the likelihood function included the ND neutrino energy spectrum parameters, the F/N flux ratio, the neutrino-nucleus cross section, efficiencies, the energy scale of SK, and the overall normalization.

N_{SK} was derived by extrapolating the measured number of interactions in the 1KT using the ratio of the expected neutrino event rate per unit mass. A correction factor for the different levels of electron neutrino contamination in the neutrino beam at 1KT and SK was estimated to be 0.996 using the MC simulation. Details of the systematic error estimations are given in Reference 4.

The number of FC events expected assuming no neutrino oscillation was $158.1^{+9.2}_{-8.6}$. Dominant systematics included uncertainties in the fiducial-volume in 1KT and SK ($^{+4.9}_{-4.8}\%$) and the F/N ratio ($\pm 2.9\%$).

The best-fit point within the physical region was found at (Δm^2, $\sin^2 2\theta$) $= (2.8 \times 10^{-3}\,\mathrm{eV}^2, 1.0)$. At the best-fit point, all fitted systematics were within 1 standard deviation of their estimated values, and the expected number of events was 107.2, in good agreement with the 112 events actually observed. The reconstructed neutrino energy spectrum is shown in Fig. 5.7, along with the expected distribution for the best-fit parameters, and the expectation with no oscillations. Consistency between the observed and the best-fit spectra was evaluated with a Kolmogorov-Smirnov (KS) test. The KS probability for the best-fit parameters was 37% , compared to a probability of 0.07% for no oscillations. The global maximum likelihood occurred just outside the physical region, at (Δm^2, $\sin^2 2\theta$)=(2.6×10^{-3} eV^2, 1.2).

The probability that the observations could be explained equally well with either the no-oscillation or the oscillation hypotheses was determined

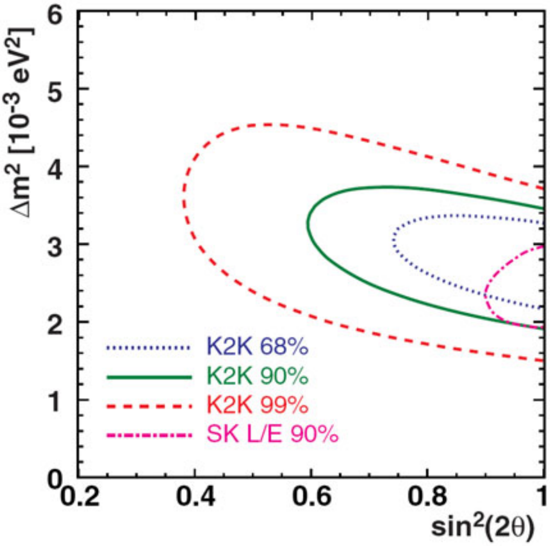

Fig. 5.8. K2K allowed region in oscillation parameter space for 2-flavor combined fits, with the SK atmospheric neutrino allowed region[2] also shown. Dotted, solid, dashed, and dash-dotted lines show the 68% , 90% , 99% C.L. allowed region contours for K2K, and 90% C.L. allowed region from SK atmospheric neutrino results.

using the difference in log-likelihood between the no-oscillation value and the (physical) best-fit point for oscillation. The relative likelihoods gave a probability of only 0.0015%, corresponding to a 4.3σ fluctuation, for such a difference. Using only the number of events, the probability was 0.06%, while it was 0.42% using only the spectrum shape. We can safely conclude that the existence of significant oscillation effects was confirmed by K2K.

The allowed region of oscillation parameters was similarly evaluated based on relative likelihoods, with results shown in Fig. 5.8, where the SK 90% allowed region is also shown.[2] Likelihood scans across the best-fit point for each of the two parameters are shown in Fig. 5.9.

5.8. Summary and Conclusions

The K2K experiment was the first long-baseline neutrino experiment to operate at a distance scale of hundreds of kilometers. The experiment was organized, built, and began taking data a remarkably short time after conception, a tribute to the foresight and hard work of many key collaborators.

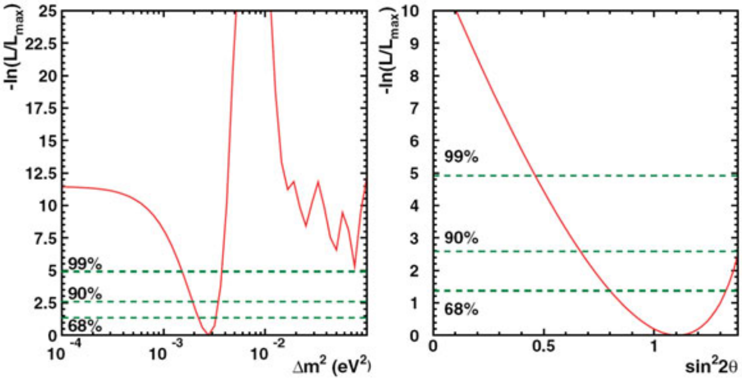

Fig. 5.9. Slices through the best-fit point in the K2K allowed region in oscillation parameter space for 2-flavor combined fits. Left: log-likelihood profile for Δm^2 at $\sin^2(2\theta) = 1.0$. Right: log-likelihood profile for $\sin^2(2\theta)$ at $\Delta m^2 = 2.8 \times 10^{-3}$. Relative likelihoods for 68, 90 and 99% CLs are shown.

Data taken by K2K between June 1999 and November 2004 were used to observe and measure the parameters of neutrino oscillation using an accelerator neutrino beam which was first sampled by detectors located approximately 300 meters from the proton target, and again by the Super-Kamiokande detector, 250 km away. The near detector complex included a 1 kt water Cherenkov detector and a fine-grained tracking detector system. The energy spectrum and flux normalization measured at the near detectors were used to predict the signal expected at Super-K in the absence of oscillation effects. A likelihood analysis based on the apparent disappearance of neutrinos and distortion of the neutrino energy spectrum showed the probability that the observations could explained by statistical fluctuations, assuming no neutrino oscillation, was 0.0015% (thus, disfavored at the 4.3σ level). K2K allowed regions confirmed neutrino oscillation parameters previously measured by the Super-Kamiokande collaboration using atmospheric neutrinos. K2K provided a valuable opportunity to prepare for future high-precision long-baseline experiments. The T2K experiment will begin data-taking in late 2009, and is now being built at the new JPARC accelerator complex in Japan. It has benefited greatly from the organizational experience, analysis tools, and detector techniques developed by K2K.

Acknowledgments

This review summarizes work done by the entire K2K collaboration, so of course thanks are due to all members past and present, as well as to the many institutions and agencies that made the project possible. All errors are the sole responsibility of the corresponding author. We gratefully acknowledge the cooperation of the Kamioka Mining and Smelting Company, and support from the Ministry of Education, Culture, Sports, Science and Technology of the Government of Japan, the Japan Society for Promotion of Science, the U.S. Department of Energy, the Korea Research Foundation, the Korea Science and Engineering Foundation, NSERC Canada and Canada Foundation for Innovation, the Istituto Nazionale di Fisica Nucleare (Italy), the Ministerio de Educacion y Ciencia and Generalitat Valenciana (Spain), the Commissariat 'a l'Energie Atomique (France), and Polish KBN grants 1P03B08227 and 1P03B03826. All figures, except Fig. 5.1 are reproduced from Reference 4.

References

1. Y. Ashie et al. (Super-Kamiokande Collaboration), Phys. Rev. D 71, 112005 (2005).
2. Y. Ashie et al. (Super-Kamiokande Collaboration), Phys. Rev. Lett. 93, 101801 (2004).
3. S. H. Ahn et al. (K2K Collaboration), Phys. Lett. B 511, 178(2001).
4. M. H. Ahn et al. (K2K Collaboration), Phys. Rev. D 74, 072003 (2006).
5. Y. Fukuda et al., Phys. Lett. B335, 237 (1994).
6. M. H. Ahn et al. (K2K Collaboration), Phys. Rev. Lett. 90, 041801 (2003).
7. E. Aliu et al. (K2K Collaboration), Phys. Rev. Lett. 94, 081802 (2005).
8. Y. Fukuda et al., Nucl. Instrum. Methods Phys. Res., Sect. A 501, 418 (2003).
9. H. Noumi et al., Nucl. Instrum. Methods Phys. Res., Sect. A 398, 399 (1997).
10. R. Brun, F. Bruyant, M. Maire, A. C. McPherson, and P. Zanarini, CERN-DD/EE/84-1, 1987.
11. C. L. Wang, Phys. Rev. Lett. 25, 1068 (1970).
12. M. G. Catanesi et al. (HARP Collaboration), Nucl. Phys. B732, 1 (2006).
13. Y. Cho et al., Phys. Rev. D 4, 1967 (1971).
14. S. Kasuga et al., Phys. Lett. B374, 238 (1996).
15. A. Suzuki et al. (K2K Collaboration), Nucl. Instrum. Methods Phys. Res., Sect. A 453, 165 (2000).
16. B. J. Kim et al., Nucl. Instrum. Methods Phys. Res., Sect. A 501, 418 (2003).
17. S. H. Ahn et al., Nucl. Instrum. Methods Phys. Res., Sect. A 451, 558 (2000).
18. S. Kawabata et al., Nucl. Instrum. Methods Phys. Res., Sect. A 270, 11 (1988).
19. K. Nitta et al., Nucl. Instrum. Methods Phys. Res., Sect. A 535, 147 (2004).

20. A. Pla-Dalmau (MINOS Scintillator Group), Proceedings of the 9th Conference on Calorimetry in High Energy Physics (CALOR 2000), Annecy, France, 2000 (Istituto Naz. Fis. Nucl., Frascati, Italy, 2001).
21. M. Yoshida et al., IEEE Trans. Nucl. Sci. 51, 3043 (2004).
22. S. Buontempo et al., Nucl. Instrum. Methods Phys. Res., Sect. A 349, 70 (1994).
23. A. Glazov, I. Kisel, E. Konotopskaya, and G. Ososkov, Nucl. Instrum. Methods Phys. Res., Sect. A 329, 262 (1993).
24. T. Ishii et al. (K2K MRD Group), Nucl. Instrum. Methods Phys. Res., Sect. A 482, 244 (2002).
25. H. G. Berns and R. J. Wilkes, IEEE Trans. Nucl. Sci. 47, 340 (2000).

This page intentionally left blank

Chapter 6

MINOS

Patricia Vahle*
Physics and Astronomy Department, University College London,
Gower Street, London, WC1E 6BT, UK
vahle@hep.ucl.ac.uk

This article describes the MINOS experiment and details the measurement of ν_μ survival probability as a function of energy after the neutrinos have traveled 735 km. Based on an exposure of 1.27×10^{20} protons on target, MINOS observes 215 ν_μ CC events below 30 GeV with an expectation of 336.0 ± 14.4 (stat + syst) events. The energy dependence of the survival probability is consistent with the two-flavor neutrino oscillation hypothesis with $|\Delta m^2_{32}| = 2.74^{+0.44}_{-0.26} \times 10^{-3}\,\mathrm{eV}^2/\mathrm{c}^4$ and $\sin^2(2\theta_{23}) > 0.87$ (68% C.L.)

Contents

6.1 Introduction 115
6.2 The NuMI Beam 116
6.3 The MINOS Detectors 118
6.4 Calibration 121
6.5 Event Selection 122
6.6 Near Detector Data and Monte Carlo 124
6.7 Predicting the Far Detector Spectrum 125
6.8 Systematics 129
6.9 Results 130
6.10 Outlook 132
References 133

6.1. Introduction

The Main Injector Neutrino Oscillation Search (MINOS) is a long baseline neutrino experiment designed to measure the survival probability of muon type neutrinos as a function of energy. MINOS uses two functionally

---

*On behalf of the MINOS collaboration.[1]

equivalent detectors to measure a beam of neutrinos at two different locations. The neutrino beam, produced in the NuMI (Neutrinos at the Main Injector) facility,[2] spans energies up to 120 GeV, but the flux is strongly peaked below 20 GeV. The Near Detector, installed at Fermi National Accelerator Laboratory (Fermilab), measures the beam energy spectrum and composition close to the production point of the neutrinos, while the Far Detector, installed in the Soudan Underground Laboratory in Northern Minnesota, measures the energy spectrum and composition of the beam after the neutrinos have propagated 735 km. By comparing the energy spectrum of charged current (CC) ν_μ interactions at each of the detector sites, the probability of ν_μ survival is measured. Using the energy dependence of the survival probability, MINOS can test the neutrino oscillation hypothesis and extract values for the oscillation parameters, namely $|\Delta m^2_{32}|$ and $\sin^2(2\theta_{23})$. With a value of L/E on the order of 735km/GeV, MINOS is sensitive to $|\Delta m^2_{32}|$ on the order of $10^{-3}\,\mathrm{eV}^2/\mathrm{c}^4$.

Figure 6.1 illustrates the technique used in the MINOS measurement. The left panel shows simulated ν_μ CC spectra in the Far Detector, both the expected spectrum in the case of no oscillations and an example, smoothed spectrum if oscillations occur with $|\Delta m^2_{32}|=3.35 \times 10^{-3}\,\mathrm{eV}^2/\mathrm{c}^4$ and $\sin^2(2\theta_{23})=1$. Oscillations distort the energy spectrum below 10 GeV, with maximal suppression of the ν_μ CC event rate occurring for neutrinos of about 2 GeV. To the right, the ratio of the spectra with oscillations over that without oscillations is shown. The energy at which the maximum suppression of events is observed gives a measure of $|\Delta m^2_{32}|$ and the magnitude of the suppression gives a measure of $\sin^2(2\theta_{23})$. The energy dependence of this ratio gives discrimination power between flavor oscillations and other exotic phenomenon proposed to explain the anomalies observed in neutrino experiments.

In this article we describe the neutrino beam and the MINOS detectors. After detailing the event selection and data analysis, we summarize the results derived from the first year of beam data collection, which were originally published in Reference 3.

6.2. The NuMI Beam

To make the NuMI neutrino beam, protons, accelerated to 120 GeV/c by the Main Injector, impinge on a graphite target. In the collisions of protons with the target nuclei, hadrons are produced, mainly pions and kaons. The positively charged hadrons are focused into a beam using two magnetic,

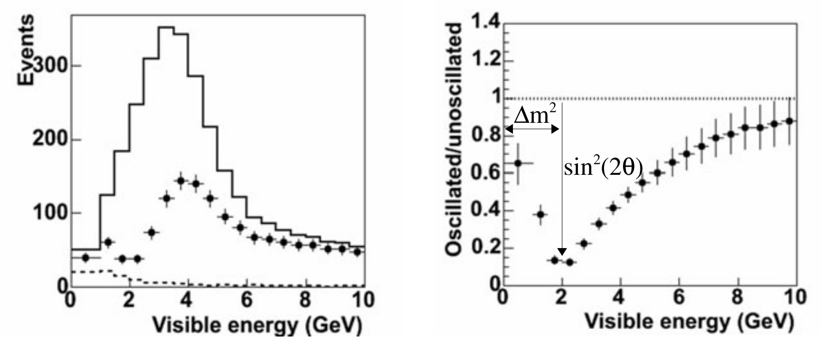

Fig. 6.1. To the left, simulated spectra expected in the Far Detector, both without neutrino oscillations (solid line) and with oscillations with $|\Delta m^2_{32}|$=3.35 × 10^{-3} $\mathrm{eV}^2/\mathrm{c}^4$ and $\sin^2(2\theta_{23})$=1 (points). Also shown is the expected NC contamination (dotted line). To the right, the ratio of simulated oscillated over non oscillated spectra in the Far detector. The energy at which maximum suppression occurs gives a measure of Δm^2, the magnitude of the suppression gives a measure of $\sin^2(2\theta)$, while the shape of the energy dependence distinguishes oscillations from other hypotheses.

parabolic focusing horns.[4] Once focused, the beam of hadrons travels down a 675 m long decay pipe, where the beam particles decay, primarily to μ and ν_μ. At the end of the decay pipe, any remaining hadrons and muons are ranged out in concrete absorber and rock, and the neutrinos travel unhindered to the Near and Far Detectors. Ionization chambers are placed upstream of the absorber and at three alcoves carved in the rock to monitor the beam by measuring the flux of hadrons and muons.[5] Figure 6.2 shows a schematic of the NuMI beam line.

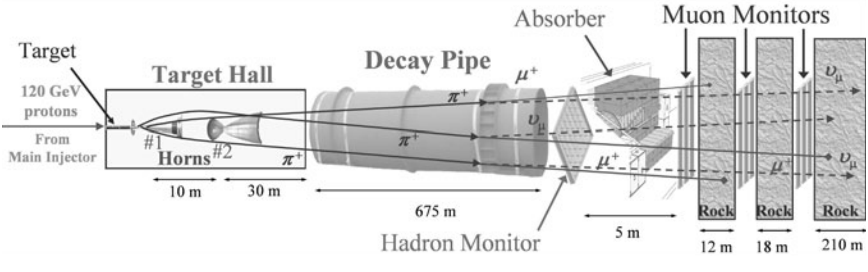

Fig. 6.2. Schematic of the NuMI beam line. Protons from the Main Injector come in from the left side of the plot, the detectors, while not pictured, would be to the right of the diagram. Reproduced from Reference 6.

The focal length of a parabolic horn depends on the momentum of the particle traversing the horn.[7] In other words, the momentum of hadrons focused by the horns, and therefore the energy spectrum of the neutrino beam, is determined by the distance between the target and the magnetic horns. If the distance between the target and horns is increased, the mean energy of the resultant neutrino beam is increased. In NuMI, the distance between the target and first horn can be remotely and continuously increased up to 2.5 m. Figure 6.3 shows simulated event spectra expected in the Near Detector for three beam configurations with different distances between the target and first horn. The peak energy of the resultant neutrino beam changes from 3 GeV to 10 GeV. Based on the range of values of $|\Delta m^2|$ indicated by Reference 8, MINOS achieves optimal sensitivity for the oscillation parameter measurement by running with the target partially inserted into the neck of the first horn. In this configuration, the neutrino energy spectrum measured in the Near Detector is peaked below 6 GeV, and the beam is made up of 92.9% ν_μ, with a 5.8% component of $\bar{\nu_\mu}$ and a 1.3% component of $\nu_e + \bar{\nu_e}$. Full advantage was taken of the flexibility of the NuMI beam by collecting approximately 5 % of the first year of MINOS beam exposure with different target positions and with different horn currents, both to commission the beam line and to perform studies of the systematic uncertainties associated with the beam.

6.3. The MINOS Detectors

The MINOS detectors are designed and constructed to perform identically so that many systematic uncertainties in neutrino interaction physics and detector response cancel. Both detectors are tracking-sampling calorimeters.[9] Steel plates, 2.54 cm thick, are used as the absorber material, while the active layers of each detector are made up of 1 cm thick plastic scintillator strips.[10] The strips are 4.1 cm wide and are arranged side-by-side to form planes. Scintillator planes are mounted on the steel planes, and successive scintillator planes are rotated 90° with respect to the previous plane to allow tracking in three dimensions. Each scintillator strip has a wavelength shifting (WLS) fiber embedded along its length. Light produced by a particle traversing the scintillator strip is captured by the WLS fiber then transported to a multi-anode photomultiplier tube (PMT). Normally incident, minimum ionizing particles produce ∼6-7 photoelectrons in a PMT in each of the detectors. Both detectors are magnetized to allow for the measurement of muon momentum via curvature as well as to separate ν_μ

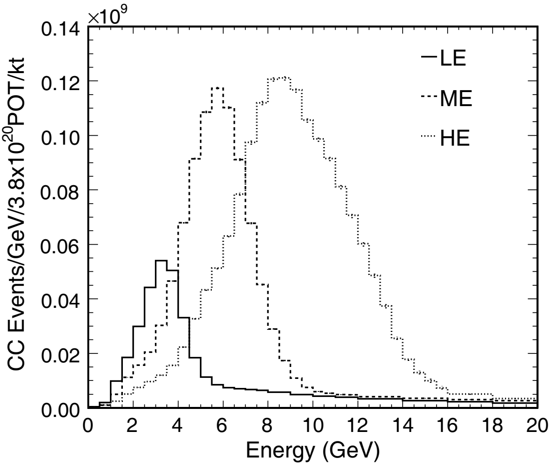

Fig. 6.3. Simulated event spectra expected at the Near Detector for three different separation distances between the target and first horn. The spectrum labeled "LE" gives the optimal sensitivity to the oscillation parameter measurement and is achieved when the target is partially inserted into the first horn. The spectrum labeled "ME" results when the distance between the target and first horn is increased to 100 cm, while the spectrum labeled "HE" results when the distance between target and first horn is increased to 250 cm.

interactions from $\overline{\nu}_\mu$ interactions.[11] Pictures of both detectors are shown in Figure 6.4 along with a schematic illustrating one detector layer.

Differences in the operating environment between the detector sites and cost considerations dictate differences in the details of the detector construction. The 0.98 kton Near Detector is located on-site at Fermilab, 1 km from the target. Installed near the neutrino source, the data rate in the Near Detector demands a readout electronics system that is capable of continuously recording signals without dead time throughout the $\sim$10 μs beam spill. This requirement is met using a system of electronics designed around the Charge to Current Encoder (QIE) chip.[12] The Near Detector consists of 282 irregular 4x6 m^2 octagonal planes. The full area is covered with active material in only every fifth plane; the other planes are instrumented in a smaller area surrounding the beam spot. The Near Detector consists of two logical units. The front section, made up of 121 planes, has every plane instrumented, while the back section has one active plane for every five absorber planes. Throughout the detector, the active planes are readout from one end, with each strip coupled to one pixel of a Hamamatsu M64

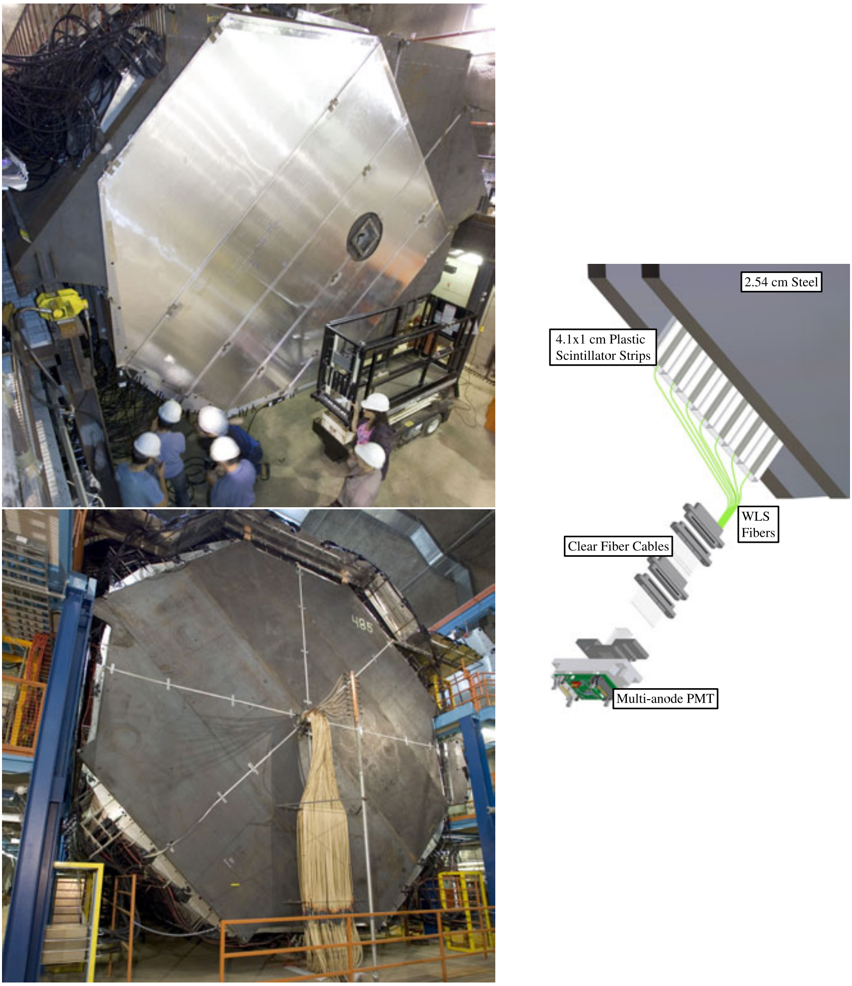

Fig. 6.4. The MINOS detectors. Top left shows the MINOS Near Detector at the time of installation of the last detector plane. Bottom left shows the MINOS Far Detector. The right picture shows a schematic of one layer of the detectors. Detector photos courtesy of Fermilab Visual Media Services, schematic courtesy of M. Proga.

PMT[13] via a WLS fiber. The Near Detector geometry and structure arises from the optimization of hadronic shower containment weighed against the cost of front end readout. Furthermore, both the shape of the planes and the placement of the Near Detector magnetic field inducing coil are chosen so that the beam interactions will occur in a region of the Near Detector with a similar magnetic field strength as that in the Far Detector.

The 5.4 kton Far Detector is located in the Soudan Underground Laboratory in Northern Minnesota, 705 m underground and 735 km away from the NuMI target. At this point the neutrino beam is much larger than the detector and so the neutrino events are evenly distributed across and throughout the Far Detector. The magnetic field is a toroidal field produced by a coil running through the center of the detector with an average value of 1.3T. The current polarity is chosen so that negative muon tracks produced in ν_μ interactions are focused toward the center. The Far Detector has 484 planes, each one a 8 m wide regular octagon. Every plane in the Far Detector is fully instrumented and the active planes are read out from both ends of the strip. The electronics are based on the Viking VA chip produced by IDE AS.[12] As a cost saving measure, eight WLS fibers from strips in the same plane, but separated by about 1 m, are coupled to a single pixel of a PMT. The coupling pattern of the strips is different at each end to resolve ambiguities in the strip to pixel mapping. The PMTs used in the Far Detector are Hamamatsu M16, which are operationally similar to the Near Detector PMTs, but have fewer pixels per tube.[14] The Far Detector has been taking cosmic ray and atmospheric neutrino data since installation began in 2001.[15–17] The full detector has been taking data since 2003.

6.4. Calibration

The MINOS technique of comparing energy spectra between two detectors separated by hundreds of kilometers requires a calibration procedure capable of ensuring the relative energy scale between the two detectors matches to 2%. The tools used to achieve a precise relative calibration are an LED based light-injection (LI) system[18] and cosmic rays. Each detector is calibrated in a multi-stage process that converts raw charge collected from a PMT to a fully calibrated unit that can be compared between the detectors. First, LED generated light is distributed via WLS fibers to all PMT channels, allowing the determination of PMT gain and the tracking of gain drift over time. Next, the energy deposited by through-going cosmic muons is used to normalize the light output of each individual scintillator strip. Finally, a standard candle that is common to the two detectors is defined using stopping muons. This unit is based on the average light produced by a muon with energy between 0.5–1 GeV crossing one scintillator plane at normal incidence.[19]

The overall energy scale for single hadron and electron interactions in the detectors is determined using a dedicated Calibration Detector (CalDet) exposed to test beam particles ranging from 0.2–10 GeV. Using this detector, MINOS confirms the efficacy of the relative calibration procedure.[20] Moreover, the CalDet provides a standard against which the detector simulation is tested. The simulation is found to reproduce the hadronic and electromagnetic response of the detector to single particle interactions to 4% and 2% respectively. The hadronic energy resolution is measured to be $56\%/\sqrt{E} \oplus 2\%$[21] and the electromagnetic energy resolution is measured to be $24.4\%/\sqrt{E} \oplus 4.1\%/E$.[22] Finally, the CalDet data provides a characterization of event topology, and demonstrates that the Near and Far electronics systems perform identically.[23]

6.5. Event Selection

MINOS classifies neutrino interactions based on the topology of the event. Since the neutrino flavor can only be identified if the neutrino undergoes a CC interaction, cuts are placed on the neutrino event sample to select CC ν_μ interactions and to reject neutral current (NC) interactions. CC ν_μ interactions are characterized by the presence of a track associated with the muon produced in the neutrino interaction. Often a cluster of hits near the interaction vertex can be identified as the result of the accompanying hadronic shower. NC interactions, on the other hand, are composed of only the hadronic shower and are best characterized by the absence of a muon track. CC ν_e interactions are also shower-like events without tracks, however such events are in general smaller, the energy deposition is more dense, and the shape is more regular than most NC events. In particular, in events where most of the neutrino energy is transferred to the electron, the longitudinal energy deposition profile is consistent with that of an electromagnetic shower. Figure 6.5 shows characteristic (simulated) events for each of the three types of interactions that MINOS attempts to classify. The events shown in Figure 6.5 all have similar reconstructed energy. The reconstructed energy of a shower is determined by the calorimetric response of the detector. The energy of a muon is determined either by range of the track in the detector, or by the curvature of the track in the magnetic field. The total energy of the ν_μ CC interaction is reconstructed as the sum of the muon energy plus the energy of the hadronic shower.

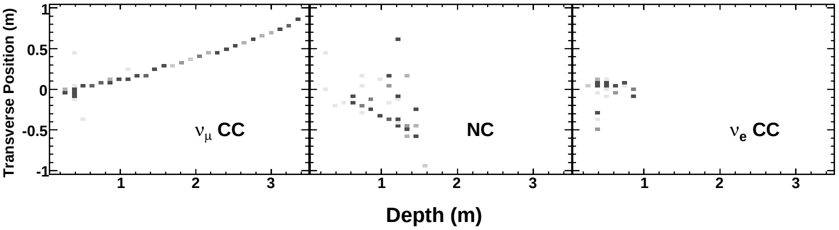

Fig. 6.5. Typical (simulated) events in the MINOS Far Detector. Each panel shows the transverse position versus the depth of illuminated strips. Shades of gray indicate the relative energy deposited in the strip. The left panel shows a ν_μ CC event; the middle panel shows a NC event; the right shows a ν_e CC event. Each event has a reconstructed energy between 3-4 GeV.

To select events for the ν_μ disappearance measurement, a series of cuts are applied to select well reconstructed ν_μ CC events and to reject NC and ν_e CC events. These require the event to be in time with the beam and have a single reconstructed track. Events are required to have the interaction vertex within the fiducial volume, which encompasses 72.9% of the Far Detector total mass and 4.5% of the Near Detector total mass. Further cuts require the track to have a negative charge to select ν_μ rather than $\overline{\nu}_\mu$ and have a reconstructed energy less than 30 GeV. Both these cuts are applied to suppress events originating from π^- and $K^\pm$ decays and thus reduce systematic errors arising from beam modeling. Cosmic ray background is further suppressed in the Far Detector by requiring the track to point to within 53° of the beam axis. Finally, a likelihood-based event selection parameter is constructed to separate CC interactions from NC interactions. Three low-level shape variables are used in the event selection parameter: the event length, the fraction of event pulse height that is associated with the track, and the pulse height associated with the track in each plane. These three variables, and the resulting event selection parameter distribution are shown in Figure 6.6 for both data and Monte Carlo in the Near Detector. The value of the cut that is placed on the event selection parameter differs between the detectors to achieve similar sample purities of ~98% in each of the detectors. After the cut on the event selection parameter, the resulting efficiency for selecting ν_μ CC events below 30 GeV interacting in the fiducial volume is 74% in the Far Detector and 67% in the Near.[3]

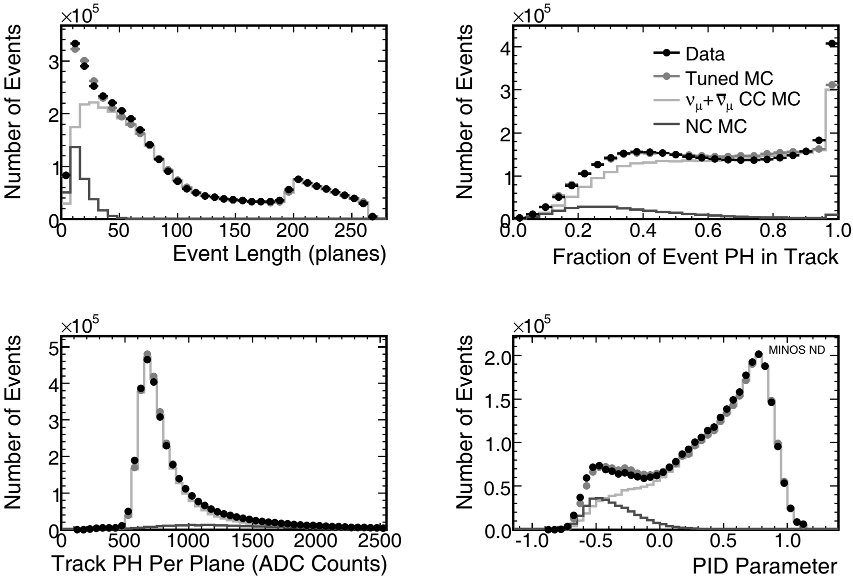

Fig. 6.6. The variables included in the CC event selection parameter. Top left shows the event length, measured in planes, top right shows the fraction of the event pulse height contained in the track, lower left shows the track pulse height per plane, while the bottom right shows the resulting log-likelihood based event selection parameter. Data and Monte Carlo are shown along with the distributions expected from ν_μ CC and NC events.

6.6. Near Detector Data and Monte Carlo

The high statistics data samples collected in the Near Detector are used to verify the basic operations of both the detector and the beam and to provide a benchmark against which beam and detector Monte Carlo are tested. The MINOS Monte Carlo proceeds via a number of different steps. First, the production of hadrons in the collisions of protons in the NuMI target is simulated using FLUKA05[24]. The resultant hadrons are then transported through the focusing system and decayed into neutrinos using a GEANT3[25] simulation that includes models of the horns, decay pipe and other beam line material. The simulation of the interaction of these neutrinos in the detector is based on the NEUGEN3[26] neutrino event generator. Finally, the detector response is simulated using GEANT3 with GCALOR[27] used to model hadronic interactions in the detector. Comparisons of many low level quantities between data and Monte Carlo show that the important features of both detector and beam are well modeled in the simulation. More importantly, comparisons of the energy spectrum below 5 GeV in the standard beam configuration show that data and Monte Carlo agree to around 15%, which is adequate agreement for a two detector oscillation experiment, since the Near Detector data is used to directly predict the Far Detector spectrum in the absence of oscillations.

Above 10 GeV the Monte Carlo disagrees with the data by about 40%, and the magnitude and energy dependence of the data versus Monte Carlo discrepancy changes depending on the beam configuration. These facts suggest that the simulation of the neutrino flux, rather than neutrino interaction or detector mis-modeling, is the primary cause of the discrepancy. The simulation of the neutrino flux depends on the underlying simulation of hadron production by the collisions of protons in the target, and presently, these models are poorly constrained at MINOS energies and for thick targets. However, by smoothly distorting the relative number and type of hadrons produced as a function of longitudinal and transverse momentum, better agreement between data and Monte Carlo can be achieved in the Near Detector energy spectra. Figure 6.7 shows the reconstructed energy spectrum of selected ν_μ CC interactions in the Near Detector for three different beam configurations. Data are shown compared to both the nominal Monte Carlo and also to the tuned Monte Carlo. After the tuning procedure, the simulated energy spectrum better represents the data, not only for the three configurations shown in Figure 6.7, but also for three other configurations not shown.

Accurate prediction of the event energy spectrum at the Near Detector is not strictly necessary in a two detector experiment. In MINOS, the Near Detector data are directly used to predict the event energy spectrum in the Far Detector without oscillations. However, the ability to tune the simulation to reproduce the data in several different beam configurations builds confidence in the simulation and ultimately reduces systematic errors in the measurement of the oscillation parameters.

6.7. Predicting the Far Detector Spectrum

Neutrinos are produced by the decay in flight of pions and kaons along the length of the decay pipe. In the lab frame, the energy of the resultant neutrino depends on the angle at which the neutrino emerges with respect to the direction of travel of the original hadron parent. For neutrinos

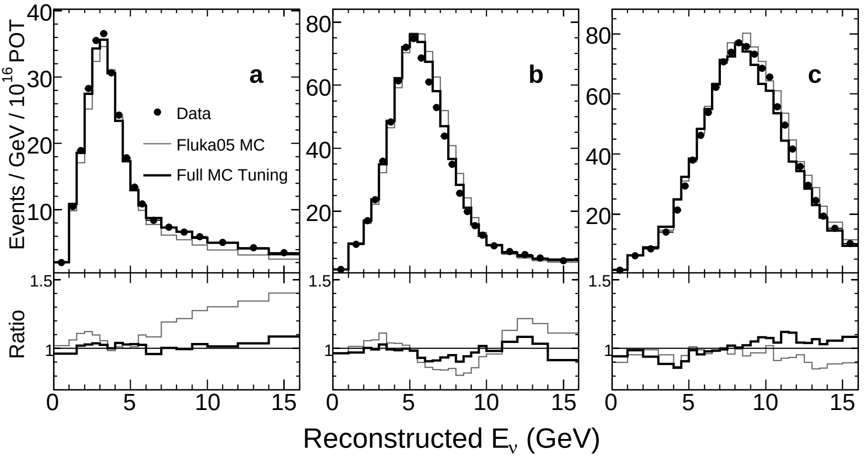

Fig. 6.7. Energy spectra of ν_μ CC selected events in the Near Detector for data, nominal Monte Carlo and Monte Carlo after hadron production tuning. Three out of 6 different beam configurations used to tune the Monte Carlo are shown. The spectra shown are produced when the target is located 10 cm (left), 100 cm (middle), 250 cm (right) from the first horn. The lower graphs show the ratio of data to Monte Carlo for each configuration before and after the tuning. Reproduced from Reference 3.

originating from pion decay, the energy of the neutrino goes as:

$$E_\nu \approx 0.43 \frac{E_\pi}{1 + \gamma^2 \theta_\nu^2} \tag{6.1}$$

where E_π is the energy of the parent pion, γ is the dilation factor of the pion, and θ_ν is the angle between the direction of travel of the neutrino and the parent pion in the lab frame. Since the Near and Far Detectors are at different distances from the decay pipe, the angular distribution of neutrinos that interact in each of the detectors differ, and the energy spectrum measured in the Near Detector is not precisely the same as the energy spectrum expected at the Far Detector in the case of no oscillations.

The ratio of the Far event energy spectrum per unit fiducial mass divided by the Near as a function of energy (F/N) provides a convenient way of characterizing the differences between the Near and Far spectra. Qualitatively, if the neutrinos emanated from a point source, the F/N ratio would be a constant function of energy and equal to the ratio of the distances from the source squared. The Far Detector is far enough away that the beam does approximate a point source. On the other hand, the Near Detector is closer to the decay pipe and the neutrinos appear to emanate from a line source, thus the F/N ratio does have an energy dependence.[7] Quantitatively, the shape of the F/N ratio depends on the details of the beam geometry and requires a full simulation to accurately predict. Figure 6.8 shows the prediction for the MINOS F/N ratio as a function of neutrino energy. The prediction of the event energy spectra at either the Near or Far detector depends on proton targeting, hadron production, hadron focusing, as well as neutrino interaction and detector modeling. However, the prediction of the ratio of F/N is robust against uncertainties in all these effects. Once the Near Detector event energy spectrum is measured, the Far Detector spectrum in the case of no oscillations can be predicted confidently.

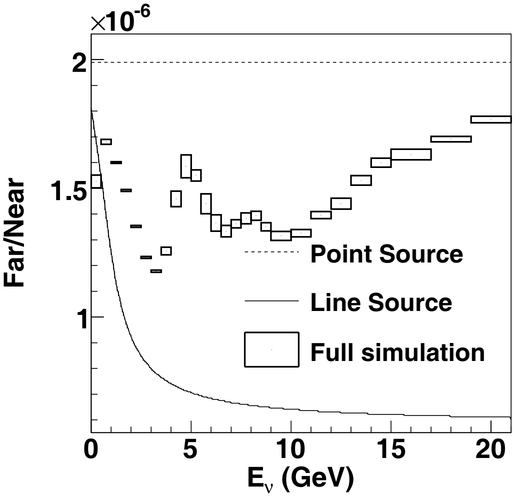

Fig. 6.8. The simulated F/N ratio of ν_μ CC selected events as a function of energy.

MINOS has developed several different techniques for extrapolating the Near Detector data to the Far Detector. The simplest method uses the F/N ratio multiplied bin-by-bin by the Near Detector measured spectrum to provide a prediction of the Far Detector spectrum in the case of no oscillations. A more sophisticated method uses a two-dimensional matrix to relate the energy of a neutrino in the Near detector to the energy that neutrino would have if it had arisen from a decay directed at the Far Detector[28]. Instead of multiplying the measured Near Detector spectrum by a one-dimensional ratio, the Near Detector data is multiplied by a matrix to produce a Far Detector prediction. Figure 6.9 shows a graphical repre-

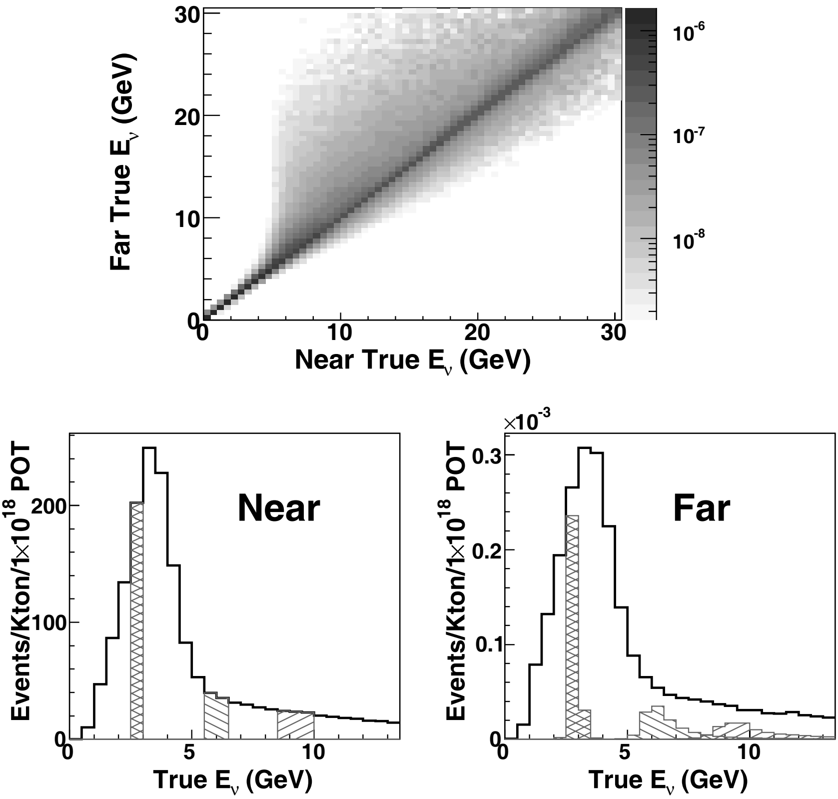

Fig. 6.9. Top panel shows the matrix used to extrapolate the Near spectrum to the far. Bottom left panel shows a simulated Near spectrum, while the bottom right panel shows the resultant Far spectrum obtained by multiplying by the matrix. The shaded areas show that events at a discrete energy in the Near Detector imply a range of energies in the Far.

sentation of the matrix used to do the extrapolation as well as the result of applying the matrix to a simulated Near Detector spectrum. The shaded areas highlight the fact that observation of events at a discrete energy in the Near Detector implies that events will be seen over a range of energies in the Far Detector. Both the F/N and matrix extrapolations directly use the Near Detector measured spectrum to predict the Far Detector spectrum. The full neutrino interaction and detector simulation is only used to make lower order corrections for efficiency, purity and detector resolution.

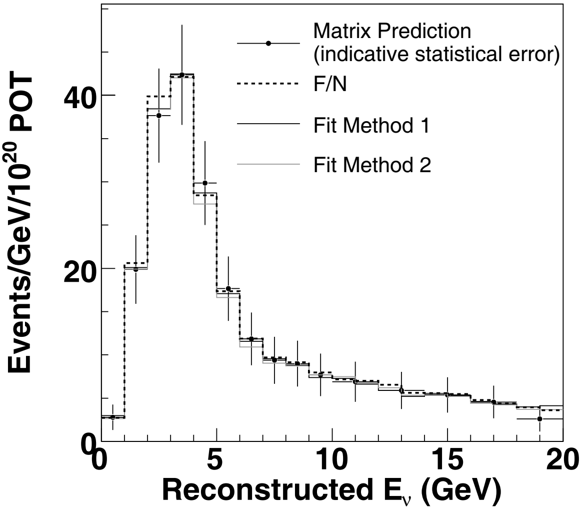

Fig. 6.10. The predicted Far Detector, non-oscillated spectra as given by four different extrapolation methods. The error bars indicated on the "matrix method" spectrum represent the statistical errors associated with an exposure of 10^{20} protons on target.

The results quoted by MINOS are based on the Far Detector prediction obtained using the matrix extrapolation.

MINOS also employs two additional extrapolation methods that involve modifying physics parameters to match the Monte Carlo to the data in the Near Detector, then use the tuned Monte Carlo to predict the Far Detector spectrum. Figure 6.10 compares the Far Detector predicted spectrum for the four different techniques of Near Detector data extrapolation. Each of the methods to extrapolate the Near Detector data have different degrees of sensitivity to different sources of systematic error, however the predictions from each of the methods agree to within 5% below 30 GeV, and the differences among the methods are much smaller than the statistical errors associated with the current data set.

6.8. Systematics

The small variation in the predicted Far Detector spectrum among the different extrapolation methods hints that the two detector approach minimizes the effects of systematic uncertainties. Direct evaluation of the systematic errors bears out that conclusion. The effects of different systematic

Table 6.1. Summary of the main systematic uncertainties and the error induced on the oscillation parameters.

Preliminary Uncertainty	Shift in Δm^2 (10^{-3}eV^2)	Shift in $\sin^2(2\theta)$
Near/Far normalization ±4%	0.050	0.005
Absolute hadronic energy scale ±11%	0.060	0.048
NC contamination ± 50%	0.090	0.050
All other systematic uncertainties	0.044	0.011
Total Sytematic	0.13	0.07
Statistical Error	0.36	0.12

uncertainties are studied by modifying the Monte Carlo to include the effect of a systematic error, then performing an oscillation fit to the energy spectrum obtained from the modified Monte Carlo. The effect of the uncertainty is expressed as the size of the shift between the fitted and input values of the oscillation parameters. It is found that three uncertainties dominate. First, the uncertainty in the relative fiducial masses between the detectors, the uncertainty in the event selection efficiency and the uncertainty in the proton on target counting contribute to a 4% uncertainty in the Far Detector predicted event rate. Second, a combination of calibration uncertainties and the uncertainty associated with intra-nuclear re-scattering give rise to a 11% systematic error on the hadronic energy scale. Finally, by varying the NC contribution to the event selection parameter distribution in different bins of neutrino energy to improve the data/Monte Carlo agreement, the level of neutral current contamination in the event sample is estimated to be uncertain at the 50% level. Table 6.1 lists the error these effects induce on the values of the fitted parameters. Added in quadrature, the total systematic error is ± 0.13 on Δm^2 and ± 0.07 on $\sin^2(2\theta)$, which is smaller than the statistical errors expected from this data set.

6.9. Results

In total, 215 ν_μ CC events are observed with energy less than 30 GeV in the Far Detector, when 336.0 ± 14.4 (stat + syst) events are expected. Assuming the deficit of ν_μ CC events is due to neutrino oscillations, a fit is performed to extract the oscillation parameters using the two flavor approximation for the survival probability:

$$P(\nu_\mu \to \nu_\mu) = 1 - \sin^2(2\theta)\sin^2\left(1.27\Delta m^2 \frac{L}{E}\right) \tag{6.2}$$

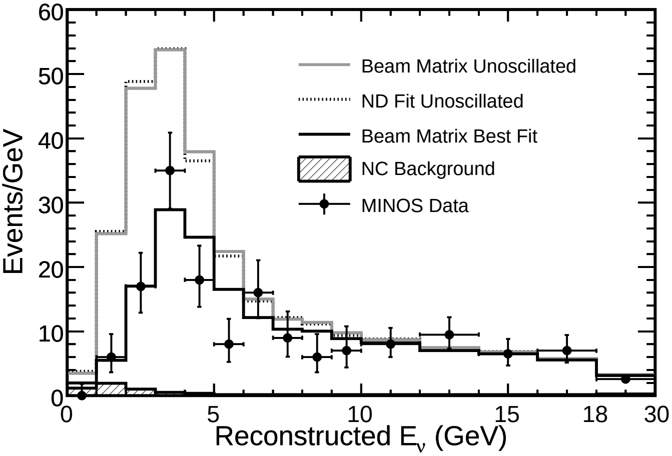

Fig. 6.11. Comparison of the Far Detector measured spectrum with the predictions for no oscillation from two extrapolation methods and for oscillations with the best fit parameters. The estimated NC background is also shown. The last energy bin shows the integral of events with energies between 18-30 GeV. Reproduced from Reference 3.

where $L = 735\,\mathrm{km}$, E is the neutrino energy in GeV, and Δm^2 is measured in $\mathrm{eV}^2/\mathrm{c}^4$. Figure 6.11 shows the measured Far Detector event reconstructed energy spectrum compared to the predictions of two extrapolation methods in the case of no oscillations as well as the spectrum resulting from the best fit. The best fit spectrum is determined by minimizing χ^2, where:

$$\chi^2 = \sum_{i=1}^{nbins} \left(2\left(e_i - o_i\right) + 2o_i \ln(o_i/e_i)\right) + \sum_{j=1}^{nsys} \frac{\Delta s_j^2}{\sigma_{s_j}^2} \tag{6.3}$$

where o_i is the observed and e_i is the expected number of events in energy bin i. The $\Delta s_j^2/\sigma_{s_j}^2$ terms are penalty terms for nuisance parameters associated with the three largest systematic uncertainties. Figure 6.12 shows the resulting confidence intervals, along with the contours from previous experiments.[8,29,30] When $\sin^2(2\theta)$ is required to be in the physical region, the oscillation parameters obtained from the fit are:[3]

$$|\Delta m^2_{32}| = 2.74^{+0.44}_{-0.26}\ (\mathrm{stat} + \mathrm{syst}) \times 10^{-3}\ \mathrm{eV}^2/\mathrm{c}^4$$
$$\sin^2(2\theta_{32}) > 0.87\ (68\%\mathrm{C.L.\ stat} + \mathrm{syst})$$

with a fit probability of 8.9%. At the 90% confidence level,

$$(2.31 < |\Delta m^2_{32}| < 3.43) \times 10^{-3}\ \mathrm{eV}^2/\mathrm{c}^4$$
$$\sin^2(2\theta_{23}) > 0.78.$$

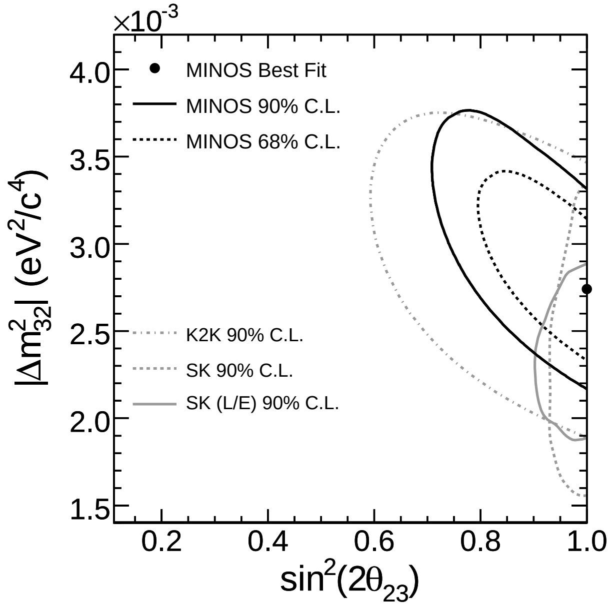

Fig. 6.12. Confidence intervals for the fit, including systematic errors. Also shown are contours from previous experiments.[8,29,30] Reproduced from Reference 3.

At the best fit value, the Monte Carlo predicts 0.76 CC ν_τ events in the final Far Detector data sample. If $\sin^2(2\theta)$ is not constrained to be in the physical region, the minimum χ^2 is reduced by 0.2 units and the best fit parameters are:

$$|\Delta m^2_{32}| = 2.72 \times 10^{-3}\ \mathrm{eV}^2/\mathrm{c}^4$$
$$\sin^2(2\theta_{32}) = 1.01$$

6.10. Outlook

At the time of writing, MINOS is nearing the end of the second year of beam operations. While this paper concentrates on the ν_μ disappearance measurement, work progresses on other analysis. First, MINOS will study the event rate and energy distribution of NC events in the Far Detector relative to the Near. While the NC distribution should not be distorted by standard neutrino flavor oscillations, non-standard phenomena like oscillations into $\nu_{sterile}$ would change the NC spectrum. Next, since both detectors are magnetized, MINOS will compare the propagation of ν_μ and

$\overline{\nu}_\mu$. CPT violation can be probed by comparing the oscillatory behavior of the neutrino and anti-neutrino, and furthermore transitions from ν_μ to $\overline{\nu}_\mu$ can be investigated. Additionally, MINOS is conducting a search for ν_e appearance in the Far Detector. Such an observation would be the first evidence of the sub-dominant oscillation mode of $\nu_\mu \to \nu_e$. Finally, improvements in both the intensity of the NuMI beam and the MINOS analysis promise increasingly precise measurements of $|\Delta m^2_{32}|$ and $\sin^2(2\theta_{23})$ over the coming years.

Acknowledgments

This work was supported by the US DOE; the UK PPARC; the US NSF; the State and University of Minnesota; the University of Athens, Greece; and Brazil's FAPESP and CNPq. We are grateful to the Minnesota Department of Natural Resources, the crew of the Soudan Underground Laboratory, and the staff of Fermilab for the contribution to this effort.

References

1. MINOS. The MINOS collaboration includes research groups from 32 institutions. Further details available at `http:://www-numi.fnal.gov`.
2. K. Anderson et al. The NuMI Technical Design Report. Technical report, Fermi National Accelerator Laboratory, (2002).
3. D. G. Michael et al., Observation of muon neutrino disappearance with the MINOS detectors and the NuMI neutrino beam, *Phys. Rev. Lett.* **97**, 191801, (2006).
4. A. G. Abramov et al., Beam optics and target conceptual designs for the NuMI project, *Nucl. Instrum. Meth.* **A485**, 209–227, (2002).
5. S. Kopp et al., Secondary beam monitors for the NuMI facility at FNAL, *Nucl. Instrum. Meth.* **A568**, 503–519, (2006).
6. R. M. Zwaska. *Accelerator systems and instrumentation for the NuMI neutrino beam.* PhD thesis, University of Texas, (2005). UMI-32-16264.
7. S. E. Kopp, Accelerator neutrino beams, *Phys. Rept.* **439**, 101–159, (2007).
8. Y. Ashie et al., A measurement of atmospheric neutrino oscillation parameters by Super-Kamiokande I, *Phys. Rev.* **D71**, 112005, (2005).
9. D. G. Michael et al. The MINOS detectors. To be submitted to Nucl. Inst. & Meth.
10. P. Adamson et al., The MINOS scintillator calorimeter system, *IEEE Trans. Nucl. Sci.* **49**, 861–863, (2002).
11. J. K. Nelson, The MINOS magnets, *Int. J. Mod. Phys.* **A16S1C**, 1181–1184, (2001).

12. J. Oliver, N. Felt, G. Feldman, A. Lebedev, and R. Lee, Design and performance of the readout system of the MINOS far detector, *IEEE Trans. Nucl. Sci.* **51**, 2193–2195, (2004).
13. N. Tagg et al., Performance of hamamatsu 64-anode photomultipliers for use with wavelength-shifting optical fibres, *Nucl. Instrum. Meth.* **A539**, 668–678, (2005).
14. K. Lang et al., Characterization of 1600 hamamatsu 16-anode photomultipliers for the MINOS far detector, *Nucl. Instrum. Meth.* **A545**, 852–871, (2005).
15. P. Adamson et al., First observations of separated atmospheric nu/mu and anti- nu/mu events in the MINOS detector, *Phys. Rev.* **D73**, 072002, (2006).
16. P. Adamson et al., Charge-separated atmospheric neutrino-induced muons in the MINOS far detector, *Phys. Rev.* **D75**, 092003, (2007).
17. P. Adamson et al., Measurement of the atmospheric muon charge ratio at TeV energies with MINOS. (2007). arXiv:0705.3815 [hep-ex].
18. P. Adamson et al., The MINOS light injection calibration system, *Nucl. Instrum. Meth.* **A492**, 325–343, (2002).
19. J. J. Hartnell. *Measurement of the MINOS Detectors' Relative Calorimetric Energy Response*. PhD thesis, St. John's College, Oxford, (2005).
20. P. Adamson et al., The MINOS calibration detector, *Nucl. Instrum. Meth.* **A556**, 119–133, (2006).
21. M. A. Kordosky. *Hadronic Interactions in the MINOS Detectors*. PhD thesis, University of Texas, (2004).
22. P. L. Vahle. *Electromagnetic Interactions in the MINOS Detectors*. PhD thesis, University of Texas, (2004).
23. A. Cabrera. *Systematic Comparison of the MINOS Near and Far Detector Readout Systems*. PhD thesis, Oxford University, (2004).
24. A. Ferrari, P. R. Sala, A. Fasso, and J. Ranft, Fluka: A multi-particle transport code (program version 2005). CERN-2005-010.
25. R. Brun et al. GEANT Detector Description and Simulation Tool. CERN Program Library Long Writeup W5013 (October, 1994).
26. H. Gallagher, The neugen neutrino event generator, *Nucl. Phys. Proc. Suppl.* **112**, 188–194, (2002).
27. C. Zeitnitz and T. A. Gabriel, The GEANT-CALOR interface and benchmark calculations of ZEUS test calorimeters, *Nucl. Instrum. Meth.* **A349**, 106–111, (1994).
28. M. Szleper and A. Para, Neutrino spectrum at the far detector: Systematic errors. (2001). hep-ex/0110001.
29. M. H. Ahn et al., Measurement of neutrino oscillation by the K2K experiment, *Phys. Rev.* **D74**, 072003, (2006).
30. Y. Ashie et al., Evidence for an oscillatory signature in atmospheric neutrino oscillation, *Phys. Rev. Lett.* **93**, 101801, (2004).

Chapter 7

The LSND and KARMEN Neutrino Oscillation Experiments

W. C. Louis

Los Alamos National Laboratory, Physics Division,
Los Alamos, New Mexico

Employing an 800 MeV, high-intensity proton beam, the LSND experiment performed a sensitive search for neutrino oscillations and obtained evidence for $\bar{\nu}_\mu \rightarrow \bar{\nu}_e$ oscillations with $\Delta m^2 > 0.2$ eV^2. Although the KARMEN experiment observed no such evidence, a joint analysis of the two experiments shows that the data sets are compatible with oscillations occurring either in a band from 0.2 to 1 eV^2 or in a region around 7 eV^2.

Contents

7.1 Introduction 135
7.2 LSND 136
  7.2.1 Description of the Experiment 136
  7.2.2 Event Selection 140
  7.2.3 Neutrino Oscillation Signal and Background Reactions 144
  7.2.4 Neutrino Oscillation Results 145
7.3 KARMEN 147
  7.3.1 Description of the Experiment 147
  7.3.2 Event Selection 148
  7.3.3 Neutrino Oscillation Signal and Background Reactions 149
  7.3.4 Neutrino Oscillation Results 150
7.4 Joint Analysis of LSND and KARMEN Data 151
7.5 Conclusions 152
References 153

7.1. Introduction

The LSND[1] experiment was designed to search for $\bar{\nu}_\mu \rightarrow \bar{\nu}_e$ oscillations with high sensitivity and to measure νC cross sections. A photograph of the inside of the detector tank is shown in Fig. 7.1. The main characteristics of the LSND experiment are given in Table 7.1. LSND had the advantage of a very high proton intensity, a large detector mass, and good particle identification. Also shown in Table 7.1 are the main characteristics of the KARMEN experiment, which had a lower duty factor than LSND and excellent energy resolution. An important difference between the experiments is that the LSND neutrino distance was 30 m, compared to 17.7 m for KARMEN, so that a combined analysis provides a more sensitive search for neutrino oscillations. Both experiments made use of a high-intensity, 800 MeV proton beam that interacted in an absorber to produce a large number of pions. Most of the pions produced are π^+, which almost all decay. The π^- are mainly absorbed and only a small fraction decay to μ^-, which in turn are largely captured. Therefore, almost all of the neutrinos produced arise from $\pi^+ \rightarrow \mu^+\nu_\mu$ and $\mu^+ \rightarrow e^+\bar{\nu}_\mu\nu_e$ decays, where most of the decays ($> 95\%$) are at rest and only a small fraction ($< 5\%$) are in flight. After six years of data collection, the LSND experiment obtained evidence for neutrino oscillations in the mass range $\Delta m^2 > 0.2\,\mathrm{eV}^2$, as shown in Fig. 7.2. Although this evidence was not confirmed by the KARMEN experiment, a joint analysis of the two experiments[3] reveals regions of compatibility in a band from 0.2 to $1\,\mathrm{eV}^2$ and in a region around $7\,\mathrm{eV}^2$.

Table 7.1. The main characteristics of the LSND and KARMEN experiments.

Property	LSND	KARMEN
Proton Energy	798 MeV	800 MeV
Proton Intensity	1000 μA	200 μA
Protons on Target	28,896 C	9425 C
Duty Factor	6×10^{-2}	1×10^{-5}
Total Mass	167 t	56 t
Neutrino Distance	30 m	17.7 m
Particle Identification	YES	NO
Energy Resolution at 50 MeV	6.6%	1.6%
Events for 100% $\bar{\nu}_\mu \rightarrow \bar{\nu}_e$ Transmutation	33,300	14,000

7.2. LSND

7.2.1. *Description of the Experiment*

The LSND experiment[4] was designed to search for $\bar{\nu}_\mu \rightarrow \bar{\nu}_e$ oscillations from μ^+ decay-at-rest (DAR) with high sensitivity. The LANSCE accelerator was an intense source of low energy neutrinos produced with a proton

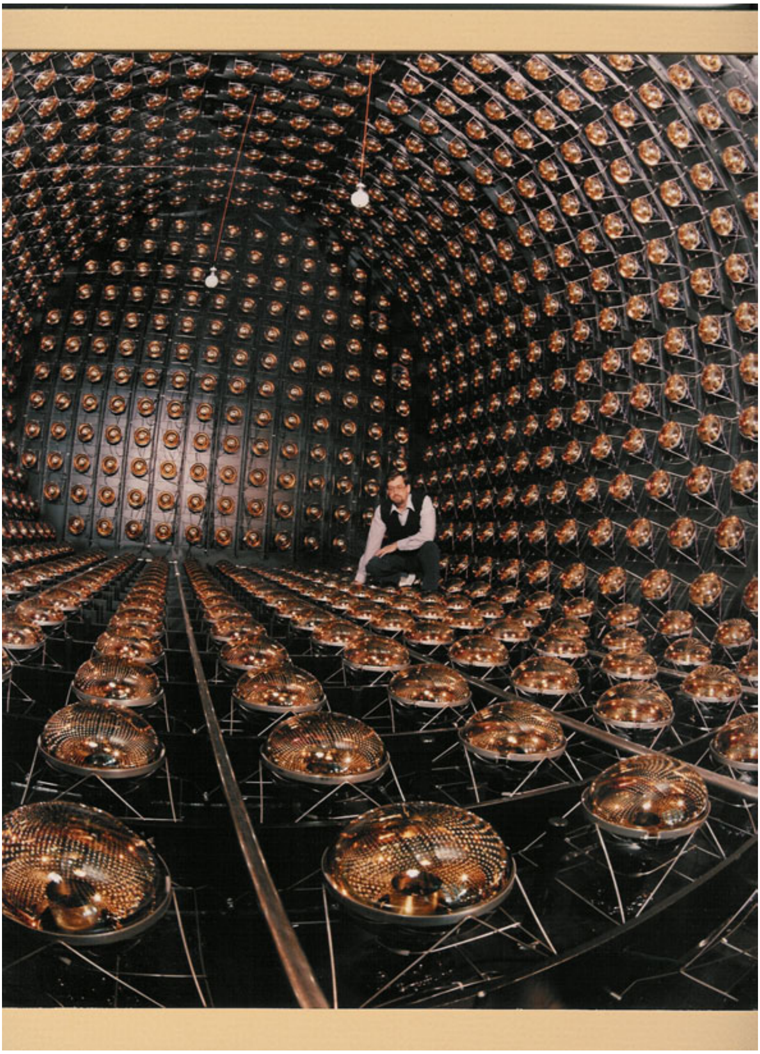

Fig. 7.1. A photograph of the inside of the LSND detector tank.

current of 1 mA at 798 MeV kinetic energy. For the 1993–1995 running period the production target consisted of a 30 cm long water target (20 cm in 1993) followed by a water-cooled Cu beam dump, while for the 1996–1998 running period the production target was reconfigured with the water target replaced by a close-packed, high-Z target. The resulting DAR

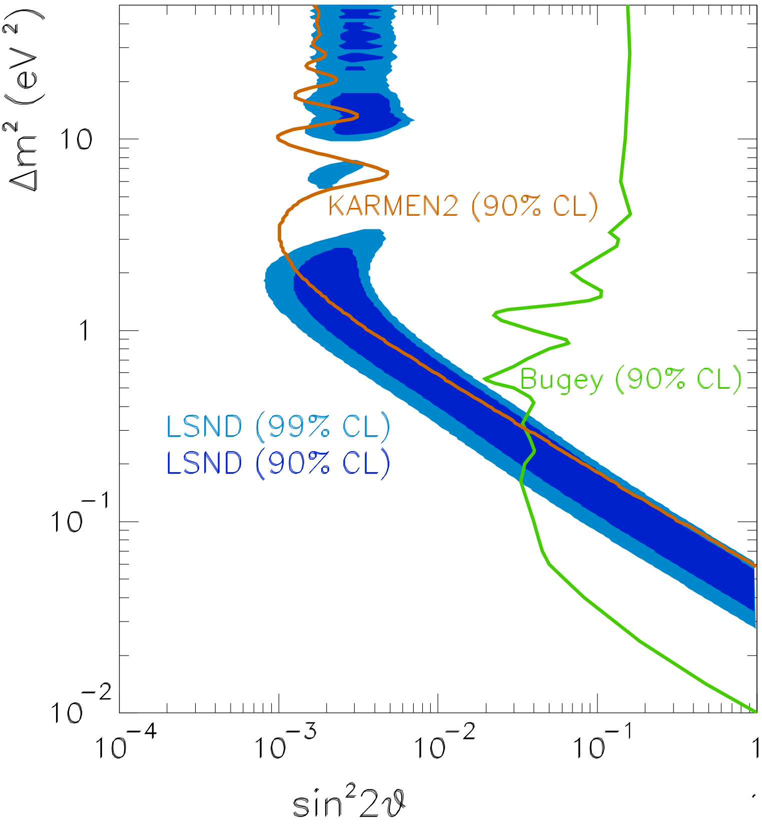

Fig. 7.2. The $(\sin^2 2\theta, \Delta m^2)$ oscillation parameter fit for the entire LSND data sample, $20 < E_e < 200$ MeV. The inner and outer regions correspond to 90% and 99% CL allowed regions, while the curves are 90% CL limits from the Bugey reactor experiment and the KARMEN experiment at ISIS.

neutrino fluxes are well understood because almost all detectable neutrinos arise from π^+ or μ^+ decay; π^- and μ^- that stop are readily captured in the Fe of the shielding and Cu of the beam stop.[5] The production of kaons or heavier mesons is negligible at these proton energies. The $\bar{\nu}_e$ flux is calculated to be only $\sim 8 \times 10^{-4}$ times as large as the $\bar{\nu}_\mu$ flux in the $20 < E_\nu < 52.8$ MeV energy range, so that the observation of a $\bar{\nu}_e$ event rate significantly above the calculated background would be evidence for $\bar{\nu}_\mu \rightarrow \bar{\nu}_e$ oscillations. Figure 7.3 shows the neutrino energy spectra from π^+ and μ^+ DAR.

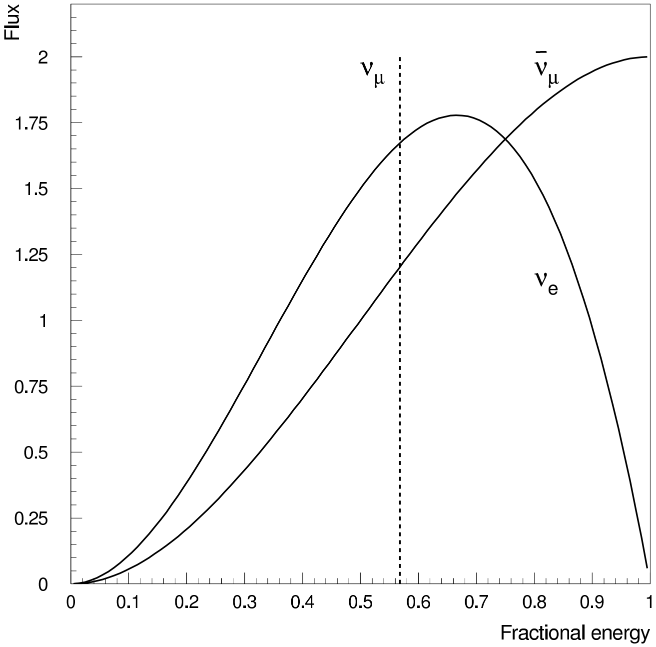

Fig. 7.3. The neutrino energy spectra from π^+ and μ^+ DAR.

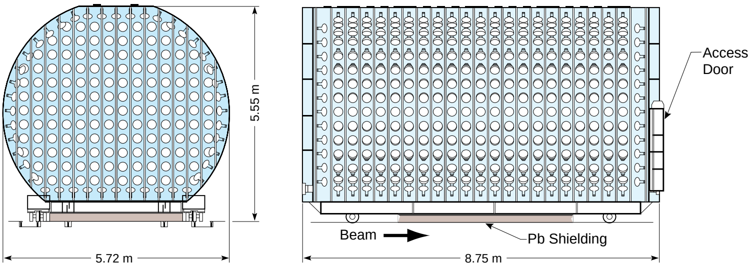

Fig. 7.4. A schematic drawing of the LSND detector.

The LSND detector[4] consisted of an approximately cylindrical tank 8.3 m long by 5.7 m in diameter. A schematic drawing of the detector is shown in Fig. 7.4. The center of the detector was 30 m from the neutrino source. On the inside surface of the tank, 1220 8-inch Hamamatsu PMTs covered 25% of the area with photocathode. The tank was filled with 167 t of liquid scintillator consisting of mineral oil and 0.031 g/l of b-PBD. This low scintillator concentration allows the detection of both Cherenkov light and scintillation light and yields an attenuation length of more than 20 m for wavelengths greater than 400 nm.[6] A typical 45 MeV electron created in the detector produced a total of ~ 1500 photoelectrons, of which ~ 280 photoelectrons were in the Cherenkov cone. PMT time and pulse-height signals were used to reconstruct the track with an average RMS position resolution of $\sim$14 cm, an angular resolution of $\sim 12^\circ$, and an energy resolution of $\sim 7\%$ at the Michel endpoint of 52.8 MeV. The Cherenkov cone for relativistic particles and the time distribution of the light, which is broader for non-relativistic particles,[4] gave excellent separation between electrons and particles below Cherenkov threshold. Identification of neutrons was accomplished through the detection of the 2.2 MeV γ from neutron capture on a free proton. The veto shield enclosed the detector on all sides except the bottom. Additional counters were placed below the veto shield after the 1993 run to reduce cosmic-ray background entering through the bottom support structure. The main veto shield[7] consisted of a 15 cm layer of liquid scintillator in an external tank and 15 cm of lead shot in an internal tank. This combination of active and passive shielding tagged cosmic-ray muons that stopped in the lead shot. A veto inefficiency $< 10^{-5}$ was achieved for incident charged particles.

7.2.2. *Event Selection*

To select events from $\bar{\nu}_\mu \to \bar{\nu}_e$ oscillations, it is necessary to identify the $\bar{\nu}_\mu$ which arise from μ^+ DAR in the beam stop and the $\bar{\nu}_e$ which are identified through the reaction $\bar{\nu}_e p \to e^+ n$. The goal of the event selection is to reduce the cosmic-ray background to as low a level as possible, while retaining a high efficiency for these neutrino-induced electron events. The selection criteria and corresponding efficiencies are shown in Table 7.2. The energy range $20 < \mathrm{E} < 200$ MeV is chosen so as to accept both DAR $\bar{\nu}_\mu \to \bar{\nu}_e$ and decay-in-flight (DIF) $\nu_\mu \to \nu_e$ oscillation candidates. The energy region $20 < E_e < 60$ MeV is required for the $\bar{\nu}_\mu \to \bar{\nu}_e$ oscillation search and $60 < E_e < 200$ MeV for the $\nu_\mu \to \nu_e$ oscillation search. Below 20 MeV there are large backgrounds from the β decay of ^{12}B created by the capture of stopped cosmic-ray μ^- on ^{12}C. Above 200 MeV the beam-related backgrounds from $\pi^+ \to e^+ \nu_e$ are large compared to any likely oscillation signal. Events with a previous activity within 12 μs, a future activity

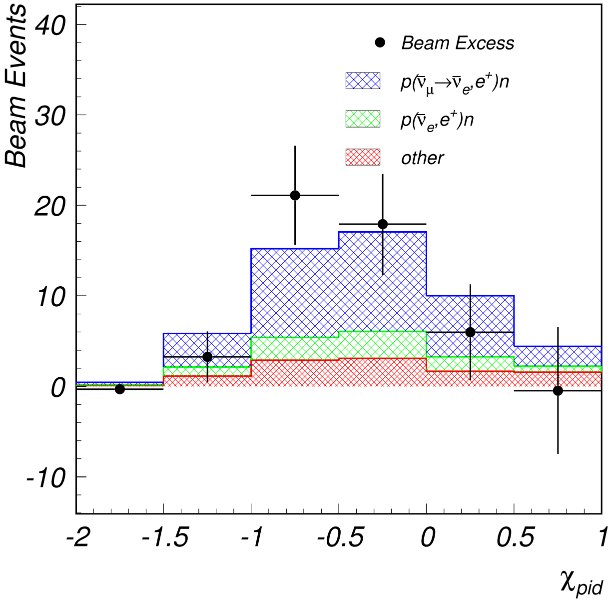

Fig. 7.5. The particle identification, χ'_{PID}, distribution for events with $R_\gamma > 10$ and $20 < E_e < 60\,\text{MeV}$. The shaded region shows the expected distribution from a combination of neutrino background plus neutrino oscillations at low $\Delta m2$. Oscillation candidate events are required to satisfy the requirement $-1.5 < \chi'_{PID} < 0.5$. Reproduced from Reference 1.

within $8\,\mu$s, or a bottom veto counter hit are rejected in order to eliminate cosmic-ray muon events. To further minimize cosmic-ray background, a tight electron particle identification is applied, $-1.5 < \chi'_{PID} < 0.5$, where the allowed range is chosen by maximizing the selection efficiency divided by the square root of the beam-off background with a correlated neutron. The χ'_{PID} parameter, shown in Fig. 7.5, depends on a product of χ parameters defined in Reference 4. Briefly, χ_r and χ_a are the quantities minimized for the determination of the event position and direction, and χ_t is the fraction of PMT hits that occur more than 12 ns after the fitted event time. The dependence of the χ parameters on energy and position for Michel electrons was studied, and a correction was developed that made χ'_{PID} independent of energy or position. Additionally, no veto hit is allowed within 30 ns of the trigger time and the reconstructed electron vertex is required to be inside a volume 35 cm from the faces of the photomultiplier tubes. Finally, the number of associated γs with $R_\gamma > 10$ (R_γ is discussed below) is required to be < 2 (< 1) for events < 60 (> 60) MeV in order to reject neutron-induced

Table 7.2. The LSND average efficiencies for electrons in the fiducial volume with energies in the range $20 < E_e < 60$ MeV.

Criteria	Efficiency
Electron Reduction	
Veto Hits < 4	0.98 ± 0.01
Loose Electron PID	0.96 ± 0.01
Cosmic Muon Cut	0.92 ± 0.01
Electron Selection	
$\Delta t_{past} > 12\mu$s	0.96 ± 0.01
$\Delta t_{future} > 8\mu$s	0.99 ± 0.01
$-1.5 < \chi'_{PID} < 0.5$	0.84 ± 0.01
$0.3 < \chi^{old}_{tot} < 0.65$ (1993 only)	0.98 ± 0.01
$\Delta t^{best}_{veto} > 30$ns	0.97 ± 0.01
D $>$ 35 cm	0.88 ± 0.02
$N_\gamma < 1$, $E > 60$	1.00
$N_\gamma < 2$, $E < 60$	1.00
Dead time	
DAQ & Tape Dead time	0.96 ± 0.02
Veto Dead time	0.76 ± 0.02
Total	0.42 ± 0.03

events, which tend to have many associated γs. In addition to the electron reduction and selection efficiencies, Table 7.2 also shows the efficiencies due to the data acquisition (DAQ) and veto dead time. The total efficiency for electrons in the fiducial volume with energies in the range $20 < E_e < 60$ MeV is 0.42 ± 0.03.

Correlated 2.2 MeV γ's from neutron capture are distinguished from accidental γ's from radioactivity by use of the likelihood ratio, R_γ, which is defined to be the likelihood that the γ is correlated divided by the likelihood that the γ is accidental. R_γ depends on three quantities: the number of hit PMTs associated with the γ (the multiplicity is proportional to the γ energy), the distance between the reconstructed γ position and positron position, and the time interval between the γ and the positron (neutrons have a capture time in mineral oil of 186 μs, while the accidental γ are uniform in time). Figure 7.6 shows these distributions, which are obtained from fits to the data, for both correlated 2.2 MeV γ's (solid curves) and accidental

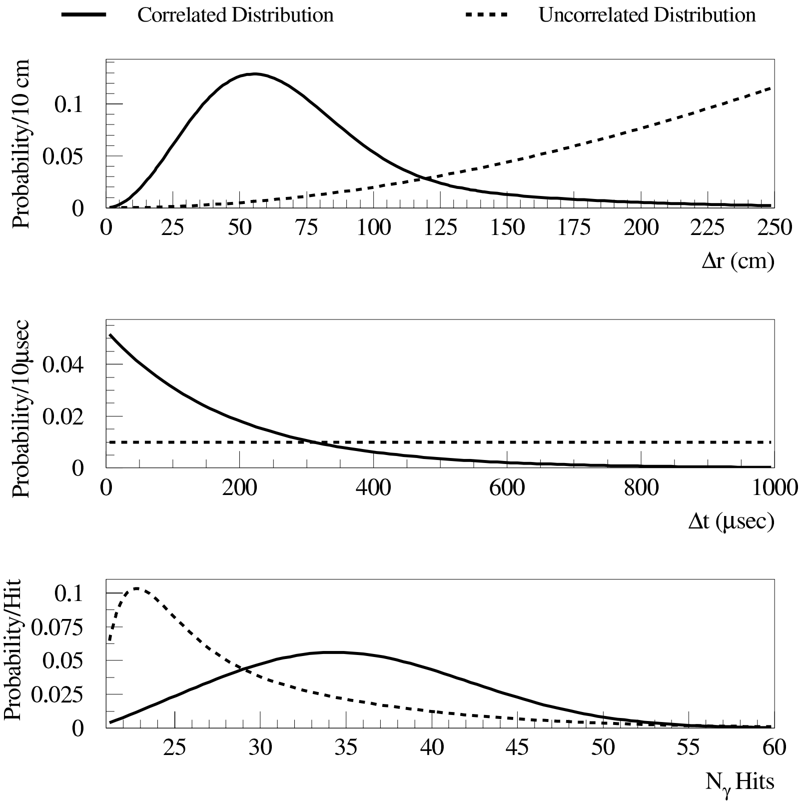

Fig. 7.6. Distributions for correlated 2.2 MeV γ (solid curves) and accidental γ (dashed curves) from LSND. The top plot shows the distance between the reconstructed γ position and positron position, Δr, the middle plot shows the time interval between the γ and positron, Δt, and the bottom plot shows the number of hit PMTs associated with the γ, N_{hits}. Reproduced from Reference 1.

γ's (dashed curves). To determine R_γ, the product of probabilities for the correlated distributions is formed and divided by the product of probabilities for the uncorrelated distributions. The accidental γ efficiencies are measured from the laser-induced calibration events, while the correlated γ efficiencies are determined from the MC simulation of the experiment. Similar results for the correlated γ efficiencies are obtained from the cosmic-ray neutron events, whose high energies give them a slightly broader position distribution. The systematic uncertainty of these efficiencies is estimated

Table 7.3. The LSND estimated number of events in the $20 < E_e < 60$ MeV energy range due to 100% $\bar{\nu}_\mu \rightarrow \bar{\nu}_e$ transmutation and to the two beam-related backgrounds with neutrons, μ^- DAR in the beam stop followed by $\bar{\nu}_e p \rightarrow e^+ n$ scattering in the detector and π^- DIF in the beam stop followed by $\bar{\nu}_\mu p \rightarrow \mu^+ n$ scattering. The events must satisfy the electron selection criteria, but no correlated γ requirement is imposed.

Neutrino Source	Reaction	Number of Events
μ^+ DAR	100% $\bar{\nu}_\mu \rightarrow \bar{\nu}_e$	33300 ± 3300
μ^- DAR	$\bar{\nu}_e p \rightarrow e^+ n$	19.5 ± 3.9
π^- DIF	$\bar{\nu}_\mu p \rightarrow \mu^+ n$	10.5 ± 4.6

to be ±7% of their values. For $R_\gamma > 10$, the correlated and accidental efficiencies are 0.39 and 0.003, respectively.

7.2.3. *Neutrino Oscillation Signal and Background Reactions*

The primary oscillation search in LSND is for $\bar{\nu}_\mu \rightarrow \bar{\nu}_e$ oscillations, where the $\bar{\nu}_\mu$ arise from μ^+ DAR in the beam stop and the $\bar{\nu}_e$ are identified through the reaction $\bar{\nu}_e p \rightarrow e^+ n$. This reaction allows a two-fold signature of a positron with a 52.8 MeV endpoint and a correlated 2.2 MeV γ from neutron capture on a free proton. There are only two significant neutrino backgrounds with a positron/electron and a correlated neutron. The first background is from μ^- DAR in the beam stop followed by $\bar{\nu}_e p \rightarrow e^+ n$ scattering in the detector. This background is highly suppressed due to the requirements that a π^- be produced, the π^- DIF, and the μ^- DAR prior to capture. The second background is from π^- DIF in the beam stop followed by $\bar{\nu}_\mu p \rightarrow \mu^+ n$ scattering in the detector. (Additional contributions are from $\bar{\nu}_\mu C \rightarrow \mu^+ n X$ and $\nu_\mu C \rightarrow \mu^- n X$ scattering.) This background will mimic the oscillation reaction if the μ^+ is sufficiently low in energy that it is below the threshold of 18 hit PMTs, corresponding to $E_\mu < 4$ MeV. Table 7.3 shows the estimated number of events in the $20 < E_e < 60$ MeV energy range satisfying the electron selection criteria for 100% $\bar{\nu}_\mu \rightarrow \bar{\nu}_e$ transmutation and for the two beam-related backgrounds with neutrons.

Table 7.4. Numbers of LSND beam-on events that satisfy the selection criteria for the primary $\bar{\nu}_\mu \to \bar{\nu}_e$ oscillation search with $R_\gamma > 1$, $R_\gamma > 10$, and $R_\gamma > 100$. Also shown are the beam-off background, the estimated neutrino background, and the excess of events that is consistent with neutrino oscillations.

Selection	Beam-On Events	Beam-Off BG	ν BG	Event Excess
$R_\gamma > 1$	205	106.8 ± 2.5	39.2 ± 3.1	$59.0 \pm 14.5 \pm 3.1$
$R_\gamma > 10$	86	36.9 ± 1.5	16.9 ± 2.3	$32.2 \pm 9.4 \pm 2.3$
$R_\gamma > 100$	27	8.3 ± 0.7	5.4 ± 1.0	$13.3 \pm 5.2 \pm 1.0$

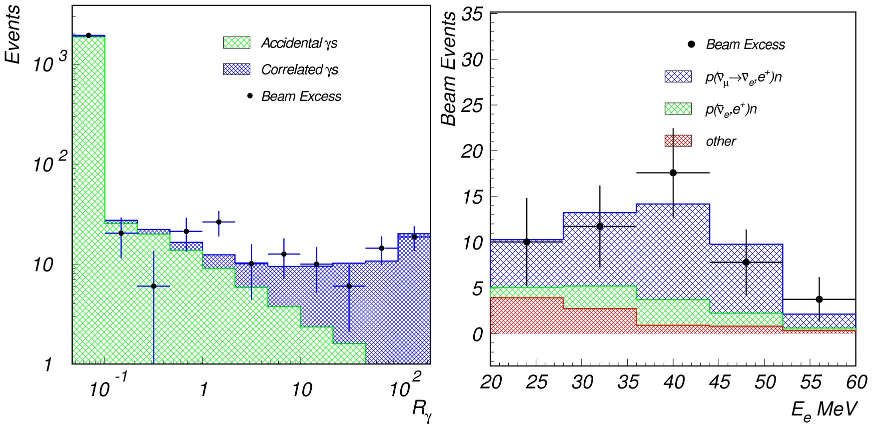

Fig. 7.7. (Left) The LSND R_γ distribution for events that satisfy the selection criteria for the primary $\bar{\nu}_\mu \to \bar{\nu}_e$ oscillation search. (Right) The LSND energy distribution for events with $R_\gamma > 10$. The shaded region shows the expected distribution from a combination of neutrino background plus neutrino oscillations at low Δm^2. Reproduced from Reference 1.

7.2.4. *Neutrino Oscillation Results*

Table 7.4 shows the statistics for events that satisfy the selection criteria for the primary $\bar{\nu}_\mu \to \bar{\nu}_e$ oscillation search. An excess of events is observed over that expected from beam-off and neutrino background that is consistent with neutrino oscillations. A χ^2 fit to the R_γ distribution, as shown in the left of Fig. 7.7, gives $f_c = 0.0567 \pm 0.0108$ ($\chi^2 = 10.7/9$ DOF), which leads to a beam on-off excess of 117.9 ± 22.4 events with a correlated neutron. Subtracting the neutrino background from μ^- DAR followed by $\bar{\nu}_e p \to e^+ n$ scattering (19.5 ± 3.9 events) and π^- DIF followed by $\bar{\nu}_\mu p \to \mu^+ n$ scattering (10.5 ± 4.6 events)^8 leads to a total excess of $87.9 \pm 22.4 \pm 6.0$ events. This excess corresponds to an oscillation probability of $(0.264 \pm 0.067 \pm 0.045)\%$,

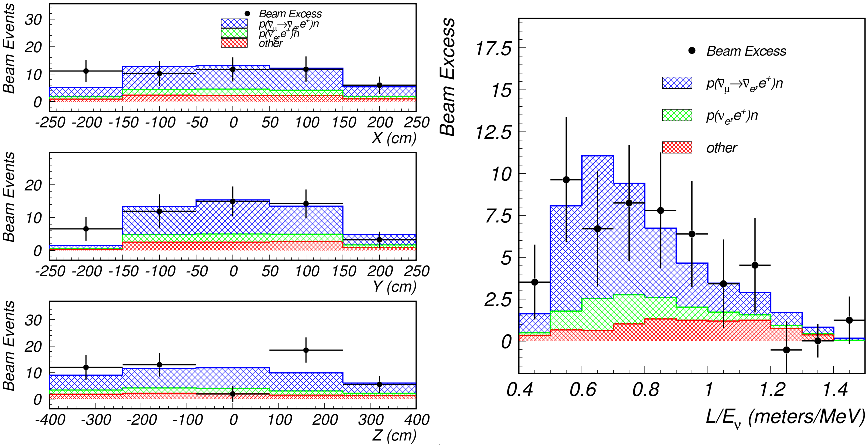

Fig. 7.8. (Left) The LSND spatial distributions for events with $R_\gamma > 10$ and $20 < E_e < 60$ MeV. The shaded region shows the expected distribution from a combination of neutrino background plus neutrino oscillations at low Δm^2. (Right) The LSND L_ν/E_ν distribution for events with $R_\gamma > 10$ and $20 < E_e < 60$ MeV, where L_ν is the distance traveled by the neutrino in meters and E_ν is the neutrino energy in MeV. The data agree well with the expectation from neutrino background and neutrino oscillations at low Δm^2. Reproduced from Reference 1.

where the first error is statistical and the second error is the systematic error arising from uncertainties in the backgrounds, neutrino flux (7%), e^+ efficiency (7%), and γ efficiency (7%).

A clean sample of oscillation candidate events can be obtained by requiring $R_\gamma > 10$, where as shown in Table 7.4, the beam on-off excess is 49.1 ± 9.4 events while the estimated neutrino background is only 16.9 ± 2.3 events. The right of Fig. 7.7 displays the energy distribution of events with $R_\gamma > 10$. The shaded regions show the combination of neutrino background plus neutrino oscillations at low Δm^2. The data agree well with the oscillation hypothesis. The left panel of Fig. 7.8 shows the spatial distribution for events with $R_\gamma > 10$ and $20 < E_e < 60$ MeV, where z is along the axis of the tank (and approximately along the beam direction), y is vertical, and x is transverse. The shaded region shows the expected distribution from a combination of neutrino background plus neutrino oscillations. Finally, the right panel of Fig. 7.8 shows the L_ν/E_ν distribution for events with $R_\gamma > 10$ and $20 < E_e < 60$ MeV, where L_ν is the distance traveled by the neutrino in meters and E_ν is the neutrino energy in MeV determined from the measured positron energy and angle with respect to the neutrino beam. The data agree well with the expectation from neutrino background plus neutrino oscillations at low Δm^2 ($\chi^2 = 4.9/8$ D.O.F.) or high Δm^2 ($\chi^2 = 5.8/8$ D.O.F.).

The $(\sin^2 2\theta, \Delta m^2)$ likelihood ($\mathcal{L}$) fitter is applied to beam-on events in the final oscillation sample and calculates a likelihood in the $(\sin^2 2\theta, \Delta m^2)$ plane in order to extract the favored oscillation parameters. The $\mathcal{L}$ product in the $(\sin^2 2\theta, \Delta m^2)$ plane is formed over the individual beam-on events that pass the oscillation cuts. This three-dimensional contour is sliced to arrive finally at the LSND allowed oscillation region. The beam-related backgrounds are determined from Monte Carlo (MC) event samples for each individual background contribution. The MC contains the trigger simulation and generally very well reproduces the tank response to all particles of interest. Agreement between the data and MC is excellent.

The $(\sin^2 2\theta, \Delta m^2)$ oscillation parameter fit for the entire data sample, $20 < E_e < 200$ MeV, is shown in Fig. 7.2. The fit includes both $\bar{\nu}_\mu \rightarrow \bar{\nu}_e$ and $\nu_\mu \rightarrow \nu_e$ oscillations, as well as all known neutrino backgrounds. The inner and outer regions correspond to 90% and 99% CL allowed regions, while the curves are 90% CL limits from the Bugey reactor experiment[10] and the KARMEN experiment at ISIS[2]. The most favored allowed region is the band from 0.2–2.0 eV^2, although a region around 7 eV^2 is also possible.

7.3. KARMEN

7.3.1. *Description of the Experiment*

The KARMEN experiment[11] made use of the ISIS rapid-cycling synchrotron, which accelerates protons up to 800 MeV at an intensity of 200 μA. The protons are extracted from the synchrotron at a frequency of 50 Hz as a double pulse consisting of two 100 ns pulses separated by 325 ns. The two bursts, therefore, occur within 600 ns and lead to an overall duty factor of about 10^{-5}. After extraction, the protons interact in a water-cooled Ta-D_2O target, producing about (0.0448 ± 0.0030) π^+ per incident proton.[5] Because the beam spill is shorter than the muon lifetime, the ν_μ from π^+ decay can be clearly separated from the $\bar{\nu}_\mu$ and ν_e from μ^+ decay. The $\bar{\nu}_e/\bar{\nu}_\mu$ background is estimated to be 6.4×10^{-4},[5] slightly smaller than for LSND.

The KARMEN detector, as shown in Fig. 7.9, is a segmented, liquid scintillator calorimeter with 608 modules and a total mass of 56 t. The liquid scintillator is made of paraffin oil (75% vol.), pseudocumene (25%

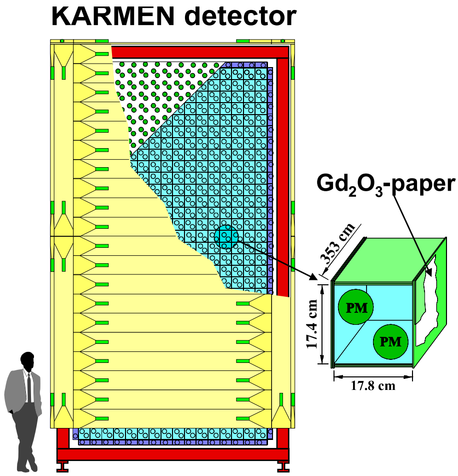

96% active volume of ^{12}C and p

$$\sigma_E = \frac{11.5\%}{\sqrt{E[\mathrm{MeV}]}} \qquad \Delta t_{\mathrm{ISIS}} \leq \pm 2\mathrm{ns}$$

Fig. 7.9. A schematic drawing of the KARMEN detector.

vol.), and PMP (2 g/l). The modules are read-out by pairs of 3-inch PMTs and are enclosed by a tank with outside dimensions 3.53 m x 3.20 m x 5.96 m. Excellent energy resolution is obtained for electrons produced inside the detector and can be parametrized by $\sigma_E = 11.5\%/\sqrt{E(\mathrm{MeV})}$. Gadolinium-coated paper was inserted between the modules for the detection of thermal neutrons. The detector is enclosed by a multilayer active veto system and 7000 t of steel shielding and is located 17.7 m from the neutrino source at an angle of 100 ° to the incident proton beam direction.

7.3.2. *Event Selection*

KARMEN searches for $\bar{\nu}_\mu \rightarrow \bar{\nu}_e$ oscillations in the same way as in LSND by looking for the reaction $\bar{\nu}_e p \rightarrow e^+ n$, which gives a two-fold signature of a e^+ followed by one or more γ from neutron capture. The neutrino oscillation event selection and corresponding efficiencies are summarized in Table 7.5. For the e^+ candidate it is required that there be no previous activity in the detector and veto, that the e^+ occur from 0.6μs to 10.6μs

Table 7.5. The KARMEN event selection and corresponding efficiencies for the $\bar{\nu}_\mu \rightarrow \bar{\nu}_e$ oscillation search.

Event	Selection	Efficiency
e^+	no previous activity	0.709
e^+	$0.6 < t_{pr} < 300\mu$s	0.840
e^+	$16 < E_{pr} < 50$ MeV	0.775
(n, γ)	$5 < \Delta t < 300\mu$s	
(n, γ)	$E_{del} < 8.0$ MeV	0.416
(n, γ)	$V_c = 1.3m^3$	

Table 7.6. The KARMEN estimated number of events in the $16 < E_e < 50$ MeV energy range due to 100% $\bar{\nu}_\mu \rightarrow \bar{\nu}_e$ transmutation and to the four backgrounds with apparent neutrons.

Process	Number of Events
100% $\bar{\nu}_\mu \rightarrow \bar{\nu}_e$	5826 ± 534
Cosmic-induced Background	3.9 ± 0.2
Charged-current Coincidences	5.1 ± 0.2
ν_e-induced Random Coincidences	4.8 ± 0.3
Intrinsic $\bar{\nu}_e$ Background	2.0 ± 0.2

after the beam spill, and that the e^+ energy be in the range from 16 MeV to 50 MeV. For the γ candidate it is required that the γ occur from 5μs to $300\,\mu$s after the e^+, that the γ have an energy less than 8.0 MeV, and that the γ be reconstructed within a coincidence volume of $1.3\,\mathrm{m}^3$. The total efficiency for the two-fold signature is estimated to be 0.192 ± 0.0145.

7.3.3. *Neutrino Oscillation Signal and Background Reactions*

Table 7.6 shows the estimated number of events in the $16 < E_e < 50$ MeV energy range for 100% $\bar{\nu}_\mu \rightarrow \bar{\nu}_e$ transmutation. Also shown are the number of events for the four backgrounds with apparent neutrons. The first background is the cosmic-induced background, which is well measured from data collected with the beam off. The second background is due to $\nu_e C \rightarrow e^- N_{gs}$, where the N_{gs} β decay to $^{12}\mathrm{C}_{gs}$ mimics the γ from neutron capture. The third background is due to normal $\nu_e C \rightarrow e^- N^*$ inclusive interactions with an accidental γ coincidence. The final background is due

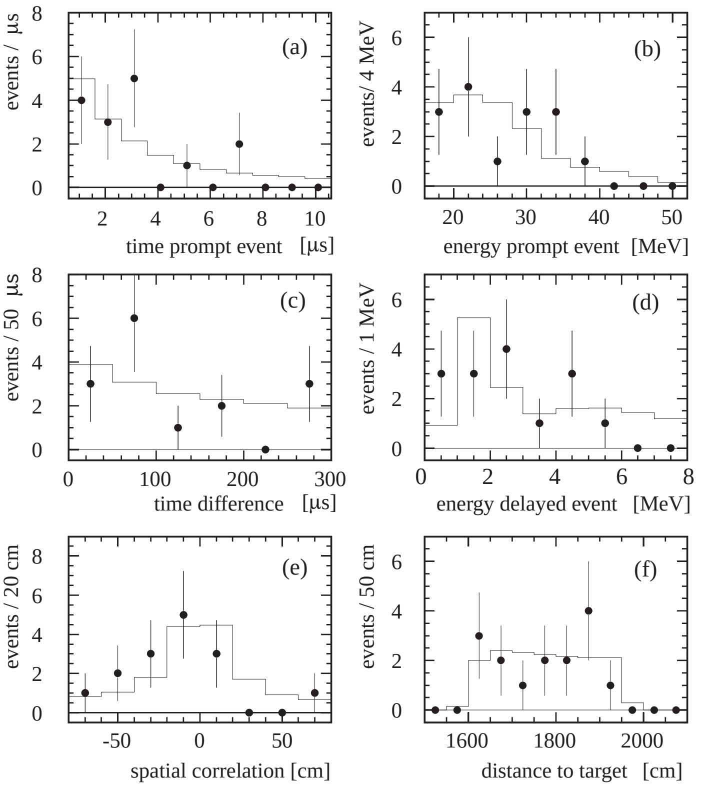

Fig. 7.10. The energy, time, and spatial distributions for the events observed by the KARMEN experiment: (a) time of prompt events, (b) energy of prompt events, (c) time difference between prompt and delayed events, (d) energy of delayed events, (e) spatial correlation, and (f) distance to target of prompt events. The 15 oscillation candidate events are in good agreement with the background expectation of 15.8 events (solid line). Reproduced from Reference 3.

to the intrinsic $\bar{\nu}_e$ contamination in the beam from μ^- DAR. The total background is estimated to be 15.8 ± 0.5 events.

7.3.4. *Neutrino Oscillation Results*

KARMEN observes 15 events that pass the selection criteria discussed above, which is consistent with the estimated background of 15.8 ± 0.5 events. The energy, time, and spatial distributions for the 15 events are shown in Fig. 7.10. Also shown are the shapes of the expected backgrounds, which are in good agreement with the data. A maximum likelihood fit to the data is performed[2] to obtain the 90% C.L. limits, as shown in Fig. 7.2. The LSND oscillation region with $\Delta m^2 > 10$ eV^2 is ruled-out by the KARMEN data; however, the regions < 2 eV^2 and around 7 eV^2 are compatible with the LSND oscillation evidence.

7.4. Joint Analysis of LSND and KARMEN Data

A joint analysis of the LSND and KARMEN experiments has been performed[3] that is based on a frequentist approach following the suggestions of Reference 12. For both experiments, the data are analyzed with a maximum likelihood analysis followed by the extraction of confidence levels in a unified approach. The two experiments are found to be incompatible at a level of combined confidence of 36%. For the cases of statistical compatibility, Fig. 7.11 shows the combined LSND and KARMEN log-likelihood function in terms of $\sin^2 2\theta$ and Δm^2. The maximum log-likelihood function occurs at $\sin^2 2\theta = 1$ and $\Delta m^2 = 0.05$ eV^2, which is 21.5 units of log-likelihood above the no oscillation hypothesis. Figure 7.12 shows the confidence regions of the oscillation parameters for the combined likelihood analysis, assuming statistical compatibility of LSND and KARMEN. By combining the two experiments, the solutions with $\Delta m^2 > 10$ eV^2 are excluded, and there remain essentially two solutions: one with $\Delta m^2 < 1$ eV^2 and the other with $\Delta m^2 \sim 7$ eV^2.

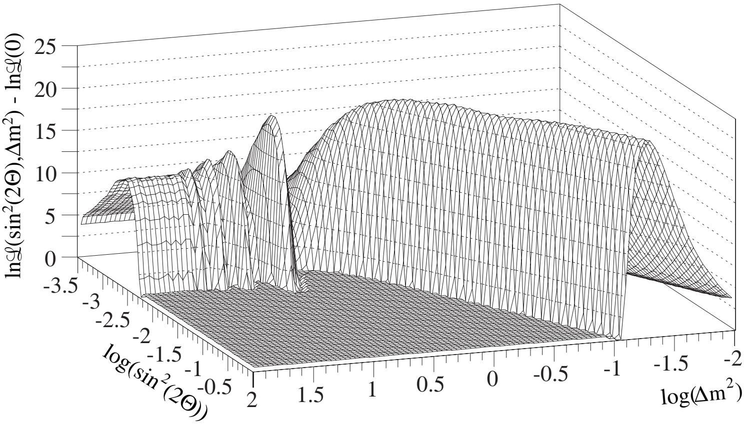

Fig. 7.11. The combined LSND and KARMEN log-likelihood function in terms of $\sin^2 2\theta$ and Δm^2. Reproduced from Reference 3.

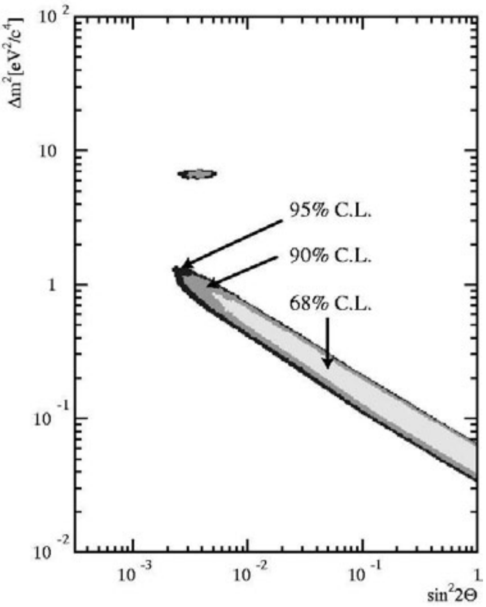

Fig. 7.12. The confidence regions of the oscillation parameters for the combined likelihood analysis, assuming statistical compatibility of LSND and KARMEN. Reproduced from Reference 3.

7.5. Conclusions

The LSND experiment has observed evidence for $\bar{\nu}_\mu \rightarrow \bar{\nu}_e$ oscillations in the $\Delta m^2 > 0.2$ eV^2 region, while a joint analysis of the LSND and KARMEN experiments reveals compatible neutrino oscillation regions in a band from 0.2 to 1 eV^2 and in a region around 7 eV^2. The confirmation of ν oscillations in this Δm^2 region would have a huge impact on astrophysics, as well as particle and nuclear physics. The MiniBooNE experiment at Fermilab[13] is designed to provide a definitive test of the LSND evidence for neutrino oscillations and is reported in the next section.

Acknowledgments

This work was made possible by the dedicated efforts of the LSND and KARMEN collaborations.

References

1. A. Aguilar *et al.*, *Phys. Rev.* **D64**, 112007, (2001).
2. B. Armbruster *et al.*, *Phys. Rev.* **D65**, 112001, (2002).
3. E. D. Church, K. Eitel, G. B. Mills, and M. Steidl, *Phys. Rev.***D66**, 013001, (2002).
4. C. Athanassopoulos *et al.*, *Nucl. Instrum. Methods* **A388**, 149, (1997).
5. R. L. Burman, M. E. Potter, and E. S. Smith, *Nucl. Instrum. Methods* **A291**, 621, (1990); R. L. Burman, A. C. Dodd, and P. Plischke, *Nucl. Instrum. Methods in Phys. Research* **A368**, 416, (1996).
6. R. A. Reeder *et. al.* , *Nucl. Instrum. Methods* **A334**, 353, (1993).
7. J. J. Napolitano *et. al.* , *Nucl. Instrum. Methods* **A274**, 152, (1989).
8. This background also includes contributions from $\bar{\nu}_\mu C \rightarrow \mu^+ nX$ and $\nu_\mu C \rightarrow \mu^- nX$.
9. C. Athanassopoulos *et al.*, *Phys. Rev.* **C 54**, 2685, (1996); C. Athanassopoulos *et al.*, *Phys. Rev. Lett.* **77**, 3082, (1996).
10. B. Achkar *et al.*, *Nucl. Phys.* **B434**, 503, (1995).
11. G. Drexlin *et al.*, *Nucl. Instrum. Methods* **A289**, 490, (1990).
12. G. J. Feldman and R. D. Cousins, *Phys. Rev.* **D57**, 3873, (1998).
13. E. Church *et al.*, “A proposal for an experiment to measure $\nu_\mu \rightarrow \nu_e$ oscillations and ν_μ disappearance at the Fermilab Booster: BooNE”, LA-UR-98-352, Fermilab experiment 898, A. O. Bazarko, *Nucl. Phys. (Proc. Suppl.)*, **B91** 210, (2001).

Chapter 8

MiniBooNE

Steve J. Brice
Fermi National Accelerator Laboratory,
Kirk and Pine Streets, Batavia, IL 60510-500, USA
sbrice@fnal.gov

MiniBooNE, the Mini Booster Neutrino Experiment, was built to test the evidence of neutrino oscillations from the LSND experiment. It did this by searching for ν_e appearance in a ν_μ beam with a neutrino baseline and energy roughly 10 times those of LSND. This makes MiniBooNE sensitive to similar regions of oscillation phase space as LSND, but with very different systematic uncertainties. With two largely independent analyses, MiniBooNE observed no significant excess of ν_e events above background for reconstructed neutrino energies above 475 MeV. The data are consistent with no oscillations within a two neutrino appearance-only oscillation model.

Contents

8.1 Introduction 155
8.2 The Experiment 156
8.3 The Monte Carlo Simulation and Predicted Event Rates 158
8.4 The Neutrino Cuts 159
8.5 The Electron Neutrino Candidate Cuts 159
8.6 The Predicted Backgrounds 162
8.7 Using MiniBooNE Data to Constrain the Simulation 163
8.8 Systematic Error Handling 164
8.9 Results 164
8.10 Conclusion 166
8.11 Future Plans 169
References 170

8.1. Introduction

MiniBooNE was motivated by the result from the Liquid Scintillator Neutrino Detector (LSND) experiment[1] in the mid 1990's, which presented evidence for $\bar{\nu}_\mu \to \bar{\nu}_e$ oscillations at the $\Delta m^2 \sim 1$ eV^2 scale, as detailed in the previous chapter. The 3.8σ excess of electron anti-neutrino candidates seen by LSND would correspond to a $\bar{\nu}_\mu \to \bar{\nu}_e$ oscillation probability of $0.26 \pm 0.08\%$. While the KARMEN experiment observed no evidence for neutrino oscillations,[2] a joint analysis[3] showed compatibility at 64% CL. Solar-neutrino[4–8] and reactor-antineutrino experiments[9] have convincing evidence for neutrino oscillations, but at two very different Δm^2 scales to that indicated by the LSND result. This necessitates the introduction of one or more new neutrino states (which must be sterile[16]) or other extensions to the Standard Model.

MiniBooNE was built with a baseline and a neutrino energy spectrum roughly 10 times that of LSND. This enabled the experiment to be sensitive to roughly the same oscillation phase space, because L/E was the same as that of LSND, but to have very different systematics, as the neutrino energy was much higher.

8.2. The Experiment

MiniBooNE has been taking data since 2002. The experiment runs the 8 GeV protons from the Fermilab Booster into a 71-cm-long Beryllium target. The proton beam typically has 4×10^{12} protons per ~ 1.6 μs beam spill at a rate of 4 Hz. The number of protons on target per spill is measured by two toroids in the beam line. The target is located inside a focusing horn, which produces a toroidal magnetic field that is pulsed in time with the beam at a peak current of 174 kA. Positively charged pions and kaons, focused by the horn, pass through a 60-cm-diameter collimator and can decay in a 50-m-long tunnel filled with air at atmospheric pressure. A schematic of the experiment is shown in Fig. 8.1.

To ensure stable, well-targeted beam at full horn current, it is required that the two monitoring toroids agree to within 5%, the estimated transverse containment of the beam in the target be greater than 95%, and the measured horn current be within 3% of its nominal value. The event time at the detector must be consistent with the beam delivery time (both determined by GPS), and the event must pass a number of data integrity checks. The beam quality requirements reject 0.7% of the events, while the detector time and quality requirements remove a further 1.8%, with the remaining data corresponding to $(5.58 \pm 0.12) \times 10^{20}$ protons on target.

The center of the detector is 541 m from the front of the beryllium target and 1.9 m above the center of the neutrino beam. The detector, which is a

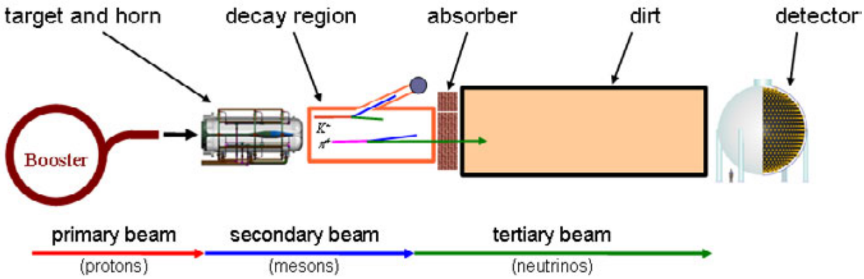

Fig. 8.1. Schematic of the MiniBooNE experiment, not to scale. 8 GeV protons from the booster hit a Beryllium target and the resulting mesons are focused by a magnetic horn and allowed to decay in a 50 m long air filled region. The beam then passes through about 541 m of dirt before reaching the MiniBooNE detector as a pure neutrino beam.

spherical tank of inner radius 610 cm filled with 800 tons of pure mineral oil (CH_2), is covered with a 3m dirt over-burden. Neutrino interactions in the oil produce charged particles which emit both directional Cherenkov light and isotropic scintillation light. The detector is separated into two regions by an optical barrier, the inner volume has a radius of 575 cm and the outer volume is 35 cm thick. The optical barrier supports 1280 equally-spaced, inward-facing, 8-inch photomultiplier tubes (PMTs), providing 10% photocathode coverage. An additional 240 tubes are mounted in the outer volume, which acts as a veto shield, detecting particles entering or leaving the detector. Approximately 98% of the PMTs worked well throughout the data taking period.

The experiment triggers on every beam spill, with all PMT hits recorded for a 19.2 μs window beginning 4.4 μs before the spill. The longer recording period after the spill is designed to maximize the chance of catching the electron that results from the 2.2 μs decay of the muon. Other triggers include a random trigger for beam-unrelated measurements, a laser-calibration trigger, cosmic-muon triggers, and a trigger to record neutrino-induced events from the nearby NuMI beam line[18]. PMT hit thresholds are ~ 0.1 photoelectrons (PE); the single-PE time resolutions achieved by this system are ~ 1.7 ns and ~ 1.2 ns for the two types of PMTs present in the array. Optical fibers are run from a laser to a dispersion flask inside the tank and provide light flashes at a continuous 3.33 Hz to determine PMT gains and time offsets. A muon hodoscope above the tank enables cosmic muons to be accurately tracked into the detector. These muons are used to calibrate and check reconstruction algorithms.

8.3. The Monte Carlo Simulation and Predicted Event Rates

Detailed Monte Carlo simulations of the beam and detector are used to estimate the flux and the detector efficiencies. The Booster neutrino beam flux at the detector is modeled using a GEANT4-based simulation[20] of the beam line geometry. The flux prediction makes use of inputs both external and internal to MiniBooNE. The most important external input is meson production data for proton-beryllium hadronic interactions for proton beam momenta in the $\sim 10\,\mathrm{GeV/c}$ range, as the neutrino flux arises from secondary meson production. Pion and kaon production in the target is parametrized[21] based on a global fit to proton-beryllium particle production data.[22] The kaon flux has been cross-checked with high-energy events above 1250 MeV. These high energy events have a large contribution from neutrinos originating from kaon decay. In addition, an off-axis muon spectrometer was used that viewed the secondary beam line from an angle of 7°. The muons produced at these large angles tend to come from kaon decays. The kaon production rate inferred from this spectrometer data is consistent with the predictions of the beam simulation. The ν_μ energy spectrum peaks at 700 MeV and extends to approximately 3000 MeV.

Neutrino interaction cross sections and event kinematics are simulated using the NUANCE Monte Carlo event generator.[23] NUANCE simulates the possible neutrino processes including quasi-elastic scattering, resonant production, coherent single pion production, and deep inelastic scattering. Several modifications were made to NUANCE based on fits to MiniBooNE ν_μ data.[24] These included the adjustment of the axial form factor of the nucleon for quasi-elastic scattering, the Pauli blocking model and coherent pion production cross sections. In addition, some of the final state interaction model processes were also tuned to reproduce external data.

Outgoing particles from neutrino interactions in the detector are simulated using a GEANT3-based simulation.[28] The simulation includes subsequent interactions and decays of the particles. The optical and near-UV photons from Cherenkov radiation and scintillation by the particles are simulated and individually tracked, including scattering, fluorescence, and reflections. This optical model has been tuned to match small-sample measurements of transmission, fluorescence, and scattering. Muon decay electrons are used to calibrate both the light propagation in the detector and the energy scale. The amount of scintillation light is constrained from neutral current elastic scattering events where the outgoing particles produce little or no Cherenkov light. The charge and time response of the electronics is simulated, and from this point onward, data and MC are treated identically by the analysis programs.

Integrated over the neutrino flux, interactions in MiniBooNE are mostly charged-current quasi-elastic (CCQE) scattering (39%), neutral-current (NC) elastic scattering (16%), charged-current (CC) single pion production (29%), and NC single pion production (12%). Multi-pion and deep-inelastic scattering contributions are $< 5\%$.

8.4. The Neutrino Cuts

PMT charge and time information in the 19.2 μs trigger window are used to reconstruct neutrino interactions and identify the product particles. This time window is defined as an "event" and is divided into "sub-events," collections of PMT hits clustered in time within ~ 100 ns. A ν_μ CCQE event with a muon stopping within the tank may have two sub-events: the first sub-event from particles produced at the neutrino interaction, the second from the muon decay to an electron. A ν_e CCQE event has a single sub-event.

With four simple cuts an extremely pure sample of neutrino events can be obtained from the MiniBooNE data with good efficiency. Events with exactly one sub-event (as expected for ν_e CCQE events) are selected. By requiring that the sub-event has fewer than 6 hits in the veto and more than 200 hits in the main tank (above the muon-decay electron endpoint), entering cosmic-ray muons and their associated decay electrons are eliminated. The average time of hits in the sub-event is required to be within the beam time window of 4–7 μs. These cuts yield a cosmic ray rejection of greater than 1000:1.

8.5. The Electron Neutrino Candidate Cuts

The neutrino cuts of Sec. 8.4 yield a dataset of pure neutrino interactions removing essentially all non-neutrino backgrounds. It remains to reduce this dataset down to one as pure in electron neutrino interactions as possible. In coarse terms the task amounts to distinguishing ν_e induced electrons from muons and π^0s from CCQE and NCπ^0 ν_μ interactions respectively. Muons have long straight tracks in MiniBooNE and the resulting Cherenkov ring has a crisp outer edge and an interior filled in by the muon travel distance. Electrons shower and have shorter tracks with Cherenkov rings that are fuzzy. A π^0 will have two electron-like rings from the two decay γs (see

Table 8.1. The observed number of ν_e CCQE candidate events and the efficiency for $\nu_\mu \to \nu_e$ CCQE oscillation events after each cut is applied sequentially.

Selection	#Events	ν_e CCQE Efficiency
Cosmic Ray Cuts	109,590	100%
Fiducial Volume Cuts	68,143	$55.2 \pm 1.9\%$
PID Cuts	2037	$30.6 \pm 1.4\%$
$475 < E_\nu^{QE} < 1250$ MeV	380	$20.3 \pm 0.9\%$

Fig. 8.2). To effect this separation the events surviving the neutrino cuts are reconstructed under four hypotheses: a single electron-like Cherenkov ring, a single muon-like ring, two photon-like rings with unconstrained kinematics, and two photon-like rings with $M_{\gamma\gamma} = m_{\pi^0}$. The reconstruction uses a detailed model of extended-track light production and propagation in the tank to predict the charge and time of hits on each PMT. Event parameters are varied to maximize the likelihood of the observed hits, yielding the vertex position and time of the event and the direction, energy, and, for photons, the conversion distance of the ring(s). For ν_e events, the event vertex, direction, and energy are reconstructed on average with resolutions of 22 cm, 2.8°, and 11%, respectively, while NC π^0 events are reconstructed with a π^0 mass resolution of 20 MeV/c^2.

The final analysis cuts are designed to isolate a sample of ν_e-induced events that are primarily CCQE. It is required that the electron-hypothesis event vertex and muon-hypothesis track endpoint occur at radii < 500 cm and < 488 cm, respectively, to ensure good event reconstruction and efficiency for possible muon decay electrons. The visible energy has a cut $E_{vis} > 140$ MeV. Particle identification (PID) cuts are then applied to reject muon and π^0 events. These are E_{vis}-dependent cuts on $\log(L_e/L_\mu)$, $\log(L_e/L_{\pi^0})$, and $M_{\gamma\gamma}$, where L_e, L_μ, and L_{π^0} are the likelihoods for each event maximized under the electron 1-ring, muon 1-ring, and fixed-mass 2-ring fits, and $M_{\gamma\gamma}$ is from the unconstrained two-ring fit. These also enhance the fraction of CCQE events among the surviving electron candidates. Table 8.1 shows the observed number of ν_e CCQE candidate events and the efficiency for $\nu_\mu \to \nu_e$ CCQE oscillation events after each cut is applied sequentially. A total of 380 data events remains after the complete selection.

MiniBooNE also developed a second set of cuts that used a different set of reconstruction programs, PID algorithms, and fitting and normaliza-

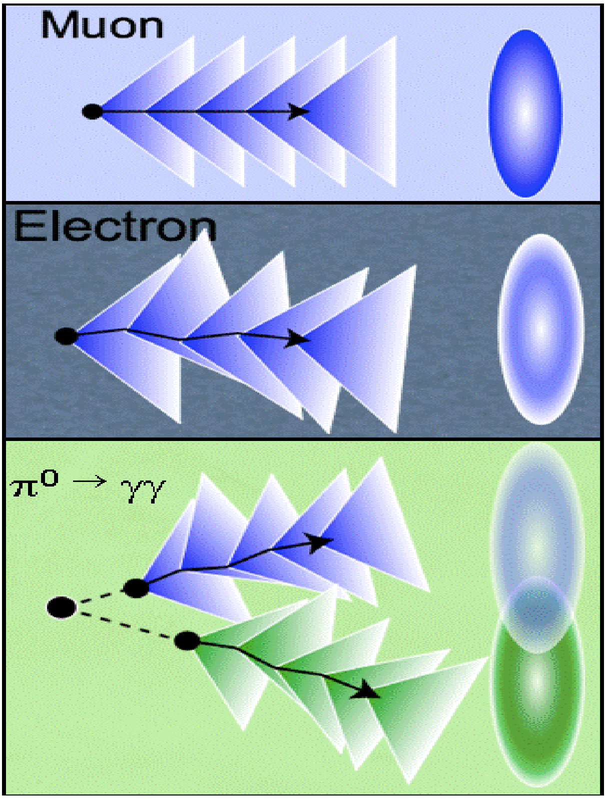

Fig. 8.2. In coarse terms the task of particle ID in MiniBooNE amounts to separating the clean, filled in Cherenkov rings from muons (top) from the fuzzy rings of electrons (middle) from the pair of fuzzy rings of a π^0 event (bottom).

tion processes. The reconstruction used a simpler model of light emission and propagation. The PID used 172 quantities such as charge and time likelihoods in angular bins, $M_{\gamma\gamma}$, and likelihood ratios (electron/pion and electron/muon) as inputs to a boosted decision tree algorithm[33] that is trained on sets of simulated signal events and background events with a cascade-training technique.[34] The two analyses are very complementary, with the second having a better signal-to-background ratio as the boosted decision tree squeezed out more PID information from the events, but the first having less sensitivity to systematic errors from detector properties as the extra information obtained by the boosted decision tree came with larger systematic uncertainties. These different strengths resulted in very

Table 8.2. The estimated number of events with systematic error in the $475 < E_\nu^{QE} < 1250$ MeV energy range from all of the significant backgrounds, together with the estimated number of signal events for 0.26% $\nu_\mu \rightarrow \nu_e$ transmutation, after the complete event selection.

Process	Number of Events
ν_μ CCQE	10 ± 2
$\nu_\mu e \rightarrow \nu_\mu e$	7 ± 2
Miscellaneous ν_μ Events	13 ± 5
NC π^0	62 ± 10
NC $\Delta \rightarrow N\gamma$	20 ± 4
NC Coherent & Radiative γ	< 1
Dirt Events	17 ± 3
ν_e from μ Decay	132 ± 10
ν_e from K^+ Decay	71 ± 26
ν_e from K_L^0 Decay	23 ± 7
ν_e from π Decay	3 ± 1
Total Background	358 ± 35
0.26% $\nu_\mu \rightarrow \nu_e$	163 ± 21

similar oscillation sensitivities and, when unblinded, yielded the expected overlap of events and very similar oscillation fit results. Based on the predicted sensitivities before the data was unblinded, the first analysis was chosen for the oscillation result, with the second serving as a powerful cross-check.

8.6. The Predicted Backgrounds

Table 8.2 shows the estimated number of events with reconstructed neutrino energy, E_ν^{QE}, between 475 MeV and 1250 MeV after the complete event selection from all of the significant backgrounds, where E_ν^{QE} is determined from the reconstructed lepton energy and angle with respect to the known neutrino direction. The background estimate includes antineutrino events, which represent $< 2\%$ of the total. Also shown is the estimated number of ν_e CCQE signal events for the LSND central expectation of 0.26% $\nu_\mu \rightarrow \nu_e$ transmutation. The small fraction of ν_e from μ, K, and π decay in the beamline gives a background that is indistinguishable from oscillations except for the energy spectrum. CC ν_μ events are distinguished from ν_e events by the distinct patterns of Cherenkov and scintillation light for muons and electrons, as well as by the observation of a delayed electron from the muon decay, which is observed $> 80\%$ of the time from ν_μ CCQE events. NC π^0 events with only a single electromagnetic shower reconstructed are the main ν_μ-induced background, followed by radiative Δ decays giving a single photon, and then neutrino interactions in the dirt surrounding the detector, which can mimic a signal if a single photon, mostly from π^0 decay, penetrates the veto and converts in the fiducial volume.

8.7. Using MiniBooNE Data to Constrain the Simulation

Measurements outside the signal region are used to constrain all of the major ν_μ-induced backgrounds. The inclusive CC background is verified by comparing data to MC for events with two sub-events, where the second sub-event has < 200 tank hits and is consistent with a muon-decay electron. As the probability for μ^- capture in the oil is 8%, there is an order of magnitude more CC inclusive scattering events with two subevents than with only one subevent, so that this background is well checked. These data events are also modified by moving the hits of the second subevent earlier in time to model early, inseparable decays which can look more like an electron.

To determine the NC π^0 background, π^0 rates are measured in bins of momentum by counting events in the $\gamma\gamma$ mass peak. The MC simulation is used to correct the production rate for inefficiency, background and resolution (corrections are $\sim 10\%$). To match the data angular distribution, the π^0 candidates are fit to MC templates (in mass and angle) for resonant and coherent production (generated using the model of Rein and Sehgal[27]) as well as a template for non-π^0 background events. The fitted parameters are used to reweight π^0 from the MC, and to constrain the $\Delta \rightarrow N\gamma$ rate, which has a branching ratio at the peak of the Δ resonance of 0.56%. The π^0 measurement is particularly powerful as it avoids the sizeable uncertainties in the ν_μ flux and the NC π^0 cross-section. Instead the rate of NC π^0 interactions is measured and used to correct the Monte Carlo predicted rate with no need to split that rate into a flux times a cross-section. NC coherent γ background[30] and NC radiative γ background[31] are both estimated to be negligible. The background from interactions in the dirt surrounding the detector is measured from a sample of inward-pointing events inside the tank at high radius.

A sample of $\sim 10^5$ candidate ν_μ CCQE events is obtained by requiring a μ-decay electron with a reconstructed vertex consistent with the estimated endpoint of the parent muon's track (60% efficiency). The observed rate of these ν_μ CCQE events is used to correct the MC predictions for ν_e signal events, ν_μ CC backgrounds, and ν_e from μ backgrounds (which share their π parentage with the ν_μ CCQE events). These constraints increase the event normalization by 32% and greatly reduce the rate uncertainties on these three components of the final analysis sample.

8.8. Systematic Error Handling

The sources of systematic error in the measurement divide into three categories: uncertainties in the neutrino fluxes, uncertainties in the neutrino cross sections, and uncertainties in the modeling of the detector. Table 8.3 lists the individual sources of uncertainty within these three groups and describes how the errors were set. These groups of errors are taken to be independent, and, for each, an individual error matrix is formed that includes the full correlation among the systematic parameters. This is mapped to a matrix describing the correlated errors in predicted background plus possible signal in eight ν_e E_ν^{QE} bins. The final covariance matrix for all sources of uncertainty (statistical and systematic) is the sum of the individual error matrices. The signal extraction is performed by computing the χ^2 comparing data to predicted background plus a ($\sin^2(2\theta)$, Δm^2)-determined contribution from $\nu_\mu \to \nu_e$ two-neutrino oscillations in the eight E_ν^{QE} bins and minimizing with respect to these two oscillation parameters across their physical range.

8.9. Results

The analysis used a blind technique where the region around any signal ($\sim$5000 events) was kept blind with all other events (several 100,000) being fully open for study. The analysis involved a good deal of tuning of the simulation as well as very exacting requirements on the particle ID. The blind analysis technique enabled the simulation to be tuned without any risk of biasing the events passing the particle ID. Once the tuning and analysis cuts were frozen, a signal-blind test of data-MC agreement in the signal region was performed. The full two-neutrino oscillation fit was done in the range $300 < E_\nu^{QE} < 3000$ MeV and, with no information on the fit parameters revealed, the sum of predicted background and simulated best-fit signal was compared to data in several variables, returning only the χ^2. While agreement was good in most of the comparisons, the E_{vis} spectrum had a χ^2 probability of only 1%. This triggered further

Table 8.3. A summary of the low level quantities whose uncertainties were propagated to form the full systematic error of the analysis. The first column describes the category of systematic, the second column how many parameters are actually varied in each low level quantity. The third column give a brief description of the low level quantity, and the fourth column gives a quick indication of how the values and uncertainties on the low level quantities were set.

Category	# Pars	Description	How Uncertainty is Set
Neutrino Fluxes	8	3-momentum distribution of π^+ from the target	Fits to E910 and HARP data[21,22]
	8	3-momentum distribution of π^- from the target	Fits to π^- production data
	9	3-momentum distribution of K^0 from the target	Fits to K^0 production data
	7	3-momentum distribution of K^+ from the target	Fits to K^+ production data
	1	Horn current	Variation in current measurement
	1	Skin depth model of current in horn inner conductor	Variation in horn parameters
	3	Nucleon cross-sections in the beam	Analysis of past nucleon data
	3	Pion cross-sections in the beam	Analysis of past pion data
Neutrino Cross-Sections	2	Binding energy and Fermi momentum in ^{12}C model	Electron scattering experiments
	7	CCQE neutrino cross-section	Fits to MiniBooNE ν_μ CCQE data
	7	non-CCQE neutrino cross-section	Previous neutrino experiments
	2	Cross-sections for $\pi^\pm$ on ^{12}C	Analysis of pion cross-section data
	9	Momentum dependent corrections to the π^0 rate	MiniBooNE π^0 measurement
	1	Rate of dirt events	Fits to MiniBooNE data samples
Detector Model	40	Optical model of light in MiniBooNE	Calibration & oil measurements
	2	Variations in the MiniBooNE electronics response	Calibrations of the electronics

investigation of the backgrounds, focusing on the lowest energies where ν_μ-induced backgrounds, some of which are difficult to model, are large. As part of this study, one more piece of information from the signal region was released: unsigned bin-by-bin fractional discrepancies in the E_{vis} spectrum. While ambiguous, these reinforced suspicions about the low-energy region. Though no specific problems with the background estimates were known, it was found that raising the minimum E_ν^{QE} of the fit region to 475 MeV greatly reduced a number of backgrounds with little impact on the fit's sensitivity to oscillations. Thus the oscillation fits were performed in the energy range $475 < E_\nu^{QE} < 3000$ MeV.

Candidate ν_e events are shown in the top plot of Fig. 8.3 as a function of E_ν^{QE}. The vertical dashed line indicates the minimum E_ν^{QE} used in the two-neutrino oscillation analysis. There is no significant excess of events ($22 \pm 19 \pm 35$ events) for $475 < E_\nu^{QE} < 1250$ MeV; however, an excess of events ($96 \pm 17 \pm 20$ events) is observed below 475 MeV. This low-energy excess cannot be explained by a two-neutrino oscillation model, and its source is under investigation. The dashed histogram in Fig. 8.3 shows the predicted spectrum when the best-fit two-neutrino oscillation signal is added to the predicted background. The bottom panel of the figure shows background-subtracted data with the best-fit two-neutrino oscillation and two oscillation points from the favored LSND region. The oscillation fit in the $475 < E_\nu^{QE} < 3000$ MeV energy range yields a χ^2 probability of 93% for the null hypothesis, and a probability of 99% for the ($\sin^2 2\theta = 10^{-3}$, $\Delta m^2 = 4$ eV^2) best-fit point.

With no evidence for a signal in the energy range $475 < E_\nu^{QE} < 3000$ MeV, a single-sided raster scan to a two neutrino appearance-only oscillation model is used to find the 90% CL limit corresponding to $\Delta\chi^2 = \chi^2_{limit} - \chi^2_{bestfit} = 1.64$. The top plot in Fig. 8.4 shows that the LSND 90% CL allowed region is excluded at the 90% CL. A joint analysis as a function of Δm^2, using a combined χ^2 of the best fit values and errors for LSND and MiniBooNE, excludes at 98% CL two-neutrino appearance oscillations as an explanation of the LSND anomaly. The bottom plot of Fig. 8.4 shows limits from the KARMEN[2] and Bugey[32] experiments.

8.10. Conclusion

In summary, while there is a presently unexplained discrepancy with data lying above background at low energy, there is excellent agreement between data and prediction in the oscillation analysis region. If the oscillations

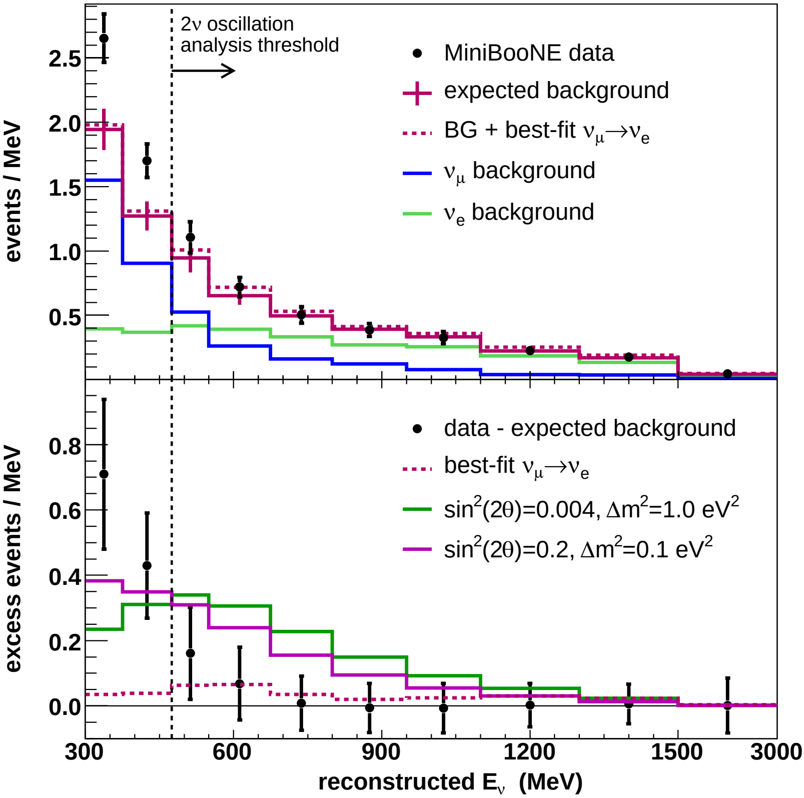

Fig. 8.3. The top plot shows the number of candidate ν_e events as a function of E_ν^{QE}. The points represent the data with statistical errors, while the histogram is the expected background with systematic errors from all sources. The vertical dashed line indicates the threshold used in the two-neutrino oscillation analysis. Also shown are the best-fit oscillation spectrum (dashed histogram) and the background contributions from ν_μ and ν_e events. The bottom plot shows the number of events with the predicted background subtracted as a function of E_ν^{QE}, where the points represent the data with total errors and the two histograms correspond to LSND solutions at high and low Δm^2. Reproduced from Reference 35.

of neutrinos and antineutrinos are the same, the first MiniBooNE result excludes two neutrino appearance-only oscillations as an explanation of the LSND anomaly at 98% CL.

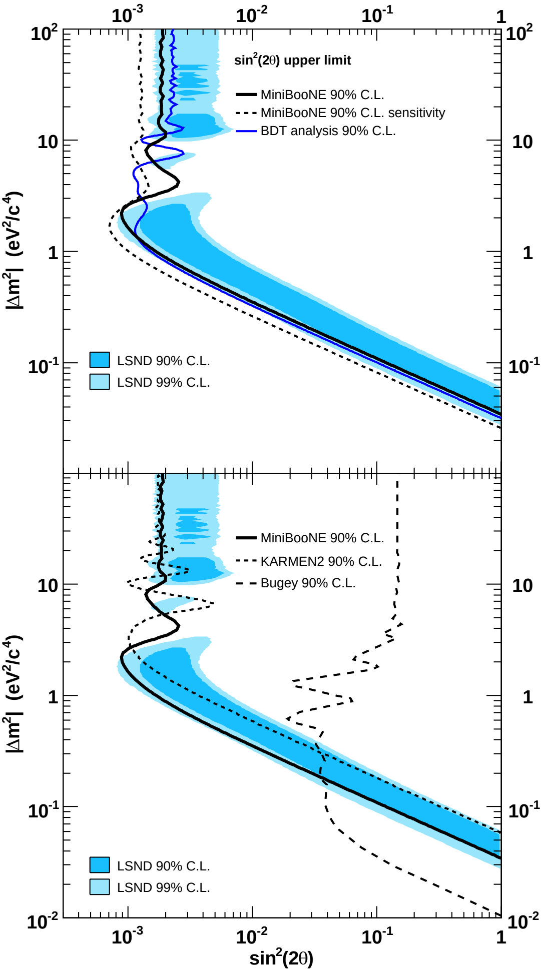

Fig. 8.4. The top plot shows the MiniBooNE 90% CL limit (thick solid curve) and sensitivity (dashed curve) for events with $475 < E_\nu^{QE} < 3000$ MeV within a two neutrino oscillation model. Also shown is the limit from the boosted decision tree analysis (thin solid curve) for events with $300 < E_\nu^{QE} < 3000$ MeV. The bottom plot shows the limits from the KARMEN[2] and Bugey[32] experiments. The MiniBooNE and Bugey curves are 1-sided upper limits on $\sin^2 2\theta$ corresponding to $\Delta\chi^2 = 1.64$, while the KARMEN curve is a “unified approach” 2D contour. The shaded areas show the 90% and 99% CL allowed regions from the LSND experiment. Reproduced from Reference 35.

8.11. Future Plans

The ν_e appearance measurement was always MiniBooNE's main purpose, but such a large dataset of neutrino interactions (far larger than any previous experiment at these energies) enables several other important measurements to also be made. MiniBooNE is currently working on detailed studies of the ν_μ CCQE and Neutral Current π^0 cross-sections. Better understanding of these processes will lead to reduced cross-section systematic errors in future oscillation searches. The collaboration also plans publications on the Neutral Current elastic scattering process and the Charged Current π^+ and π^0 production channels. With about 200,000 ν_μ CCQE events passing the cuts, the MiniBooNE collaboration also plans to conduct a search for ν_μ disappearance. This is a tricky measurement without a near detector, but the investment that the collaboration has made in a precise understanding of the beam, cross-section, and detector systematics should enable a sensitive result.

The data for the ν_e appearance analysis presented here was taken between 2002 and late 2005. In January 2006 the horn polarity was switched and, since that time, the beam line has been running in anti-neutrino mode. At the time of writing about 1.7×10^{20} protons on target have been delivered in this mode (to be compared with the 5.7×10^{20} pot delivered and passing quality cuts in neutrino mode). This anti-neutrino dataset is being analyzed with a view to measuring a series of anti-neutrino cross-sections and to performing both a $\overline{\nu}_\mu$ disappearance measurement and a $\overline{\nu}_e$ appearance search. This latter is particularly interesting as the LSND measurement was of $\overline{\nu}_e$. It is possible there may be CP violation in the lepton sector, in which case the oscillations of ν_μ into ν_e may not be the same as those of $\overline{\nu}_\mu$ into $\overline{\nu}_e$. To make a $\overline{\nu}_e$ appearance measurement that is sensitive to the LSND region of oscillation parameter space will probably need several times the anti-neutrino running than has been currently accumulated as the rate of interactions is about 4 times lower than in neutrino mode, but the collaboration is considering this possibility.

Acknowledgments

MiniBooNE was supported by Fermilab, the Department of Energy, and the National Science Foundation as well as by LDRD funding from Los Alamos National Laboratory.

References

1. C. Athanassopoulos *et al.*, Phys. Rev. Lett. 75, 2650 (1995); C. Athanassopoulos *et al.*, Phys. Rev. Lett. 77, 3082 (1996); C. Athanassopoulos *et al.*, Phys. Rev. Lett. 81, 1774 (1998); A. Aguilar *et al.*, Phys. Rev. D 64, 112007 (2001).
2. B. Armbruster *et al.*, Phys. Rev. D 65, 112001 (2002).
3. E. Church *et al.*, Phys. Rev. D 66, 013001 (2002).
4. B. T. Cleveland *et al.*, Astrophys. J. 496, 505 (1998).
5. J. N. Abdurashitov *et al.*, Phys. Rev. C 60, 055801 (1999).
6. W. Hampel *et al.*, Phys. Lett. B 447, 127 (1999).
7. S. Fukuda *et al.*, Phys. Lett. B 539, 179 (2002).
8. Q. R. Ahmad *et al.*, Phys. Rev. Lett. 87, 071301 (2001); Q. R. Ahmad *et al.*, Phys. Rev. Lett. 89, 011301 (2002); S. N. Ahmed *et al.*, Phys. Rev. Lett. 92, 181301 (2004).
9. K. Eguchi *et al.*, Phys. Rev. Lett. 90, 021802 (2003); T. Araki *et al.*, Phys. Rev. Lett. 94, 081801 (2005).
10. K. S. Hirata *et al.*, Phys. Lett. B 280, 146 (1992); Y. Fukuda *et al.*, Phys. Lett. B 335, 237 (1994).
11. Y. Fukuda *et al.*, Phys. Rev. Lett. 81, 1562 (1998).
12. W. W. M. Allison *et al.*, Phys. Lett. B 449, 137 (1999).
13. M. Ambrosio *et al.*, Phys. Lett. B 517, 59 (2001).
14. M. H. Ahn *et al.*, Phys. Rev. Lett. 90, 041801 (2003).
15. D. G. Michael *et al.*, Phys. Rev. Lett. 97, 191801 (2006).
16. M. Sorel, J. M. Conrad, and M. H. Shaevitz, Phys. Rev. D 70, 073004 (2004).
17. T. Katori, A. Kostelecky and R. Tayloe, Phys. Rev. D 74, 105009 (2006).
18. S. Kopp, Phys. Rept. 439, 101 (2007).
19. C. Athanassopoulos *et al.*, Nucl. Instrum. Meth. A388, 149 (1997).
20. S. Agostinelli *et al.*, Nucl. Instrum. Meth. A506, 250 (2003).
21. J. R. Sanford and C. L. Wang, Brookhaven National Laboratory, AGS internal reports 11299 and 11479 (1967) (unpublished).
22. M. G. Catanesi *et al.* [HARP Collaboration], arXiv:hep-ex/0702024; T. Abbott *et al.*, Phys. Rev. D45, 3906 (1992); J. V. Allaby *et al.*, CERN 70-12 (1970); D. Dekkers *et al.*, Phys. Rev. 137, B962 (1965); G. J. Marmer *et al.*, Phys. Rev. 179, 1294 (1969); T. Eichten *et al.*, Nucl. Phys. B44, 333 (1972); Aleshin *et al.*, ITEP-77-80 (1977); Vorontsov *et al.*, ITEP-88-11 (1988).
23. D. Casper, Nucl. Phys. Proc. Suppl. 112, 161 (2002).
24. A. Aguilar-Arevalo *et al.*, in preparation.
25. D. Ashery *et al.*, Phys. Rev. C 23, 2173 (1981).
26. H. Ejiri, Phys. Rev. C 48, 1442 (1993); F. Ajzenberg-Selove, Nucl. Phys. A506, 1 (1990); G. Garvey private communication.
27. D. Rein and L. M. Sehgal, Annals Phys. 133, 79 (1981).
28. CERN Program Library Long Writeup W5013 (1993).
29. B. C. Brown *et al.*, IEEE Nuclear Science Symposium Conference Record 1, 652 (2004).
30. D. Rein and L. M. Sehgal, Phys. Lett. B 104, 394 (1981).

31. T. Goldman, private communication.
32. Y. Declais *et al.*, Nucl. Phys. B434, 503 (1995).
33. B. P. Roe *et al.*, Nucl. Instrum. Meth. A543, 577 (2005); H. J. Yang, B. P. Roe, and J. Zhu, Nucl. Instrum. Meth. A555, 370 (2005); H. J. Yang, B. P. Roe, and J. Zhu, Nucl. Instrum. Meth. A574, 342 (2007).
34. Y. Liu and I. Stancu, arXiv:Physics/0611267 (to appear in Nucl. Instrum. Meth.).
35. A. A. Aguilar-Arevalo *et al.*, Phys. Rev. Lett. 98, 231801 (2007).

Chapter 9

The OPERA Experiment in the CNGS Beam

D. Autiero
IPN Lyon, UCBL/IN2P3/CNRS, 69622 Villeurbanne Cedex, France

M. Komatsu
Nagoya University, Nagoya 464-8602, Japan

P. Migliozzi
I.N.F.N., Sezione di Napoli, I-80126 Naples, Italy

F. Terranova
I.N.F.N., Laboratori Nazionali di Frascati,
Via E. Fermi, 40, I-00044 Frascati, Italy

The OPERA experiment is designed to investigate $\nu_\mu \rightarrow \nu_\tau$ oscillations in the atmospheric neutrino sector by searching directly for ν_τ appearance with the CNGS high energy neutrino beam. This challenging goal requires tracking capabilities with μm accuracy and sophisticated kinematic reconstruction, both implemented at the kton target mass scale. This is made possible by the modular concept of the Emulsion Cloud Chambers integrated in a hybrid detector. Given its good electron identification capabilities, OPERA can also look for sub-leading $\nu_\mu \leftrightarrow \nu_e$ oscillations. The construction of the experiment has required many years of R&D, test-beam measurements and large engineering efforts. OPERA will start the exposure to the CNGS beam of the ECC bricks composing its target during the fall 2007. The experiment is then foreseen to run for 5 years.

Contents

9.1 Introduction 174
9.2 The OPERA Detector 177
9.3 ECC Analysis 182

9.4 Physics Performance: $\nu_\mu \to \nu_\tau$ Search 187
9.5 Search for $\nu_\mu \leftrightarrow \nu_e$ Appearance 191
References 194

9.1. Introduction

The OPERA (Oscillation Project with Emulsion Tracking Apparatus) experiment aims at the direct observation of ν_τ appearance from $\nu_\mu \to \nu_\tau$ oscillations in the CNGS long-baseline beam from the CERN SPS to the Gran Sasso underground laboratory (LNGS)[1]. This observation would clarify unambiguously the nature of the oscillation mode in the atmospheric neutrino sector. OPERA can also search for the sub-leading $\nu_\mu \leftrightarrow \nu_e$ oscillation, which is governed by the still unknown θ_{13} parameter.

To be sensitive to the oscillation parameters indicated by the muon neutrino deficit in the Super-Kamiokande data ($\Delta m^2 = 1.9 - 3.1 \times 10^{-3}$ eV^2, 90% C.L., full mixing,[2] see Chapter 2) and confirmed by the K2K[3] (Chapter 5) and MINOS[4] (Chapter 6) experiments, the CNGS beam is characterized by a baseline of 730 km from the neutrino source to the LNGS laboratory, combined with an energy spectrum optimized for ν_τ appearance. This tuning was performed by matching the neutrino spectrum to the convolution of the ν_τ Charged Current (CC) cross-section with the $\nu_\mu \to \nu_\tau$ oscillation probability, to obtain the maximum number of ν_τ CC interactions at LNGS. The average CNGS ν_μ energy is about 17 GeV. CNGS is supposed to run for 5 years, delivering 4.5×10^{19} protons on target per year.

The past CERN generation of short-baseline neutrino oscillation experiments (CHORUS and NOMAD[5,6]), performed about 10 years ago on the WANF beam, developed the two distinct approaches to detecting ν_τ appearance via the ν_τ CC interaction followed by the tau decay. NOMAD developed the kinematical method, which exploits the missing transverse momentum due to the presence of neutrino(s) in the tau decay and its angular correlations, in the transverse plane, with the direction of the visible tau daughter particle(s) and the direction of the hadronic system resulting from the recoiling quarks. More generally, the 3D isolation of the visible decay daughters of the tau with respect to the hadronic system was exploited. This technique requires hermetic detectors with good energy and momentum resolution, and it has been pursued by the ICARUS[7] collaboration. The background comes mainly from mis-reconstructed neutrino interactions. The electronic decay channel of the tau is the one with best sensitivity since its main background is due to CC interactions of the ν_e originally present in the beam, which in a standard high energy neutrino beam (like WANF or CNGS) is about 100 times smaller than the ν_μ CC sample. The program concerning the ICARUS detector on the CNGS beam is limited to the first 600 tons prototype built in 2002. Its installation at LNGS should be completed by the end of 2007.

OPERA, like CHORUS, is instead based on the direct detection of the decay of the tau lepton produced by ν_τ CC interactions. Its decay topology is characterized by the "kink", a sharp deviation (>20 mrad) from the direction of the original tau lepton, typically occurring after a path of about 1 mm, due to its decay to charged particle + neutrino(s). The decay mode to 3 charged particles + neutrino relies on the reconstruction of the tau decay vertex. A major background to the topological detection comes from the decay of charmed particles, which are produced in ordinary ν_μ (ν_e) CC interactions and have similar decay topologies as the tau. The identification, with high efficiency, of the primary lepton from the neutrino interaction that also produces the charmed particle allows the suppression of this background. The reconstruction of the tau decay topology requires very high spatial resolution, which can be provided by a target of nuclear emulsion sheets. Nuclear emulsions have the unique tridimensional resolution which allows the direct observation of short-lived particle decays and the discrimination between decays and nuclear interactions. Past experiments, like CHORUS, were based on a hybrid set-up where nuclear emulsions were used as an active target. The analysis of nuclear emulsions was fully automated, but the final step of the analysis chain included validation by an experienced physicist who visually inspected the result obtained from the automatic scanning.

Both approaches for ν_τ identification require sophisticated detectors. At a long-baseline this search is even more challenging. Given the neutrino oscillation probability, the ν_τ CC interaction cross-section and the neutrino fluxes obtainable at large distances from the source, such a detector must combine the massive targets needed to obtain significant event rates with very accurate topological or kinematical event reconstruction. In the OPERA case this implies a massive (about 1.8 kton) neutrino target and μm resolution tracking to reconstruct the tau decay topology. It was unfeasible, given the cost, to build such a target just with nuclear emulsions. Another concept, the Emulsion Cloud Chamber (ECC) detector had to be adopted in order to achieve the needed target mass. The impressive scanning power achieved in the last decade together with the ECC technique made it possible to achieve the same discrimination between decays and nuclear interactions without the need for manual scanning; the idea consists of profiting from the intrinsic emulsion resolution to make a full kinematical reconstruction of the event and its topology and therefore achieve a very high signal to background ratio.

The ECC, exploited in the year 2000 by the DONUT collaboration for ν_τ detection in a beam-dump experiment,[9] combines the high-precision tracking capabilities of nuclear emulsions and the large target mass provided by lead or iron plates in a sandwich-like cell. More precisely, in OPERA, the basic ECC module (brick) is made up of 57 12.7×10.2 cm^2 emulsion films interleaved with 56 lead sheets (1 mm thickness). Each film is actually made up of two 42 μm emulsion layers separated by a 205 μm thick plastic base. The OPERA design is completely modular and allows for real-time analysis of neutrino interactions. The target is built up with 206,336 bricks (8.3 Kg each).

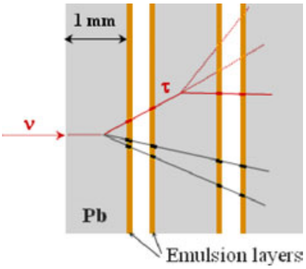

Fig. 9.1. Schematic view of a tau decay reconstructed in a ECC brick.

The brick is a complete standalone detector. It allows for neutrino vertex and tau decay topology reconstruction with μm accuracy, as shown in Fig. 9.1. It can also be considered a finely segmented electromagnetic calorimeter (its thickness is equivalent to 10 X_0), providing for electron and gamma identification and their energy reconstruction. The momentum of charged particles can be reconstructed by measuring their multiple scattering through the lead plates. Together with the calorimetric measurement of electromagnetic showers, the reconstruction of the kinematics of the interaction is achieved. These measurements are generally limited to the hit brick and the one immediately downstream. In addition, particle identification (muons, pions, protons) can be provided by measuring the specific ionization of tracks close to their stopping points. However, the brick is a passive detector which cannot provide a trigger for the neutrino interaction, and it is too small to contain muons. Therefore, the bricks have to be integrated in a hybrid detector design and the tasks related to triggering, tracking and event localization, muon identification and their charge and momentum measurement have to be performed by external electronic detectors.

The bricks are arranged in two target sections, each one instrumented with scintillator planes called "Target Trackers" (TT). The TT provide a trigger for neutrino interactions, localize the particular brick in which the neutrino interacted and perform initial muon tracking within the target. The brick localization is the first step for finding the event location within the emulsions. The electronic trackers provide predictions for the positions of the particle tracks in the vertex brick with a position resolution of the order of 1 cm and an angular accuracy (on the muon tracks) of about 20 mrad. Muon identification and charge measurement are needed for the study of the muonic tau decay channel and, in general, are fundamental handles for the suppression of the background coming from the decay of charmed particles, which are mostly produced via ν_μ CC interactions. The identification of the primary muon in these events with more than 95% efficiency, allows for the suppression of this background. For this purpose each target section is followed by a large, finely segmented muon spectrometer which, together with the TT, contributes to the muon identification by range and allows for muon momentum and charge measurement.

9.2. The OPERA Detector

OPERA has brought the technology of the hybrid ECC system to an unprecedented scale. The amount of nuclear emulsions produced for this experiment exceeds by forty times that of CHORUS, with an overall target mass of $\mathcal{O}(10^6)$ kg. Such a leap in scale poses several technological challenges. First, the ECC production and installation chain had to be fully automated. Second, engineering and mass production of the electronic detectors was required, since a surface of about 10,000 m^2 had to be instrumented. Finally, intense research and development was required to improve emulsion development and emulsion scanning to cope with the rate of neutrino interactions in the target. All of this involved the special development of scanning microscopes, the automation of brick production and handling, emulsion processing and chemical development chains. The solution adopted in the design of OPERA optimizes the ECC modularity to match the resolution of the electronic detectors and the surfaces that can be reasonably scanned by automatic microscopes, (see Sec. 9.3).

The thickness of the lead (1 mm) is a compromise between the need to sample as often as possible the path of the outgoing tau and the amount of emulsion that can be produced and scanned at a reasonable cost. The choice of lead as the target material follows similar constraints: at a fixed thickness, dense materials are highly desirable since larger target masses can be obtained with the same amount of emulsion. Among the various candidate materials (lead, iron, tungsten etc.), lead provides a reasonable compromise between density, cost per unit mass and ease of production and machining. Moreover, it has a rather small radiation length, which enhances momentum reconstruction from multiple scattering and electromagnetic (EM) shower containment (see Sec. 9.3).

A minimum ionizing particle crossing the film perpendicularly creates two short tracks ("micro-tracks") in the two emulsion layers. The presence of the plastic base is crucial to screen the background from α and β decays in lead. Still, the combinatorial background for the association of two micro-tracks highly depends on the lead radioactivity, especially β decays from ^{210}Po. OPERA makes use of commercial lead doped with Calcium, whose β activity does not exceed 30 Bq/kg. Each brick is made of the above-mentioned stack of lead and emulsion films, its container, and a doublet of emulsion films enclosed in a thin plastic box. This additional doublet "Changeable Sheet" (CS) is glued to the container and plays a crucial role in the scanning strategy of OPERA, as will be explained later.

Cloning this basic unit to reach a 1.8 kton size target has been a major engineering challenge. The bricks are produced underground at LNGS using five "piling" stations. These stations are located in a dark room and fed with emulsions and lead sheets by an automatic system. The piling stations build the emulsion-lead "pile" and fix it with a plastic and aluminum container just after the pile is produced. Later on, an anthropomorphic robot wraps an aluminum tape around the pile to guarantee light tightness. Finally, these bricks are moved outside the dark room by rollers and reach an assembly line where the CS is glued, the identifying number of the brick is printed and the brick itself is inserted into a large temporary container ("drum") that will be transported to the OPERA experimental area. This large automatic system is called the "Brick Assembly Machine" (BAM) and is currently operating. Completion of the brick production is expected in 2008.

OPERA is located in one of the three large experimental halls of Gran Sasso (Hall C). When the drums reach this area, they are positioned into a loading station, and another robot, the "Brick Manipulation System"

(BMS), puts the bricks into their final containers with a precision of about 1 mm. Such containers (“walls”) are made of thin stainless steel vertical bands welded to light horizontal trays and have been designed to minimize the amount of passive material in the target area. Each wall contains 3328 bricks and it is followed by two planes (one per view) of electronic detectors. The choice of segmented plastic scintillators as real time detectors has been mainly driven by the results obtained from the MINOS experiment.[8] The OPERA TT plastic scintillators are made of polystyrene bars doped with p-Terphenyl (2%) and POPOP (0.02%), co-extruded with a TiO_2 reflective coating. The visible light produced by the passage of charged particles through the bars is transported to photomultipliers by WLS fibers. Multianode PMT’s are located at both sides of a group of 64 bars. This detector option has several advantages. First of all, large surfaces of segmented plastic scintillators can be built at relatively low costs while retaining cm-scale granularities. In OPERA, each bar has a pitch of 2.6 cm and a thickness of 1 cm, but it extends up to 6.86 m. At least 6 photoelectrons per side of scintillator strip are collected after the passage of a minimum ionizing particle. Moreover, the TT provide an analog signal proportional to the energy deposited in the bar. This information can be exploited to trigger $\tau \rightarrow e$ or ν_e quasi-elastic events, where the only signature is the development of an EM shower in the brick up to the TT. Two-dimensional information is obtained by installing pairs of orthogonal scintillator planes. Each brick wall is followed by a TT doublet. 31 wall+TT planes constitute the OPERA instrumented target. In fact, the whole apparatus consists of two adjacent “Super-modules”, each made of an instrumented target (5900 m^2 of TT planes in total) followed by a large magnetic spectrometer, as shown in Fig. 9.2

As mentioned in Sec. 9.1, a magnetic spectrometer is used to measure the momentum and charge of penetrating tracks (mainly muons) and to estimate the energy of the hadronic component that punches through the target area. The OPERA magnets are made up of two large iron arms of rectangular cross section (8.7×8.2 m^2) separated by a 1.2 m gap. Two chambers of drift tubes, called “High precision trackers” (PT), have been installed in front of each arm and in the gap (six chambers per magnet) with the aim of measuring the horizontal deflection of charged particles in the magnetized iron. The arms are made up of twelve, 5 cm thick iron layers interleaved with planes of Bakelite Resistive Plate Chambers (RPC). They are connected through massive return yokes running above and below the arms. The two coils that magnetize the iron are wound along the

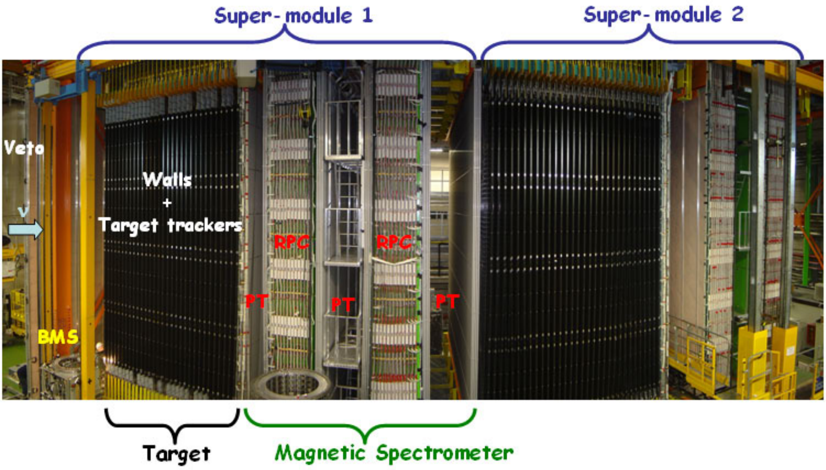

Fig. 9.2. Fish-eye view of the OPERA detector.

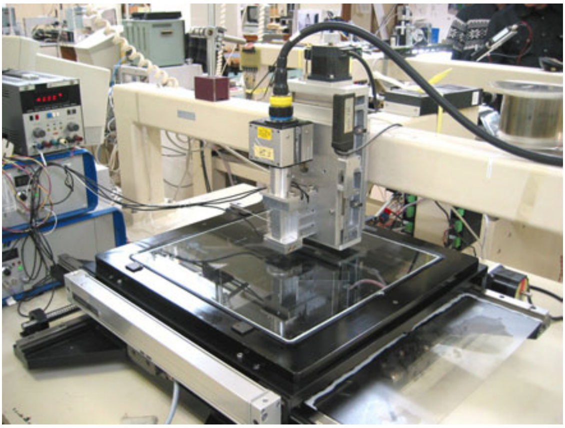

Fig. 9.3. Automated emulsion scanning system.

yokes. The advantage of this configuration is that the magnetic field along the arm is extremely uniform (variations along the height never exceed 5% with a mean value of 1.52 T) and always parallel to the vertical direction. Hence, 1-dimensional trackers can be exploited to determine the particle momentum. The only disadvantage with respect to the more traditional toroidal configuration is the presence of relatively large dead zones (return yokes), where the field is highly non-uniform. Their presence is immaterial in OPERA as far as the instrumented arms exceed the size of the target area and the geometrical acceptance for outgoing tracks. Momentum measurement in OPERA is dominated by Multiple Scattering (MS) in iron, the resolution of the tracker is negligible in the energy range of interest for the ν_τ appearance analysis. In fact, the PT have been designed to achieve a single-tube resolution of 300 μm. In this case, the momentum resolution in a single spectrometer is MS-dominated below 30 GeV ($\Delta p/p \sim 20\%$) and the charge reconstruction efficiency for muons crossing the whole spectrometer exceeds 99.5%. The OPERA PT are 8 m tall, 38 mm diameter cylindrical drift tubes and are assembled in stations made up of four staggered layers. At the time of writing, 10 out of 12 stations have been installed and commissioned at LNGS.

As already noted, the arms of the magnets are also instrumented with RPCs (1525 m^2 per magnet). Therefore, for stopping muons the spectrometers can measure the momentum from range with a resolution of about 30 MeV, and the RPCs also perform hadronic calorimetry. The RPCs are operated with an $\mathrm{Ar/C_2H_2F_4/i\text{-}C_4H_{10}/SF_6}$=75.4/20.0/4.0/0.6 gas mixture, and the signals are readout by horizontal and vertical strips of ~3 cm pitch. The same technology has been used for additional RPCs located in front of the first two chambers of the spectrometer whose strips are inclined by 45° with respect to the vertical axis to disentangle the left-right ambiguity of the drift tubes. Finally, glass RPCs have been installed in front of the first OPERA wall to veto incoming charged particles produced before the target area of the first super-module.

Trigger rates in OPERA are completely dominated by cosmic ray particles and are rather small since the minimum rock coverage in Hall C is 3200 $\mathrm{kg/cm^2}$ and the rate of cosmic muons is ~1 $\mathrm{muon/h/m^2}$. For this reason, the OPERA data acquisition system (DAQ) has been built as a standard Ethernet network whose nodes are Linux-based CPU's embedded in the front end boards which are self-triggering and take data asynchronously. A clock distribution system, connected with the LNGS GPS unit, sends a synchronization signal to all the DAQ nodes which can time-stamp the hits from the front-end electronics of the different sub-detectors with 10 ns relative accuracy. The signal from the TT constitutes the building block of the trigger and brick extraction strategy during the CNGS data taking. An interaction in one of the bricks produces outgoing charged tracks crossing one or more TT doublets. The corresponding scintillator hits are recorded. Offline, the hits are time ordered and an absolute UTC time is attributed to the event. The correlation with the CNGS beam spill is then performed, with an accuracy of about 100 ns, by combining the event time information from the OPERA raw data database with the UTC time of the SPS proton extractions, recorded in the CNGS database.

Selected data are post-processed by the offline reconstruction programs, and the hit pattern is exploited in a highly non-trivial manner. The combination of a wall probability map generated with a neural network and the tracking information from the muon and the hadronic shower is used to determine the brick where the primary vertex occurred. This brick finding procedure provides a probability map for the occurrence of the primary vertex in a given ECC. The bricks with the largest probability are extracted from the target by the BMS on a daily basis and the corresponding changeable sheets are detached, developed and scanned according to the procedure described in Sec. 9.3. The CS provide a first confirmation of the presence of the neutrino interaction and initialize the scanning analysis of the brick. About 30 bricks will be extracted from the target (1800 emulsion foils) each day. The total emulsion surface to be measured corresponds to a few thousand square meters in 5 years. In order to cope with the real-time analysis of neutrino interactions, high speed automatic scanning microscopes had to be developed in Europe and in Japan, improving respectively by a factor 20 and 60 the scanning speed achieved in CHORUS.

Most of the analysis chain was validated in the first CNGS run in August 2006.[13] This crucial technical run was conducted with electronic detectors only (TT and RPC: at that time, bricks were not yet available and the drift tubes were still under installation). Neutrino interactions were mainly produced in the rock surrounding OPERA and in the iron of the magnets (990 t per magnet). During the run, the CNGS integrated 7.6×10^{17} pot in $\sim$10 days of operation at reduced intensity, and 319 time-correlated events were observed, in agreement with expectations. A first test of consistency between the TT predictions and the emulsion data has also been accomplished: 300 CS were installed in one wall of the first super-module and the TT predictions were tested by scanning the CS doublets hit by muons during exposure to CNGS.

9.3. ECC Analysis

Automatic scanning systems are a key element of the OPERA experiment and they can be considered to be its DAQ sub-system generating the largest data-volume. The development of this system and its associated analysis tools started with CHORUS. This technique was then successfully used by DONUT, where new analysis methods were developed by using fully digitized information from the automatic scanning systems.[10] New automatic scanning systems for OPERA were developed in both Europe and Japan. The required scanning load for OPERA is much larger than in CHORUS and DONUT because of the poorer resolution of the TT in pointing back to the neutrino interaction point. A photograph of one of the scanning systems developed for OPERA is shown in Fig. 9.3.

An automatic scanning system provides five track parameters and quality information for each track. These parameters are the X,Y and Z starting coordinates, measured with μm accuracy, and the slopes in the XZ and YZ projections with about 7 mrad accuracy for a 42 μm thick emulsion layer. By using the tracking information from both sides of an emulsion layer (base-track) an angular resolution of a few mrad is achieved at high speed read-out.

The basic principle of automatic scanning is the same for both European and Japanese systems. Both systems have a computer controlled X,Y and Z microscope stage and a high speed CMOS camera to take microscopic emulsion images. Emulsion films record charged particle trajectories with 0.6 μm diameter silver grains. Minimum ionizing tracks produce about 35 grains in 100 μm thick emulsion (15 grains in the 42 μm thick OPERA films). Both systems take multiple tomographic images of each emulsion layer to reconstruct a track from the silver grains along its trajectory. Reconstructed tracks are provided with full 3D position and slope vector informations.

Once neutrino events are triggered and reconstructed by the TT, the emulsion scanning procedure starts with the CS analysis. The CS can be seen as an interface emulsion film from the TT to the brick. The TT provides the event localization over the full volume of OPERA . It identifies the wall containing the vertex and then the hit brick in that wall, by restricting the surface by a factor of $25\,\text{cm}^2/64\,\text{m}^2 = 4 \times 10^{-5}$. Then the CS allows for a further localization of the tracks at microscopic level. The CS scanning is the heaviest task in the emulsion analysis. In CHORUS and DONUT, the electronic detectors pointing accuracy was a few 100 μm, compared to a few cm in OPERA, where a single track in a few ten cm^2 area has to be localized at microscopic level. The level of background tracks in the CS is therefore a very important aspect. OPERA films have the new feature of controlled fading (so called refresh capability).[12] The CS refreshing is performed underground at LNGS in order to erase all tracks accumulated during transportation from Japan to LNGS. In order to suppress background tracks, coincidences are required by using a doublet of OPERA films as the CS (four emulsion layers). Given the brick thickness, the accuracy of the predictions given by TT on the CS is affected by multiple scattering and by electromagnetic and hadronic showers. In the case of ν_μ CC events, the prediction accuracy for a muon track is well within 5 cm. However, in the case of NC like events, single track reconstruction in the TT is quite difficult. A better estimation can be obtained by projecting the center of the shower on the CS with about 10 cm accuracy. The scanning load needed for the CS analysis is then $25\,\mathrm{cm}^2 \times 4$ layers and $100\,\mathrm{cm}^2 \times 4$ layers for CC like and NC like events, respectively.

The CS scanning was tested during the CNGS 2006 August run.[13] Nine muons produced by neutrino interactions in the rock surrounding the detector crossed the CS. Five muon tracks predicted by TT were found by scanning the emulsion films. The reasons for the inefficiency can be traced back to the tight cuts applied in this preliminary analysis and the significant decrease of the fiducial volume. In fact, the dead space between adjacent emulsion films was about 10% and the scanning was only performed up to 3 mm from the film edge, bringing the overall dead space to 20%. However, the test proved the capability in passing from the cm scale of the electronic tracker resolution to the μm resolution of nuclear emulsions. The CS analysis procedure was demonstrated with both the European and Japanese systems.

Once tracks are tagged on the CS, the event location reconstruction proceeds as per the CHORUS and DONUT experiments. The tracks found on CS will be traced back to the neutrino interaction vertex. The main difference with respect to the CHORUS and DONUT experiments consists of the number of events accumulated in a single emulsion module. In the case of OPERA, there is only one neutrino interaction in the brick. Since the bricks must be disassembled before development, a very important step is the fast alignment procedure of the films. A first alignment of the films in a brick is performed by X-ray marking, after the brick extraction from the detector. The X-ray marks provide an alignment accuracy better than $100\,\mu$m, which is smaller than the microscope field of view. For finer alignment(μm level), needed for vertex analysis and kinematical analysis (momentum measurement), the brick is exposed to cosmic rays after the extraction from the target before being disassembled for development.

The vertex analysis and kinematical analysis procedures were also well established in CHORUS[14,15] and DONUT.[9,10] During the vertex analysis all the tracks recorded on the emulsion films around the neutrino interaction point are read out by the automatic scanning system and globally reconstructed by the offline software. In this analysis, decay of taus produced by ν_τ CC interactions will be tagged. Once decay candidates are found in the vertex analysis, the kinematical analysis of the event is performed. The kinematical analysis is needed to increase the signal to background separation. It consists of invariant mass reconstruction and the transverse momentum measurement of the decay. These analyses provide electron and gamma identification and energy measurement through the induced shower measurement, momentum measurement for charged particles through the multiple Coulomb scattering detection (see below) and pion-muon separation. Other kinematical analyses such as the π^0 detection and energy measurement and the $\tau \to \rho$ detection are related to this. In the following we show the principles and the results already achieved in several test-beam experiments.

The cumulative effect of multiple scattering for a particle traversing a given thickness of material can be represented by an approximatively Gaussian distribution of the scattering angle in a plane with the RMS, θ_0, inversely proportional to the momentum of the particle. One can measure θ_0 by simply taking the difference between the angles in two consecutive emulsion films. This method is called the "angular method". A resolution, $\delta\theta$, of about 2 to 3 mrad can be routinely obtained.[16] The RMS of the measured scattering angles, θ_M^2, is the quadratic sum of the scattering signal θ_S and of the measurement error $\delta\theta$: $\theta_M^2 = \theta_S^2 + \delta\theta^2$. With this method $\theta_S = \theta_0$. The error on θ_S when N independent measurements are performed is:

$$\frac{\delta\theta_S}{\theta_S} = \frac{1}{\sqrt{1 - (\delta\theta/\theta_M)^2}} \frac{1}{\sqrt{N}}. \tag{9.1}$$

Using N_{film} emulsion films, this method provides $N = (N_{film} - 1) \times 2$, since each of the two projections provides a set of independent measurements. One can obtain a $\delta p/p \sim 10\%$ with a brick of about 50 emulsion films. The momentum resolution experimentally achieved with this method with an angular resolution of 3 mrad for 2, 3 and 4 GeV negative pions impinging on a 3 X_0 ECC (17 emulsion films)[16] is respectively 28%, 35%, and 36%. A different method, the so-called "position method", can also be used for the momentum measurement and it is especially suitable for higher momenta. Details of this method and of the achieved results can be found in

Ref. 20. In the DONUT experiment a systematic momentum measurement for all tracks from neutrino interaction events was performed.[17]

A typical example of electrons identified in a ECC brick is shown in Fig. 9.4. The identification is done by means of both the multiple scattering before the shower starts and the number of electrons when the shower develops. In particular, the distinctive energy loss rate of electrons before interaction is used to discriminate between electrons and hadrons: the energy is practically unchanged for hadrons while it is decreasing for electrons while traversing the brick. Two approaches are possible, either a χ^2 corresponding to the two possible interpretations (hadrons or electrons) is built and it is used as a separator,[23] or a Neural Network is built with the aim of assigning a probability to each particle of being either an electron or a pion.[24] ECCs have been exposed to electron and pion beams with the aim of measuring the electron to pion separation. Results show that, depending on the requirements of the analysis, it is possible to achieve either high electron identification efficiency (more than 80%) or small pion mis-identification (smaller than 1%).

By counting the number of segments associated with an electromagnetic shower and by fitting both the longitudinal and transverse shower profile it is also possible to measure the energy of the electrons. Monte Carlo studies show that a 20% energy resolution can be achieved.

Fig. 9.4. xz projection (left) and yz projection (right) of a reconstructed shower generated by a 6 GeV electron interacting in the ~3.3 X_0 ECC exposed at DESY. Each segment corresponds to a base-track associated with the reconstructed electromagnetic shower.

Particle identification by observing the energy losses close to the stopping point is a well established technique.[19] In this regime, the energy loss rate is given by a constant (k) divided by the square of the speed of the particle ($\beta^2 = (v/c)^2$): $I = dE/dx = k/\beta^2$. Since $E = M\beta^2/2$, where M is the mass of the particle, one can get $M = (2/k)I^2x$. Therefore the particle mass can be extracted by measuring I at a distance x from the stopping position. The error on the mass has a contribution from δx and another one from δI, which is the leading one when the particle stops in a brick. The grain measurement amounts to about $(30 \pm \sqrt{30})/100\mu$m. By measuring only one emulsion sheet one can get about 18% resolution on the ionization measurement. Test experiments have been performed in order to measure the proton, pion and muon identification by means of this method. Although their mass is quite similar, it is still possible to separate muons from pions. If 10 emulsion films are crossed after entering into the non-relativistic regime, a mass resolution $\delta M/M \simeq 2\delta I/I = 0.12$ is achievable which means a $\delta M = 16$ MeV for a pion. This mass resolution allows the separation between muons and pions. ECC exposures have been performed in the pure and low energy muon and pion beams available at the Paul Scherrer Institut (PSI). The preliminary results are encouraging: about 30% μID efficiency with a few percent π mis-identification. Results on the proton to pion separation can be found in Ref. 18. Pion and proton separation greater than 3 sigma was achieved at momentum of 1.2 GeV/c by detecting the 14% difference in ionization energy loss.

A complete test experiment was performed at Fermilab in 2005-2006, T952 (PEANUT). The old DONUT scintillating fiber tracker was brought to the MINOS Near Detector Hall to expose opera bricks to the NuMI neutrino beam. X-ray mark alignment tests, event location tests by trace back, and vertex analysis tests are ongoing for 6000 neutrino interactions in 85 bricks. Most of the analysis tools were tested with the PEANUT experiment, apart from the CS analysis.

9.4. Physics Performance: $\nu_\mu \rightarrow \nu_\tau$ Search

The τ decay channels investigated by OPERA (e, μ, single- and multi-prong decays) cover all the decay modes. They are classified in “long” and “short” decays. Short decays correspond to the cases where the τ decays in the same lead plate where the neutrino interaction occurred. In this case τ candidates are selected on the basis of the impact parameter (IP) of the τ daughter track with respect to the interaction vertex (IP > 5-20 μm). For long decays the τ does not decay in the same lead plate and its track can be reconstructed in one film. The τ candidate events are selected either on the basis of the existence of a kink angle between the τ and the daughter tracks ($\theta_{kink} > 20\,\mathrm{mrad}$) or on the presence of a secondary multi-prong vertex along the τ track.

For the candidates satisfying the topological criteria discussed above, the signal to background ratio can be improved by applying a kinematical analysis. Since for short decay candidates the main background comes from charm production, a lower cut at 2 GeV on the invariant mass of the hadronic system, as computed from the momenta measured in the ECC, is imposed. This cut reduces the background by more than a factor 1000, while retaining about 15% of the signal.

For long decay candidates it is worthwhile considering leptonic, single-prong and multi-prong decays separately. For leptonic decays, soft cuts on the daughter momentum, a lower one to minimize the effect of the particle mis-identification ($p > 1$ GeV) and an upper one ($p < 15$ GeV) to suppress the beam related background, and a cut on the measured transverse momentum (p_T) at the decay vertex are enough to reduce the background to a reasonable level. The applied cut at the decay vertex is $p_T > 100$ MeV and $p_T > 250$ MeV for the electronic and muonic decay channel, respectively.

For the single-prong decay the kinematical analysis is more complicated. The main background for this channel originates from the reinteraction of primary hadrons without any visible recoil at the interaction vertex. In order to keep the background for this channel as low as possible, kinematical cuts are applied both at the decay and at the primary vertex. The kinematical analysis is qualitatively similar to that of the electronic and muonic channels. However, the cut applied on the p_T is harder ($p_T > 300$ MeV if a γ is attached to the decay vertex, $p_T > 600$ MeV if not[a]). The daughter particle is required to have a momentum larger than 2 GeV. The kinematical analysis at the primary vertex uses the missing transverse momentum, p_T^{miss}, and the angle in the transverse plane, ϕ, between the parent track and the shower direction. Due to the unobserved outgoing neutrino, p_T^{miss} is expected to be large in NC interactions. Conversely, it is expected to be small in CC interactions. For τ candidates the measured p_T^{miss} is required to be lower than 1 GeV. The ϕ angle is expected to peak at π, because the τ and the hadronic shower are back-to-back in the transverse plane. Conversely, in NC interactions the hadron mimicking a $\tau \rightarrow h$ decay is produced inside the hadronic shower. Therefore, ϕ peaks near 0. For τ candidates the ϕ angle is required to be larger than $\pi/2$.

---

[a] This choice originates from the fact that the fraction of secondary vertexes in ν_μNC events with an attached γ is very small. Furthermore, by reconstructing the γ the measured p_T increases, hence the τ detection efficiency increases at constant background.

For the multi-prong decay channel the main background is given by decays of charmed particles while the hadronic reinteraction background is not a major issue. Indeed, the probability for a hadron to undergo a multi-prong interaction is much smaller (1-2 order of magnitudes) than for single-prong interactions. The signal to background ratio is enhanced by performing a kinematical analysis mainly based on p_T^{miss}, the invariant mass of the hadronic system and the total energy of the event.

The total ν_τ appearance efficiency including the branching ratios of all channels amounts to 12.5%. The background is due to the following sources:

- prompt ν_τ production in the primary proton target and in the beam dump;
- background from π^0 and prompt electrons;
- production and decay of charmed particles;
- large angle muon scattering;
- hadronic reinteractions.

The first two backgrounds are very small, while the the others contribute equally to the overall expected background. One of the main backgrounds for all channels of the OPERA experiment is the charm production induced by neutrinos[22] when the primary (typically low energy) muon is not identified. Therefore, the key issue is to achieve a high efficiency for muon identification (see Sec. 9.2). By using a combined analysis of the electronic detectors and of the ECC bricks, it is possible to achieve a muon identification efficiency of about 95%. However, the other handle in identifying low momentum muons and, consequently, reducing the charm background exploits the different energy loss of pions and muons at the end of their range (see Sec. 9.3).

Presently, the main background for the muonic channel is the large angle scattering of muons off 1 mm lead. Data measuring the rate of the process are sparse. Furthermore, there is about a one order of magnitude discrepancy between the predicted rate with GEANT3 and an analytical calculation[21] that gives a lower rate (background). To have an experimental determination of this background, a dedicated measurement of large angle scattering of 9 GeV muons in lead plates was performed. The measured rate ($p_T > 250$ MeV) for 2 mm lead is $(0.6^{+0.7}_{-0.6}) \times 10^{-5}$, based on one observed event. This has to be compared with the predicted rate of 0.2×10^{-5} from the analytical calculation. Unfortunately, this measurement was not conclusive. Therefore, an exposure with a silicon tracker telescope and a pure μ beam has been performed. The analysis is still in progress, but the expected background measured with an empty target is of the order of 10^{-6} and it will allow the measurement with the needed accuracy. Conservatively, for OPERA background calculations we assumed a rate of 1×10^{-5}.

An important source of background for both the hadronic and muonic channels is due to reinteractions of hadrons produced in ν_μ NC and in ν_μ CC without any visible activity at the interaction vertex. Hadronic reinteractions constitute a background for the hadronic channel if they occur in ν_μ NC events or in ν_μ CC events with the muon not identified. The expected background rate from hadronic reinteractions in the hadronic channel is about 4×10^{-6}. However, hadron reinteractions also constitute a large source of background for the muonic τ decay channel. This contamination can arise in ν_μ NC events because a hadron can be misidentified as a muon, or in ν_μ CC events if a genuine μ identified in the electronic detector is mismatched to a hadron track in the emulsions. Because the kinematical analysis in the muonic channel is very loose (no kinematical analysis at the primary vertex, $p_T > 250$ MeV at the decay vertex) the expected background rate from hadronic reinteractions in the hadronic channel is about 7×10^{-6}. The prong multiplicity and angular distribution in pion interactions on lead nuclei below 10 GeV are poorly known. In order to accurately measure this background, exposures of a brick to pion beams from 1 to 6 GeV have been carried out and the analysis is in progress (foreseen precision $\sim 10\%$).

It is also planned to measure the background in the OPERA experiment itself. Indeed, once the primary neutrino interaction is reconstructed, it will be possible to search for decay-like topologies away from the tau decay vertex. This will give a direct, Monte Carlo independent, background measurement. Similarly, Monte Carlo efficiencies for the decay detection and the kinematical analysis can also be validated on the data. By searching for all charm decay topologies (both neutral and charged) when the primary muon is correctly identified and attached to the primary vertex, one can check the decay detection efficiency. The expected number of charm events produced in the target can be extrapolated from the CHORUS measurements[25] with an accuracy in the 10-20% range. Therefore, the decay detection efficiency for each decay topology can be checked with such an accuracy. In order to check the reliability of the kinematical analysis based on Monte Carlo simulation (Fermi motion and nuclear re-interactions strongly affect the kinematics at the interaction vertex), the complete emulsion analysis (full kinematical reconstruction) is planned to be performed for a minimum bias sample of about 1000 neutrino interactions. All the measurements discussed above will provide a solid cross-check for the OPERA results.

The total background is estimated to be 1 event. However, recent achievements in the pattern and track reconstruction algorithm allowed a higher muon identification efficiency and a reduction of the probability to mismatch a genuine μ identified in the electronic detector with a hadron track in the emulsions. Consequently the total background should be reduced by about 10%. Furthermore, a preliminary analysis has shown that low energy muons can be identified in the bricks, using the dE/dx measurement in the emulsions (grain density) as a function of the particle range. Applying this idea reduces the estimated background from 1 to 0.8 without changing the signal efficiency (see Table 9.1).

Table 9.1. Summary of the OPERA signal and background for different values of Δm^2 at full mixing.

	1.9×10^{-3}eV^2	2.4×10^{-3}eV^2	3.0×10^{-3}eV^2	Back.
	8.0	12.8	19.9	1.0
+back.reduction	8.0	12.8	19.9	0.8

The OPERA discovery potential is shown in Fig. 9.5. It gives the probability of observing a number of events larger than a background fluctuation with 4 σ equivalent probability in a 5 year run. The continuous and the dashed lines correspond to the first and the second row of Table 9.1, respectively. The latest 90% C.L. Super-Kamiokande allowed region based on the L/E analysis is reported for comparison. From this plot one may conclude that in the worst case (lowest allowed Δm^2) there is a $\sim$ 70% probability to observe $\nu_\mu \rightarrow \nu_\tau$ oscillations with a 4σ significance. In case no signal is observed, the OPERA experiment will be able to exclude the 99% C.L. Super-Kamiokande plus K2K allowed region with a C.L. of 99%, as shown in the bottom panel of Fig. 9.5.

9.5. Search for $\nu_\mu \leftrightarrow \nu_e$ Appearance

In addition to the dominant $\nu_\mu \rightarrow \nu_\tau$ oscillation, it is possible that a subleading transition involving ν_e also occurs at the atmospheric scale. This oscillation is driven by the mixing angle, θ_{13}, which is constrained by the CHOOZ experiment to be small ($\sin^2(2\theta_{13})$ <0.14).[27]

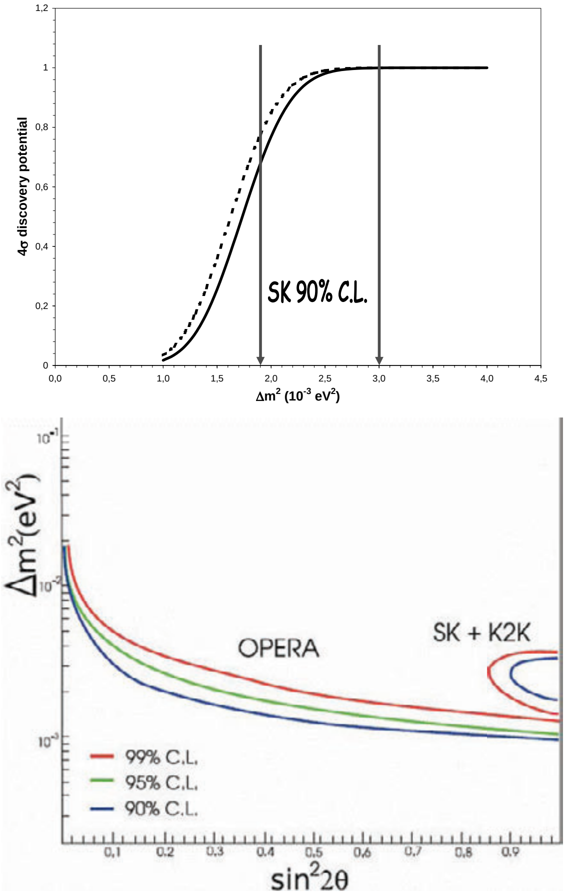

Fig. 9.5. (Top) OPERA $\nu_\mu \to \nu_\tau$ oscillation discovery potential. Dashed line corresponds to the improvements expected with additional background reduction. (Bottom) OPERA $\nu_\mu \to \nu_\tau$ exclusion plot computed at 99%, 95% and 90% C.L.

Having excellent electron identification capabilities, OPERA has estimated its sensitivity for $\nu_\mu \leftrightarrow \nu_e$ appearance with the CNGS beam. The analysis principle is based on a search for an excess of ν_e CC events at low neutrino energies. The main background comes from the ν_e contamination in the beam. The $\nu_\mu \leftrightarrow \nu_e$ analysis looks for neutrino interactions with a candidate electron from the primary vertex with an energy greater than 1 GeV (this cut reduces the soft γ component) and a visible event energy smaller than 20 GeV (this cut reduces the prompt ν_e component of the background). Moreover, a cut on the number of grains associated with the track of the candidate electron is also applied. The latter has a strong impact on the reduction of the background from ν_μ CC and ν_μ NC events and allows for a softer cut on the electron energy. Finally, a cut on the missing p_T of the event is applied ($p_T < 1.5$ GeV) to further reduce NC contaminations and suppress $\tau \to e$ background.

The overall efficiency including brick finding, vertex finding, trigger efficiencies and the fiducial volume cuts, is shown in Table 9.2 and is indicated with ξ. The final efficiencies (ϵ) for both the signal and the background channels are shown in the second row of Table 9.2.

Table 9.2. Signal and background efficiencies for the $\nu_\mu \leftrightarrow \nu_e$ oscillation search with OPERA. Notice that the $\tau \to e$ efficiency includes the $\tau \to e\nu\bar{\nu}$ branching ratio.

	ν_eCC signal	$\tau \to e$	ν_μCC $\to \nu_\mu$NC	ν_μNC	ν_eCC beam
ξ	0.53	0.53	0.52	0.48	0.53
ϵ	0.31	0.032	0.34×10^{-4}	7.0×10^{-4}	0.082

If we assume that both $\nu_\mu \to \nu_\tau$ and $\nu_\mu \leftrightarrow \nu_e$ oscillations occur simultaneously with oscillation parameters $|\Delta m^2_{32}| = 2.5 \times 10^{-3}$ eV^2, $\theta_{23} = 45°$ and $\theta_{13} \in [3°, 9°]$, the expected number of signal and background events in OPERA is given in Table 9.3. The rates are normalized to 5 years data taking and assume the nominal intensity of the CNGS beam.

Table 9.3. Expected number of signal and background events for OPERA assuming 5 years data taking with the nominal CNGS beam and oscillation parameters $|\Delta m^2_{32}| = 2.5 \times 10^{-3}$ eV^2, $\theta_{23} = 45°$ and $\theta_{13} \in [3°, 9°]$.

θ_{13}	$\sin^2 2\theta_{13}$	ν_eCC signal	$\tau \to e$	ν_μCC $\to \nu_\mu$NC	ν_μNC	ν_eCC beam
9°	0.095	9.3	4.5	1.0	5.2	18
8°	0.076	7.4	4.5	1.0	5.2	18
7°	0.058	5.8	4.6	1.0	5.2	18
5°	0.030	3.0	4.6	1.0	5.2	18
3°	0.011	1.2	4.7	1.0	5.2	18

An increase in sensitivity to $\nu_\mu \leftrightarrow \nu_e$ oscillations can be obtained by fitting the kinematical distributions of the selected events. The $\nu_\mu \leftrightarrow \nu_e$ events are balanced, while $\nu_\mu \to \nu_\tau$ show a sizable transverse momentum due to the presence of two neutrinos in the final state. The transverse missing momentum is a handle to disentangle $\nu_\mu \leftrightarrow \nu_e$ and $\nu_\mu \to \nu_\tau$

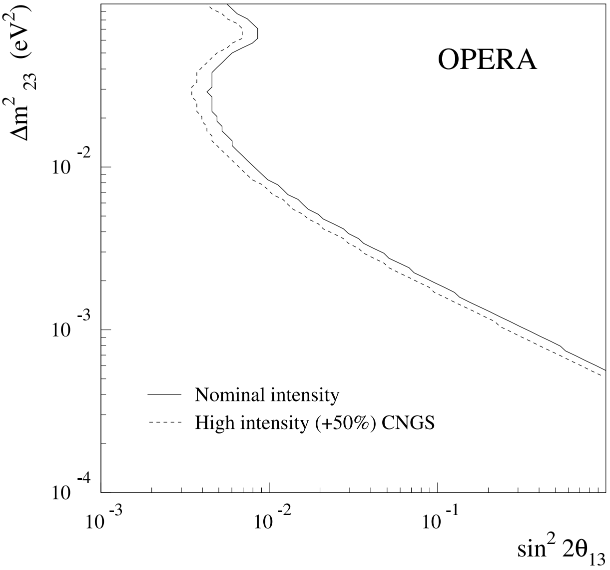

Fig. 9.6. OPERA sensitivity to the parameter θ_{13} at 90% C.L. in a three family mixing scenario, in the presence of $\nu_\mu \leftrightarrow \nu_\tau$ oscillations with $\theta_{23} = 45°$. The sensitivity with the higher intensity CNGS beam is also given.

oscillations. The visible energy and the missing transverse momentum are combined into a binned χ^2-fit, in which the three oscillation parameters are allowed to vary. By fitting simultaneously the E_{vis}, E_e, p_T^{miss} distributions, one can obtain the sensitivity represented by the exclusion plot shown in Fig. 9.6 under the assumption $\theta_{23} = 45°$. A comprehensive analysis of the sensitivity achievable in searching for θ_{13} with the present CNGS beam by the OPERA experiment has been presented in Ref. 26.

References

1. The CERN Neutrino beam to Gran Sasso (Conceptual design), Ed. K. Elsener, CERN 98-02, INFN/AE-98/05.
2. Evidence for an oscillatory signature in atmospheric neutrino oscillation, Y. Ashie *et al.*, Phys. Rev. Lett. 93 (2004) 101801.
3. Measurement of Neutrino Oscillation by the K2K experiment, M. H. Ahn *et al.*, Phys. Rev. D74 072003 (2006).
4. Observation of muon neutrino disappearance with the MINOS detectors and the NuMI neutrino beam, D. G. Michael *et al.*, Phys. Rev. Lett. 97 (2006) 191801.

5. Final NOMAD results on $\nu_\mu \rightarrow \nu_\tau$ and $\nu_e \leftrightarrow \nu_\tau$ oscillations including a new search for ν_τ appearance using hadronic decays, P. Astier *et al.*, Nucl. Phys. B 611 (2001) 3–39.
6. New results from a search for $\nu_\mu \rightarrow \nu_\tau$and $\nu_e \leftrightarrow \nu_\tau$oscillation," E. Eskut *et al.*, Phys. Lett. B **497** (2001) 8.
   The CHORUS experiment to search for $\nu_\mu \rightarrow \nu_\tau$oscillation, E. Eskut *et al.*, Nucl. Instrum. Meth. A410 (1997) 7–44.
7. The ICARUS project: a 3000 t LAr TPC for neutrino physics and search for nucleon decays A. Badertscher, Nucl. Instrum. Meth. A535 (2004) 129–133.
8. Extruded plastic scintillator for the MINOS calorimeters, A. Pla-Dalmau, for the MINOS Scintillator Group, Frascati Phys. Ser. **21**, 513 (2001).
9. Observation of tau neutrino interactions, K. Kodama *et al.*, Phys.Lett.B503:1-9,2001.
10. Detection and analysis of tau neutrino interactions in DONUT emulsion target, K. Kodama *et al.*, Nucl.Instrum.Meth.A493:45-66,2002.
11. High speed particle tracking in nuclear emulsion by last generation automatic microscopes, N. D'Ambrosio, Nucl.Instrum.Meth.A551:261-270,2005.
12. The OPERA film: New nuclear emulsion for large scale, high precision experiments, T. Nakamura *et al.*, Nucl.Instrum.Meth.A556:80-86,2006.
13. "First events from the CNGS neutrino beam detected in the OPERA experiment", R. Acquafredda *et al.*, New J.Phys.8:303,2006.
14. Determination of the semi-leptonic branching fraction of charm hadrons produced in neutrino CC interactions, A. Kayis-Topaksu *et al.*, Phys. Lett. B549: 48–57, 2002.
15. Measurement of Λ_c^+ production in neutrino charged-current interactions, A. Kayis-Topaksu *et al.*, Phys. Lett. B555: 156–166, 2003.
16. Momentum measurement by the angular method in the Emulsion Cloud Chamber, G. De Lellis *et al.*, Nucl. Instrum. Meth. A512: 539–545, 2003.
17. Study of electron identification in a few-GeV region by an emulsion cloud chamber, K. Kodama *et al.*, Rev. Sci. Instrum. 74: 53–56, 2003.
18. pi/p separation at 1.2-GeV/c by an emulsion cloud chamber, T. Toshito *et al.*, Nucl. Instrum. Meth. A516: 436–439, 2004.
19. The study of elementary particles by the photographic method, C. F. Powell *et al.*, Pergamon Press (1959).
20. Detection and analysis of tau neutrino interactions in DONUT emulsion target, K. Kodama *et al.*, Nucl. Instrum. Meth. A493 (2002) 45.
21. M. Guler *et al.* [OPERA Collaboration], CERN-SPSC-2000-028.
22. Charm physics with neutrinos, G. D. Lellis, P. Migliozzi and P. Santorelli, Phys. Rept. 399 (2004) 227 [Erratum-ibid. 411 (2005) 323].
23. K. Kodama *et al.*, Rev. Sci. Instrum. 74 (2003) 53.
24. Electron / pion separation with an emulsion cloud chamber by using a neural network, L. Arrabito *et al.*, JINST 2, P02001 (2007).
25. Measurement of D*+ production in CC neutrino interactions, G. Onengut *et al.*, Phys. Lett. B 626 (2005) 34 and references therein.

26. Sensitivity to θ_{13} of the CERN to Gran Sasso neutrino beam, M. Komatsu, P. Migliozzi and F. Terranova, *J. Phys. G* 29 (2003) 443–452.
27. Limits on neutrino oscillations from the CHOOZ experiment, M. Apollonio *et al.*, Phys. Lett. B466 (1999) 415–430.

Chapter 10

The T2K Experiment

David L. Wark*
Imperial College, Blackett Laboratory, Department of Physics,
Prince Consort Road, London, SW7 2BW, UK
d.wark@imperial.ac.uk

The T2K experiment is a future long-baseline experiment designed to study neutrino oscillations in the atmospheric neutrino regime. Using an off-axis neutrino beam created at the J-PARC accelerator facility being built in Tokai, Japan, T2K will use the massive Super Kamiokande detector and an array of near detectors to precisely measure the parameters involved in ν_μ disappearance, and more importantly, look for evidence of ν_e appearance in a ν_μ beam.

Contents

10.1 The Goals of T2K 197
10.2 Critical Issues for T2K Oscillation Measurements 200
10.3 The Beam Line and Off-Axis Geometry 203
10.4 The 280 m Detectors 206
    10.4.1 INGRID 206
    10.4.2 The 280 m Off-Axis Detector–ND280 207
10.5 Super Kamiokande 209
10.6 Sensitivity of the First Phase of T2K 211
10.7 The 2 km Detectors 213
10.8 The Further Future 214
References 215

10.1. The Goals of T2K

The experiments described in the preceding chapters have established a case for neutrino oscillations which appears compelling. The goal of experimentalists is now to explore this phenomenon further. Of the 8 effective

---

*On behalf of the T2K collaboration.

parameters which control oscillations (the 3 angles of the MNS matrix, the two independent mass-squared differences, the signs of these two mass differences, and the CP-violating phase) we have so far only determined 5. The next priority must be to determine the remaining 3 (the value of θ_{13}, the sign of Δm^2_{32}, and δ). The main target, of course, is δ, as this would give a window into CP violation in the neutrino sector, which may hold the answer to the question of where the matter in the universe comes from, one of the greatest mysteries in fundamental physics today. Sadly, there does not seem to be any model-independent connection between the δ phase measurable in experiments and the CP violating phases controlling the leptogenesis which would generate the matter excess, however a measurement of a non-zero δ would still demonstrate directly that CP violation does take place in the neutrino sector, an important step in establishing the credibility of leptogenesis (and provide a useful constraint on models). Since the effects of δ in oscillations always appear multiplied by $\sin^2(2\theta_{13})$, finding a non-zero value for θ_{13} is a critical step in the campaign to measure δ. However, one should not forget that we are not just filling out tables of numbers for the sake of completeness, but are trying to understand the underlying physics which generates neutrino mixing. Right now we know that of the three neutrino mixing angles, two are “large”, and one is “small”, but the uncertainties are still large, and in fact, within existing errors, the three numbers look like three random numbers in the allowed range and carry little useful information about the underlying physics. However if the errors could be reduced, we might find that we were seeing “special” numbers, i.e., a θ_{13} very close to zero or θ_{23} very close to maximal, which could point to an underlying symmetry that a more fundamental theory must explain. This suggests a two-fold measurement program to better determine the already observed quantities and to get first measurements of the unknown ones. The measurement of θ_{13} is critical to both of these efforts.

The T2K experiment is designed to be a major step forward on both fronts. The proposal takes advantage of the juxtaposition of two facilities which would be available in Japan–the Super Kamiokande detector, which already has a distinguished record of neutrino measurements (as discussed in Chapter 2), and the J-PARC accelerator under construction in Tokai, on the east coast of Japan. The basic idea is the same as most long-baseline neutrino oscillation experiments such as the K2K[1], MINOS[2] and NOνA experiments discussed in other chapters (See Chapters 5, 6 and 11), and indeed as most accelerator neutrino experiments dating back to the first neutrino horn at CERN in the early 1960's.[3] Specifically in the T2K proposal, the proton beam from the main synchrotron at J-PARC will impinge on a target to produce intense bursts of pions. These pions are collected and focused forward by a magnet system consisting of 3 "horns" (selecting one charge, usually positive, in the process) into a decay volume. The resulting pion decays produce beams of ν_μ and muons, and the decay volume length is adjusted so that most of the pions, but as few of the muons as possible, decay before they reach the beam dump at the end. The properties of the resulting neutrino beam are measured by a system of near detectors at J-PARC, and the beam then propagates underground nearly across the width of Japan before reaching the Super Kamiokande detector (see Figure 2.14). The Super Kamiokande detector consists of an enormous right circular cylinder (40 m in diameter and 40 m high) filled with ultra-pure water in which are suspended 11,000 photomultipliers which, despite their large size (50 cm diameter), are sensitive enough to detect single photons.[4] Surviving ν_μ, and any ν_e they have oscillated into, can undergo charged-current quasi-elastic (CCQE) interactions with the nuclei in the water and produce charged muons and electrons which retain most of the energy of the incoming neutrinos (the beam energy at T2K is too low for ν_τ produced by oscillations to undergo CCQE interactions, as it is below threshold for τ production). The resulting muons and electrons are relativistic and therefore cause the water to emit Cherenkov radiation, which is detected by the phototubes. The total amount of light produced gives a measurement of the particle's energy, while the positions and times of hits in the phototubes allow its position and direction to be reconstructed. Furthermore, muons tend to travel in fairly straight tracks, while electrons scatter and shower in the water, producing distinct hit patterns which can, with quite high accuracy, distinguish muons from electrons and hence ν_μ from ν_e.

While this scheme takes advantage of existing facilities, in fact the properties of both the accelerator and the detector are very well matched to the needs of a next-generation oscillation experiment. The distance between these two facilities (295 km) is such that the peak of the oscillation for the atmospheric neutrino oscillation would occur at ~600 MeV, close to the energy at which the ν_μ charged-current quasi-elastic (CCQE) scattering cross section peaks as a fraction of the total cross-section. At these energies neutrino interactions are relatively simple, with few particles in the final state. Such final states are well-reconstructed in water Cherenkov detectors like Super Kamiokande, allowing advantage to be taken of its huge size (50 kton total mass). The J-PARC facility is designed to reach the highest average beam power of any pulsed proton beam, which is another critical parameter for maximizing the event rate, and hence sensitivity, in a long-baseline neutrino experiment.

10.2. Critical Issues for T2K Oscillation Measurements

T2K will make two related measurements of oscillations of the ν_μ beam aimed at the two different measurement programs discussed above. The first of these will look at the disappearance of the ν_μ beam by observing muons from CCQE reactions from the surviving beam. For the parameters of T2K, this oscillation is absolutely dominated by the atmospheric oscillation, and therefore its measurement will allow the accurate determination of the values of $\sin^2(2\theta_{23})$ and Δm^2_{32}. The critical issues for this measurement are:

- The energy spectrum of the ν_μ beam before any oscillations take place must be accurately known. Oscillations produce a "dip" in the energy spectrum (see Figure 10.1), and in principle the depth of this dip directly determines $\sin^2(2\theta_{23})$ and its position in energy determines Δm^2_{32}. However this dip is superposed on a spectrum which (for reasons which will be discussed shortly) is quite strongly peaked in energy, so this spectrum before oscillations must be known with considerable precision before the actual properties of the dip can be inferred from the observed spectrum after oscillations.
- A second problem is also shown in Figure 10.1, which is that the events reconstructed as CCQE muons in Super Kamiokande are not purely from CCQE interactions, but may arise from other, more complex, interactions. There may be other particles in these events which are missed, either because they are neutral and therefore do not emit Cherenkov radiation or because they are below Cherenkov threshold (and, occasionally, pions are mistaken for muons). Most of these events are rejected during analysis, but a few sneak through and produce a non-CCQE background where the energy of the reconstructed "muon" does not give the correct reconstructed neutrino energy. The effect of this is to fill in and shift the dip in the spectrum, so the effects of non-CCQE events must be well understood before reliable oscillation parameters can be extracted from the data.
- Part of the problem of understanding these non-CCQE backgrounds is that exclusive cross-sections (the probabilities of each specific type of

interaction, a charged-current interaction with the production of one additional pion from the vertex, called CC1π, for instance) for neutrino interactions in this energy range are very poorly known, so it is difficult to predict from simulations the exact nature of the CCQE background.

- As the position of the dip in energy gives the value of Δm^2_{32}, the energy calibration of all detectors (in particular Super Kamiokande) must be well understood.

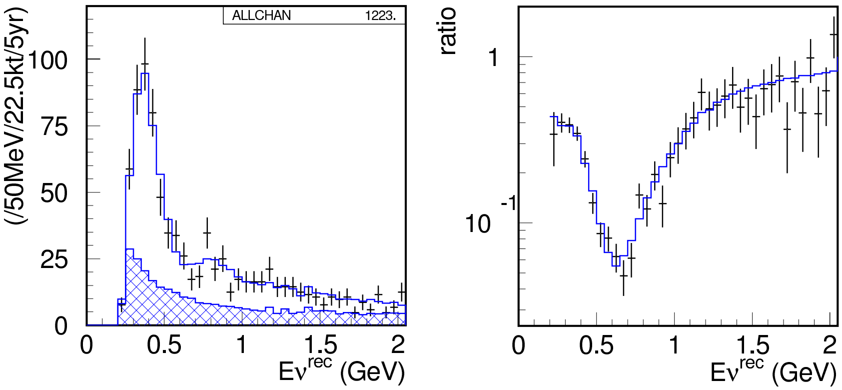

Fig. 10.1. (Left) The simulated reconstructed neutrino energy distribution including oscillations with ($\sin^2(2\theta_{23})$,Δm^2_{32}) = (1.0, 2.7×10^{-3} eV^2). The solid histogram shows the expected spectrum at Super Kamiokande, after oscillations, but without statistical fluctuations. The points with error bars show a typical spectrum that can be expected from a nominal run. The hatched area shows the non-CCQE component. (Right) The ratio of the expected reconstructed neutrino energy distribution with oscillations to the no-oscillation prediction. Note that the dip is clearly visible in the right plot, but in the left plot it would be obscured by the sharp peak of the underlying neutrino spectrum.

The second T2K oscillation measurement is to look for appearance of ν_e in the ν_μ beam. If $\theta_{13} = 0\,°$, then the ν_μ would oscillate to ν_τ and we would see no ν_e in the beam (ignoring a tiny contribution from the oscillations that produce the solar neutrino deficit, which are negligible at the energy and baseline of T2K). However if $\theta_{13} \neq 0\,°$, there is a sub-dominant oscillation that does produce ν_e in the beam, and hence an observation of these ν_e (via the observation of the electrons produced by their CCQE interactions) would allow a measurement of θ_{13}. The issues here are (see Figure 10.2):

- Even before oscillations, there is a small contamination of ν_e in the ν_μ beam which arises primarily from the decay of K's produced at the

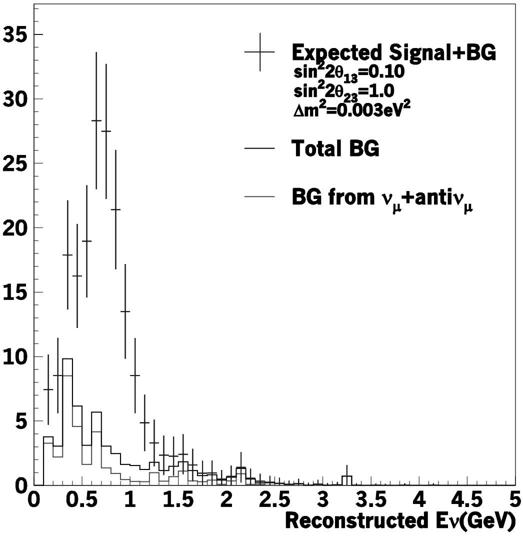

Fig. 10.2. Energy spectrum of candidate electron appearance events for the oscillation parameters shown. The points with error bars show the spectrum from the expected signal plus background, the light grey histogram shows the background from the ν_μ (mostly from NC created π^0), while the black histogram shows the total background including the intrinsic contamination of the beam.

same time as the $\pi's$, and from the decay of the $\mu's$ before they can be stopped. This contamination must be accurately determined so that its effects can be subtracted when looking for ν_e from oscillations.

- Any flavor neutrino, oscillated or not, can interact with the target via neutral current interactions. One of the products of these interactions are neutral pions. These π^0's decay immediately into two gamma rays, which shower within the detector. If the decay is highly asymmetric, and one of the gamma rays has very low energy, it might be missed, resulting in detection of a single gamma ray shower which looks very much like the single electron seen in CCQE events. This produces a background to the ν_e oscillation search, and therefore it is necessary to understand in detail the production of these π^0's and to minimize their number by eliminating any neutrinos from the beam which are not near the oscillation maximum (which contribute to this background, but not to the signal).
- Sensitivity to the smallest values of θ_{13} is primarily limited by statistics and by systematic uncertainties in determining the above backgrounds.

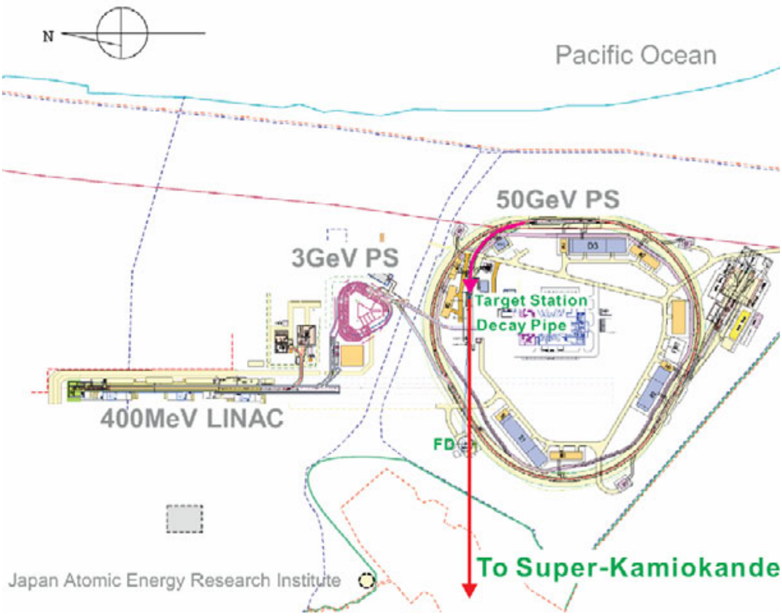

Fig. 10.3. The overall layout of the T2K beam line. The proton beam is extracted in a single turn and bent inside the 50 GeV ring where it hits a pion production target. The resulting pions are focused into a decay volume to produce the neutrino beam.

We therefore need the most intense beam possible, and need to quantify the backgrounds as precisely as possible.

The combination of these issues has strongly driven the design of the T2K experiment, resulting in decisions to adopt an off-axis geometry (with, of course, the highest proton intensity available) and a complicated suite of near detectors at J-PARC to understand the beam and its interactions in detail before it has time to oscillate. We will now discuss these design decisions in more detail.

10.3. The Beam Line and Off-Axis Geometry

The layout of the T2K beam line and 280 m detectors (described below) at the J-PARC site is shown in Figure 10.3. Due to space constraints on the J-PARC site, the proton beam line for the T2K beam has to be bent in a tight radius inside the 50 GeV ring. This requires the use of dual-function (dipole and quadrupole) superconducting magnets that are currently under construction at KEK. Once the proton beam is pointing in the right direction, which in addition to the beam line itself requires a complicated system of monitors to determine the position and direction of the beam at each point, the next step is to collide it with the pion production target. This target is a 90 cm long graphite rod cooled by high-pressure He gas flow. To maximize the pion collection efficiency, the target is located inside the first horn magnet. The target/horn system is the most technically challenging part of the beam line design project. If a single pulse of the 0.75 MW beam hits a solid iron block it would raise the internal temperature of the block to 1100 ° C and produce stresses exceeding the tensile strength of the material. The target must survive such pulses every 3.64 seconds for roughly 1/3 of the year without failing, and it must have very little material around it so that the pions can escape and be efficiently collected, and it must not interfere with the horn magnet which surrounds it. Additionally, the targets and horns will become very heavily activated within a very short time of the beginning of operation, so any maintenance/repair activities will have to be conducted remotely, and any damaged/discarded targets will have to be stored as high-level waste.

The pions exit the horns into a ∼110 m long He-filled decay volume where the neutrinos are produced. At the end of this decay volume is the beam dump, where any remaining pions, the lower energy muons from the pion decays, and the remaining proton beam are stopped (this amounts to about 1/4 of the total initial proton beam power). This beam dump is also an engineering challenge, as it will also become highly active and cannot be altered or replaced once the beam begins operation. It is therefore being designed to handle the largest power planned for future upgrades of the J-PARC/T2K facility, which is 4 MW average beam power. Behind the dump is a set of detectors to measure the position and direction of muons from the high-energy tail of the beam. Looking at these muons will enable the operators to monitor on a spill-by-spill basis the position and direction of the beam, insuring that it is aimed properly with respect to Super Kamiokande.

A key element of the design of the T2K facility is that the neutrino beam is very carefully pointed so that the beam axis actually misses Super Kamiokande. Doing so, perhaps surprisingly, results in a considerable improvement in the quality of the beam for the ν_e appearance experiment. This improvement arises from the kinematics of π decay, which give an enhancement in the neutrino flux produced over a very narrow range of energies depending on the exact off-axis angle (see Figure 10.4). If

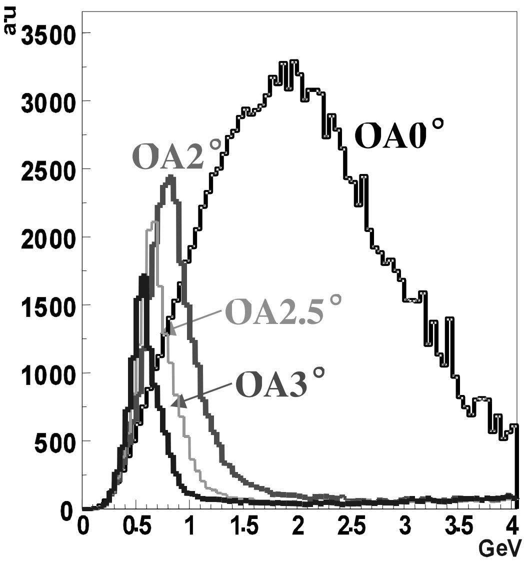

Fig. 10.4. Neutrino spectrum for various off-axis angles in degrees.

the angle is carefully selected, this narrow peak can be put exactly on the oscillation maximum at the far detector. This has three major advantages over a conventional on-axis beam. Firstly, the off-axis neutrino flux at the desired energy (the oscillation maximum) is actually higher than on-axis. Secondly, there are fewer high-energy neutrinos, which do not contribute to the appearance signal but do contribute to its backgrounds, in particular through the neutral-current production of π^0's. Thirdly, the background due to the intrinsic contamination of the beam by ν_e is actually less at the off-axis position due to the different kinematics of the decays that lead to ν_e.

The off-axis position therefore looks like a free lunch–there are all advantages and no disadvantages. However the very kinematics that give a useful selection in energy mean that the characteristics of the beam change rapidly with angle. If a detector is near enough to the beam that the neutrino source does not appear point like, that detector sees a different neutrino spectrum than if it were far away. This fact contributes to conflicting requirements for near detectors. On the one hand we need to make detailed measurements of the properties of neutrino interactions, including relatively rare interactions which may provide backgrounds to the appearance measurement. This requires high rates, which means we need to put our detector as close as possible to the source of neutrinos. However very high rates rule out the detector technology (water Cherenkov) which is used for the far detector, and placing the detector near the pion beam creates the difference between the near and far neutrino spectra mentioned above. These conflicting requirements have pushed T2K toward an array of near detectors which will be built in phases. The first phase will be a set of near detectors 280 m from the target which will be completed at about the same time as the beam line (the distance of 280 m selected to maximize the rates and keep the detector on the J-PARC site). Later, a second near detector complex will hopefully be added approximately 2 km from the target, with advantages which will be discussed below.

10.4. The 280 m Detectors

The 280 m detector complex will contain two detectors, the on axis detector, INGRID, and the off-axis detector. The purpose of the former is to determine the neutrino beam profile and direction, while the latter will measure the beam spectrum, make measurements of neutrino interactions, and determine the intrinsic ν_e contamination of the beam. A measurement of the energy spectrum at 280 m must be corrected for the differences in the near and far spectra mentioned above before it can be used to predict the spectrum at Super Kamiokande in the absence of oscillations, and this correction requires a precise simulation of the beam. One of the key inputs to such a simulation is the knowledge of cross-sections for hadron production when the proton beam hits the target. Current knowledge is insufficiently precise and the resulting systematic would limit the eventual sensitivity of the T2K disappearance measurement. A new experiment at CERN (NA61) will be done to better measure these hadron production cross sections, and so in some sense NA61 constitutes another “near detector” for T2K in that it is critical to the determination of the beam properties before oscillation.

10.4.1. *INGRID*

The INGRID detector consists of an array of iron-scintillator tracking modules (see Figure 10.5). Each module is roughly a 1 m cube consisting of ten 1x1 m^2 plates of 10 cm thick iron separated by layers of plastic scintillator strips. A wave-length shifting optical fiber is embedded in each strip, which captures the light and channels it out to a photosensor on the end of the strip (the photosensors will be discussed below). The modules are de-

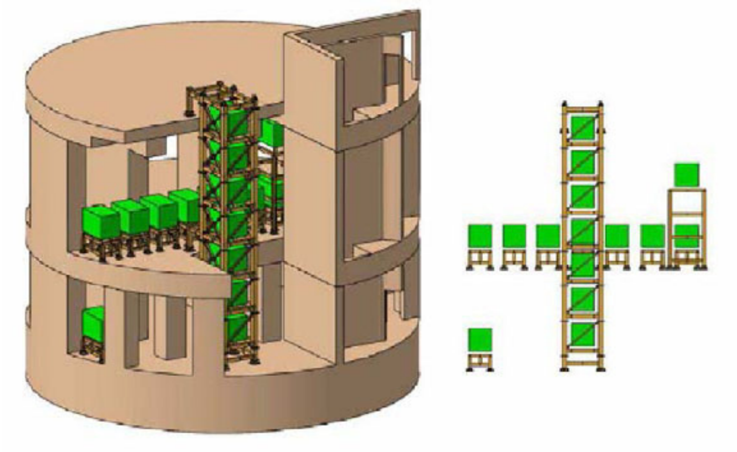

Fig. 10.5. The INGRID on-axis neutrino detector configuration. Each green box is a roughly 1 m^3 iron-scintillator tracking detector as described in the text. The cross is centered on the beam direction, with the signals in the detectors allowing the beam profile and direction to be precisely determined.

signed to have extremely high efficiency for the detection of CCQE muons ($> 99\%$), where each muon will appear as a line of hit strips in different planes. The relative muon rates in the different modules will be used to reconstruct the beam profile and direction, where the goal is to measure the direction to 0.06 ° each day.

10.4.2. *The 280 m Off-Axis Detector–ND280*

The ND280 detector will sit on the line between the mean pion decay position in the beam and Super Kamiokande, where it gives the best approximation of the beam distribution as seen at Super Kamiokande. A schematic view of the detector is shown in Figure 10.6. It is surrounded by the UA1/NOMAD magnet (kindly donated to the experiment by CERN), which provides the 0.2 T magnetic field used to determine the momentum of CCQE muons. The central part of the detector consists of two sections with different capabilities:

(1) The Pi-Zero Detector, or P0D, sits at the upstream end of ND280, and is optimized for measuring the rate of neutral current π^0 production. The P0D consists of tracking planes composed of scintillating bars alternating with lead foil. Inactive layers of water in sections of the P0D

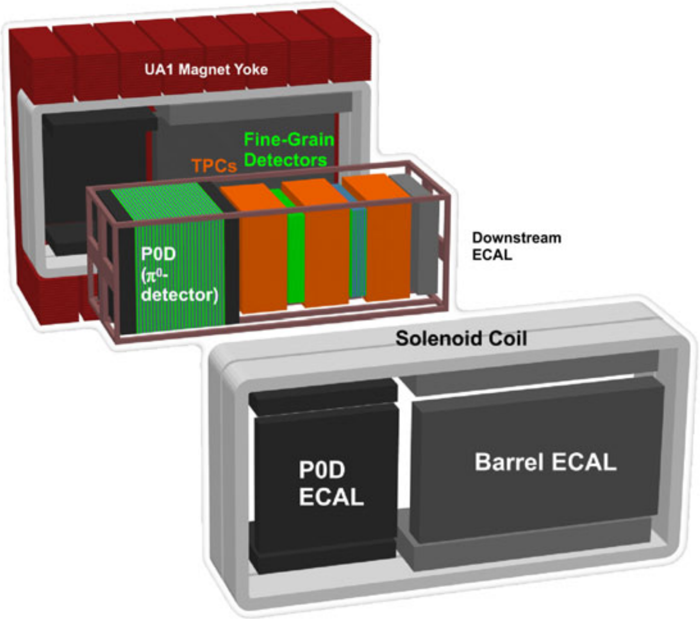

Fig. 10.6. The 280m Off-Axis detector layout (exploded view). The various detector elements are described in the text. The magnet yoke has been omitted from the side nearer the viewer so that the other elements are visible. The thin slots in the yokes in which the SMRD scintillators are inserted are visible.

provide a target for measuring interactions on oxygen, which can be identified by doing measurements with and without the water present.

(2) Tracker: Downstream of the P0D is a tracking detector optimized for measuring the momenta of charged particles, particularly muons and pions produced by CC interactions, and for measuring the ν_e background in the beam. The tracker consists of two detector technologies: Time Projection Chambers (TPCs) and Fine Grained Detectors (FGDs):

    - Time Projection Chambers: Three TPCs will measure the 3-momenta of muons produced by charged current interactions in the detector, and will provide the most accurate measurement of the neutrino energy spectrum. The 3D tracking and dE/dx measurements in the TPC will also determine the sign of charged particles and identify muons, pions, and electrons.

- Fine Grained Detectors: Two FGD modules, placed after the first and second TPCs, consist of layers of finely segmented scintillating tracker bars. The FGDs provide the target mass for neutrino interactions that will be measured by the TPCs, and also measure the direction and ranges of recoil protons produced by CC interactions in the FGDs, giving clean identification of CCQE and CC non-QE interactions. One FGD module will consist entirely of plastic scintillator, while the second will consist of plastic scintillator and water to allow the separate determination of exclusive neutrino cross-sections on carbon and on water.

These inner detectors will be surrounded by an electromagnetic calorimeter, or ECAL, which will consist of alternating layers of scintillating bars and Pb sheets. The purpose of the ECAL is to reconstruct any electromagnetic energy produced by events generated in the inner detectors (or, in the case of the P0D, any electromagnetic energy leaking out of the side from events near the edge of the detector). This will allow a measurement of the π^0 created in neutrino interactions, a critical input to determining the background these particles create in Super Kamiokande (and their effect on the CCQE/non-CCQE ratio), and also assist in determining the intrinsic ν_e contamination of the beam.

At most accelerator fixed-target experiments the particles of interest go primarily forward, i.e., continue in the beam direction. However at the peak of the oscillation energy for T2K the muons produced in CCQE interactions actually occur primarily at large angles to the beam. Some of these muons penetrate all the way through the inner detectors and the ECAL and hit the magnet. In order to get a clean measurement of these events we will partially instrument the magnet yokes with scintillator bars (which have slots built in for this purpose, as the magnet was used as the hadronic calorimeter by the UA1 experiment) to produce the Side Muon Range Detector, or SMRD.

10.5. Super Kamiokande

The Super-K detector has been successfully operated for atmospheric and solar neutrinos since 1996[4] (as described in Chapter 2). In the energy range of interest the detector has a well-understood response to electrons, muons, and pions, and will be further studied and optimized as T2K continues. The accident in November 2001 has been widely reported, however the detector has now been completely rebuilt (with modifications to prevent the accident from reoccurring) and is once again in operation. For T2K there will be, however, a significant modification. The Super Kamiokande collaboration are building new, dead-time free DAQ electronics which will be deployed on the experiment at the beginning of 2008, allowing a full year to become familiar with the new mode of operation before the beginning of the T2K beam.

As mentioned above, the high effective granularity of the Super Kamiokande detector allows the accurate measurement of the energy, position, and direction of charged particles in the few MeV to the few GeV energy range, and the pattern of hit phototubes also allows electrons to be distinguished from heavier particles like muons or pions. For T2K it is also critical to distinguish π^0's from electrons, which is possible because π^0's decay to two gammas which leave two rings in the detector. This fails if the decay is highly asymmetric and one of the gammas produces too few hits to be identified as a second ring, however this happens rarely (and since the decay kinematics are known, the number of events with missed rings can be accurately estimated from the number of well-reconstructed events). Figure 10.7 (page 212) illustrates this, showing the hit patterns from typical muon, electron, and π^0 events.

Table 10.1. The number of events selected by the ν_e appearance analysis, as predicted by NEUT Monte Carlo for 5×10^{21} POT exposure. For the calculation of oscillated ν_e, Δm^2_{32}=$2.5 \times 10^{-3}\,\mathrm{eV}^2$ and $\sin^2(2\theta_{13}) = 0.1$ (just below the current limit) are assumed.

	ν_μ CC	ν_μ NC	beam ν_e	ν_e CC signal
Fully Contained				
$E_{vis} \geq 100\,\mathrm{MeV}$	2215	847	184	243
1 ring e-like, no decay-e	12	156	71	187
$0.35 \leq E_\nu^{rec.} \leq 0.85\,\mathrm{GeV}$	1.8	47	21	146
e/π^0 separations	0.7	9	13	103

Table 10.1 shows how well this separation should work in practice (based on simulations). The top line shows the number of events at nominal luminosity from 4 categories of neutrino interactions: CC and NC events from the remaining ν_μ, events from the intrinsic ν_e in the beam, and the signal events from ν_e produced by oscillations. Each succeeding line shows the number of events surviving after cuts are applied to the data. The first cut selects those events which have a single reconstructed track that looks like

an electron track (and the absence of a delayed event from the subsequent decay of a muon produced in the interaction). This cut almost eliminates the CC ν_μ events. The direction of the neutrino is known, and under the assumption of a CCQE event, the direction along with the measured energy of the recoil charged lepton allows the energy of the neutrino to be reconstructed (this is the major advantage of using CCQE events as the dominant signal category). The next cut is on this reconstructed energy (the oscillated neutrinos will all be near the oscillation maximum, while background events have a much broader energy distribution). The final cut looks for any sign of a second ring in the event, and rejects such events as potential π^0 events. The bottom line shows that the overwhelming majority of the background events can be rejected at the cost of a 42% efficiency for signal events. It may seem surprising that these cuts are so effective at distinguishing intrinsic ν_e from ν_e produced by oscillations, but the former are mostly at higher energy than the latter and hence fail the first two cuts.

10.6. Sensitivity of the First Phase of T2K

From the above table the two main issues for sensitivity of the appearance analysis are clear. Firstly, the number of events is small, and therefore everything must be done to increase the integrated beam power (and the efficiency of the analysis). Secondly, as the value $\sin^2(2\theta_{13})$ is reduced below the current limit, the background becomes a significant fraction of the total event rate so systematic uncertainties in estimating the background become significant. The disappearance measurement, on the other hand, is mostly about systematics, particularly the energy scale and the shape and normalization of the non-CCQE background. Based on an analysis of simulated data from the T2K beam and estimates of the near detector performance, we believe that we will be able to achieve the following targets for systematic uncertainties:

- Uncertainty below 10% in the number of appearance backgrounds.
- ν_μ event rate normalization uncertainty less than 5%.
- Width of the ν_μ spectrum known to better than 10%.
- Linear distortion of the ν_μ spectrum known to better than 20%.
- Energy scale understood at the 2% level.
- CCQE/non-CCQE event ratio known to better than 5-10%.

Assuming these are achieved, and assuming a run equivalent to 5×10^{21} protons on target at the nominal main ring beam energy of 50 GeV,

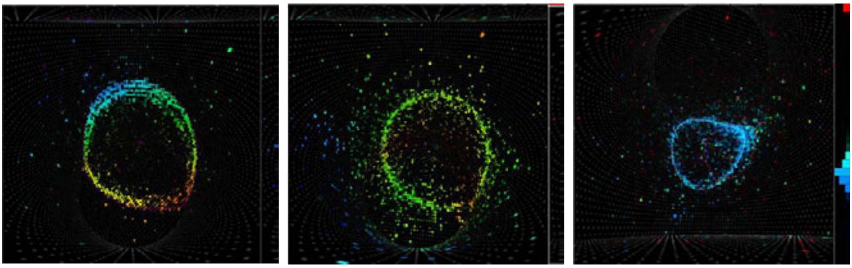

Fig. 10.7. Hit patterns for three event types in Super Kamiokande. On the far left is a muon, showing the clearly defined ring structure. In the middle is an electron, showing the fuzzier ring caused by showering. The far right event is from a π^0, and a second ring can be seen on the right edge of the main ring. Each colored square indicates a hit photomultiplier, with the size of the square showing the amount of charge in the phototube and the color the relative timing.

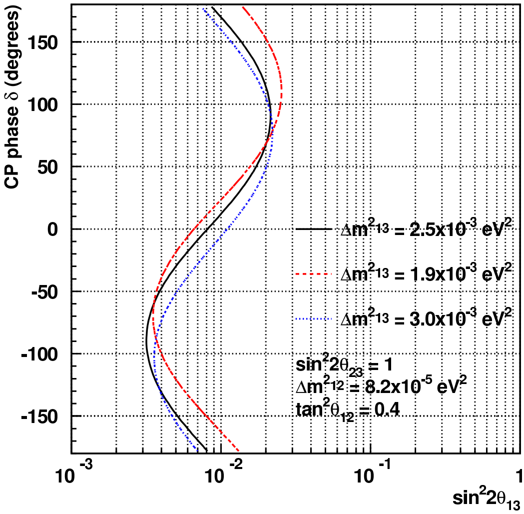

Fig. 10.8. Sensitivity limit for detecting electron neutrino appearance as a function of other oscillation parameters. Note the variation in sensitivity with CP phase, which is bad (as it lessens the sensitivity to θ_{13} for some values of δ), however also good, as it shows that for θ_{13} within the sensitivity range of T2K there are effects due to δ that could be demonstrated by an upgraded experiment.

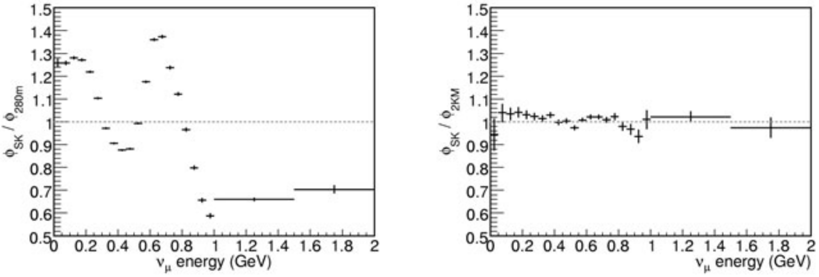

Fig. 10.9. Ratio of the near detector spectra to the Super Kamiokande spectrum in the absence of oscillations for the 280 m (Left) and 2 km (Right) detector positions.

which corresponds to five years of running (at 100 days per year) at the nominal accelerator power of 750 kW, we expect the appearance sensitivity shown in Figure 10.8. The precision for the disappearance analysis depends on the actual values of the mass difference and mixing angle, but should approach a few percent for both parameters. How long it actually takes to get to this statistical precision is a bit hard to say. The accelerator will turn on in April 2009 at lower power (a limit of 100 kW in the first year) and lower energy (30 GeV, however the neutrino flux is almost independent of the beam energy, it depends primarily on the beam power). Plans are in place to increase this power even beyond the nominal value of 750 kW over the first five years of accelerator running, which will allow us to compensate to some extent for the lower initial beam power. Hopefully it will not take longer than the assumed 5 years of running to reach the nominal statistical sensitivity.

10.7. The 2 km Detectors

Two aspects of the combination of the 280 m and Super Kamiokande detectors are less than ideal. First, there is the difference between the near and far neutrino spectra mentioned above (see Figure 10.9), which particularly complicates the disappearance analysis. Second, the detector medium and technology are different for the near and far detector, so some systematics are harder to cancel out from the two measurements. For these reasons the collaboration is actively pursuing a plan to build a second set of near detectors 2 km from the target. This would allow the construction of a small water Cherenkov detector with smaller phototubes than Super Kamiokande (so that the solid angle subtended by a phototube is about the same in both detectors, which makes analysis of the hit patterns of the events very similar in the two cases), with additional detectors to measure the muon spectrum and other details of neutrino interactions.

The 2 km detectors would allow T2K to improve the systematic uncertainties by about a factor of two for some of the key parameters, allowing it to gain benefit from improvements in the beam power for another factor of two in integrated flux. Perhaps more important than that would be the confidence that the 2 km detectors would give in the reliability of the results. The goals of the T2K experiment are extremely challenging, and the 2 km detectors would give T2K the opportunity to confirm their results to the community in a very convincing fashion. The 280 m detectors, coupled with the NA61 experiment and the beam simulations, can be used to predict the results expected at 2 km. Given the great similarity in the detectors and beam spectra at 2 km and Super Kamiokande, any significant difference in their measurements of neutrino events must be due to oscillations, greatly reducing the chance of experimental error and thereby increasing the confidence in the conclusions.

10.8. The Further Future

The longer-term plans for the J-PARC facility call for an increase in the beam power to 4 MW, which (assuming that we can modify our target to survive a beam of that power) would allow T2K to explore still smaller values of $\sin^2(2\theta_{13})$ or (if the value of $\sin^2(2\theta_{13})$ turns out to be favorable, i.e., not too far below the current limit) to search for CP violation. In order to do the latter, however, we will need a detector even bigger than Super Kamiokande. This has led to the proposal to build the Hyper Kamiokande experiment, which would consist of two 450 kton water Cherenkov detectors (see Figure 10.10). A variant on this idea would be to place one of the two 450 kton modules at Kamioka, the other in South Korea where the T2K neutrino beam re-emerges from under the earth. The resulting observations of the beam at three locations (including the near detector measurements) would allow the disentangling of the effects of CP-violation and matter effects in the oscillations.

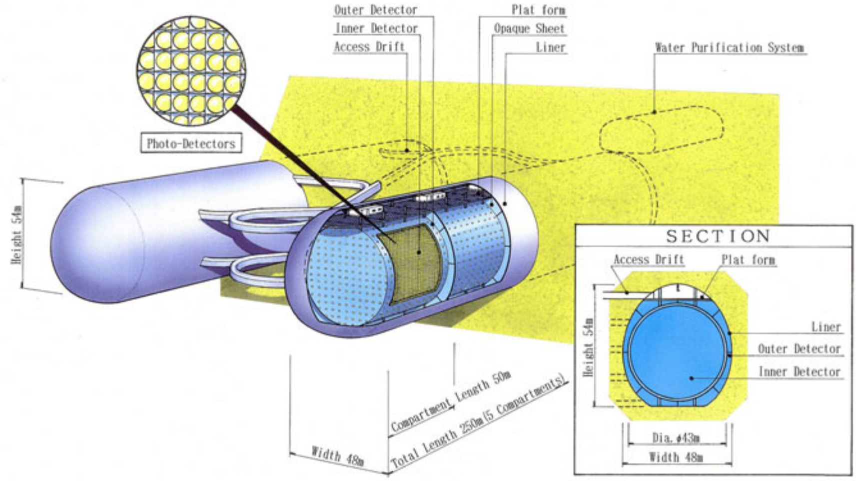

Fig. 10.10. Schematic of one module of the Hyper Kamiokande detector.

References

1. E. Aliu et al., Evidence for muon neutrino oscillation in an accelerator- based experiment, *Phys. Rev. Lett.* **94**, 081802, (2005).
2. D. G. Michael et al., Observation of muon neutrino disappearance with the MINOS detectors and the NuMI neutrino beam, *Phys. Rev. Lett.* **97**, 191801, (2006).
3. S. van der Meer, A directive device for charged particles and its use in an enhanced neutrino beam. CERN-61-07.
4. Y. Fukuda et al., The Super-Kamiokande detector, *Nucl. Instrum. Meth.* **A501**, 418–462, (2003).

This page intentionally left blank

Chapter 11

The NOνA Experiment

Gary J. Feldman*
Department of Physics, Harvard University,
Lyman Laboratory, 17 Oxford Street,
Cambridge, MA 02138, USA
feldman@physics.harvard.edu

The NOνA experiment is a future second-generation experiment on Fermilab's NuMI beam line. It is optimized for the detection of $\nu_\mu \rightarrow \nu_e$ oscillations and it seeks to improve the sensitivity for the study of this reaction by approximately an order of magnitude from that of the first-generation MINOS experiment. The unique characteristic of the NOνA experiment is its long baseline, which allows it access to matter effects that can be used to determine the ordering of the neutrino mass states. The experiment has two detectors, both located 14.5 mrad off the axis of the NuMI beam line. The Near Detector is located on the Fermilab site approximately 1 km from the NuMI target. The Far Detector is located 810 km from Fermilab, near Ash River, Minnesota. Both detectors are totally-active, tracking liquid scintillator calorimeters with transverse segmentation of 4 cm and longitudinal segmentation of 0.15 radiation lengths. The NOνA project includes improvements to the Fermilab accelerator complex and the NuMI beam line to allow 700 kW of beam power. A further project is expected to increase the beam power to 1.2 MW.

Contents

11.1 Introduction 218
11.2 Detector Siting 218
11.3 The Far Detector 220
    11.3.1 Structure and Assembly 220
    11.3.2 Enclosure 221
    11.3.3 Readout 222
    11.3.4 Data Acquisition 222

---

*On behalf of the NOνA collaboration.[1]

11.3.5 Data Quality . . . 223
11.4 Near Detector . . . 223
11.5 NuMI Beam Upgrades . . . 224
11.5.1 Accelerator and NuMI Upgrades . . . 225
11.5.2 Super NuMI . . . 225
11.6 Physics Capabilities . . . 225
11.6.1 $\nu_\mu \rightarrow \nu_e$ Oscillations . . . 226
11.6.2 ν_μ Disappearance . . . 228
11.7 Schedule . . . 230
References . . . 230

11.1. Introduction

Measurement of the presently unknown parameters of neutrino oscillations, the mixing angle θ_{13}, the sign of Δm^2_{32}, and the CP-violating phase δ, will require studies of oscillations in the atmospheric domain. The NOνA experiment will attempt to study these oscillations with approximately an order of magnitude better sensitivity than that of the presently running MINOS experiment (See Chapter 6). NOνA has been optimized to have maximum sensitivity to the sign of Δm^2_{32}, that is, whether the doublet of mass eigenstates responsible for the solar neutrino oscillation length lies higher or lower than the third mass eigenstate. This quantity can only be determined through the measurement of matter effects, the coherent forward scattering of neutrinos off the electrons in the earth. Of the presently planned experiments, NOνA is the only one with a sufficiently long baseline to have sensitivity to these effects.

The order of magnitude increase of sensitivity over that of the MINOS experiment is obtained through four features of the NOνA experiment:

(1) The siting of the experiment off the beam axis. This increases the neutrino flux near the oscillation maximum and reduces the backgrounds.
(2) The optimization of the detector for the identification of ν_e charged current events by decreasing the longitudinal segmentation from 1.5 radiation lengths to 0.15 radiation lengths.
(3) The increase in the mass of the detector by a factor of 3.33.
(4) The increase in the NuMI beam power by a factor of 6 over its present value.

11.2. Detector Siting

The NOνA Far Detector will be located 11.8 km off the NuMI beam axis, 810 km from the NuMI target, off the Ash River Trail in northern

Minnesota. The Ash River Trail is the most northern road in the United States near the NuMI beam line. The reason for siting the experiment off the center of the beam line is due to a feature of relativistic kinematics. A pion of energy E produces a neutrino at laboratory angle θ with energy E_ν according to the formula:

$$E_\nu = \frac{0.43E}{1 + E^2\theta^2/m_\pi^2}. \tag{11.1}$$

Thus, while in an on-axis beam the energy of the neutrino is proportional to pion energy, in an off-axis beam the energy of the neutrino is less dependent on the pion energy and depends largely on the off-axis angle, yielding a narrow-band beam. This is illustrated in Figures 11.1 and 11.2. An off-axis beam provides more flux in the region of the oscillation than the corresponding on-axis beam. It also suppresses backgrounds since higher-energy neutral current events, which can be confused with lower energy ν_e charged current events, are largely absent.

The reason for siting the Far Detector as far from Fermilab as practical is to enhance the matter effects, which allow the mass ordering of neutrino

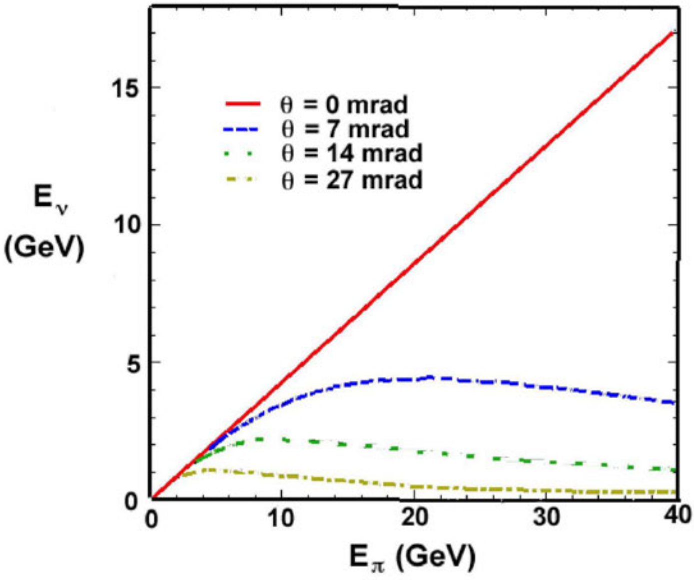

Fig. 11.1. Neutrino energy versus pion energy for different laboratory angles.

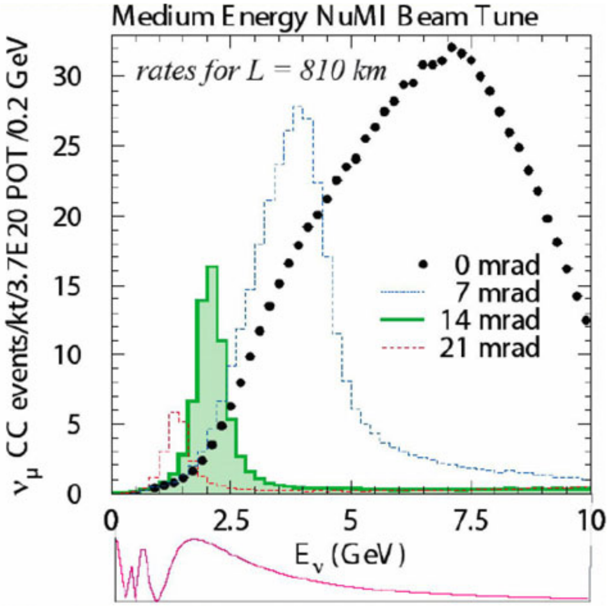

Fig. 11.2. Beam spectra for off-axis, "medium energy tune" NuMI beams with different off-axis angles. The dots show the on-axis beam and the shaded region shows the NOνA beam. The insert on the bottom shows the relative $\nu_\mu \rightarrow \nu_e$ oscillation probability as a function of energy.

states to be determined. The off-axis angle was also chosen to maximize sensitivity to the mass ordering. Maximum sensitivity to the measurement of $\sin^2(2\theta_{13})$ occurs at a slightly lower off-axis angle.

11.3. The Far Detector

11.3.1. *Structure and Assembly*

The NOνA detectors can be described as being totally active, tracking, liquid scintillator calorimeters. The basic cell of the Far Detector is a column or row of liquid scintillator with approximate transverse dimensions 4 cm by 15.7 m and longitudinal dimension 6 cm, encased in a highly-reflective polyvinyl chloride (PVC) container. A module of 32 cells is constructed from two 16-cell extrusions glued together and fitted with appropriate end pieces. Twelve modules make up a plane, and the planes alternate in having their long dimension horizontal and vertical. The planes are grouped into

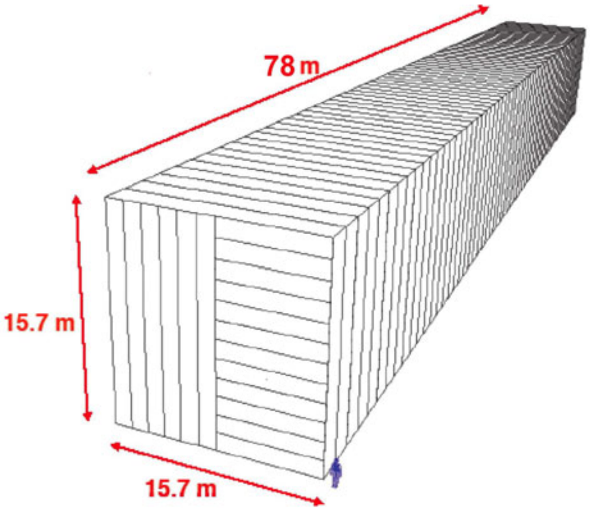

Fig. 11.3. A cartoon of the NOνA Far Detector. The first plane is cut away to show the alternating planes of horizontal and vertical modules. Note the figure in the lower right corner for scale.

31-plane blocks. Our present plan (as of April 2007) is to build 38 blocks, a total of 1178 planes, corresponding to 18 kT. This mass could expand to as much as 20 kT if we have excess contingency. A cartoon of the detector is shown in Figure 11.3

The Far Detector is assembled by gluing a block of 31 planes together on a flat horizontal table and then hydraulically pivoting the block to a vertical position. Five blocks are placed next to each other to form a superblock. There is a small gap between the superblocks to allow for a bulging near the bottom of the detector due to the hydraulic pressure. After the full detector is assembled and filled with scintillator, it is encased by "bookends" to prevent creep of the PVC modules. Note that the Far Detector is filled with scintillator as it is being constructed, so that data taking can begin before the entire detector is completed.

11.3.2. *Enclosure*

The Far Detector enclosure will be largely below grade to provide full secondary containment of the liquid scintillator. Simulations have shown that the photon component of the cosmic-ray background is the only part that can be misidentified as ν_e charged-current events to a significant extent. To reduce this background to an insignificant level, the roof of the enclosure will be composed of a combination of normal concrete and barite-enhanced concrete to form a twelve radiation length overburden.

11.3.3. *Readout*

Light is extracted from each Far Detector cell by a U-shaped 0.7 mm wavelength-shifting fiber, the ends of which terminate on a pixel of a 32-pixel avalanche photodiode (APD), which is mounted on the module. The APD is custom-made for the NOνA experiment by the Hamamatsu Corporation to optimize the match to the two fiber ends per pixel.

Light from the far end of the cell is preferentially attenuated at the lower wavelengths, so that the peak of the spectrum is at about 540 nm. The use of APDs is crucial for the experiment since they have a quantum efficiency of approximately 85% at this wavelength compared to 10% for a photomultiplier with a bialkali photocathode.

The system is designed to produce a minimum of 20 photoelectrons from the far end of the cell for the passage of a minimum ionizing particle at normal incidence. The APD is run at a gain of 100, so low noise is required for efficient operation. The APD is cooled to -15° C by a thermoelectric cooler to reduce the thermal noise of the APD to an acceptable limit.

The output of the APD is sent to a custom application-specific integrated circuit (ASIC), which consists of a low-noise amplifier and shapers. The electronic noise will be equivalent to 2.3 photoelectrons.

The front-end electronics runs in continuous digitization mode at 2 MHz. The output of the ASIC is multiplexed to an external analog-to-digital converter (ADC) running at 16 MHz. Its output is sent to a field-programmable gate array (FPGA), which performs multiple correlated sampling to reduce noise and increase time resolution.

11.3.4. *Data Acquisition*

The data acquisition system (DAQ) receives GPS time-stamped, pedestal subtracted, and zero-suppressed data from the FPGAs and buffers it for up to 20 seconds while awaiting a beam spill time message from Fermilab via Internet. All data within a 30 μs window around the 11 μs beam spill will be recorded for offline analysis.

11.3.5. *Data Quality*

Figure 11.4 shows a simulation of a 2 GeV electron and a 2 GeV muon track the NOνA Far Detector. The muon appears as a straight minimum ionizing track while the electron appears as a fuzzy track with the typical longitudinal and transverse electromagnetic shower profile.

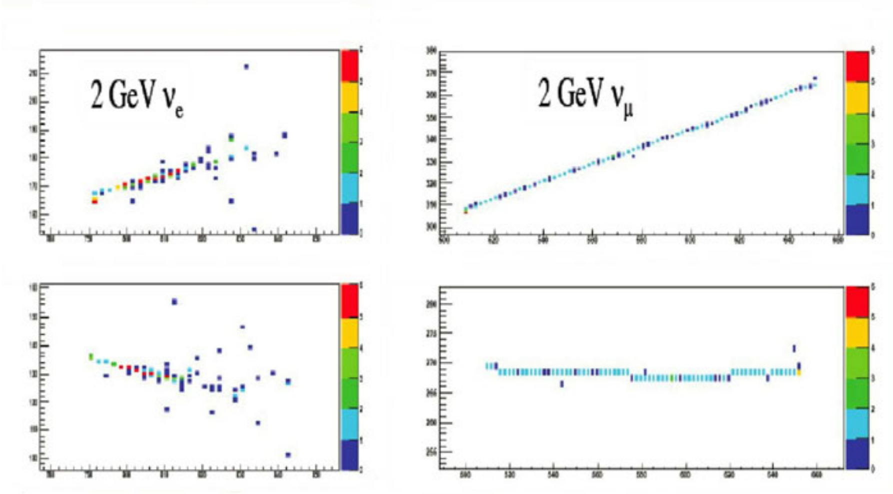

Fig. 11.4. x and y views of a 2 GeV electron track (left, top and bottom panels) and a 2 GeV muon track (right, top and bottom panels) in the NOνA Far Detector. The color scale indicates the relative pulse height of the energy depositions.

11.4. Near Detector

The NOνA Near Detector will be located on the same off-axis angle as the Far Detector in a cavern off the MINOS Near Detector hall, about one km from the NuMI target. The NOνA Near Detector is identical to the Far Detector, except that it is considerably smaller. Its transverse dimensions are two 32-cell modules wide and three modules high. It has 200 planes, which are logically divided as follows: six planes for a veto of particles coming from the front cavern wall, 108 planes for the fiducial region, 76 planes for shower containment, and 10 planes for a muon catcher. The muon catcher has 10-cm iron plates inserted in front of each of the active planes. The fiducial volume is logically further defined as having transverse dimensions of 1.17 m by 2.45 m, leaving a 70 cm border on all sides for event containment. The mass of the fiducial volume is 20 T; the total active mass of the Near Detector is 129 T and the total mass is 212 T. Figure 11.5 shows a drawing of the Near Detector.

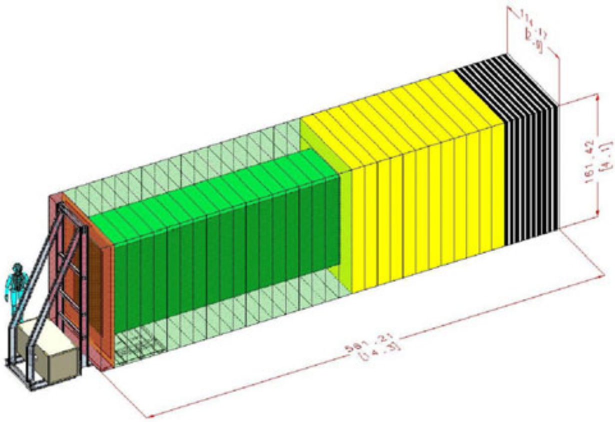

Fig. 11.5. The NOνA Near Detector. From left to right, the drawing shows the veto region, the fiducial region, with the fiducial volume shown in darker shading, the event containment region, and the muon catcher.

There will be multiple neutrino events in the Near Detector in each 11 μs beam pulse. These events must be disentangled using temporal and spatial information. In order to obtain more temporal precision, the Near Detector electronics will run with a sampling time of 125 ns, compared to the 500 ns in the Far Detector, with a corresponding reduction in the shaping time.

11.5. NuMI Beam Upgrades

Fermilab will take advantage of the parts of the accelerator complex that will become available due to the termination of the Tevatron Collider program at the end of 2009 to upgrade the beam power in the NuMI beam line. This will occur in two steps. The first step will increase the beam power to 700 kW. This step is part of the NOνA project and is referred to simply as Accelerator and NuMI Upgrades (ANU). The second step will increase the beam power to 1.2 MW and is referred to as Super NuMI (SNuMI).

11.5.1. *Accelerator and NuMI Upgrades*

Currently the NuMI beam line runs by extracting bunches of protons from the 8 GeV Booster at 15 Hz into the Main Injector, then accelerating, or ramping, the particles in the Main Injector to 120 GeV, then extracting the beam. Using a technique of manipulating the Booster batches within the Main Injector ring, called slip-stacking, a maximum of 11 Booster batches can be inserted into the Main Injector. The Main Injector must sit at 8 GeV for $11/15 = 0.733$ s in this mode to allow it to be loaded with the Booster batches.

The key to increasing the power of the NuMI beam is to overlap the Main Injector loading time with its ramping time. This can be done after the termination of the Tevatron Collider program by slip stacking 12 Booster bunches into the Recycler, an 8 GeV permanent-magnet ring in the Main Injector tunnel. The stored Recycler beam can then be loaded into the Main Injector. Combined with decreasing the Main Injector ramp time to 1.33 s, this will yield a beam power of 700 kW.

11.5.2. *Super NuMI*

A further gain in beam power can be obtained by using the Accumulator ring in the Antiproton Source. Three Booster batches will be stacked into the Accumulator and then transferred to the Recycler. This will be done six times for a total of 18 Booster batches, which will be then loaded into the Main Injector. With a small increase in the number of protons in each Booster batch, a beam power of 1.2 MW can be achieved.

11.6. Physics Capabilities

NOνA's physics capabilities for $\nu_\mu \rightarrow \nu_e$ oscillations are based on a full simulation including generated raw data in the Far Detector, reconstruction, and event type identification through an artificial neural net. The capabilities are calculated for the 1.2 MW beam with 3 years each of neutrino and antineutrino running assuming 44 weeks/year . However, based on experience with the NuMI beam, a derating factor of 0.61 is applied to give an average beam power of 730 kW. The derating factor is a product of three factors: accelerator uptime (0.85), accelerator average to peak power (0.90), and NuMI uptime (0.80).

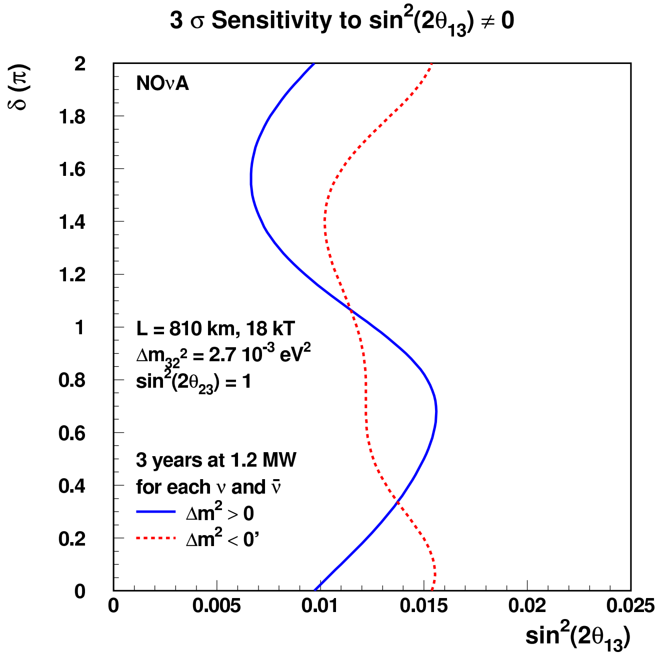

Fig. 11.6. Three standard deviation sensitivity to $\sin^2(2\theta_{13}) \neq 0$ as a function of the CP-violating phase δ and the sign of Δm^2_{32} for a six-year run as described in the text.

11.6.1. $\nu_\mu \longrightarrow \nu_e$ *Oscillations*

Figure 11.6 shows the three standard deviation sensitivity to $\sin^2(2\theta_{13})$, i.e., an observation of $\nu_\mu \to \nu_e$ oscillations three standard deviations above the small contribution from the solar-length oscillation term. The sensitivities are plotted as a function of the CP-violating phase δ and the mass ordering. Running both neutrinos and antineutrinos reduces the sensitivity on these two parameters for this measurement. The three standard deviation sensitivities are approximately an order of magnitude beyond the 90% confidence level set by the CHOOZ reactor experiment of $\sin^2(2\theta_{13}) < 0.13$ at $|\Delta m^2_{32}| = 0.0027\,\text{eV}^2$.[2,3]

Figure 11.7 shows the 95% confidence level sensitivity to the mass ordering, i.e., the sign of Δm^2_{32}, as a function of δ. Because of the inherent ambiguity between true CP violation and the apparent CP violation caused by matter effects in the earth, NOνA data alone can only determine the mass ordering for about half the possible values of δ, those in which the two effects go in the same direction. For the other values of δ a third mea-

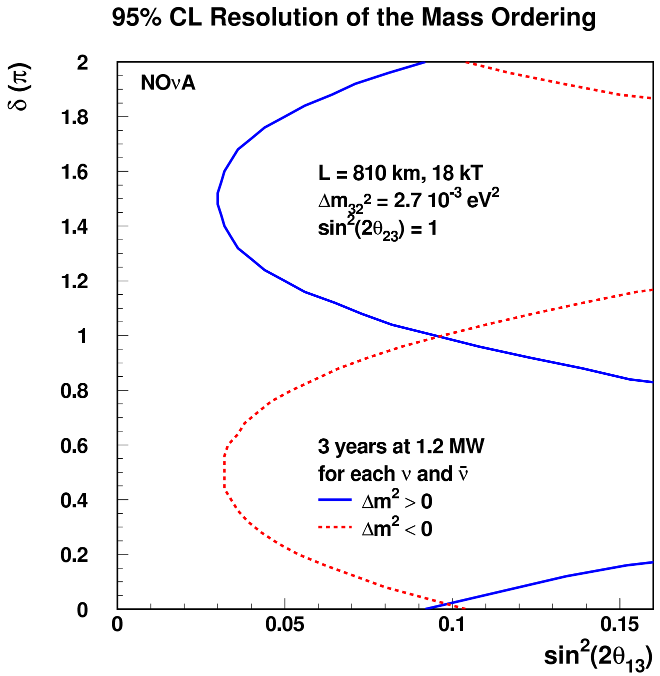

Fig. 11.7. 95% confidence level sensitivity to the sign of Δm_{32}^2 as a function of the CP-violating phase δ for a six-year run as described in the text.

surement is required, either of the second oscillation maximum at the same baseline or the first oscillation maximum at a different baseline. In principle, a combination of NOνA and T2K data (see Chapter 10) would do this, but for the first phase of both these experiments, the mass ordering in this region can only be resolved if $\sin^2(2\theta_{13})$ is near the CHOOZ limit.

Figure 11.8 shows an example of the kind of information NOνA will be able to obtain on the CP-violating phase δ. The figure shows the one, two, and three standard deviation contours for a test point at $\sin^2(2\theta_{13}) = 0.06$, $\delta = 3\pi/2$, and normal mass ordering. The mass ordering is resolved for this point, but if it were not, then there would also be contours for the alternative ordering. Since the relative size of the CP-induced asymmetry between neutrinos and antineutrinos grows as the inverse of θ_{13}, the resolution in δ is almost independent of θ_{13}.

If the dominant atmospheric oscillation is not maximal, it is interesting to determine whether θ_{23} is greater than or less than $\pi/4$, which measures whether ν_e oscillates more strongly to ν_μ or ν_τ. This can be done most

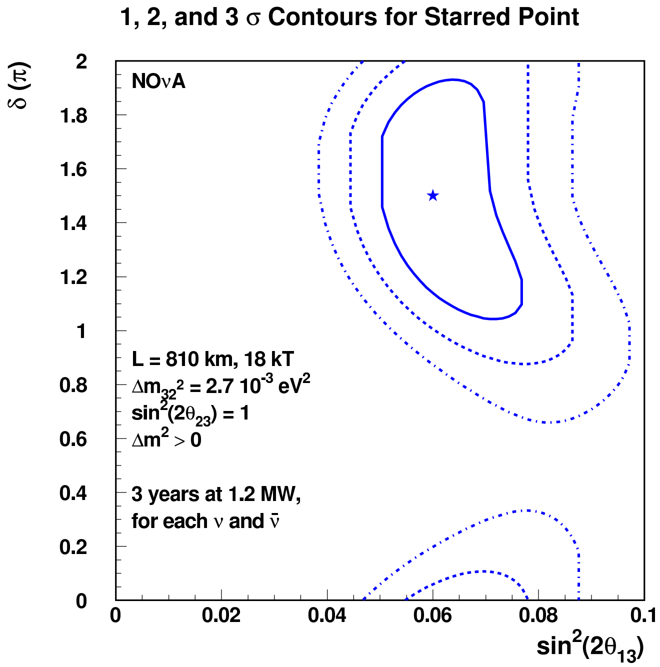

Fig. 11.8. One, two, and three standard deviation contours in δ and $\sin^2(2\theta_{13})$ for the starred point.

easily by comparing the results of the NOνA experiment with a reactor experiment, such as Daya Bay (see Chapter 13), since a reactor experiment will measure the oscillation of $\overline{\nu}_e$ into the sum of $\overline{\nu}_\mu$ and $\overline{\nu}_\tau$ while an accelerator experiment will measure the oscillation of ν_μ into ν_e.

Figure 11.9 shows the region of $\sin^2(2\theta_{23}) - \sin^2(2\theta_{13})$ parameter space for which this measurement can be made at the 95% confidence level assuming that a reactor experiment can reach a one standard deviation precision of 0.005 on $\sin^2(2\theta_{13})$. The limits are functions of δ, the mass ordering, and the sign of $\cos 2\theta_{23}$; the values in Figure 11.9 are averages over the parameter space.

11.6.2. ν_μ *Disappearance*

Although the primary NOνA physics goal is the study of $\nu_\mu \rightarrow \nu_e$ oscillations, NOνA will also be able to make significant measurements of the dominant mode oscillation parameters, $\sin^2(2\theta_{23})$ and Δm^2_{32}.

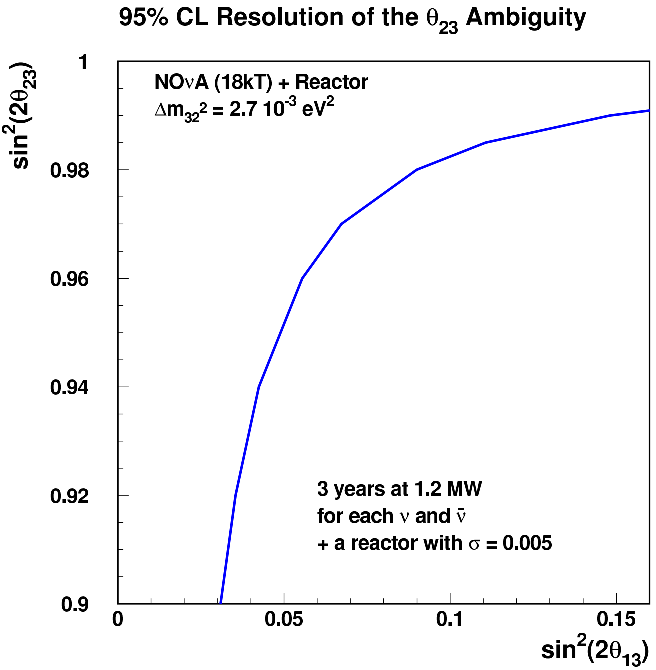

Fig. 11.9. The $\sin^2(2\theta_{23}) - \sin^2(2\theta_{13})$ regions to the right of the curves are those in which the sign of $\cos 2\theta_{23}$ can be resolved at the 95% confidence level by a comparison of data from NOνA and a reactor experiment that can achieve a one standard deviation sensitivity of 0.005 in $\sin^2(2\theta_{13})$. The regions are sensitive to δ, the mass ordering, and the sign of $\cos 2\theta_{23}$; the curves represent an average over the parameter space.

It appears that the best way to meet these requirements is to limit the analysis to totally contained quasi-elastic events, i.e., those events in which the geometrical pattern of energy deposition is consistent with the presence of only an energetic muon and a possible recoil proton. So far we have only performed a preliminary study of how well NOνA can use these events to measure $\sin^2(2\theta_{23})$ and Δm_{32}^2 using a parametric representation of the energy. This procedure is justified by the nature of these events, which are extremely clean. The calculated one and two standard deviation contours are displayed in Figure 11.10 for assumed values of $\sin^2(2\theta_{23})$ of 0.95, 0.98, and 1.00. The energy resolution has been assumed to be 2%, but the contours do not change markedly as one increases the resolution to 4%. Note that the precision of the $\sin^2(2\theta_{23})$ measurement increases as the

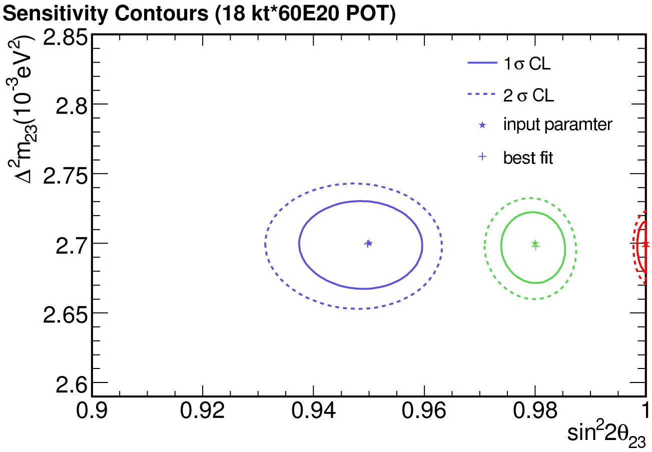

Fig. 11.10. One and two standard deviation contours for a simultaneous measurement of $|\Delta m^2_{32}|$ and $\sin^2(2\theta_{23})$ for a six-year run at 1.2 MW beam power equally divided between neutrinos and antineutrinos. The three input values are indicated by a star and the best fit for each is indicated by a plus sign.

value approaches unity. For maximal mixing, the error on the measurement of $\sin^2(2\theta_{23})$ is less than 0.002.

11.7. Schedule

The NOνA Far Detector is modular and can begin taking data as soon as a significant part is installed. Assuming a project start in October 2007, as envisioned in the President's FY2008 budget request, we expect this to happen by January 2012.

Acknowledgments

This work was supported by the U.S. Department of Energy.

References

1. NOνA. The NOνA Collaboration currently consists of 163 physicists and engineers from Argonne National Laboratory, University of Athens, California Institute of Technology, University of California/Los Angeles, College de France, Fermi National Accelerator Laboratory, Harvard University, Indiana University, ITEP/Moscow, Lebedev Physical Institute, Michigan State University,

University of Minnesota/Twin Cities, University of Minnesota/Duluth, Technical University Munich, Northern Illinois University, Ohio State University, PUC do Rio de Janeiro, University of South Carolina, Southern Methodist University, Stanford University, State University of New York/Stony Brook, University of Texas/Austin, University of Texas/Dallas, Texas A&M University, Tufts University, University of Virginia, and College of William and Mary.

2. M. Apollonio et al., Limits on neutrino oscillations from the CHOOZ experiment, *Phys. Lett.* **B466**, 415–430, (1999).
3. M. Apollonio et al., Search for neutrino oscillations on a long base-line at the CHOOZ nuclear power station, *Eur. Phys. J.* **C27**, 331–374, (2003).

Chapter 12

Double Chooz

Glenn A. Horton-Smith
Physics Department, Kansas State University, USA

Thierry Lasserre
CEA/DSM/DAPNIA/SPP & Laboratoire Astroparticule et Cosmologie (APC), Paris, France

Double Chooz is an experiment to search for the electron neutrino component of the third neutrino mass eigenstate (*i.e.*, a non-vanishing θ_{13} mixing angle) by measuring reactor antineutrino disappearance over a 1 km baseline. The experiment uses infrastructure at the site of the previous CHOOZ experiment, and is designed to measure the quantity $\sin^2 2\theta_{13}$ to a precision of better than ±0.02; if θ_{13} is small, then an upper limit of 0.03 (90% CL) will be established on $\sin^2 2\theta_{13}$.

Contents

12.1 Introduction 233
12.2 Scientific Goals 234
12.3 Historical Context 236
12.4 Laboratory and Detectors 236
    12.4.1 The Chooz Nuclear Power Station 236
    12.4.2 The Detectors 237
12.5 Measurement of Antineutrino Flux and the Mixing Angle θ_{13} 241
12.6 Connection with Other Experiments 244
12.7 Connection with Non-Proliferation 245
12.8 Conclusion 246
References 246

12.1. Introduction

Double Chooz is an experiment, currently under construction, which will consist of two liquid scintillator antineutrino detectors located ∼270 m and ∼1 km from the reactor cores at the CHOOZ nuclear power station in the Ardennes region of northern France. This is the same site which hosted the previous most sensitive θ_{13} experiment at this baseline, CHOOZ. The use of two detectors constructed to be as nearly identical as possible is the primary distinguishing characteristic of Double Chooz. By comparing the electron antineutrino flux at the two detectors, Double Chooz will be remarkably sensitive to transformation of electron antineutrinos into other neutrino flavors: up to 5 times more sensitive than CHOOZ. In particular, Double Chooz is designed to detect oscillations arising from a third mass eigenstate component of the electron antineutrino, whose amplitude is set by the magnitude of the U_{e3} element of the PMNS matrix, $|U_{e3}| = \sin\theta_{13}$.

The reactor antineutrinos are detected through the charged current interaction of antineutrinos with free protons, $\bar{\nu}_e + p \rightarrow e^+ + n$, commonly referred to as inverse beta decay. The signature of non-zero θ_{13} is the "disappearance" of some reactor antineutrinos over a distance of order 1 km.

In the sections below, we first review the scientific goals and historical context of the Double Chooz experiment. We then describe the experimental site, the detectors currently under construction, and the measurement to be made. We conclude by discussing connections with other experiments.

12.2. Scientific Goals

There is now convincing evidence for flavor conversion of atmospheric, solar, reactor and accelerator neutrinos[2–8] (See Chapters 2, 3, 4, 5 and 6). Thus, neutrinos do have mass, and neutrino oscillation is the most promising scenario to explain the data. Reactor neutrino experiments measure the survival probability $P(\bar{\nu_e} \rightarrow \bar{\nu_e})$ of the $\bar{\nu_e}$ emitted by nuclear power stations at a given distance (L). This disappearance probability does not depend on the Dirac CP phase δ. Furthermore, thanks to the combination of the MeV range neutrino energies (E) and the short baselines (less than a thousand kilometers) the modification of the oscillation probability induced by the coherent forward scattering from matter electrons (the so-called matter effect) can be neglected to first approximation. If neutrino masses satisfy $m_1 < m_2 < m_3$ (so-called "Normal Hierarchy"), the survival probability can be written:

$$\begin{aligned} 1 - P(\bar{\nu_e} \rightarrow \bar{\nu_e}) = 4\sin^2\theta_{13}\cos^2\theta_{13}\sin^2\frac{\Delta m^2_{31}L}{4E} &+ \\ \cos^4\theta_{13}\sin^2(2\theta_{12})\sin^2\frac{\Delta m^2_{21}L}{4E} &- \\ 2\sin^2\theta_{13}\cos^2\theta_{13}\sin^2\theta_{12}\left(\cos\frac{(\Delta m^2_{31} - \Delta m^2_{21})L}{2E} - \cos\frac{\Delta m^2_{31}L}{2E}\right)&. \quad (12.1) \end{aligned}$$

The first two terms of the right hand side of Equation 12.1 are, respectively, the atmospheric ($\Delta m^2_{31} = \Delta m^2_{atm}$) and solar driven ($\Delta m^2_{21} = \Delta m^2_{\odot}$) oscillations, while the third term is an interference between both contributions.[9] We note here that θ_{13} is the mixing angle that couples the electron field to the heaviest neutrino field (in the normal hierarchy). If $\Delta m^2_{\odot} << \Delta m^2_{atm}$ and/or θ_{13} is small enough, the solar driven and the atmospheric driven neutrino oscillations decouple. The mixing is then radically simplified, leading to the two neutrino mixing formula:

$$1 - P(\bar{\nu_e} \to \bar{\nu_e}) = \sin^2 2\theta_{ij} \sin^2 \left(1.27 \frac{\Delta m^2_{ij}[eV^2]L[m]}{E_{\bar{\nu_e}}[MeV]} \right) . \qquad (12.2)$$

For the reactor neutrino oscillations we can consider two extreme cases: $\Delta m^2_{ij} = \Delta m^2_{21}$ and $\theta_{ij} \sim \theta_{\odot}$ if the baseline considered exceeds a few tens of kilometers, and $\Delta m^2_{ij} = \Delta m^2_{31}$ and $\theta_{ij} = \theta_{13}$ if it is does not exceed a few kilometers. The latter is the case of Double Chooz.

Considering only the three known families, the neutrino mixing matrix is parametrized by three mixing angles. The angle θ_{12} has been measured to be large, $\sin^2(2\theta_{12}) \sim 0.8$, by the combination of the solar neutrino experiments and KamLAND[6] (See Chapters 2, 3, and 4). The angle θ_{23} has been measured to be close to maximum, $\sin^2(2\theta_{23}) > 0.9$, by atmospheric neutrino experiments[2] as well as the long baseline accelerator neutrino experiments K2K[7] and MINOS[8] (See Chapters 2, 5, and 6). However, we only have an upper limit to the mixing angle θ_{13}, given mainly by the CHOOZ experiment, $\sin^2(2\theta_{13}) < 0.2$. The large values of both θ_{12} and θ_{23} indicate a significant difference between leptonic and quark mixing, whereas the smallness of θ_{13} testifies to the peculiarity of the neutrino sector. The value of θ_{13} is not only of fundamental interest to understand leptonic mixing, but it is also necessary to plan for the future experimental program in neutrino physics, since CP-violating effects are scaled by $\sin^2 \theta_{13}$.

New accelerator neutrino beams coupled with off-axis detectors, will search for a ν_e appearance signal (See Chapters 10 and 11). The observation of a ν_e excess in an almost pure ν_μ neutrino beam would be evidence for a non-vanishing θ_{13}. But on the top of the statistical and systematic uncertainties, correlations and degeneracies between θ_{13}, θ_{12}, sign(Δm^2_{31}), and the CP-violating δ phase degrade the accessible knowledge on θ_{13}.[10] Both reactor and accelerator programs will provide complementary results to better constrain the last undetermined parameters.

12.3. Historical Context

The CHOOZ experiment was located in the Ardennes region of France, 1050 m away from the double unit Chooz nuclear reactors (PWR, 8.4 Gigawatt Thermal Power, or $\mathrm{GW_{th}}$). The detector was housed in an underground laboratory below a 100 m rock overburden, or 300 m of water equivalent (mwe), providing, for the first time at a reactor, a strong reduction of the cosmic ray induced backgrounds. The homogeneous detector was filled by a 5 ton Gd-doped liquid scintillator target, surrounded by a thick active (scintillating) buffer and a muon veto. The external tank was surrounded by an additional layer of low radioactivity sand. This composition of shielding moderates neutrons induced by muons outside of the detector as well as the γ's produced by the rocks. Since the two Chooz reactors were commissioned after the start of the experiment, there was a unique opportunity to perform an in-situ background measurement.

The Palo Verde experiment was located in an underground bunker under 12 meters of rock (32 mwe), 750 and 890 meters away from a 3-unit nuclear power station (11.6 $\mathrm{GW_{th}}$) in the Arizona desert. The low overburden required the use of a segmented detector to reduce the background. It was composed of 66, 9 meter acrylic cells filled with a Gd-doped liquid scintillator, surrounded by 1 meter of water shielding and an efficient liquid scintillator muon veto.

Neither CHOOZ nor Palo Verde observed any evidence of neutrino oscillation. The results could be presented as the energy averaged ratio (R) between $\bar{\nu_e}$ detected and expected with $R_{CHOOZ} = 1.01 \pm 2.8\%\ (stat.) \pm 2.7\%\ (syst.)$ and $R_{PaloVerde} = 1.01 \pm 2.4\%\ (stat.) \pm 5.1\%\ (syst.)$. Both experiments excluded any $\bar{\nu_e} \to \bar{\nu_x}$ oscillation driven by $\Delta m^2_{atm} \sim 10^{-3}\ eV^2$, except for small mixing. Assuming the conservation of CPT, they excluded the $\nu_\mu \to \nu_e$ oscillation solution in the Kamiokande experiment.[2] The CHOOZ experiment still provides the world's best constraint on the θ_{13} mixing angle: $\sin^2(2\theta_{13}) < 0.14$, at $\Delta m^2_{atm} = 2.5 \times 10^{-3}\ eV^2$.[16]

12.4. Laboratory and Detectors

12.4.1. *The Chooz Nuclear Power Station*

Both of the Double Chooz experimental halls and related support buildings are sited within the boundaries of the Chooz nuclear power station, which is operated by Électricité de France (EDF). Access to the site is provided courtesy of EDF, and is generally available during customary working hours, with access at other times available by special arrangement. Remote operability is planned for most subsystems of the experiment. Two 4.27 GWth reactor cores are operated at this site. Each has operated since 2001 with a cumulative load factor exceeding 75%,[19] including 60 days of planned shutdown per year per core for refueling and maintenance.[20]

Double Chooz is re-using the same underground tunnel previously used for the completed CHOOZ experiment. This location is approximately 1000 m from the reactor cores, and is covered by 300 mwe of 2.8 g/cm^3 rock overburden. This location is known as the far experimental hall. A pit 7 meters deep and 7 meters in diameter housed the CHOOZ detector; the old detector, tank, and low-activity sand have been removed, making way for the far detector and its shielding to be installed.

The collaboration is currently investigating two possible locations to host the near detector: the first at the bottom of a 40 m deep shaft, 300 m away from the nuclear cores (80 mwe overburden), and the second 400 m away from the cores, at the end of a 150 m long tunnel (110 mwe overburden). A final decision awaits the completion of on-going borehole studies.

12.4.2. *The Detectors*

The Double Chooz detector is shown schematically in Fig. 12.1. The same design is used for the central detectors at the near and far site. In this design, a target of Gd loaded liquid scintillator is contained within an acrylic vessel. Antineutrinos interact with free protons in the target to form neutrons, which produce gamma rays when they capture on Gd, and positrons. A layer of unloaded liquid scintillator surrounds the target to improve the neutron capture detection efficiency and to reduce systematic errors associated with neutron diffusion in and out of the target. A layer of non-scintillating oil provides shielding against external radioactivity. Phototubes in the oil buffer detect light emitted by the scintillator. A 3-mm-thick stainless steel tank contains the buffer oil, provides support for the photomultiplier tubes, and provides a barrier against light, gasses, and liquids from outside the central detector.

The liquid scintillator for the target uses a mixture of phenyl-xylylethane (PXE) and dodecane as its base, plus wavelength shifter and a soluble Gd complex, with a Gd concentration of 1.00 g/L. The gamma catcher scintillator uses a mixture of PXE, dodecane, and mineral oil, with wavelength shifter but without the Gd complex, to match the density and

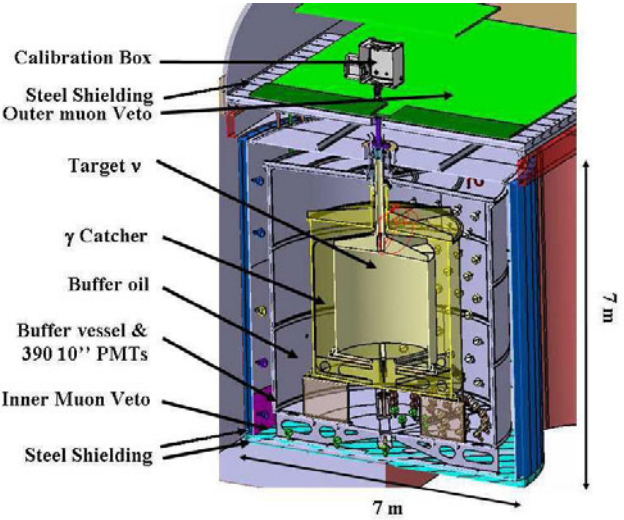

Fig. 12.1. Cutaway rendering of the Double Chooz detector. Figure produced by CEA/DSM/DAPNIA/SIS.

light yield of the Gd-loaded target scintillator. The yield matching is based on a detailed model of the scintillation and self-quenching mechanisms.[21] The non-scintillating buffer liquid is a mixture of dodecane and mineral oil, matched in density to the other liquids. The target density of all liquids is 0.800 g/mL. A summary of detector liquid composition is given in Table 12.1.

Table 12.1. Liquids in the central detector.

Region	Volume (m^3)	Design content
Target	10.3	20 v% PXE + 80 v% dodecane + waveshifter + Gd complex
Gamma catcher	22.6	5 v% PXE + 60 v% dodecane + 35 v% mineral oil + waveshifter
Buffer	114.2	43 v% dodecane + 57 v% mineral oil

The detector design includes a "veto" region filled with liquid scintillator surrounding the central detector, as shown in Fig. 12.1. This region is optically and mechanically separated from the central detector by the stainless steel tank containing the central detector, and is contained within a 10 mm thick steel tank which isolates it from the exterior environment. Phototubes detect light from muons and high energy particle interactions in the veto scintillator. Note that this “veto detector” will not be used to veto any triggers at the hardware or DAQ level, but rather the data from the “veto” will be acquired and stored along with inner detector data, to be used for removing muon-related backgrounds in later analysis.

The Double Chooz detector design includes a 150 mm thick layer of demagnetized, low radioactivity steel surrounding the inner veto, shielding the detector against radioactivity from the surrounding rock. The steel shield is composed of many long bars of steel, and covers the bottom, sides, and top, as seen in Fig. 12.1. This steel replaces the low activity sand used in CHOOZ, and allows the Double Chooz detectors to be larger than the CHOOZ detector.

An outer muon detector is to be placed above and extend beyond the inner detectors and steel shielding. This detector subsystem is to consist of layers of MINOS-style scintillator bars. Data from this system will allow direct measurement of the efficiency of the inner veto and central detector for grazing muons, improve the tracking resolution of muons, and enable the study of muon-induced backgrounds from muons that miss the inner veto detector.

The primary Double Chooz readout is based on 8-channel, 8-bit, 500 MS/s digitizer modules, co-developed by the Laboratoire Astroparticule et Cosmologie (APC) and Costruzioni Apparecchiature Elettroniche Nucleari (CAEN) corporation, now commercially available as the CAEN V1721. These modules continuously digitize and record to an internal ring buffer of ring buffers (1024 buffers, 1024 samples each); each ring buffer is available for readout upon receipt of a signal from the trigger system.

For maximum control of detector efficiency, the trigger system is designed to give a trigger to the digitizers (“level 1 trigger”) on every energy deposit of more than 0.5 MeV in the inner detector or 5 MeV in the inner veto. The low-level readout software will implement a second level of trigger logic (“level 2 triggers”) which will determine whether to save the entire waveform of each phototube (such as delayed coincidences, possible antineutrino candidates) or only charge and time information from each phototube (such as muon crossings and isolated single events).

Muon crossing events deposit orders of magnitude more energy and occur in the near detector at a rate orders of magnitude higher than other events. Therefore, a second set of electronics is being provided to directly digitize and save the time and charge of every muon event. This scheme will be implemented for both the near and far detectors to preserve the identical nature of the two detector systems.

The inner veto uses the same electronics as the central detector, while the outer muon tracker will have its own readout, synchronized to the main electronics by a common time stamp and master clock.

Careful monitoring and control of the internal and external environments of the detectors is essential to maintaining the low systematic errors required for the experiment. To minimize fluctuations in the number of protons in the fiducial volume and to avoid excessive pressure on the thin acrylic vessels, it is necessary to monitor both the level of liquid in the chimney and the temperature of the inner detector liquid. To maintain stability in photomultiplier tube gain and efficiency, it is necessary to monitor the magnetic field in the inner detector, the photomultiplier high voltages, and the temperatures and voltages in the readout electronics. Monitoring of the external environment of the detectors, such as experimental hall temperatures, atmospheric pressure, radon level, power mains, and so on, also serves to eliminate potential sources of systematic error. These data will be collected by a variety of hardware systems, such as the popular low-cost Maxim/Dallas “1-Wire” network devices. Monitor data will be stored in a database designed to accommodate up to 5 years of monitor data with rapid random access through Structured Query Language (SQL). Software data sources, such as run conditions and data rates, will also be recorded in the database in real time.

The calibration of the detectors will be performed using a variety of sources and deployment systems designed to measure the energy scales and efficiencies of the detectors. Although some details are subject to improvement as of this writing, the system will certainly include deployment of gamma and neutron sources along the axis of symmetry of each detector, on-axis and peripheral laser and/or LED flashers, calibration using neutrons and ^{12}B from cosmic ray spallation, and (subject to final technical review) off-axis calibration using wires in small guide tubes attached to the acrylic vessels and/or full-volume calibration using an articulated arm.

The energy scales for positrons and neutron capture gammas will be calibrated primarily using the gamma sources. Uniformity of detector response will be established using the off-axis and full-volume sources. Based on detailed simulations including uncertainties in scintillator quenching and optical parameters, the maximum uncertainty on the absolute energy scales will be less than 1%; the relative uncertainty between detector energy scales will be substantially less.

Detector efficiencies will be calibrated to better than 0.5%, including neutron capture efficiency, gamma containment efficiency, dead time of various kinds, and all energy and time event selection cuts. The calibration program is designed to achieve this goal in the absolute sense for each detector, and to surpass it in the relative sense: the absolute efficiency uncertainty in each detector will be less than 0.5%, and the relative uncertainty will also be less than 0.5% (not 0.7%) due to cancellation of common systematic errors. Systematic errors are discussed further in the next section.

12.5. Measurement of Antineutrino Flux and the Mixing Angle θ_{13}

Like most reactor neutrino experiments, Double Chooz detects antineutrinos using the charged current interaction of antineutrinos with free protons: $\bar{\nu}_e + p \to e^+ + n$. This produces a characteristic delayed coincidence signature of a "prompt" energy deposit, arising primarily from e^+ energy loss and annihilation plus a small contribution from neutron kinetic energy loss, followed by a "delayed" energy deposit, arising from gamma rays emitted by neutron radiative capture on a nucleus. The total prompt energy deposit is equal to the energy of the antineutrino minus the difference in the neutron and proton mass, $E_{\text{prompt}} = E_{\bar{\nu}} - m_n + m_p = E_{\bar{\nu}} - 0.8$ MeV. With a gadolinium concentration of 1.00 g/L in the central target, most of the neutron captures will be on gadolinium, causing a delayed energy deposit of approximately 8 MeV shared among several gamma rays.

The inner detector electronics will digitize every energy deposit of more than 0.5 MeV in the inner detector, storing full information for all delayed coincidences and for a fraction of isolated single energy deposits, as well as summary information for all energy deposits. Using a time window of 100 μs (to select delayed coincidences) will limit backgrounds while maintaining a high efficiency and low systematic efficiency uncertainty for antineutrino events. Table 12.2 summarizes the expected antineutrino event rates and efficiencies in the two detectors.

Backgrounds for the experiment arise from many sources. Some arise from random coincidences of uncorrelated positron-like and neutron-like signals, so-called "accidental" backgrounds. The accidental background rate can be estimated quite accurately by measuring a fraction of the energy deposits which do not occur in temporal proximity to any other energy deposit. More difficult are correlated positron-like and neutron-like signals,

Table 12.2. Antineutrino event rates and efficiencies.

	Near detector	Far detector
Distance from West reactor (m)	290[a]	$1,114.6 \pm 0.1$
Distance from East reactor (m)	260[a]	998.1 ± 0.1
Detector efficiency	80%	80%
Dead-time efficiency	70%[b]	97%
Reactor efficiency	78%	78%
Rate without efficiency (d^{-1})	1012[b]	68.8
Rate w. detector & dead-time efficiency (d^{-1})	566[b]	53.4
Integrated rate (y^{-1})	161,260[b]	15,200

[a] Near detector distances quoted from preliminary design; actual near detector distance will be 300 or 400 m. (See text.)

[b] Actual near detector dead-time, rate, and integrated rate will vary depending on final near site selection.

Table 12.3. Backgrounds.

Detector	Site		Background			
			Accidental		Correlated	
			Materials	PMTs	Fast n	^{9}Li
CHOOZ	Far	Rate (d^{-1})	0.42 ± 0.05		$1.01 \pm 0.04 \pm 0.1$	
		bkg/ν	1.6%		4%	
		systematics	0.2%		0.4%	
Double Chooz (69 ν/d)	Far	Rate (d^{-1})	0.5 ± 0.3	1.5 ± 0.8	0.2 ± 0.2	1.4 ± 0.5
		bkg/ν	0.7%	2.2%	0.2%	1.4%
		systematics	<0.1%	<0.1%	0.2%	0.7%
Double Chooz (1012 ν/d)	Near	Rate (d^{-1})	5 ± 3	17 ± 9	1.3 ± 1.3	9 ± 5
		bkg/ν	0.5%	1.7%	0.13%	0.9%
		systematics	<0.1%	<0.1%	<0.1%	0.5%

which arise primarily from cosmic ray interactions. Cosmic rays outside the detector may produce one or more energetic neutrons, which may travel into the detector, deposit energy in a positron-like event, and subsequently capture. Cosmic rays passing through the detector may produce relatively long-lived beta-delayed-neutron emitting isotopes, in particular ^{9}Li, which later emit an electron and a neutron in coincidence, closely mimicking the antineutrino signal. The inner and outer veto systems and the inner detector muon electronics are all designed to address these correlated backgrounds. Table 12.3 summarizes the expected background rates and uncertainties

Table 12.4. Systematic errors.

		CHOOZ	Double Chooz
Reactor Solid Angle		—	0.06%
Free H in target	Volume	0.3%	0.2%
	Fiducial Volume	0.2%	negligible
	Density		negligible
	H/C	0.8%	negligible
Electronics	Dead Time	—	negligible
Positron	Escape	0.1%	negligible
	Energy Cut	0.8%	negligible
Neutron	Escape	1.0%	negligible
	Capture (% Gd)	0.85%	0.3%
	Energy Cut	0.4%	0.2%
Antineutrino Coincidence	Time Cut	0.4%	0.1%
	Distance Cut	0.3%	not used
	Single neutron	0.5%	not used
Total		1.5%	0.5%

after tagging and measurement of these backgrounds. These estimates are based on data from the CHOOZ experiment as well as simulation.[18]

Table 12.4 summarizes the systematic uncertainties in the measurement of the antineutrino flux. We are able to obtain somewhat lower absolute systematic uncertainties than CHOOZ, allowing for an improvement on the current best limit even using only the far detector. However, the greatest improvement over previous reactor neutrino experiments is obtained using the cancellation of common systematics between the near and far detectors.

Because of the schedule of construction at the site, the Double Chooz experiment will proceed in two phases. In the first phase, only the far detector will be available. Double Chooz will be able to rapidly improve on the CHOOZ result in this phase due to a larger target volume and more stable reactor operation with respect to the earlier experiment. The second phase will commence after construction of the near detector. The sensitivity as a function of time under this scenario is shown in Fig. 12.2.

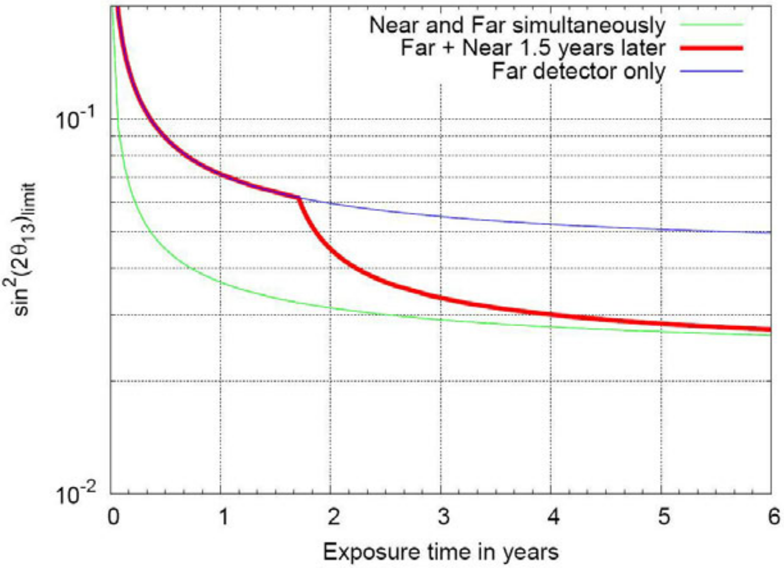

Fig. 12.2. The $\sin^2(2\theta_{13})$ sensitivity limit (90%CL) of Double Chooz assuming the real value of θ_{13} is zero and the near detector is built 1.5 years after the far detector.[18]

12.6. Connection with Other Experiments

Several sites are currently being considered for a new reactor experiment to search for θ_{13}:[17] Angra dos Reis (Angra, Brazil), Chooz (Double Chooz, France, and possibly Triple Chooz), Daya Bay (Daya Bay, China), Kashiwazaki (KASKA, Japan) and Yonggwang (RENO, Korea). All these experiments may be classified in two generations. The first aims to probe the value of $\sin^2(2\theta_{13})$ to $0.02-03$, and the second to track $\sin^2(2\theta_{13})$ down to 0.01 (90 % C.L.). The first phase concerns Double Chooz, RENO, and possibly Daya Bay (with its phase I). This phase should end by 2013. Angra, Daya Bay (nominal setup with 8 detectors), KASKA and possibly Triple Chooz are focusing on the second phase. For these second generation experiments, a significant R&D effort is required since the effective Gd-scintillator mass will be increased by, at least, one order of magnitude, and systematics, as well as background uncertainties, have to be further reduced with respect to the first phase experiments.

The Daya Bay experiment is the focus of Chapter 13. The RENO experiment[23], another promising phase II reactor experiment, will be located close to the Yonggwang nuclear power plant in Korea, about 400 km southeast of Seoul. The power plant is a complex of six reactors, each of them producing a thermal power of 2.73 GW, providing 16.4 $\mathrm{GW_{th}}$. These six reactors are equally distributed on a straight segment spanning 1.5 km. The average cumulative duty factors for the reactors are all above 80%. The near and far detectors will be located 150 m and 1,500 m away from the center of the reactor row, and will be shielded by a 88 m hill (230 m.w.e) and a 260 m "mountain" (675 m.w.e) respectively. Two neutrino laboratories have to be excavated and equipped in order to host the detectors. They will be located at the edge of two tunnels having a length of 100 m and 600 m for the near and far detector, respectively. With identical systematic errors as for Double Chooz, RENO could obtain a final sensitivity after 3 years of data taking of $\sin^2(2\theta_{13}) = 0.021$ at 90 % C.L.[24]

12.7. Connection with Non-Proliferation

As the verification authority of the Treaty on the Non-Proliferation of Nuclear Weapons (NPT), the International Atomic Energy Agency (IAEA) uses many different tools to inspect civil nuclear installations and related facilities under safeguard agreements in more than 140 states. Looking for innovative methods, the IAEA has asked member states to study the feasibility of using antineutrino detection methods to provide practical safeguard tools for selected applications.

The Double Chooz experiment is in a good position to evaluate many aspects of the use of antineutrino detection to monitor nuclear power stations. Indeed, without any extra experimental effort, the near detector of the Double Chooz experiment will provide a very large dataset of detected antineutrinos with remarkable energy calibration and flux normalization precision. The precise energy spectrum recorded at a given time will be correlated to the fuel composition and to the thermal power provided by the reactor operators. It is expected that individual components due to fissile elements (^{235}U, ^{239}Pu) could be extracted with some modest precision.

The IAEA recommends the study of specific safeguard scenarios; the small magnitude of the antineutrino signature of such scenarios requires careful feasibility studies, the details of which are beyond the scope of this article. Further discussion of this subject may be found in Refs. 27 and 25.

12.8. Conclusion

Double Chooz is now (May 2007) completing the final technical reviews prior to the start of its construction phase. The "far" detector will be installed in the existing underground laboratory starting in late 2007 or early 2008. The nearly identical "near" detector will be constructed in a new neutrino laboratory that will be excavated 300 or 400 m from the cores. The Double Chooz experiment will substantially improve our knowledge of θ_{13}, first using the far detector alone, and then using the far and near detectors, ultimately achieving a 90% CL sensitivity of 0.03 on $\sin^2 2\theta_{13}$.

References

1. The Double Chooz collaboration is composed of institutions from Brazil, France, Germany, Japan, Russia, Spain, United Kingdom, and United States. 32 institutions are participants in the experiment: CBPF Rio, AstroParticule et Cosmologie (APC), DAPNIA CEA/Saclay, Subatech Nantes, University of Aachen, Universität Hamburg, Max Planck Institut für Kernphysik Heidelberg, Technischen Universität München, Eberhard-Karls Universität Tübingen, Hiroshima Institute of technology, Kobe University, Miyagi University of Education, Niigata University, Tohoku University, Tohoku Gakuin University, Tokyo Institute of Technology, Tokyo Metropolitan University, Institute for Nuclear Research RAS, Institute of Physical Chemistry RAS, RRC Kurchatov Institute, CIEMAT Madrid, University of Oxford , University of Sussex, University of Alabama, Argonne National Laboratory, Drexel University, Illinois Institute of Technology, Kansas State University, Lawrence Livermore National Laboratory, University of Notre Dame, Sandia National Laboratories, University of Tennessee. A full list of collaborators may be found in the full collaboration proposal.[18]
2. Y. Fukuda *et al.*, Phys. Rev. Lett. **81** (1998) 1562.
3. S. Fukuda *et al.*, Phys. Rev. Lett, **86** (2001) 5656 ; S. Fukuda *et al.*, Phys. Lett. B**539** (2002) 179.
4. Q.R. Ahmad *et al.*, Phys. Rev. Lett. **89** (2002) 011301 ; Q.R. Ahmad *et al.*, Phys. Rev. Lett. **89** (2002) 011302.
5. S.N. Ahmed *et al.*, nucl-ex/0309004 (2004).
6. K. Eguchi *et al.*, Phys. Rev. Lett. **90** (2003) 021802.
7. M.H. Ahn *et al.*, Phys. Rev. Lett. **90** (2003) 041801.
8. D.G. Michael *et al.*, Phys. Rev. Lett. **97** (2006) 191801
9. S. Schönert, Th. Lasserre and L. Oberauer, Astropart. Phys. **18** (2003) 565.
10. P. Huber *et al.*, Nucl. Phys. B**665** (2003) 487.
11. G. Zacek *et al.*, Phys. Rev. D**34** (1986) 2621.
12. A.F. Afonin *et al.*, Sov. Phys. JETP Lett. **66** (1988) 213.
13. G.S. Vidyakin *et al.*, JETP Lett. **59** (1994) 390.
14. B. Achkar *et al.*, Nucl. Phys. B**434** (1995) 503.

15. Y. Déclais et al., Phys. Lett. B**338** (1994) 383.
16. M. Apollonio *et al.*, Eur. Phys. J. C**27** (2003) 331.
17. K. Anderson *et al.*, "White Paper For a New Reactor Neutrino Experiment for θ_{13}", hep-ex/0402041 (2004).
18. F. Ardellier *et al.* (Double Chooz Collaboration), hep-ex/0606025 (2006); F. Ardellier *et al.* (Double Chooz Collaboration), hep-ex/0405032 (2004); S. Berridge *et al.* (Double Chooz Collaboration), hep-ex/0410081 (2004).
19. Power Reactor Information System database (PRIS), International Atomic Energy Agency, `http://www.iaea.org/programmes/a2/`, browsed March 27, 2007.
20. International Nuclear Safety Center (INSC), Argonne National Laboratory, `http://www.insc.anl.gov/`, browsed March 27, 2007.
21. C. Buck, F. Hartmann, D. Motta, and S. Schoenert, Chem. Phys. Lett. 435 (2007) 262-256.
22. X. Guo [Daya Bay Collaboration], hep-ex/0701029. Yifang Wang, hep-ex/0610024. Seminar of D. Jaffe at CEA/Saclay on October 23 2006, `www-dapnia.cea.fr/Phocea/file.php?class=std&file=Seminaires/1425/1425.pdf`
23. `http://neutrino.snu.ac.kr/RENO/`
24. G. Mention, Th. Lasserre, D. Motta, arXiv:0704.0498 [hep-ex] (2007).
25. M. Cribier, proceedings of the XXII International Conference On Neutrino Physics And Astrophysics (Neutrino 2006), Santa Fe, USA (2006); also arXiv:0704.0891v1 [nucl-ex].
26. A. Bernstein, Y. Wang, G. Gratta, and T. West, J. Appl. Phys. 91, 4672 (2002)
27. P. Huber and T. Schwetz, Phys.Rev. D70 (2004) 053011; also arXiv:hep-ph/0407026v2.

Chapter 13

Daya Bay: A Sensitive Determination of θ_{13} with Reactor Antineutrinos

K. B. Luk

University of California and Lawrence Berkeley National Laboratory,
Berkeley, CA 94720, USA
k_luk@lbl.gov

Y. Wang

Institute of High Energy Physics,
Yu-Quan Road 19, 100049, Beijing, China
yfwang@ihep.ac.cn

Daya Bay is a reactor neutrino oscillation experiment designed to determine the least-known neutrino mixing angle θ_{13} with a sensitivity of 0.01 or better in $\sin^2 2\theta_{13}$ at the 90% confidence level, an improvement over the current limit by more than one order of magnitude. The goal will be accomplished in a three-year run by measuring the relative rates and energy spectra of reactor electron antineutrinos with multiple detectors positioned at different baselines.

Contents

13.1 Introduction 250
13.2 Methodology 250
13.3 Design of Experiment 252
    13.3.1 Experimental Layout 252
    13.3.2 Antineutrino Detectors 253
    13.3.3 Muon System 255
13.4 Background 256
13.5 Systematic Uncertainties 256
13.6 Sensitivity 257
13.7 Status and Plan 258
References 259

13.1. Introduction

Recently there has been intense interest in measuring the value of the neutrino mixing angle θ_{13}, which determines the contribution of the mass eigenstate ν_3 to the weak eigenstate ν_e. Unlike the other two mixing angles, θ_{13} known to be small, less than $\sim 10°$.[1] Besides being an important ingredient for mapping out the neutrino mixing matrix that will guide the building of theoretical models for physics beyond the standard model, the value of θ_{13} has significant implications for measuring the CP-violating phase δ_{CP}. If $\sin^2 2\theta_{13}$, the amplitude of the sub-dominant oscillation, is greater than 0.01, the design of future CP-violation experiments in the neutrino sector is within present capabilities;[2] otherwise, new experimental approaches and accelerator technologies will be required. It is thus highly desirable to measure $\sin^2 2\theta_{13}$ to the level of 0.01, which is the primary goal of the Daya Bay reactor antineutrino experiment. A comprehensive discussion of the Daya Bay experiment can be found in Ref. 3.

13.2. Methodology

An operating nuclear reactor is a copious source of low-energy electron antineutrinos that come from the beta decays of radioisotopes. These unstable isotopes are created in the fission processes involving primarily $^{235}\mathrm{U}$, $^{238}\mathrm{U}$, $^{239}\mathrm{Pu}$, and $^{241}\mathrm{Pu}$ in the reactor core. The antineutrino can be detected with a liquid scintillator detector via its inverse beta-decay reaction $\overline{\nu}_e + \mathrm{p} \rightarrow \mathrm{e}^+ + \mathrm{n}$ that has a threshold of 1.8 MeV. Typically, a 3 $\mathrm{GW_{th}}$ reactor generates about 1.5×10^{20} $\overline{\nu}_e$'s per second, with energy between 1.8 MeV and 8 MeV. As the fuel is consumed, the mix of radioisotopes changes, leading to a time-dependent energy distribution for the antineutrinos.

In a reactor-based antineutrino experiment the measured quantity is the survival probability for $\bar{\nu}_e \rightarrow \bar{\nu}_e$ which is given by

$$\begin{aligned} \mathrm{P_{sur}} \approx 1 - \sin^2 2\theta_{13} \sin^2\left(\frac{\Delta \mathrm{m}^2_{31}\mathrm{L}}{4\mathrm{E}}\right) \\ - \cos^4\theta_{13} \sin^2 2\theta_{12} \sin^2\left(\frac{\Delta \mathrm{m}^2_{21}\mathrm{L}}{4\mathrm{E}}\right). \end{aligned} \tag{13.1}$$

At the first oscillation maximum due to θ_{13}, occurring at $\mathrm{L} \approx 1.8$ km with E integrated from 1.8 MeV to 8 MeV, the size of the θ_{12} term is about 25% of the θ_{13} term for $\Delta \mathrm{m}^2_{31} = 2.5 \times 10^{-3}\mathrm{eV}^2$ and $\sin^2 2\theta_{13} = 0.01$. Yet, the θ_{12} term uncertainty leads to a systematic error of <0.005 for $\sin^2 2\theta_{13}$.

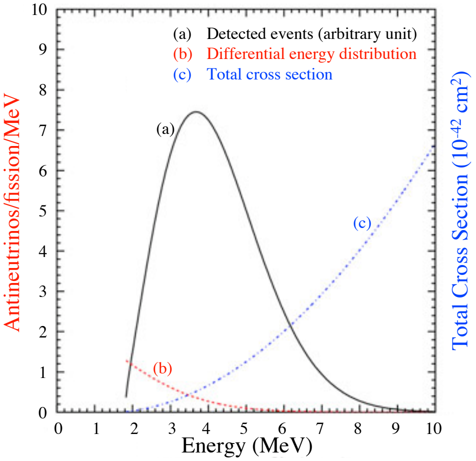

Fig. 13.1. Differential energy distribution of reactor antineutrinos, total cross section of the inverse beta-decay reaction, and the number of detected antineutrinos as a function of the antineutrino energy.

The value of $\sin^2 2\theta_{13}$ can be extracted by comparing the observed antineutrino rate and energy spectrum with the predictions with no oscillation. The number of detected antineutrinos, $\mathrm{N_{det}}$, shown in Fig. 13.1, is given by

$$\mathrm{N_{det}} = \frac{\mathrm{N_p}}{4\pi \mathrm{L}^2} \int \epsilon(\mathrm{E})\sigma(\mathrm{E})\mathrm{P_{sur}}\mathrm{S}(\mathrm{E})d\mathrm{E} \qquad (13.2)$$

where $\mathrm{N_p}$ is the number of free protons in the target, $\epsilon(\mathrm{E})$ is the detection efficiency, $\sigma(\mathrm{E})$ is the total cross section of the inverse beta-decay reaction, and $\mathrm{S(E)}$ is the differential antineutrino energy distribution at the reactor. In practice, in order to measure $\sin^2 2\theta_{13}$ precisely, all systematic uncertainties must be minimized. This criterion can be achieved by placing two detectors at two different locations.[4] In this case, the value of $\sin^2 2\theta_{13}$ can be extracted from the ratio of the numbers of detected events in the two detectors. For events with energy between E and E+dE detected at a distance $\mathrm{L_f}$ (far detector) and at a baseline $\mathrm{L_n}$ (near detector) the ratio is

$$\frac{\mathrm{N_f}}{\mathrm{N_n}} = \left(\frac{\mathrm{N_{p,f}}}{\mathrm{N_{p,n}}}\right)\left(\frac{\mathrm{L_n}}{\mathrm{L_f}}\right)^2\left(\frac{\epsilon_\mathrm{f}}{\epsilon_\mathrm{n}}\right)\left[\frac{\mathrm{P_{sur}}(\mathrm{E},\mathrm{L_f})}{P_{\mathrm{sur}}(\mathrm{E},\mathrm{L_n})}\right]. \qquad (13.3)$$

The remaining systematic uncertainties are the relative errors in the number of the protons, the detection efficiency, and the distances from the reactor. These relative errors can be determined more precisely than the individual absolute values.

Another important consideration is the reduction of background. Since the signal rate is low, it is desirable to conduct the experiment underground to reduce cosmic-ray induced background.

13.3. Design of Experiment

The design involves optimizing baselines, choosing the detector technology and geometry, and optimizing the shielding of the detectors.

13.3.1. *Experimental Layout*

The Daya Bay experiment will be set up at the Daya Bay nuclear power complex which is about 45 km east of Shenzhen City in China. There are three nuclear power plants in this complex: Daya Bay, Ling Ao, and Ling Ao II, which is under construction and will be operational by 2010–2011. Each plant has twin reactors such that each core can generate 2.9 $\mathrm{GW_{th}}$ during normal operation. The Ling Ao cores are about 1.1 km east of the Daya Bay cores, and about 400 m west of the Ling Ao II cores. There are mountain ranges to the north which provide the required overburden.

We plan to build one far and two near sites. One near site is primarily for housing detectors for monitoring the Daya Bay cores and the other is for the four Ling Ao cores. In optimizing the baselines, the event rate, oscillation probability, overburden, background and estimated systematic uncertainties are taken into account. Cross-contribution of events from the other cores is also included. A carefully optimized layout for the experiment is shown in Fig. 13.2. The Daya Bay near site with a vertical overburden of 98 m (255 m.w.e.) is located at 363 m from the center of the Daya Bay cores whereas the Ling Ao near hall with an overburden of 112 m (291 m.w.e) is 481 m from the Ling Ao cores, and 526 m from the Ling Ao II cores. The distances from the far site, which has an overburden of 350 m (910 m.w.e), to the midpoint of the Daya Bay cores and to the Ling Ao–Ling Ao II cores are 1985 m and 1615 m respectively.

The experimental halls are connected with three horizontal tunnels fanning out near the mid site. The Daya Bay near site is accessed from the entrance portal with a 292 m long, 9.6%-grade access tunnel. The construction tunnel is used for removing debris during excavation. The antineutrino detectors will be assembled in the surface assembly building near the entrance and be filled with scintillator and buffer oil in the underground filling hall.

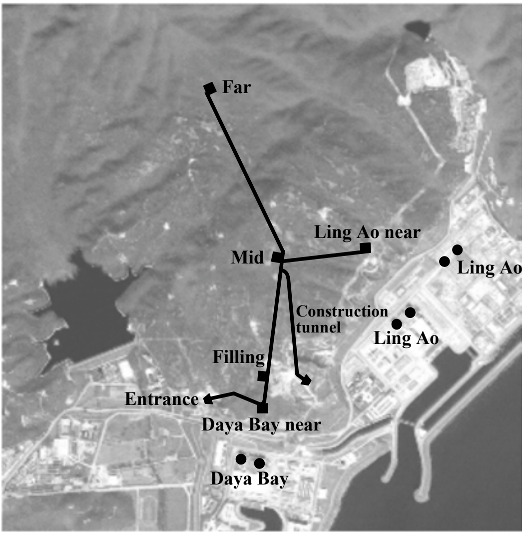

Fig. 13.2. Layout of tunnels and underground experimental halls.

13.3.2. *Antineutrino Detectors*

We intend to build eight identical antineutrino detectors. Four of them will be deployed to the far site, and each near hall will receive two. Having at least two detectors at each site permits internal consistency checks. In addition, smaller detectors intercept fewer cosmic-ray muons, resulting in less cosmogenic background and less dead time.

As shown in the top panel of Fig. 13.3, each detector consists of three vertical concentric cylinders. The 3.1 m tall and 3.1 m diameter innermost vessel filled with 20 tonnes of Gd (0.1% by weight) loaded Linear Alkyl Benzene (LAB) based liquid scintillator is the antineutrino target which is embedded inside an acrylic vessel filled with unloaded LAB-based liquid scintillator. This approximately 40-cm-thick zone between the two acrylic tanks, called the gamma-catcher, is used to capture the gamma rays from the antineutrino events that leak out of the target. This arrangement substantially reduces the systematic uncertainties in the fiducial volume, a positron energy cut near threshold, and a possible position cut. The outermost zone between the steel tank and the outer acrylic tank, filled with mineral oil, shields against external gamma rays entering the active scintillator volume. A total of 192 20-cm photomultiplier tubes (PMTs) arranged in eight horizontal rings are installed along the inner surface of the

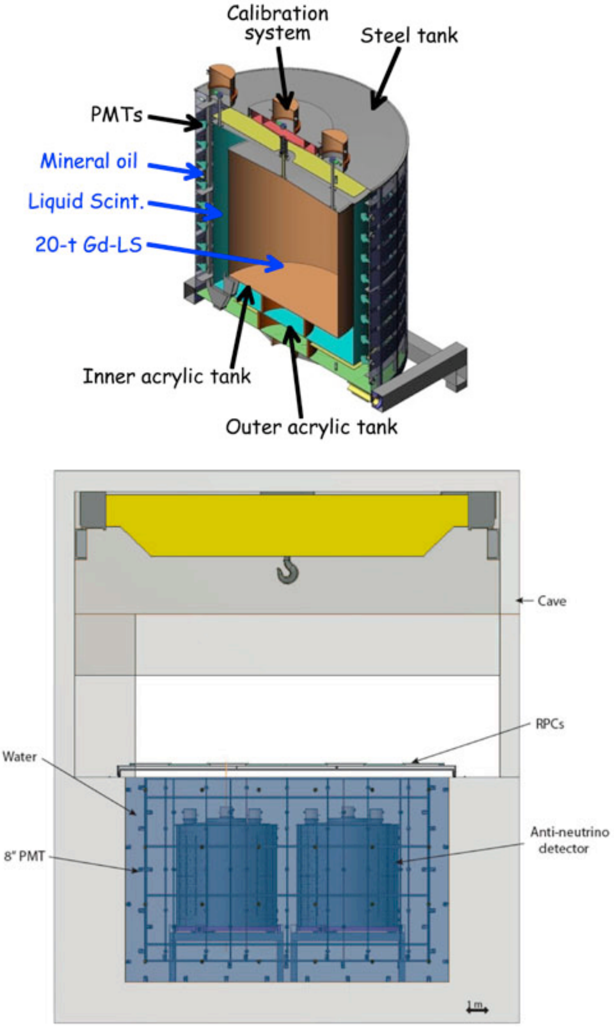

Fig. 13.3. (Top) A cross section of the antineutrino detector. (Bottom) The cross section of the experimental hall.

5 m tall and 5 m diameter steel tank. The effective photocathode coverage is increased to about 12% by placing optical reflectors at the top and the bottom of the gamma-catcher. Simulations indicate this will yield about 105 detected photoelectrons per MeV, and an energy resolution of about $12\%/\sqrt{\mathrm{E}}$.

The antineutrino detectors are enclosed by at least 2.5 m of purified water in a pool as shown in the bottom of Fig. 13.3. The gamma rays and spallation neutrons emerging from the surrounding granite walls are attenuated by 10^5 and one order of magnitude respectively.

13.3.3. *Muon System*

Since the majority of the background is induced by cosmic-ray muons interacting with materials in the vicinity of, and inside the detector, each experimental hall will be instrumented with a muon system that consists of Resistive Plate Chambers (RPCs) placed above a radon-shielded cover of the water pool which is also used as a Cherenkov counter. This kind of redundancy allows the detectors to determine the efficiency of each other.

As shown in Fig. 13.3, the water pool is optically isolated into inner and outer sections with Tyvek films. The inner partitions are populated with 20 cm PMTs facing the antineutrino detectors. For the 1 m thick outer sections, the PMTs are offset and are facing each other. The density of PMTs provides about 0.8% photocathode coverage for both sections. Assuming a singles rate of 50 kHz per PMT and limiting the dead time of the random coincidence to $<1\%$, the efficiency of the inner Cherenkov in identifying a muon is better than 98% when the multiplicity of hit PMTs is ≥ 12. Using the same criterion for the random rate, the efficiency of the outer Cherenkov with a minimal hit-PMT multiplicity of 13 is close to 99%. The inefficiency in both Cherenkov counters is due to corner-clipping muons that have a short path length in the water.

The RPCs will be made of a new kind of phenolic paper laminate developed at IHEP, Beijing. Each RPC having either x or y readout strips operates in the streamer mode with a noise rate of 1.6 kHz/m^2. The expected efficiency of the RPC is about 98% at 8 kV for a threshold of 150 mV. Four RPCs, electrically shielded from one another to avoid cross talk, are combined to form a module such that each module will provide two x and two y measurements of a muon. By requiring three out of the four RPCs to have hits, the tracking efficiency of a module is calculated to be about 99%.

The total efficiency of the muon system in identifying a muon is expected to be about 99.5%. We shall measure this efficiency to a precision of 0.25%.

13.4. Background

There are two classes of background: uncorrelated and correlated background. The uncorrelated background is the accidental coincidence of a gamma ray and a low-energy spallation neutron, where the gamma ray comes from natural radioactivity in the near-by materials. Correlated background can be due to a fast neutron that has interacted with a proton before it is captured, or the beta-neutron decay of ^{8}He and ^{9}Li produced by a muon reacting with a carbon nucleus in the antineutrino detector.

Using a modified Gaisser parametrization[3] for cosmic-ray muons at the surface, a three-dimensional profile of the Daya Bay site, and the MUSIC package[5] to transport the muons through the mountain, the muon intensity at each underground hall can be estimated. Based on the layout shown in Fig. 13.3, the natural radioactivity of materials, and the efficiency of tagging muons, the amount of background is then estimated and summarized in Tab. 13.1.

Table 13.1. Signal and background rates for each detector.

	Daya Bay Near	Ling Ao Near	Far Hall
Radioactivity (Hz)	<50	<50	<50
Muon rate (Hz)	36	22	1.2
$\overline{\nu}_e$ Signal (events/day)	930	760	90
Accidental/Signal (%)	<0.2	<0.2	<0.1
Fast neutron/Signal (%)	0.1	0.1	0.1
^{8}He+^{9}Li/Signal (%)	0.3	0.2	0.2

13.5. Systematic Uncertainties

Besides background, the other two major sources of systematic uncertainty stem from our understanding of the reactor and the detector. For Daya Bay, with multiple cores and several baselines, the systematic uncertainty due to reactor power is related to the difference in the fractions of events contributed by a given reactor to the near and far detectors.[3] Based on the baselines given in Sec. 13.3.1 and event rates shown in Tab. 13.1, a 2% uncertainty in the thermal power for each core leads to a reactor systematic uncertainty of 0.1% for six cores.

The relative uncertainty in the number of protons appearing in Eq. 13.3 can be controlled by building the detectors with tight tolerances. Mixing and filling of liquids will be done with a pair of near and far detectors together to ensure they have the same chemical composition. During filling, high-precision mass flow meters and load cells will be used to make sure the two detectors received equal amounts of liquid scintillator.

To reduce the uncertainty of the energy scale in the analysis, each detector will be stringently calibrated. The presence of spallation neutrons and cosmogenic radioisotopes allows continuous calibration. With automatic systems on top of the steel tank, radioactive sources and LEDs will be remotely deployed along the vertical axes of the target and the gamma-catcher volumes for routine calibration. Comprehensive calibration of the entire target volume will be carried out with sources using a manual system during commissioning.

Table 13.2 summarizes the estimated systematic uncertainties that have been investigated. The total systematic uncertainty is 0.38% per detector.

Table 13.2. Summary of systematic uncertainties.

Source	Uncertainty (%)
Energy cuts	0.2
Time cuts	0.1
H/Gd ratio	0.1
n multiplicity	0.05
Trigger	0.01
Live time	<0.01
Total detector-related uncertainty	0.38
Number of protons	0.3
Reactor power and location (6 cores)	0.126

13.6. Sensitivity

The sensitivity in $\sin^2 2\theta_{13}$ depends on the number of observed antineutrino events, systematic uncertainties, and the amount of background to be subtracted. The systematic uncertainties can be classified into correlated and uncorrelated uncertainties. Based on the layout shown in Fig. 13.2, the sensitivity is obtained by minimizing a χ^2 function with pull terms that account for the correlated uncertainties:

$$\chi^2 = \min_{\gamma} \sum_{\mathrm{A}=1}^{8} \sum_{\mathrm{i}=1}^{\mathrm{N_{bins}}} \frac{[\mathrm{M_i^A} - \mathrm{T_i^A}\left(1 + \alpha_\mathrm{c} + \sum_\mathrm{r} \omega_\mathrm{r}^\mathrm{A} \alpha_\mathrm{r} + \beta_\mathrm{i} + \varepsilon_\mathrm{D} + \varepsilon_\mathrm{d}^\mathrm{A}\right) - \eta_\mathrm{f}^\mathrm{A} \mathrm{F_i^A} - \eta_\mathrm{n}^\mathrm{A} \mathrm{N_i^A} - \eta_\mathrm{s}^\mathrm{A} \mathrm{S_i^A}]^2}{\mathrm{T_i^A} + (\sigma_\mathrm{b2b} \mathrm{T_i^A})^2}$$

$$+ \frac{\alpha_\mathrm{c}^2}{\sigma_\mathrm{c}^2} + \sum_\mathrm{r} \frac{\alpha_\mathrm{r}^2}{\sigma_\mathrm{r}^2} + \sum_{\mathrm{i}=1}^{\mathrm{N_{bins}}} \frac{\beta_\mathrm{i}^2}{\sigma_\mathrm{shp}^2} + \frac{\varepsilon_\mathrm{D}^2}{\sigma_\mathrm{D}^2} + \sum_{\mathrm{A}=1}^{8} \left[\left(\frac{\varepsilon_\mathrm{d}^\mathrm{A}}{\sigma_\mathrm{d}}\right)^2 + \left(\frac{\eta_\mathrm{f}^\mathrm{A}}{\sigma_\mathrm{f}^\mathrm{A}}\right)^2 + \left(\frac{\eta_\mathrm{n}^\mathrm{A}}{\sigma_\mathrm{n}^\mathrm{A}}\right)^2 + \left(\frac{\eta_\mathrm{s}^\mathrm{A}}{\sigma_\mathrm{s}^\mathrm{A}}\right)^2\right]$$

where A sums over the antineutrino detectors, i sums over energy bins, and $\gamma = \{\alpha_{\rm c}, \alpha_{\rm r}, \beta_{\rm i}, \varepsilon_{\rm D}, \varepsilon_{\rm d}^{\rm A}, \eta_{\rm f}^{\rm A}, \eta_{\rm n}^{\rm A}, \eta_{\rm s}^{\rm A}\}$ is a set of minimization parameters that are used to introduce the different sources of systematic uncertainties. Their corresponding uncertainties are reactor correlated error $\sigma_{\rm c} \approx 2\%$, reactor uncorrelated error $\sigma_{\rm r} \approx 2\%$, uncertainty in the antineutrino production spectrum $\sigma_{\rm shp} \approx 2\%$, detector correlated uncertainty $\sigma_{\rm D} \approx 2\%$, detector uncorrelated uncertainty $\sigma_{\rm d} = 0.38\%$, uncertainty in the number of fast neutrons $\sigma_{\rm f}^{\rm A}$, uncertainty in the accidental background $\sigma_{\rm n}^{\rm A}$ and uncertainty in the ^{8}He/^{9}Li background $\sigma_{\rm s}^{\rm A}$. The last three uncertainties are derived from Tab. 13.1. The term $\rm T_i^A$ is the expected number of events in the i-th energy bin in detector A, and $\rm M_i^A$ is the corresponding observed number of antineutrino events. The terms $\rm F_i^A, N_i^A, S_i^A$ are the number of fast neutron, accidental, and ^{8}He/^{9}Li events, respectively. For each energy bin, the variance comes from $\rm T_i^A$ and a bin-to-bin systematic uncertainty $\sigma_{\rm b2b}$. For each point in the oscillation space, the χ^2 function is minimized with respect to the set of parameters γ.

The efficiencies used to calculate $\rm T_i^A$ are 0.78 for neutron detection, and 0.98 for positron detection. The live time of each site related to vetoing muons is taken to be 0.95 for both the near and far detectors. The remaining live time of the experiment and the reactors is 0.82. For $\Delta m^2_{31} = 2.5 \times 10^{-3}$ eV^2, the expected sensitivity in $\sin^2 2\theta_{13}$ as a function of run time is shown to the left in Fig. 13.4.

We plan to collect over 300,000 antineutrino events at the far site in a three-year run. The dependence of $\sin^2 2\theta_{13}$ on Δm^2_{31} in this case is depicted to the right in Fig. 13.4. Daya Bay can reach and exceed the goal of determining $\sin^2 2\theta_{13}$ with a sensitivity of 0.01 at the 90% confidence level.

13.7. Status and Plan

The Daya Bay experiment was initiated in 2003. Since then it has grown into an international effort with over one hundred collaborators from China, the United States of America, Czech Republic, Hong Kong, Russia, and Taiwan.

In parallel to the design and fabrication of the apparatus, construction of the tunnels, experimental halls and the surface assembly building will begin in the summer of 2007. Operation of the first two detectors in the Daya Bay near hall is scheduled to take place in early 2009. This will provide an opportunity for studying background and systematic issues prior to data

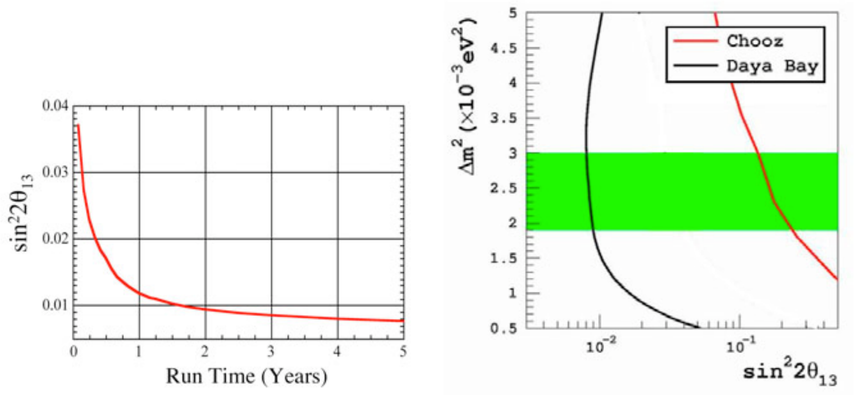

Fig. 13.4. To the left, the sensitivity in $\sin^2 2\theta_{13}$ verses run time (with $\Delta m^2_{31} = 2.5 \times 10^{-3}$ eV^2). To the right, the sensitivity in $\sin^2 2\theta_{13}$ against $\Delta \mathrm{m}^2_{31}$ for a 3-year run.

taking with all eight detectors in place in the summer of 2010. A three-year run reaching the designed sensitivity will be completed in 2013.

Acknowledgments

We are very grateful to our collaborators for their excellent contributions and numerous stimulating discussions. This work was supported in part by the Chinese Academy of Sciences, and the United States Department of Energy.

References

1. M. Apollonio *et al.* (Chooz Collaboration), *Eur. Phys. J.* **C27**, 331 (2003).
2. K. Anderson, *et al.*, White paper report on using nuclear reactors to search for a value of θ_{13}, arXiv:hep-ex/0402041.
3. X. Guo *et al.* (Daya Bay Collaboration), A Precision measurement of the neutrino mixing angle θ_{13} using reactor antineutrinos at Daya Bay, arXiv:hep-ex/0701029.
4. L.A. Mikaelyan and V.V. Sinev, *Phys. Atomic Nucl.* **63**, 1002 (2000).
5. P. Antonioli et al., *Astro. Phys.* **7**, 357 (1997).

Author Index

Autiero, D., 173

Brice, S. J., 155

Feldman, G. J., 217

Heeger, Karsten M., 71
Horton-Smith, G. A., 233

Komatsu, M., 173

Lasserre, T., 233
Louis, W. C., 135
Luk, K. B., 249

Migliozzi, P., 173

Parke, S. J., 1
Peeters, S. J. M., 45

Terranova, F., 173

Vahle, P., 115

Walter, C. W., 19
Wang, Y., 249
Wark, D. L., 197
Wilkes, R. J., 91
Wilson, J. R., 45

Subject Index

Cherenkov
  counter, 255
  detector, 20, 46, 74, 92, 199, 214
  radiation, 47, 140, 157, 199
  rings, 98, 212

Accelerator neutrino experiments, 91, 115, 135, 155, 173, 197, 217, 235
Angra, 244
Atmospheric neutrinos, 10, 22, 235

Beam extrapolation matrix, 127
Beta decay, 11, 72, 149, 178
  inverse, 35, 74, 234, 250
  neutrinoless double, 4
Bugey, 72, 147, 166

CERN SPS, 174
Chlorine solar neutrino oscillation experiments, 84
CHOOZ, 6, 32, 72, 191, 226, 233, 236
CHORUS, 101, 175, 177
CNGS, 174
Cowan, Clyde, 72
CP violation, 3, 12, 14, 32, 84, 169, 198, 214, 218, 235, 250
CPT invariance, 2, 79, 81, 87, 133, 236

Davis, Ray, 84
Day-night effect, 34, 35, 54
Daya Bay, 6, 228, 244, 249
Dirac neutrino, 4
DONUT, 176
Double Chooz, 6, 233

East-West effect, 27
Elastic scattering, 34, 46, 85, 159
Emulsion Cloud Chamber, 175

Far/Near ratio, 96, 104, 126
Fermilab Booster, 156, 225
Fermilab Main Injector, 116, 225

Gallex, 84
Geo-neutrinos, 77
Goesgen, 72

Hadron production, 96, 125, 158, 206
HARP, 95
Hyper Kamiokande, 214

ICARUS, 174
ILL, 72
IMB, 20, 22, 97
INGRID, 206
ISIS, 147

JPARC, 111, 198

K2K, 10, 22, 91, 174, 191, 198, 235
Kamioka, 20, 92, 214
Kamiokande, 19, 22, 24, 34, 236
KamLAND, 5, 71, 235
KARMEN, 135, 147, 156, 166
KASKA, 244
KEK, 92, 93
Krasnoyarsk, 72

LANSCE, 136
Large mixing angle (LMA), 8, 34, 58, 65, 79
LNGS, 174
Long base-line experiments, 91, 115, 197, 217, 235
LSND, 2, 13, 135, 155, 166

Majorana neutrino, 4
Mass hierarchy, 4, 12, 67, 218, 226, 234
Matter effect, *see* MSW effect
MiniBooNE, 14, 152, 155
MINOS, 10, 115, 174, 187, 198, 218, 223, 235, 239
MNS mixing matrix, 2, 198, 234
Monte Carlo Simulations
  FLUKA, 124
  GCALOR, 124
  GEANT, 95, 124, 158, 189
  NEUGEN, 124
  NEUT, 103, 210
  NUANCE, 158
MSW effect, 8, 28, 54, 65, 73, 79, 84, 218
MUNU, 72, 83

NA61, 206
Neutrino appearance, 3
  ν_e, 11, 30, 135, 155, 201, 217
  ν_τ, 28, 32, 173
Neutrino disappearance
  ν_e, 5, 32, 45, 71, 233, 234, 249
  ν_μ, 10, 24, 91, 115, 200, 213, 228
Neutrino magnetic moment, 35, 72, 82
NOνA, 10, 198, 217
NOMAD, 174, 207
NuMI, 116, 157, 187, 218, 224

Off-axis experiments, 197, 217, 235
OPERA, 173

Palo Verde, 6, 72, 236
PEANUT, 187
Pontecorvo, Bruno, 73
Proton decay, 20, 36

Q-Balls, 37
Quasi-elastic scattering, 92, 99, 104, 158, 179, 199, 229

Reactor neutrino experiments, 6, 71, 233, 249
Reines, Frederick, 72
RENO, 244

SciBar, 100

Scintillator
  bars, 97, 207
  fiber detector, 92
  light, 157
  liquid, 140
  liquid detector, 73, 74, 220, 233, 250
  plastic, 100, 118, 179, 206
Seasonal solar neutrino variation, 34
SNO, 8, 35, 45
Solar neutrinos, 7, 20, 32, 45, 57, 65, 72, 75, 79, 235
Spin-flavor precession, 35
Standard Model, 1
Standard solar model, 34, 57, 65
Sterile neutrino, 14, 28, 132, 156
Super-K, 10, 11, 19, 92, 174, 191, 198, 199, 209
Super-symmetry, 37
Supernova neutrinos, 37, 82

T2K, 10, 22, 111, 197
T2KK, 13, 214
Three flavor oscillations, 11, 30, 133, 191, 197, 217, 233, 234, 250
TOPAZ, 100

Upward-going muons, 25

Vacuum oscillation, 12, 72, 84

WIMP dark matter, 38, 82

Zenith angle suppression, 23